Experimental and Analytical Investigation of Seismic Performance and Retrofit Techniques for Non-Ductile RC Structural Walls

J. Ann Albright

Dissertation submitted to the Faculty of the
Virginia Polytechnic Institute and State University
in partial fulfillment of the requirements for the degree of

Doctor of Philosophy
in
Civil Engineering

Ioannis Koutromanos, Chair
Juan Murcia-Delso
Eric Jacques
Matthew R. Eatherton

May 6, 2025
Blacksburg, Virginia

Keywords: Shear Walls, Seismic Assessment, Retrofit, Lap-splice, Analytical Modeling

Experimental and Analytical Investigation of Seismic Performance and Retrofit Techniques for Non-Ductile RC Structural Walls

J. Ann Albright

(ABSTRACT)

Reinforced concrete (RC) walls are widely used as lateral-force-resisting systems. Despite the interest in retrofitting techniques, critical knowledge gaps remain regarding the reliability and validity of current retrofit design guidelines and procedures, particularly for barbell walls with single sided retrofit strategies, and barbell walls with inadequate lap splices. This dissertation is aimed at addressing this need through a combination of experimental and numerical investigations focused on non-ductile RC structural walls. Six non-ductile barbell experimental specimens were built and designed with varying retrofit strategies including single sided fiber reinforced polymer (FRP) overlay, single sided RC overlay, end wrapped bar buckling and lap splice confinement. Brittle shear deformation was precluded in the web through shear strengthening strategies, while bar buckling and lap splice slip were effectively prevented through the current ACI-440 design equations. The end wrapping strategies also had the unintended consequence of localizing strains to the base of their respective specimens, which resulted in a large number of fractured rebar.

The experimental results were compared to numerical models through the nonlinear truss analogy, which was adapted for this work to incorporate lap splice slip and overlay considerations. The experimental results were well estimated by this numerical modeling approach, achieving within 6% of the peak strength of all experimentally obtained values, as well as accurately predicting the failure modes. The nonlinear truss model is a computationally efficient and user-friendly implementation of a nonlinear finite element strategy.

A parametric study was undertaken on a set of 200 rectangular and barbell walls to assess the sensitivity of several parameters typical in older (pre-1970s) structural walls, as well as to compare two assessment methodologies: a set of strain-based criteria and the current ASCE-41 guidelines. The results of the parametric study indicate a reasonable ability of the strain-based methodology to consistently capture key performance metrics of the backbone curve while maintaining a similar statistical spread and trend to the performance metrics obtained through the ASCE-41 guidelines for most cases of flexurally-controlled walls. This indicates that the strain based failure criteria can be an equally effective method used to capture seismic behavior of older RC walls and may even be preferred as an alternative assessment procedure, since it relies on a local assessment framework which can be uniquely adapted for any structure or retrofit configuration.

Experimental and Analytical Investigation of Seismic Performance and Retrofit Techniques for Non-Ductile RC Structural Walls

J. Ann Albright

(GENERAL AUDIENCE ABSTRACT)

Reinforced concrete buildings are incredibly common structures around the world. They are also often found in historically active earthquake regions. It is imperative that these structures are strong enough and flexible enough to withstand large earthquakes without collapsing or having rapid collapses. Structures designed pre-1970s in the US are at an inherent deficit for adequate response during earthquake events due to their lack of sufficient steel in critical regions to maximize their deformability. Therefore, to increase the capacity and the safety of these structures this dissertation explored the retrofitting techniques of concrete overlay and fiber reinforced polymer wrap. Both of these techniques were found to be effective in strengthening the specimens and improving their ductile response during loading. Furthermore, numerical models were developed to gain a broad understanding of typical older wall structures and their failure patterns.

Dedication

To my parents and Matthew.

Acknowledgments

The research presented in this dissertation was supported by the National Institute for Standards and Technology (NIST) under grant No. 70NANB19H060N.

Generous support was also provided to me by the ACI Foundation, through their award of the ACI President's Fellowship, which provided financial support, as well as invaluable contacts, mentorship, and opportunity for this research, as well as my future career in this industry. The Charles E. Via Department of Civil and Environmental Engineering at Virginia Tech is also graciously acknowledged for their abundant support through the Charles E. Via Fellowship.

I'd like to acknowledge the help of a professional advisory panel in establishing the configuration of the tested specimens and of the retrofit overlays. The advisory panel consisted of the following persons (listed in alphabetical order): Gabriel Acero (AECOM, Orange, CA), Prof. Sergio Alcocer (UNAM, Mexico), Scott Arnold (Fyfe FRP, Houston, TX), Dr. Aniket Borwankar (Simpson Strong-Tie), Dr. Jazalyn Dukes (NIST), John Hooper (MKA, Seattle, WA), Dr. Insung Kim (Degenkolb Engineers, San Francisco, CA), Dr. Marios Panagiotou (NYASE, Los Angeles, CA), and Dr. Siamak Sattar (NIST).

Special thanks are due to Simpson Strong-Tie for donating all the material and labor required for application of the FRP retrofit measures in experimentally tested specimens. Thank you to the Commercial Metals Company (CMC) and Headed Reinforcement Corporation (HRC) for donations of reinforcing steel for the specimens, as well as Brett Lord from the Concrete Reinforcing Steel Institute (CRSI) for providing advice and information for securing donations of reinforcing steel bars.

Thank you to my primary advisor, Dr. Koutromanos, and the co-principle investigator for

this project, Dr. Murcia-Delso. Thank you for trusting me with this project. Thank you as well to the other members of my committee who offered thoughtful input and guidance, Dr. Jacques and Dr. Eatherton. I'd like to acknowledge the support of my fellow graduate students on this project, without whom the project could not have been completed. Thank you to Kevin Escobar for developing and running half of the analytical models, namely the barbell wall models, and answering my endless email questions about python script. Mojtaba Aliasghar was also an incredibly significant contributor to this work, particularly with the initial experimental specimen and the testing/loading apparatus design and setup. Thank you also to the Virginia Tech graduate student Colson Brandetsas on the preparation of the first RC wall specimen, and of UPC graduate students Mathías Maldonado, Diego Palacios, and Brandon Pulido on the analytical study and design of the RC retrofit overlay. Thank you to Mohammad Owais Ahmad and Raja Saketh Yelishetty for their contributions to this work through many hours of hard labor in producing these specimens in the lab. The support of the personnel at the Virginia Tech Structural Engineering Laboratory, is gratefully acknowledged, without whom I would never have been able to build the walls. Garrett Blankenship, Brett Farmer, and Dr. Dave Mokarem. A big thank you also needs to go out to to Johnny and his team at Blackstone Construction.

I'd like to acknowledge all of the [incredible, patient, supportive, and collaborative] [engineers, friends, mentors, family] who were unfailingly kind and helpful during and leading up to this entire doctoral process. I could not have made it through without you. To name a few... My UW mentors: Dr. Steve Meunch, Dr. Joe Mahoney, Dr. John Stanton, Dr. Richard Wiebe, Dr. Palo Calvi, Dr. Laura Lowes. My Swedish research collaborators: Dr. Andreas Andersson, Dr. Raid Karumi, Dr. Jean-Marc Cassini. My Virginia mentors: Dr. Carin Roberts-Wollmann, Dr. Gregor Wollmann, Dr. David Mokarem, Debbie Cooper. My colleagues and friends through all walks of life: Kory Swabb, Camilla Forsgren, Chin Tang, Kim Tsai, Nigel Lyons, Sara Tari, Steph MacPherson, Morgan Fromme, Andrei Arevalo,

Jared Rose, Jason Wells, Ray Yu, Leo Tsellos, Lexie England, Juan Camilo Avendaño, Wiebke Belitz-Hellwich, Chiara Cannizzaro, Joe Eberhardt, Andrew Tran, Anne Struefurt, Morgan Oheler, Tat Thum, Heather Brouwer, Kayla Wigle, Sam Trehey, Axel Soto, Abdullah Al Rufaydah, Omar Almasarani, Ruben Jerves Coello, Zack Coleman. Finally, to part of my incredible family who inspired and helped me particularly for this journey: Randi Albright, Jason Albright, Grandpa Bob Serafin, Grammy Elizabeth Albright, Charles Albright, Ty Albright, Marianne Goodell, Scott Goodell, Josh Goodell, Natalie Amano, Rachel Serafin, Tess Kennedy, Taylor Kavanaugh. Thank you all!

Contents

List of Figures

List of Tables

LIST OF TABLES

Chapter 1

Introduction

1.1 Motivation

Reinforced concrete (RC) walls are widely used as lateral force-resisting systems, particularly in seismically active regions such as the western United States, New Zealand, Chile, central and eastern Europe, and Japan. A significant number of RC wall buildings in the United States were constructed before 1970, prior to the development of modern seismic design standards. Consequently, structural RC walls within these buildings often lack adequate reinforcement detailing and ductile design features necessary to ensure sufficient inelastic deformability while maintaining sufficient strength. This can lead to catastrophic failure during seismic events, which can have ramifications for community resilience, public safety, and economic stability. Therefore, it is important to accurately characterize the retrofit needs of such older walls to ensure their safety.

Modern design guidelines are governed by a 'capacity-based' design philosophy, stemming from the work of Paulay and Priestley (Paulay and Priestly, 1992). An entire structure can be thought of as a single chain made up of many links. If one link is designed intentionally weaker than the others, it can be anticipated that the failure of the entire chain will occur in this singular weak link. The method of failure can then be designed to satisfy a safe, ductile, slow, and yielding failure. This will ensure the entire system will fail with a duc-

tile mechanism, slowly deforming and degrading in strength while maintaining most of the strength characteristics. RC structural walls that satisfy these principles of ductile design are generally characterized by large amounts of vertical reinforcement steel in the end regions, with adequate confinement, as well as sufficient shear steel in the web regions. Ductile structures will also adequately consider the preclusion of other brittle failure modes, such as lap splice slip. The inelastic behavior of a ductile wall will be evident in degradation of the toes through steel yielding, concrete crushing and spalling, and bar fracture. An image of a typical ductile failure pattern is shown in Figure 1.1, beside a simplified force versus deformation relationship for a structure with a ductile failure mechanism compared with a non-ductile failure mechanism. Figure 1.2 shows experimental results of ductile failure mechanisms.

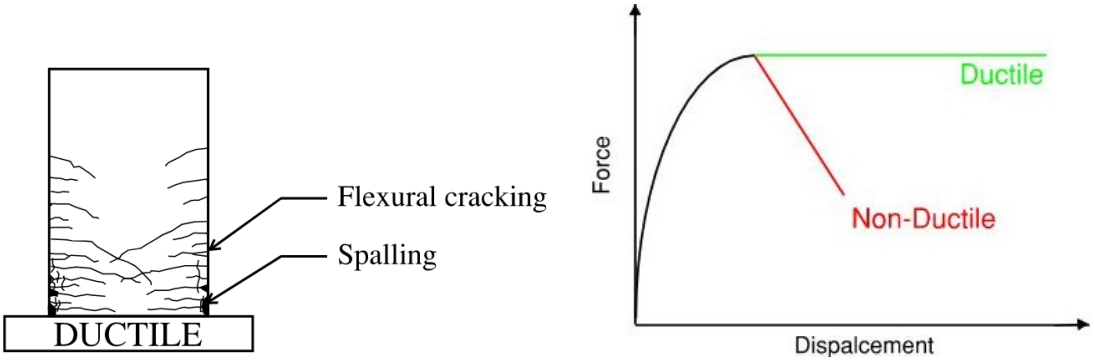

(a) Ductile RC Wall Failure Pattern

(b) Ductile vs Non-ductile General Force Deformation Relationship

Figure 1.1: Flexurally-controlled General Behavior for RC Walls

Walls designed without the explicit intention of inelastic deformability are classified as non-ductile. Non-ductile RC walls are susceptible to brittle strength degradation due to shear failure, concrete toe crushing, bar buckling, or lap-splice failures, which are described in further detail in Chapter 2 (Oesterle et al., 1979; Abdullah, 2019). Visual examples of non-ductile damage patterns in shear walls are shown in Figure 1.3. The propensity of these structures to exhibit this type of damage is attributed to inadequate web horizontal shear

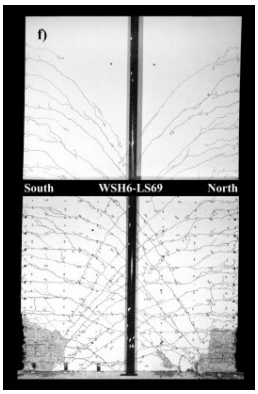

(a) Flexural Bar Rupture (Dazio et al., 2009)

(b) Toe Concrete Crushing and Bar Buckling (Thomsen and Wallace, 1995)

Figure 1.2: Experimental Wall Flexural Failure Mode Responses

reinforcement, inadequate transverse confining steel in the end corner toe regions, and the placement of short lap splices in critical regions of increased flexural moment demands.

To eliminate these previously mentioned vulnerabilities, retrofitting techniques have been developed to improve the seismic performance of existing non-ductile RC walls. These retrofit techniques are aimed at strengthening structural elements to enable the development of flexural inelasticity. This should bring the structure into better alignment with current design standards and, therefore, enhance the structure's safety. Retrofitting through an externally applied material that is bonded to the underlying existing structure is also a popular choice because it is faster, more cost-effective, and has an inherently smaller carbon footprint than replacing the building. Common external retrofitting techniques for RC structural walls include the application of carbon fiber reinforced polymer (CFRP) or glass fiber reinforced polymer (GFRP) sheets bonded with epoxy resin, external reinforced concrete overlays, externally bonded steel plates, and additional steel bracing, among others (Priestley et al., 1996; Prakasam and Murthy, 2019; Dukes and Sattar, 2022a; Chakrabarti et al., 2008).

Despite the interest in retrofit techniques, critical knowledge gaps remain, particularly regarding the reliability and validity of current retrofit design guidelines and procedures. The

(a) Web Wall Crushing, Bar Buckling, Out of Plane Failure. Turkey 2023 (Işık et al., 2024)

(b) Sliding, Crushing, Spalling. Chile 2010 (Maffei et al., 2012)

(c) Diagonal Tension (shear) Damage. Turkey 2023 (Işık et al., 2024)

Figure 1.3: Typical Damage in Non-ductile RC Walls

primary guiding document for the seismic assessment and retrofit of existing buildings in the United States is ASCE/SEI 41-23 (ASCE/SEI-41, 2023), hereafter referred to as ASCE-41. The specific document outlines an assessment procedure that typically focuses on three critical performance levels, namely immediate occupancy (IO), life safety (LS), and collapse prevention (CP). Figure 1.4 illustrates the qualitative observed damage for each performance level. These limits are qualitatively defined as follows. IO indicates that the structure has

maintained most of its pre-earthquake stiffness and strength; LS should align with a damaged state that has a margin against collapse; CP is associated with the structure at a point that no longer has a margin against collapse.

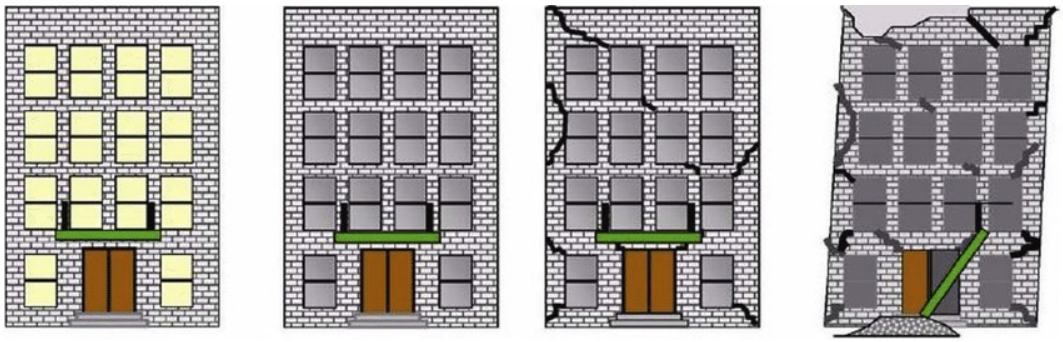

(a) Operational (b) Immediate Occupancy (c) Life Safety (d) Collapse Prevention

Figure 1.4: Qualitative Performance Levels (FEMA, 2004)

At each level, ASCE-41 defines quantitative acceptable deformation limits for the structure. These acceptance limits are based on empirical data (Epackachi et al., 2018; Abdullah, 2019) and therefore may not be adequate for all wall configurations, especially those configurations not found in the empirical database. Additionally, US design guidance for FRP retrofit, specified in ACI 440.2-23 (ACI 440 Committee, 2023), hereafter referred to as ACI-440, also relies on limited empirical test data, especially for RC structural walls (Dukes and Sattar, 2020). It is important to note that ACI-440 and ASCE-41 are not fully consistent in terms of the seismic assessment of a structure. ASCE-41 does not account for FRP overlays through modeling guidance, nor does it provide acceptance criteria directly for an FRP retrofitted component.

These limitations in assessment and retrofit guidelines underscore the need for further research on non-ductile RC walls, particularly regarding seismic strengthening techniques. Additional experimental research and analytical investigations are required to address these knowledge gaps and refine the guidelines. Experimental research provides direct insights

into the behavior of retrofitted non-ductile RC walls under controlled conditions. Numerical computation allows for a broader exploration of various design parameters (and their effects) on wall performance in a much greater quantity than can be achieved experimentally.

There are urgent research needs to consider experimental retrofit strategies for RC structural walls, along with adequate consideration of the current assessment procedures for these structures. This dissertation is aimed at addressing this need through a combination of experimental and numerical investigations focused on non-ductile RC walls.

1.2 Executive Summary

The goal of the experimental investigation was to provide insights into the anticipated performance and failure patterns of non-ductile RC walls, as well as to consider the effectiveness of retrofit strategies through the use of FRP or reinforced concrete overlays. In conjunction with a professional advisory panel, the experimental program was organized into two groups of RC wall specimens: four walls without a lap splice and two walls with a lap splice in the plastic hinge region. The six experimental specimens had identical cross sections and reinforcement quantities, which were meant to adequately represent construction practices and design for RC structural walls built on the West Coast of the US between the 1950s and 1960s. The specimens consisted of barbell-shaped cross sections with so-called pilaster configurations for the end regions, with relatively lightly reinforced web regions in between. This cross section was also selected for consideration as one of the more challenging configurations for retrofit installation faced in modern practice. The specimens were built and tested at the Thomas M. Murray Structural Engineering Laboratory at Virginia Tech. A photograph and a schematic overview of the specimen setup configuration are provided in Figure 1.5. The specimens were loaded in-plane with a constant axial force applied through

prestressed rods and a cyclic lateral load applied through a servo-controlled actuator.

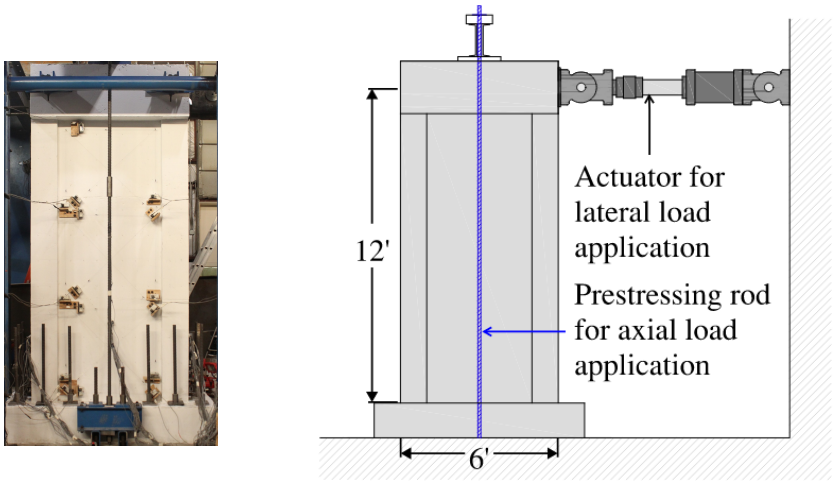

(a) Example Specimen Photograph

(b) Experimental Schematic Test Setup

Figure 1.5: Experimental Test Program General Setup

The first group of experimental specimens, specimens without a lap splice, considered three retrofit strategies: a one-sided reinforced concrete overlay, one-sided FRP shear strengthening, and FRP for shear strengthening with end region FRP toe bar buckling wrap. The strengthening strategies were determined based on the initial response of the control specimen, which exhibited diagonal web cracking, brittle shear failure, toe crushing, and bar buckling. The goal of the retrofit was to delay and potentially eliminate the possibility of a shear failure, ensuring a meaningful increase in the flexural inelastic deformability of the wall through the formation of a flexural hinge at the base. The end wrapping of the pilaster was meant to delay or prevent the bar buckling observed in the control specimen to hopefully further increase the flexural inelastic deformability. Modern design codes such as ACI 440 Committee (2017) and ACI-318 (2019) were utilized in the design of the retrofitting strategies.

The second group of experimental specimens considered only one retrofit strategy: FRP

shear web strengthening with end region FRP lap splice wrap. The control specimen for this group exhibited vertical bar failure through lap splice slip. The goal of the retrofit strategy was to delay or prevent the lap splice slip. The design code ACI 440 Committee (2017) was used for determining the quantity of FRP required to increase the strength of the lap splice through confining contribution, which would in turn resist the formation and propagation of splitting cracks and associated slipping of bars. All of the retrofitted specimens, from both groups one and two, achieved a flexurally-controlled failure.

The experimental program served to further validate the numerical modeling technique of the non-linear truss analogy for shear walls, which has a unique ability to capture failure modes of non-ductile shear walls, as shown in Deng et al. (2021). The method was adapted for this research to include lap splice slip considerations, as well as overlay modeling capabilities. The performance of each retrofitting strategy was also modeled and validated with experimental results. Reliable numerical models are crucial for demonstrating the performance of various retrofitting techniques. Such models enable design engineers, code officials, and researchers to accurately simulate the behavior of retrofitted RC walls, promoting the broad implementation of effective retrofitting strategies.

The numerical models of the unretrofitted specimens reproduced the limited ductility and failure modes of the physical specimens quite well. The specimens which were strengthened for shear were also reasonably well reproduced by the numerical modeling scheme. The numerical models for the specimens with end-wrapping strategies captured the initiation of failure through vertical bar rupture but subsequently over-predicted the drift deformation capacity of the structures as compared to the tests. The models in these cases do not capture the localized strains exhibited at the base of the end toe regions in the vertical reinforcement steel in the physical experiments.

The numerical program also involved a parametric study that assessed the general seismic

behavior of a subset of reasonably accurate RC structural walls with rectangular and barbell cross sections designed prior to the 1970s. The first motivation of the parametric study was to determine the exceedance of seismic performance limits for this representative group of walls through material level strains and strain-related quantities. Secondly, the capability of the strain-based criteria to consistently determine key parameters on the backbone hysteretic curve was assessed. The third motivation of the parametric study was to compare the current acceptance criteria in ASCE/SEI-41 (2023) for RC structural walls against that of the aforementioned strain-based criteria.

For this purpose, nonlinear truss models were developed for 200 walls representing a prototype 24-foot-tall cantilever RC structural wall with varying design and loading characteristics, such as web thickness, the amount of vertical and horizontal reinforcement, the spacing of confining ties, and axial load. Each model was loaded with a similar protocol to that of the experimental tests for both lateral and axial loads. Figure 1.6 shows an example model setup from the parametric study, showcasing the maximum principal strain values at the peak drift of the model. The seismic performance was determined through strain-based exceedance thresholds proposed by Deng et al. (2021) for the IO, LS, and CP limits. The limits were then compared with typical strength degradation guidelines found in the literature. Finally, the results of the analysis were compared with the performance limits established in ASCE/SEI-41 (2023).

The results of the parametric study indicate a reasonable ability of the strain-based methodology to consistently capture key performance metrics of the backbone curve while maintaining a similar statistical spread and trend to the performance metrics obtained through the ASCE/SEI-41 (2023) guidelines for most cases of flexurally-controlled walls. This indicates that the strain-based assessment criteria can be an equally effective method used to capture the seismic behavior of older RC walls and may even be preferred as an alternative

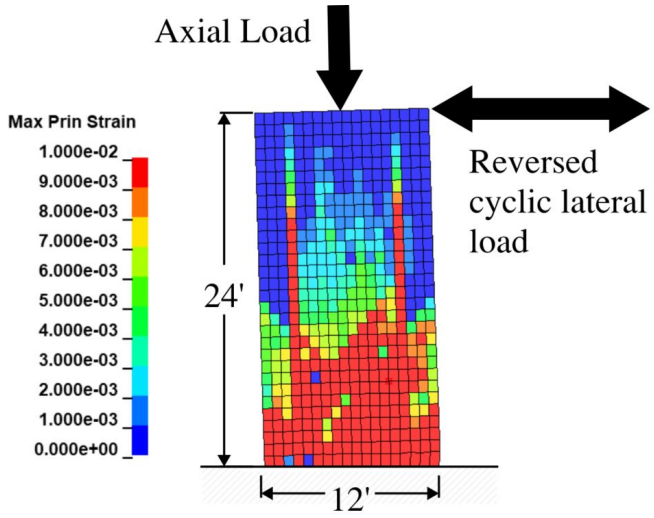

Figure 1.6: Numerical Model Setup Example

assessment procedure since it relies on a local assessment framework, which can be uniquely adapted for any structure or retrofit configuration.

Through the integration of experimental data and numerical modeling, this dissertation contributes to the development of more robust retrofit guidelines for non-ductile RC structural walls, providing structural engineers with the insights necessary to mitigate seismic risks associated with non-ductile RC walls.

1.3 Objectives

The overarching objectives of this research are:

1. Determine the anticipated failure modes of unretrofitted non-ductile reinforced concrete structural walls.

2. Investigate the effectiveness of various retrofit configurations using fiber reinforced polymer (FRP) and concrete overlay strategies.

3. Further validate numerical modeling with nonlinear truss elements, particularly for retrofitted specimens and specimens with a lap splice.

4. Compare the performance of retrofitted structures to that of a structure with modern RC detailing for seismic considerations per ACI-318 (2019).

5. Conduct a parametric analysis to assess the sensitivity of different parameters such as web thickness and reinforcing steel amounts, on the performance of non-ductile structural walls.

6. Assess the seismic response of RC structural walls through local (strain-based) criteria, building on the work by Deng et al. (2021), and drawing comparisons with meaningful parameters associated with typical key strength values on a backbone curve of a hysteretic plot.

7. Compare the outcomes of the strain-based criteria with that of the ASCE/SEI-41 (2023) acceptance criteria for structural walls.

1.4 Scope of the Dissertation

This dissertation is comprised of seven chapters. Chapter 1 gives a brief background on reinforced concrete shear walls and the main motivation for the present dissertation. Chapter 2 comprises the literature review, including general background on RC structural walls, retrofitting techniques, current assessment guidelines for existing and retrofitted structures, previous experimental studies, previous numerical/analytical studies for both unretrofitted and retrofitted RC structural walls, and previous attempts to utilize or define appropriate strain-based assessment limits in the literature. Chapter 3 describes the experimental test program, including specimen design, specific retrofit material properties, and instru-

mentation. Chapter 4 presents the results from the experimental program with discussions regarding the effectiveness of the retrofit strategies considered. Chapter 5 describes in detail the modeling framework (i.e. the nonlinear truss analogy) utilized for this study and makes specific comparisons to the effectiveness of the scheme to model the experimental tests discussed in the previous chapter. Chapter 6 outlines the parametric study and discusses the ability of the strain-based assessment to achieve desired outcomes and how it may be considered with regard to the current guidelines for assessment and retrofit of existing structures. Chapter 7 concludes this scope, reviewing the main points of this program and the conclusions that came from it.

Chapter 2

Background and Literature Review

2.1 General

This chapter provides a comprehensive background and literature review on the structural behavior and retrofitting strategies for reinforced concrete (RC) shear walls. It begins by examining typical damage patterns observed in shear walls, including flexural, shear diagonal, sliding, and lap splice failures. Next, it delves into various retrofitting procedures used in the field, specifically focusing on fiber reinforced polymer (FRP) and shotcrete applications. The chapter then reviews current assessment procedures and retrofit guidelines, highlighting key standards such as ACI 369, ASCE 41, and ACI 440 (ACI-369, 2022; ASCE/SEI-41, 2023; ACI 440 Committee, 2023). Additionally, it discusses previous experimental work on both unretrofitted and retrofitted shear walls, detailing the methodologies and findings. Finally, the chapter covers previous analytical work, providing insights into the modeling and analysis techniques used for shear walls and their retrofitted counterparts.

2.2 Typical Shear Wall Damage Patterns

Shear walls are a popular lateral force resisting system used to resist lateral forces due to seismic forces or wind loads and transfer them safely to the building's foundation. However, older RC buildings with concrete walls have been found to be deficient due to low global

strength, highly torsional plan layouts, or poor detailing, which results in premature shear failure (FEMA, 2006). Consequently, shear walls have been extensively studied since the 1950s. An innovative program of research was undertaken by the Portland Cement Association through several collaborations aimed at identifying some of the typical damage patterns of buildings with RC shear walls. From this research, they published their findings in the book *Earthquake Resistant Structural Walls* by Oesterele (1976) published in 1978.

In addition to the large number of experimental programs focused on RC structural walls, numerous post-disaster assessments have examined RC structural wall behavior. Their damage following major earthquakes has been widely reported (Fintel, 1995; Pan et al., 2018; Demirel et al., 2022; Kam and Pampanin, 2011). These reports provide valuable insights into real-world seismic events. In actual earthquakes, walls experience torsional demands that are often overlooked in laboratory studies. This information serves as a critical comparison to the isolated and controlled conditions of lab experiments, which aim to minimize variables.

These broad observations of structural RC walls have led to comprehensive documentation of their general damage patterns. A concise summary of their behavior is published in detail by *FEMA 306: Evaluation of Earthquake Damaged and Concrete and Masonry Wall Buildings* (Council, 1998). Shear walls can fail in flexure, showing good displacement capacity without significant loss of strength, thereby exhibiting high ductility. This is the desired dominant behavior in modern codes, as it is accepted as the safest structural design (Priestley et al., 2008). Less desirable damage propagation includes moderately ductile and non-ductile damage patterns. Moderately ductile behavior occurs when there is initially some level of flexural yielding in the structure, along with concrete damage, but ultimately the structure exhibits a shear-controlled response. The concrete damage can occur due to diagonal compression, diagonal tension, sliding shear, boundary zone compression, lap splice slip, or out-of-plane buckling. When the structure exhibits an initial elastic range, followed by a plastic range,

followed by strength degradation, the behavior may be classified as 'deformation-controlled' according to FEMA 547, (FEMA, 2006). See Figure 2.1 for a brief visual representation of some of these modes of failure.

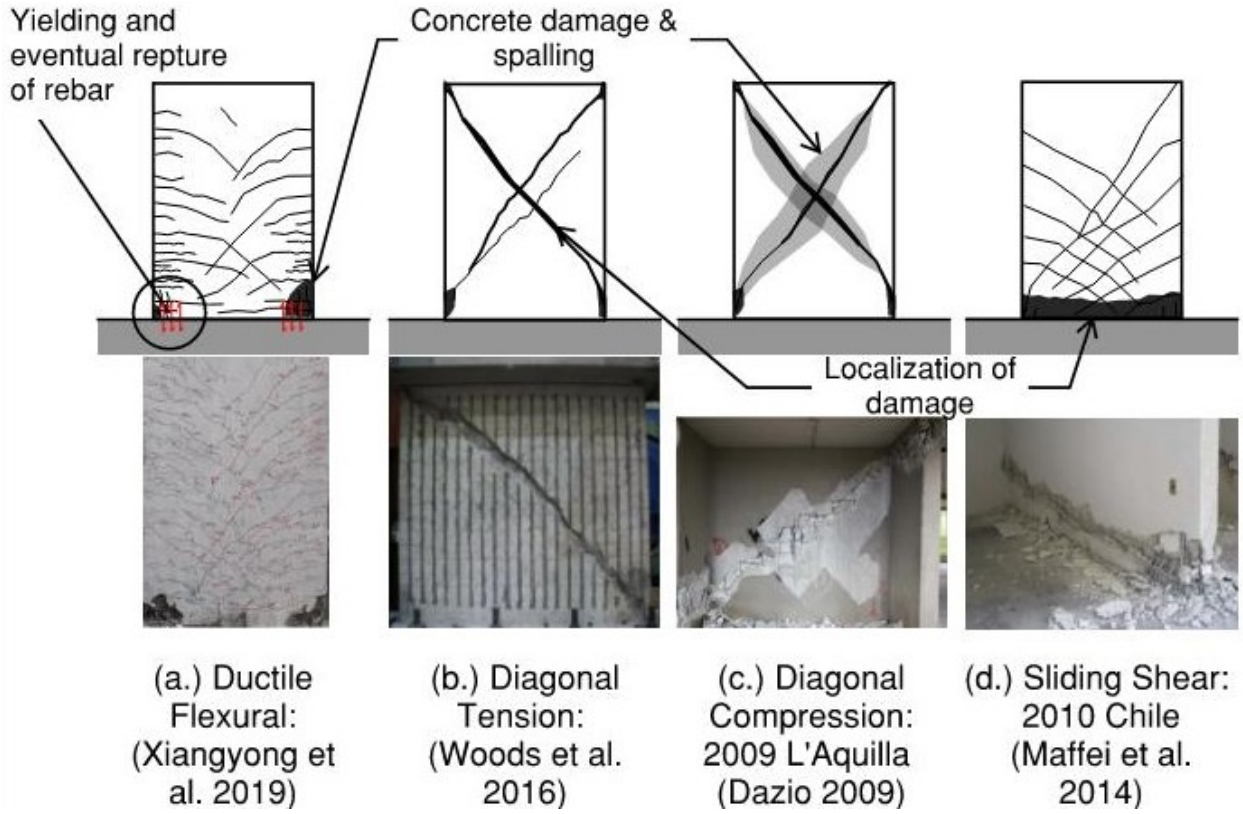

Figure 2.1: Typical RC Shear Wall Damage Patterns

The following is a brief description of the FEMA 306 shear wall damage patterns as they relate to inelastic deformation governing behavior. Note, the term 'failure' is used loosely herein to describe the overall governing inelastic deformations of a structure or the predominant behavior.

2.2.1 Flexural Damage Patterns

A flexural failure occurs when a RC shear wall is able to develop its full flexural capacity and exhibits inelastic deformation, which is driven by the yielding of boundary reinforcement

steel concurrent with high compression in the concrete. This occurs when the shear strength of the wall is higher than its flexural strength, meaning its behavior will be dominated by the weaker condition, i.e., the flexural strength. The reinforcement in the end regions will yield and may eventually even rupture. The initial stages of this failure mode can be seen through cracking at the toes of the structure, perpendicular to the longitudinal axis of the structure. These develop as the rebar is strained vertically, essentially forcing the bonded concrete to form horizontal cracks perpendicular to the reinforcement. In the ultimate stages, the concrete in compression may begin to crush, and as the concrete cover spalls off, the rebar in the toes is more likely to buckle.

2.2.2 Diagonal Tension and Diagonal Compression Damage Patterns

Diagonal tension is characterized by fully localized diagonal cracks in the web, which can ultimately lead to rupture of the horizontal reinforcement in tension.

Diagonal compression is characterized by high compressive demands in the web of a wall and is occasionally referred to as "web crushing." This failure typically occurs in squat walls with flanged edges, which increases shear demands in the web of the wall.

Diagonal compression and diagonal tension can often be difficult to distinguish, especially when the internal reinforcement does not rupture.

2.2.3 Sliding Shear Damage Patterns

Sliding shear often occurs in squat walls with poor construction joints between the foundation and the wall, particularly when there is insufficient vertical reinforcement across this construction joint. This failure is characterized by the structure's inability to develop flexural resistance, which results in it simply "sliding" as one cohesive unit between the foundation

and the wall.

2.2.4 Lap Splice Damage Pattern

Lap splice slip occurs when there is an inadequate lap splice between the foundation reinforcement and the wall reinforcement. As the wall attempts to develop its flexural capacity, the lapped rebar acts as unrestrained reinforcement and "slips" free from the surrounding concrete. This results in an inability to resist force and, therefore, an inability to develop yielding capabilities. This can be expressed as the wall exhibiting a bond failure between the rebar and the surrounding concrete. Characteristic visual damage includes vertical splitting of the concrete within the lap splice region, with eventual rocking behavior in the lap splice region under cyclic loading.

2.3 Retrofitting Procedures Considered

Retrofitting is a method of modifying an existing structure with a new technology to improve its performance. In the case of non-ductile RC shear wall, the goal of the retrofitting strategies is to improve the ductility, energy dissipation, while changing the ultimate dominating behavior from a shear response to a ductile one (see Section 2.2 for more details on damage patterns related to observed behavior). Altering the structure in this way will bring it into better alignment with current design standards and therefore improve the safety of the structure. This is inherently a more sustainable practice with a smaller carbon footprint (Dukes and Sattar, 2023). Retrofitting can also have less impact on the day-to-day operations of a structure and may utilize a shorter timeline than full reconstruction, which can be appealing to building owners.

Historically popular retrofitting techniques for non-ductile shear walls have included glass

fiber reinforced polymer (GFRP), carbon fiber reinforced polymer (CFRP), steel plates externally connected to the walls through chemical and mechanical bonds, external steel frames, and concrete collars or jackets. Only the two retrofit strategies selected for this project are detailed in this dissertation, namely fiber reinforced polymer(FRP) and shotcrete, described in the next Sections 2.3.1 and 2.3.2.

2.3.1 Fiber Reinforced Polymer (FRP)

Fiber reinforced polymer is a lightweight, low-profile, and corrosion-resistant material, making it convenient for retrofitting. The lightweight aspect of this retrofit scheme is particularly appealing since it does not significantly increase the structure's weight and, therefore, the anticipated dynamic effects during an earthquake. The fiber, known as 'sheets' or 'wrap', is adhered to the concrete surface with a thermosetting polymer that is the reaction product of epoxy resin and an amino hardener, simply referred to as the 'epoxy'. The sheets are also typically anchored to the underlying concrete substrate, either through steel bolts with plates or FRP fiber splay anchors and additional epoxy. Numerous experimental investigations have showcased the importance of adequate anchorage to preclude premature FRP debonding (Lombard et al., 2000; Antoniades et al., 2005). The typical failure modes for FRP are either debonding of the entire sheet from the concrete substrate, pullout of the anchors, or FRP rupture. When these phenomena occurs, the material can no longer act cohesively with the concrete substrate, and thus it does not contribute to the overall specimen strength.

The installation procedure of FRP is crucial to the overall effectiveness of this retrofit strategy. Debonding remains a major concern for partially wrapped strengthening strategies (Teng et al., 2002; Kalfat et al., 2013). FRP will often debond rather than rupture, as its maximum strain capacity is approximately 0.01 to 0.02, which is less than the strain capac-

ity of reinforcing bars (typically > 0.12). There are many modes of debonding failure that can govern the ultimate strength of a retrofitted member. The strength of the materials themselves is not as great a concern as the methods by which they are applied, including the substrate bond and the anchoring scheme (ACI 440 Committee, 2023). The surface must be adequately prepared, including grinding and dust removal, prior to the installation of the FRP. The FRP comes in non-woven fabric sheets that are impregnated with a two-part epoxy mixture. The wall is subsequently pre-applied with the same epoxy mixture, and the FRP sheet is smoothed onto the wall. The FRP sheet must then be anchored with either steel or FRP anchors to the concrete substrate. Additional epoxy is layered over the FRP sheet and anchors (if applicable). FRP has been shown in numerous studies to be an effective retrofitting technique for increasing strength, ductility, and energy dissipation in existing structures, provided that appropriate application procedures are followed. See Figure 2.2 for an example of the required surface preparation and installation process.

(a) Surface Preparation and Anchor Holes (b) FRP Sheet Installation

Figure 2.2: FRP Surface Preparation and Installation Technique

2.3.2 Reinforced Concrete Overlay

The reinforced concrete overlay installed for this project was through a specific methodology called 'shotcrete'. Shotcrete is a pneumatically sprayed wet-mix concrete that adheres to a prepared surface typically roughened and installed with an external reinforcement grid. This technique is advantageous compared to traditional concrete because it requires no form-work. It is most commonly used in mining and tunneling stabilization (Galan et al., 2019). Prior to installation of the shotcrete, the surface must be roughened, and all loose material (such as old concrete, debris, or loose/cracked rock) should be removed. Then, a reinforcement cage must be installed into the substrate which acts as a support system for the shotcrete and also creates a typical reinforced concrete behavior of the shotcrete post-hardening. The force with which it hits the surface, and the supporting rebar cage, allows the concrete to self-compact in place. The wet mix should have aggregate no larger than 3/4 inches to be sprayed without blockage through a hose nozzle. Additives can be included in this mix to improve the strength of the shotcrete, adhesive properties, cohesive properties, and freezing/thawing and abrasion resistance characteristics (Prudêncio, 1998).

This is equivalent to adding reinforced concrete thickness to an existing specimen, provided there is a good bond. This increases the compressive capacity of the specimen, and can increase the flexural or shear strength, depending on how the additional rebar cage is designed. Shotcrete is currently designed according to ACI 506R-16, which offers design recommendations, including surface preparation, submittals, and quality control during and after construction (ACI Committee 506, 2018). See Figure 2.3 for a photo showcasing the roughened surface, embedded external rebar cage, and sprayed shotcrete installation.

Figure 2.3: Shotcrete Installation

2.4 Seismic Assessment and Retrofit Guidelines

2.4.1 Relevant Practice in the United States

The current standard for concrete structural assessment in the United States falls under the jurisdiction of ASCE/SEI-41-23 (ASCE/SEI-41, 2023) (henceforth referred to as ASCE-41), which is based on several FEMA publications, most notably FEMA 273/274 and FEMA 356. Additionally, ACI 369.1-22 (ACI-369, 2022) (henceforth referred to as ACI 369) is closely tied to ASCE-41, as ASCE-41 calls for specific compliance with ACI-369 and substitutes sections with its own standard. For example, section 10.3 from ASCE-41 requires "...replacing the referenced section in ACI 369.1 with the provisions of this section" (ASCE/SEI-41, 2023).

ASCE-41 provides four options for the analysis of existing buildings: linear static, linear dynamic, nonlinear static, or nonlinear dynamic procedures. Analysis often requires three performance levels to be considered: immediate occupancy (IO), life safety (LS), and collapse prevention (CP). Figure 2.4 shows a qualitative visualization of these performance levels with approximations of observed damage along a structural response curve. At each

performance level of interest, a prescribed hazard should be applied to the structure. The overall performance objectives of a structure are therefore the combination of the hazard and the performance level; this is generally referred to as Performance-Based Seismic Design (PBSD). Depending on the occupancy category of the structure (i.e., what risk the failure of the structure would pose to the public), different standards are set. Most structures fall under Risk Category I/II, or non-critical infrastructure. For these buildings, the most commonly used performance objective is the Basic Performance Objectives for Existing Buildings (BPOE). The BPOE consists of considerations of the Basic Safety Earthquake (BSE)-1E and the BSE-2E for differing performance levels. BSE-1E is a hazard with a 20% probability of exceedance in 50 years at LS, while BSE-2E is a hazard with a 5% probability of exceedance in 50 years at CP. See Figure 2.5 for a graphical depiction of this performance objective.

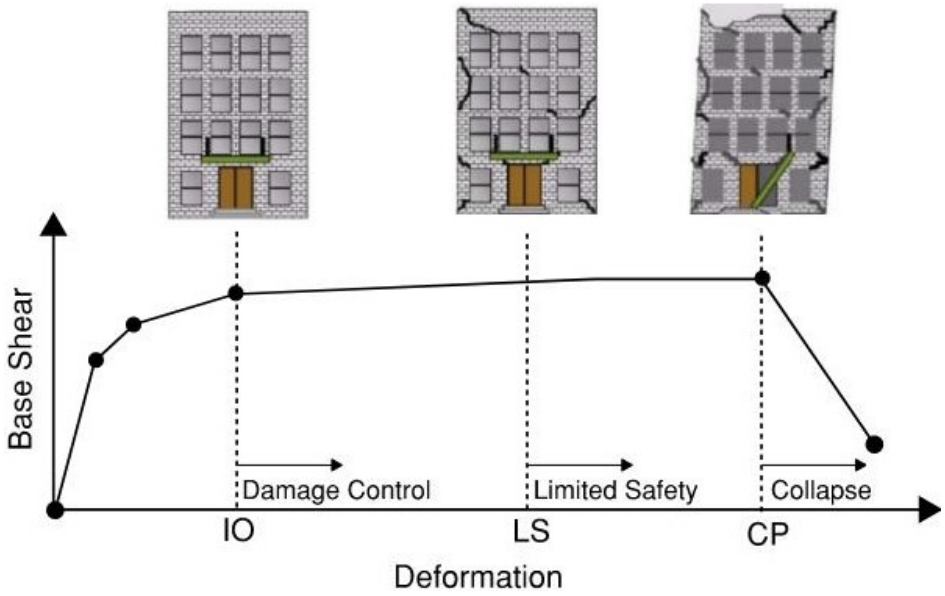

Figure 2.4: Qualitative Damage States; Figure Adapted From Abd-Elhamed and Mahmoud (2016)

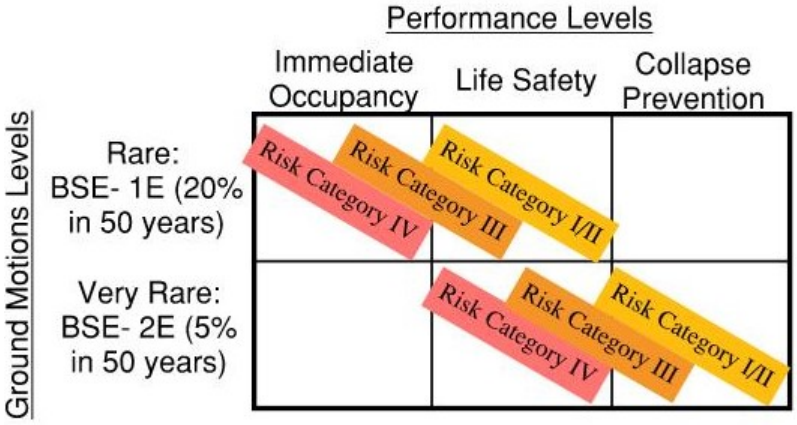

Figure 2.5: Basic Performance Objective for Existing Buildings per ASCE-41

All four analysis procedures for structural walls depend on whether they are classified as 'shear controlled', 'shear-friction controlled', or 'flexure controlled' per ASCE 41 Table 7.3.2a, reproduced in Table 2.1.

- The **flexural strength** of an existing reinforced concrete structural wall, corresponding to V_{MCultE}, may be calculated with fundamental principles given in ACI 318 Chapter 22, and with expected material properties (ACI-318, 2019). Subsequently, V_{MCultE}, may be calculated with Equation 2.1. This is equation 7.3.2a from ASCE-41.

$$V_{MCultE} = \frac{M_{CultE}}{M_{UD}} V_{UD} \qquad \text{(Eq. 2.1)}$$

  where M_{CultE} is the moment capacity of the structure calculated with the expected material properties and the ACI-318 chapter 22 principles, including the magnitude of the extreme compression fiber strain of 0.003, M_{UD} is the deformation-controlled moment demand and V_{UD} is the shear associated with this demand.

- The **shear strength**, $V_{CydWallE}$, of an existing reinforced concrete shear wall may be

calculated with Equation (Eq. 2.2a). This is equation 7.2.2c in ASCE-41.

$$0.8V_{CWall318E} \leq V_{CydWallE} \leq 1.8V_{CWall318E} \quad \text{(Eq. 2.2a)}$$

where

$$V_{CydWallE} = \left(2.0 - \frac{V_{CWall318E}}{\omega_v V_{MCultE}}\right) V_{CWall318E} \quad \text{(Eq. 2.2b)}$$

and

$$V_{CWall318E} = (\alpha_c \lambda \sqrt{f'_{cE}} + \rho_t f_{ytE}) A_{cv} \quad \text{(Eq. 2.2c)}$$

where α_c is equal to 3 when the aspect ratio of the wall is less than or equal to 1.5, and 2 when the aspect ratio is 2 or greater, and varies linearly for aspect ratios between 1.5 and 2, and the expected material properties are used for the concrete strength and yield strength of the reinforcement and the area of shear area is equivalent to the length of the wall multiplied by the web width.

- The **shear friction strength**, $V_{CyfWallSE}$, may be calculated with Equation (Eq. 2.3a). This is Equation 7.2.4 in ASCE-41. The variable, ω_v, is the dynamic shear amplification factor, calculated from Equation 7.3.2b from ASCE-41, and depends on the number of stories in the structure.

$$0.8V_{CWall318SE} \leq V_{CyfWallE} \leq 1.8V_{CWallSE} \quad \text{(Eq. 2.3a)}$$

where

$$V_{CyfWallE} = \left(2.5 - 2.15\frac{V_{CyfWallSE}}{\omega_v V_{MCyDE}}\right) V_{CWallSE} \quad \text{(Eq. 2.3b)}$$

and

$$V_{CyfWallSE} = \mu(A_{vf} f_{yfE} + N_{UG}) \leq 0.2 f'_{cE} A_g \quad \text{(Eq. 2.3c)}$$

where A_{vf} is the area of the shear reinforcement, the expected material properties are again used for the reinforcement steel and the concrete strength, N_{UG} is the design axial load based on the gravity load combinations in ASCE-41, and A_g is the gross area of the cross section.

Table 2.1: ASCE 41 Table 7.3.2a Wall Controlling Behavior Criteria

Criteria	**Expected Controlling Behavior**
$V_{CWall318E} \leq V_{CyfWallSE} < (\omega V_{MCultE}$	Shear
$V_{CyfWallSE} \leq V_{CWall318E} < (\omega V_{MCultE})$	Shear-friction
Otherwise	Flexure

As can be seen, there is a heavy emphasis on the relationship between the shear friction strength (a function of the axial load and amount of shear steel), and the shear strength corresponding to the flexural demand at ultimate conditions (i.e., $\varepsilon_c = 0.003$ corresponding to concrete crushing).

The numerical model of the structure can now be built. From an element level, each element of the structure must be defined as 'primary' or 'secondary'. Primary elements are required to resist seismic forces and accommodate deformation levels to achieve the selected performance level. Ideally, primary components should be deformation-controlled and therefore have a ductile response. Secondary components may be force-controlled and have a brittle response. The components of a structure must be accurately modeled based on 'as-built' information. After determining the overall behavior of the structural wall (i.e., whether it is shear or flexure controlled) the appropriate backbone curve of the component can be evaluated and assigned. See Figure 2.6 for the ASCE-41 reproduced figure describing the component level backbone curve for a deformation-controlled component such as a reinforced concrete structural wall.

If the nonlinear static procedure is selected, a 'target displacement' is then calculated, and the structure is pushed to this displacement, with the appropriate proportional displacement

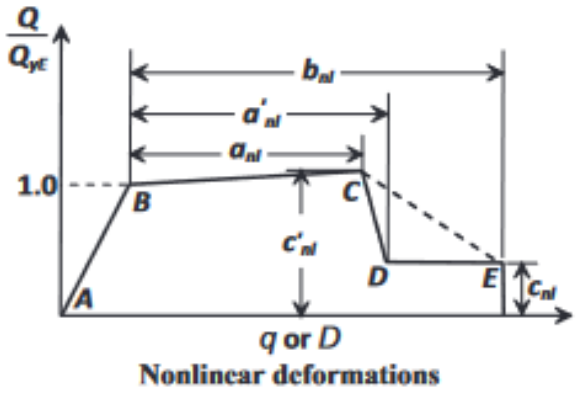

Figure 2.6: ASCE 41-23 Generalized Force-deformation Relation for Concrete Elements or Components

distributed to each story. At this target displacement, each element is assessed for compliance with the appropriate acceptance criteria. Acceptance criteria for force-controlled elements is given in section 7.5.3.2 of ASCE-41 *Acceptance Criteria for Force-Controlled Actions for NPS or NDP* and is replicated here in Equation (Eq. 2.4) where Q_{UF} is the force controlled demand, Q_G is the gravity load, and γ and χ are factors for load and performance level respectively.

$$\gamma\chi(Q_{UF} - Q_G) + Q_G \leq Q_{CL} \tag{Eq. 2.4}$$

For deformation-controlled elements, such as a structural wall, the acceptance criteria is defined whether the wall is flexurally controlled or shear controlled. Structural walls are limited by the maximum rotation in the plastic hinge region. The maximum hinge rotation in flexurally controlled walls shall not be greater than the value calculated with Equation 2.5(b-d). Values of d_{nl} and e_{nl} shall be taken directly from ASCE-41 Tables 7.4.1.1.1a and 7.4.1.1.1b for conforming and nonconforming RC walls respectively. Shear controlled structural walls shall have a maximum rotation in the plastic hinge region calculated with Equation 2.5(e-g). Values of d_{nl}, e_{nl}, and g_{nl} shall be taken directly from ASCE-41 Table 7.4.1.1.2.

$$\theta_{Max@TargetDisplacement} \leq \theta_{Accept@PerformanceLevel} \quad \text{(Eq. 2.5a)}$$

θ_{Accept} for flexure controlled walls per Equation 2.5a for Immediate Occupancy, Life Safety, Collapse Prevention are calculated by Equation 2.5b Equation 2.5c and Equation 2.5d respectively.

$$\theta_{yE} + 0.1(d_{nl} - \theta_{yE}) \quad \text{(Eq. 2.5b)}$$

$$0.75e_{nl} \quad \text{(Eq. 2.5c)}$$

$$0.85e_{nl} \quad \text{(Eq. 2.5d)}$$

θ_{Accept} for shear controlled walls per Equation 2.5a for Immediate Occupancy, Life Safety, Collapse Prevention are calculated by Equation 2.5e Equation 2.5f and Equation 2.5g respectively.

$$g_{nl} + 0.1(d_{nl} - g_{nl}) \quad \text{(Eq. 2.5e)}$$

$$0.65e_{nl} \quad \text{(Eq. 2.5f)}$$

$$0.80e_{nl} \quad \text{(Eq. 2.5g)}$$

The current design standard for retrofit of existing structures with FRP in the United States is through the ACI 440.2-23 (from here on referred to as ACI-440) which is a guideline document based on experimental data. The experimental data has been ongoing since the 1980s, however there was a more concerted effort funded by the National Science Foundation (NSF) and the Federal Highway Administration (FHWA) in the 1990s. See Neale (2000) for some examples of this work. However, despite this effort, the knowledge base surrounding RC structural walls retrofitted with FRP is still sparse (Dukes and Sattar, 2022b). Currently,

to consider retrofitting techniques one can use the strengthening equation from ACI-440 in Chapter 13, reproduced here in Equation 2.6. V_n^* is the nominal strength of the concrete and steel calculated per ACI-318, ψ_f is the reduction factor from ACI-440, and V_f is the contribution of shear strength due to the FRP retrofit. However, this guidance is not explicit, rather it can be deduced from an example worked problem in the FEMA P-2006 publication, *Example Application Guide for ASCE-41 Seismic Evaluation and Retrofit of Existing Buildings with Additional Commentary for ASCE/SEI 41-17* FEMA (2018a).

$$V_n = V_n^* + \psi_f V_f \tag{Eq. 2.6}$$

Additionally, FEMA 547 (FEMA, 2006) describes techniques for FRP Composite overlays on existing structures. They note that once the fibers begin to debond at 1/32 of an inch displacement normal to the concrete substrate, they are weaker, and the complete loss of bond strength occurs at 1/3 inch displacement normal to the concrete substrate. They highlight how prevalent FRP anchors are and the research going into them today, and how it is important to fully wrap the ends of walls, when applicable, since it helps in the anchoring of the wrap on the wall. However, they also claim in 13.4.1, "Enhance Shear Wall with Fiber-Reinforced Polymer Composite Overlay" that there is "...no confining pressure afforded by the use of FRP overlay...[and] [t]herefore, lap splice performance is not enhanced..." (FEMA, 2006). This claim is in contradiction to the findings in the present study, for more details, please see Chapter 4.

Finally, it is interesting to note that several studies have considered the discrepancies between the two most common prescriptive design standards for performance-based seismic design: ASCE/SEI 7 and ASCE-41, along with a subsequent model following the analysis of existing buildings. Ideally, a brand-new structure should easily meet current assessment

criteria for existing buildings since it is designed with the proper standards. However, this has not been shown to be the case. Sattar (2018) and Harris and Speicher (2018) both examined the anticipated outcome of a new structure designed per ASCE 7 and compared it to the assessment procedure outlined in ASCE 41. They found discrepancies between the outcomes, occasionally failing to meet the minimum assessment requirements of ASCE 41 despite being newly designed buildings per ASCE 7. This situation appears confusing and unsafe, highlighting the necessity of a more robust assessment protocol.

2.4.2 Relevant Practice Internationally

In Europe, existing structures can be analyzed through the procedure outlined in the Eurocode (CEN, 2005) (note that the next updated generation of the Eurocode is anticipated in 2027 and is anticipated to have updates to the assessment of existing structures and CFRP strengthening strategies). The limit states per the Eurocode 2005 are damage limitation (DL) for low damage, significant damage (SD) for moderate to significant damage, and near collapse (NC) when the structure is heavily damaged. Typically the following probability of exceedance is paired with each limit state:

- DL - 20% probability of exceedance in 50 years.
- SD - 10% probability of exceedance in 50 years.
- NC - 2% probability of exceedance in 50 years.

Existing material properties and geometries must be used, similar to the ACI requirements, as well as reductions for confidence of material properties. Components may be categorized as ductile or brittle, and may be designated as 'secondary' or 'primary'. Members deemed to be both brittle and primary must incorporate a strength reduction factor through a partial factor of the material. Accidental torsion needs to be accounted for, similarly to ACI,

but secondary seismic elements may be neglected against seismic effects for strength and stiffness. Structures may be analyzed with a lateral force analysis (linear), a modal response spectrum analysis (linear), a nonlinear static (pushover) analysis, a nonlinear time history dynamic analysis, or a q-factor approach. For whichever approach is taken, the deformation levels should be taken for the ductile elements of a structure while the force or strength values should be taken for the brittle elements. These demands due to the selected analysis procedure should be compared with the capacity of the structure at the component level. The capacity to demand ratio is recommended to be 2.5 to be an acceptable structure.

Canada produces a National Building Code (NBC) of Canada produced by the Canadian Commission on building and Fire Codes (NBC, 2020). The commentary of this code, Commentary L: Application of the NBC Part 4 of Division B for the Structural Evaluation and Upgrading of Existing Buildings offers guidance to practicing engineers for assessment of existing structures. Structures are assessed based on a specific seismic event and considering the strength and drift capacity of the structure under that hazard. Level 1 assessment/upgrades are for voluntary minimal seismic upgrades. Level 2 assessment/upgrading suggests the use of a spectral response acceleration with probability of exceedance of 10% in 50 years. Level 3 assessment suggests consideration of a hazard with 5% exceedance in 10 years. They reference ASCE 41 as an acceptable source for analysis. The code states that engineers should consider 'the ability of the structure to absorb local failures without widespread collapse' (NBC, 2015) Commentary L, page L-12. Ultimately, the code allows for experimental testing as adequate proof of the existing structure's capacity to withstand a major seismic event.

In New Zealand the assessment of existing buildings is governed by the Engineering Assessment Guidelines (Zealand, 2017), which is put out by a joint team of public authorities, engineers, researchers and professional societies. New Zealand has a detailed procedure

outlined for the assessment of existing structures in this code. Modeling of the structure and the geotechnical effects, especially the soil-structure-interaction (SSI). They detail two non-linear assessment procedures: a static pushover procedure and a nonlinear time history procedure. They assign specific displacement capacity of the primary lateral system, focusing on a displacement-based assessment. They allow for lumped-plasticity models, as well as fiber models (which it should be noted, ASCE-41 also allows for these types of models). They also allow for solid finite element models. Accidental torsion and higher mode effects must be taken into account, similarly to ASCE 41. The component level and the global level response under design hazards are compared with the initial assumed capacity of the structure. The global response is conducted through assumed governing displacement mechanisms of the entire structure, i.e., weak story. This code also appears to have much more consideration for damping, both inherent and hysteretic, for the overall analysis. For example, percentages of hysteretic damping values are offered for specific structural systems based on the initial simplified analysis to determine the system's ductility.

2.4.3 Previous Critique of ASCE-41

Structural engineers often use a simplified method of analysis of existing structures and their probability of collapse through the use of FEMA P- (FEMA, 2018b). This document allows a specific drift capacity for a structural wall to be calculated based on the neutral axis depth and the length of the wall, as well as a ratio of the length of the wall with the width of the wall. While they also put limits on the allowable ratio of $L_w c/b_w^2$ and the method of anticipate failure should be determined, the capacity is not related to the specified limits in ASCE-41 of IO, LS, or CP.

Cook and Sen (2023) conducted a review six low rise reinforced concrete structures which had been damaged in either real earthquakes or in a shake-table laboratory. They compared

the linear ASCE 41-17 procedures with FEMA P-2018 seismic evaluation methodology. In general, the linear procedures in ASCE-41 accurately predicted the failure mode (beyond CP) of a structure, as well as the failure mode of a particular components, but tends to under-predict the drifts and over-predict the floor accelerations. The study also concluded that the FEMA P-2018 simplified collapse evaluation seemed to generally confirm with observed damage the collapse method and the critical story. It is suggested that FEMA P-2018 provides a good global understanding of seismic vulnerabilities of a structure while the ASCE-41 procedures are generally better at identifying specific (local) component vulnerabilities. The two methods appear to complement one another in this way.

There have been several additional attempts to assess the validity of the assessment outcomes of ASCE-41 code. It is important to note that the latest edition of this code was released in 2023, and the publications referenced herein were undertaken prior to this latest edition release. Analysis done by Harris and Speicher (2018) indicated that a steel moment frame structure designed in accordance with ASCE-7 could have difficulty satisfying the acceptance criteria for collapse prevention outlined in ASCE-41. Hernández-Bassal et al. (2020) showed the varying effect ground motion selection can have on the outcome of assessment though the ASCE 41-17 guidelines, considering both linear and nonlinear static and dynamic procedures. Sattar (2018) considered the general performance of RC moment frame systems designed by ASCE 7-code and assessed with ASCE-41; their results showed that depending on which method of analysis was selected from the ASCE-41 guidelines, the structure may be shown to either meet or not meet the expected performance levels of LS and CP and may require retrofit. Several other researchers have assessed the validity of the guidelines for assessment in the ASCE 41 standards for code-conforming structures. Their results unanimously found that a structure may not necessarily achieve acceptable seismic performance per the ASCE 41-17 standards, despite its modern design (Daei and Zarrin, 2023; Buniya et al., 2017; Sattar

and Hulsey, 2015).

2.5 Previous Experimental Studies

2.5.1 General

There has been extensive experimental and field studies of structural walls and structural wall damage. One database compiled over 1000 tests (Abdullah, 2019). While this is advantageous for understanding the most critical failure behavior of non-ductile structural walls, there is a severe lack of experimental work on *retrofitted* RC structural walls (Dukes and Sattar, 2020). This section will cover an overview of the most significant studies and relate their relevance to this thesis.

Beginning with experimental work, the sections will be divided into two parts corresponding to the relevant work of this thesis. Namely fiber reinforced polymer (FRP) experimental results, and shotcrete experimental results. It is also important to note that experimental studies can generally fall into two categories: (1) damaged and repaired, and (2) strengthened prior to any load applied to the specimens. The specimens which have been only strengthened, and not repaired, will be the focus of this literature review as it is relevant to the current program area. Additionally, this study will mainly focus on carbon FRP, rather than glass or other materials; carbon FRP is by far the most prevalent material used in retrofitting with FRP (Dukes and Sattar, 2023). Finally, this study does not consider pre-cast RC panels which have been fabricated off-site.

2.5.2 Reinforced Concrete Walls

Prior to studies on retrofitted walls, there was a significant investment in research for RC structural walls in the 1970s by the Portland Cement Association and the Earthquake Engi-

neering Research Center, University of California Berkeley (Elnashai et al., 1990). This was undertaken due to the obvious success of well-designed structural walls under severe earthquakes, and the obvious failures of poorly designed ones, including Chile in 1960, Macedonia in 1963, Caracas in 1967, Mexico City in 1985, and Armenia in 1988 to name a few (Fintel, 1995). Through these studies an understanding of what constitutes a non-ductile structural wall began to emerge. Specific variables have been under scrutiny in these studies, such as the slenderness ratio of the walls length to the width, the axial load ratio, and the shear span ratio (Elnashai et al., 1990).

Cardenas et al. (1980) tested thirteen walls, varying the shear span ratio from 1.0 to 2.0 and considering different vertical and horizontal reinforcement distributions, without special boundary elements. They found that low-rise walls can develop shear stresses on the order of $10\sqrt{f'_c}$ psi. Oesterle et al. (1984) considered flanged, barbell, and rectangular sections. See Figure 2.7 which depicts one of their flanged wall specimens failing through web crushing. They concluded that providing an adequate amount of shear reinforcement would allow a flexural behavior to develop, and could avoid a premature shear failure. They developed an equation anticipating the web crushing strength as a function of the concrete strength, axial load, and lateral inter-story drift.

Vallenas et al. (1979) considered structural RC wall shapes, boundary element confinement, shear stress, and loading history. Iliya and Bertero (1980) continued this work by considering the effects of varying arrangements of web reinforcement. It was concluded that the boundary confinement was more important to the ductility of RC walls than the web reinforcement. See Figure 2.8 to see a specimen from their experimental program with exposed and buckled panel reinforcement.

Along with tests by Paulay and Goodsir (1985), this culmination of research resulted in the introduction of detailing provisions for wall boundary elements in the ACI 318-83 code. Tests

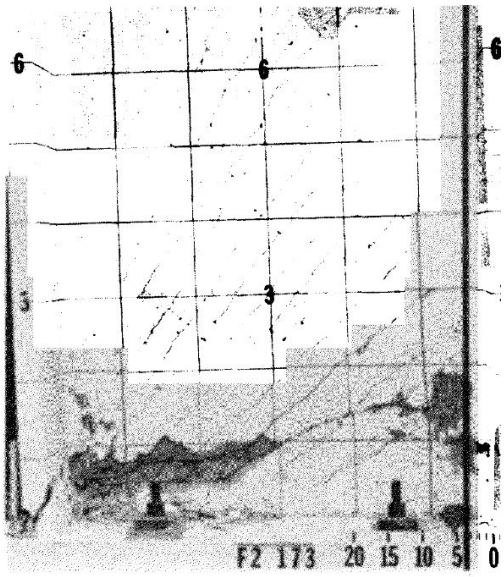

Figure 2.7: Experimental Specimen Web Crushing per Oesterle et al. (1984)

from Thomsen and Wallace (1995) pushed the ACI 318-99 code to introduce a displacement-based design procedure for slender RC walls with boundary elements.

Salonikios et al. (1999) considered 11 specimens with shear span ratios of 1.0 and 1.5, and utilized cross-inclined reinforcement can prevent shear failures under cyclic loading. See Figures 2.9a and 2.9b for photos from the experiment. Lefas et al. (1990) also considered RC walls through experimental means. The results of both experimental programs showed that ductility of the structure was influenced most heavily by boundary confinement, rather than shear reinforcement in the web. Shear resistance of the walls was found to be due to more triaxial compression in the base of the wall rather than the strength in the tensile zone.

Lowes et al. (2012) have shown the importance of including shear considerations even for walls which have a flexural controlling mode. Neglecting to include shear considerations in structural wall assessments

Almeida et al. (2017) provided a general overview database of the recent experimental data for lap splice conditions. They deduce there is a severe lack of experimental data on lap

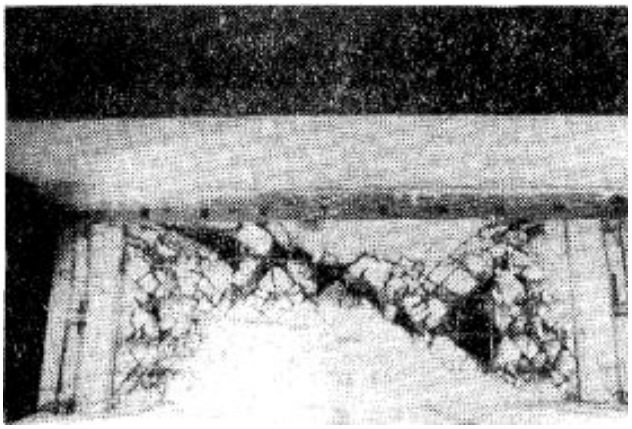

Figure 2.8: Experimental Specimen Web Damage from Iliya and Bertero (1980)

splice conditions, with 10 of the 16 total experimental tests having taken place since 2010.

2.5.3 FRP Retrofit

Fiber reinforced polymer(FRP) became popular as a retrofitting strategy in the late 20th century, but only for slabs, beams, and columns (Priestley et al., 1996; Balaguru et al., 2009; Teng et al., 2001). There was no testing of FRP retrofitting for structural walls until the year 2000 (Lombard et al., 2000). Several researchers have investigated this topic, but the entire field is still sorely lacking in breadth (Dukes and Sattar, 2020). The following figure is reproduced from Dukes and Sattar (2020) and it shows the number of known test programs for FRP retrofit in 2020. There are barely 40 test programs in total, with Canada and Japan leading the world. These studies include both repaired and strengthened walls and walls with openings, and ductile and non-ductile wall designs. A rough estimate indicates there are approximately 10 times as many experimental tests for unretrofitted walls than for those with retrofits.

The first study of FRP retrofitted RC shear walls is from a Canadian team in 2000 with Lombard et al. (2000). They conducted an experimental investigation for both retrofitting and repair of a modern wall (from 2000). The specimens were rectangular with an aspect

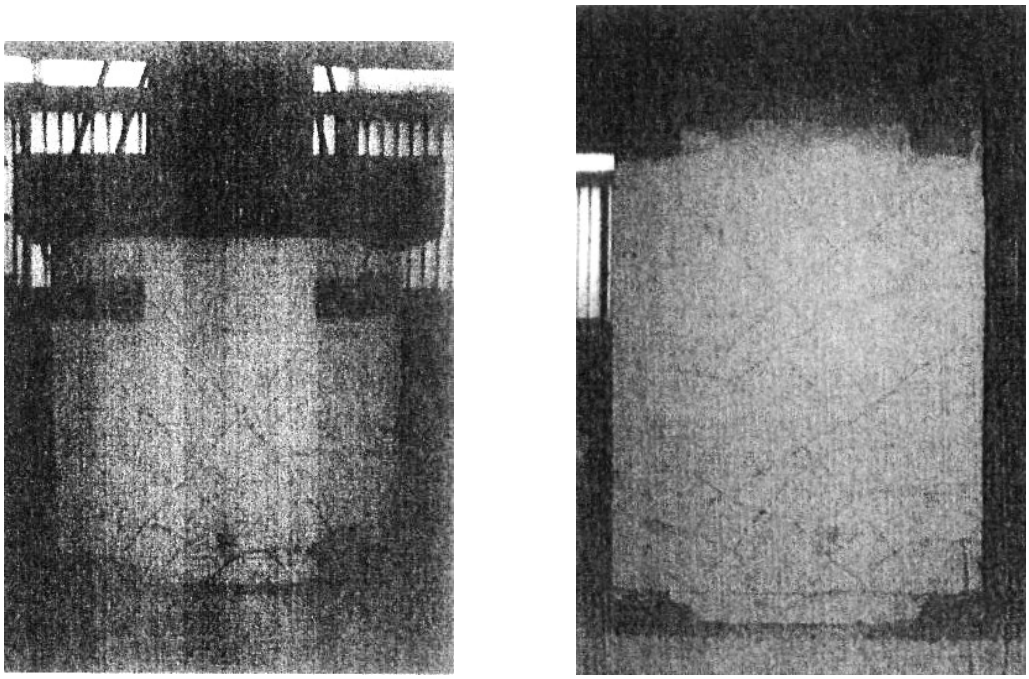

(a) 1.0 Shear Span Ratio (b) 1.5 Shear Span Ratio

Figure 2.9: Experimental Tests from Salonikios et al. (1999)

ratio of 1.2 and a thickness of 0.10 m. The FRP sheets that were applied to both faces of the specimen in vertical or vertical and horizontal configurations were successful in increasing the stiffness, improving the ductility, and increasing the strength of undamaged walls. They were also able to recover the initial stiffness of the initially damaged specimen, which was repaired with conventional concrete and then retrofitted with FRP. However, they did have a failure through pullout of the steel anchor. The flange rotations in the steel angle anchor caused premature debonding.

The research conducted by Hiotakis (2004) was a continuation of the work done by Lombard; however, they were able to improve the out of plane setup in their lab, and they considered a different approach for anchorage into the foundation. They successfully eliminated the premature failure due to anchor pullout; see Figure 2.11 for a view of one of their specimens at failure due to toe crushing, with the successful implementation of FRP attachment. The

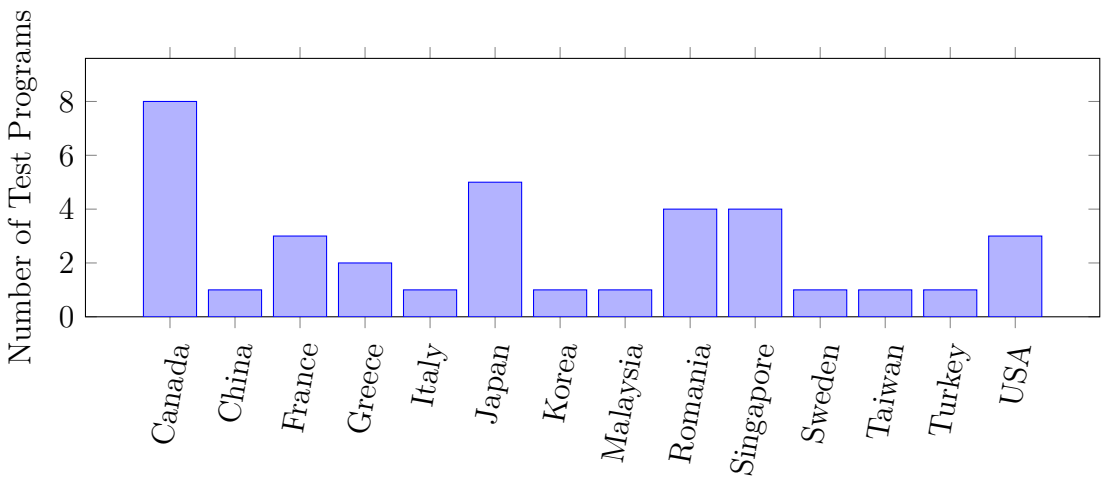

Figure 2.10: Country of Origin of All Research Programs in FRP Shear Wall Experimental Retrofit Database - Reproduced from Dukes and Sattar (2020)

strengthened specimens were rectangular with similar design specifications as the Lombard walls, i.e., a code compliant modern wall of 2000. Similarly to Lombard, they used FRP retrofitting on both faces of the walls with both vertical and horizontal configurations. They found success in improving the overall strength and ductility of the specimens, but it took 3 layers of FRP to ensure the wall reached its full flexural capacity. Overall, they concluded that the in plane stiffness may be increased with the application of FRP overlays, and that delamination of CFRP sheets is a major concern for design.

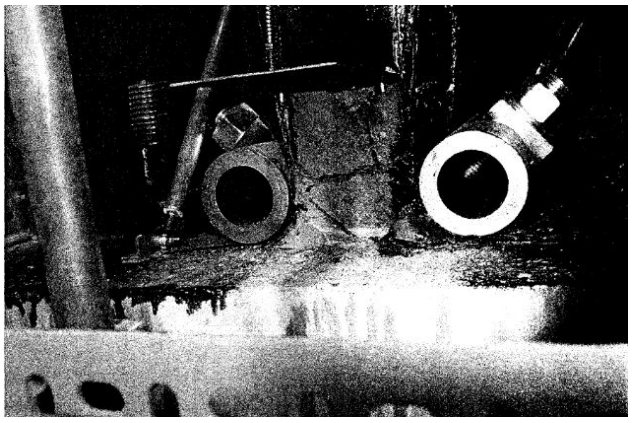

Figure 2.11: Compression Failure (toe crushing) and FRP Connection to Specimen per Hiotakis (2004)

Paterson and Mitchell (2003) investigated two retrofitting strategies for a pre-1960s building in Berkeley, California. The specimens were rectangular with an aspect ratio of 3 and a thickness of 0.3 m. The specimens' deficiencies included lap splices in the plastic hinge region, inadequate boundary confinement, and inadequate anchorage of the transverse steel. The test specimens were planar rectangular walls. They considered the effectiveness of using combined retrofit strategies. The retrofit strategies included 1.) An RC collar utilizing headed bars (at the top) doweled into the foundation extended over the plastic hinge region, see Figure 2.12 for photos of this retrofit strategy. Additionally, there were headed rebar through the wall and in the transverse direction of the wall to ensure the collar acted cohesively. Furthermore, they utilized horizontal FRP strips along the height of the wall, meant to increase the shear strength 2.) The second specimen was retrofitted with FRP sheets to increase the shear capacity of the wall and headed bars through the specimen to increase confinement. The lap splice of this specimen was about 1/4 of the way up from the foundation (simulating a lap splice at a floor level). The retrofitted specimens were tested in the horizontal configuration. The energy dissipation capacity of retrofitted specimen was 7x as much as the control specimen, and the energy dissipation of the second specimen was 3x as much as the control. The different confinement strategies were effective in eliminating lap splice slip as a failure mode and changed the ultimate behavior of the specimens to be flexurally dominated.

Khalil and Ghobarah (2005) experimented with non-ductile walls. The specimens were rectangular, with an aspect ratio of 1.1 and a thickness of 0.12 m. A moment was applied to the top of the wall with two actuators and beam, along with an axial load. The two retrofit strategies were 1.) bi-directional carbon fiber, where primary fibers were in the 45 degree direction, and a gap of 30 mm at the foundation interface to let a flexural hinge develop. The end regions were wrapped with uni-direction horizontal FRP with FRP anchors 2.)

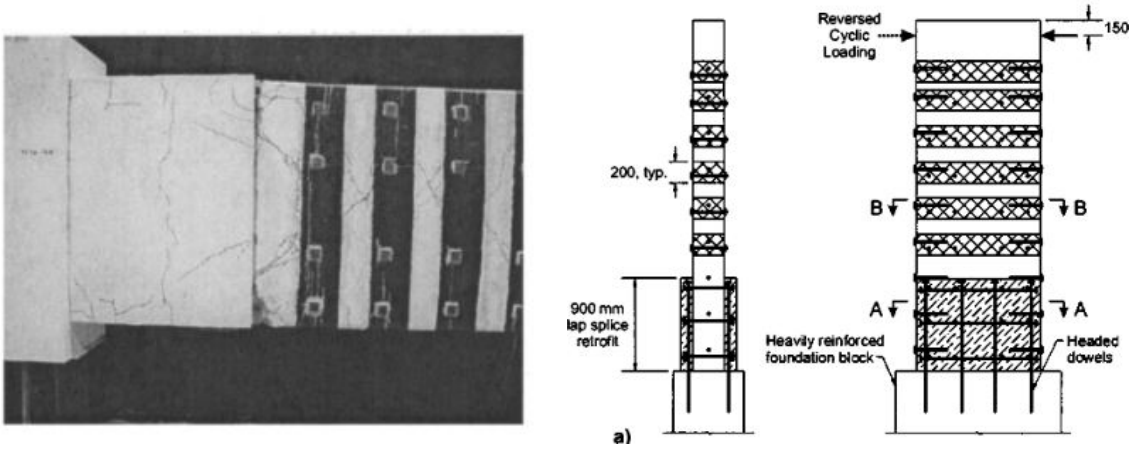

(a) Photo of Retrofit (b) Plan for Retrofit

Figure 2.12: Experimental Tests from Paterson and Mitchell (2003)

the use of 45 degree carbon fiber sheets again on the main face, bolted at the top and bottom of the wall with two steel rods, see Figure 2.13 for photos of the experimental setup. The end regions were again wrapped in uni-direction horizontal FRP and steel rods. The retrofitted specimens sustained on average 50% more load and 60% more lateral drift than the unretrofitted specimen. The shear wall was also able to achieve about 4 times more rotation capacity at the base as compared to the control. The energy dissipation increase was also significant for each of the retrofitted specimens.

Antoniades et al. (2005) tested six experimental tests which involved initial failure and subsequent repair. The specimens had been designed for current standards and therefore were expected to deliver flexural failures. They were then conventionally repaired with concrete and then strengthened with FRP strips, see Figure 2.14, with the intent of increasing both the flexural and shear capacity and increasing the ductility. The final failure was brittle, via the FRP, but it was always post peak strength and generally followed the fracture of steel in critical areas - resulting in a moderately ductile system.

Elnady (2008a) earned their Ph.D. through a dissertation considering the experimental re-

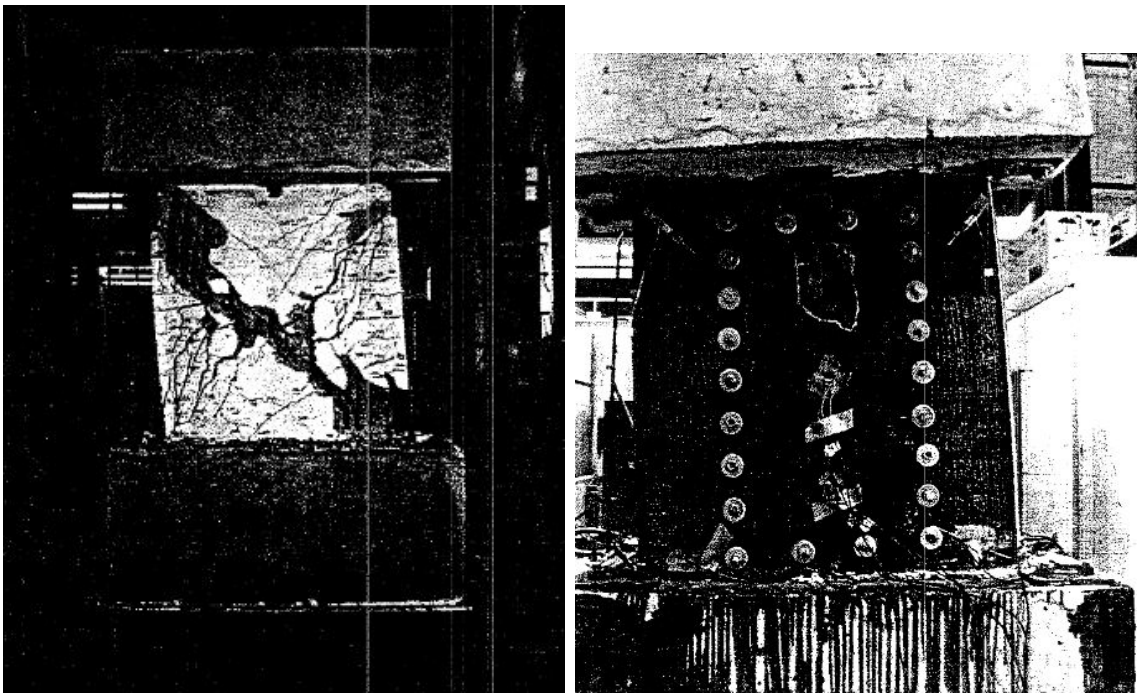

(a) Photo of Control Specimen (b) Photo of Retrofit Specimen

Figure 2.13: Experimental Tests from Khalil and Ghobarah (2005)

sults of 10 shear walls retrofitted with different configurations of FRP. The control wall had been designed to ACI-318-68 code with a lap splice length of 24 times the bar diameter. They were built in tilt-up construction, in one cohesive pour for the foundation, wall, and cap beam. The walls were rectangular with an aspect ratio of 1.1 and a thickness of 0.12 m. The specimens were subjected to applied moment, axial, and shear forces with the use of three actuators. The moment to shear ratio was kept constant at either 1.5, 2.25, or 5 throughout the experiment. The retrofit schemes included shear strengthening of the wall with horizontal FRP and end confinement FRP, anchored with steel plates and steel bars. They found that in general, the higher the moment to shear demand on a wall the more likely the wall was to fail in flexure. Subsequently, lower moment to shear ratios resulted in more mixed or shear failures. They found that CFRP was successfully able to prevent brittle shear failures. Additionally, their results showed end region confinement with CFRP was

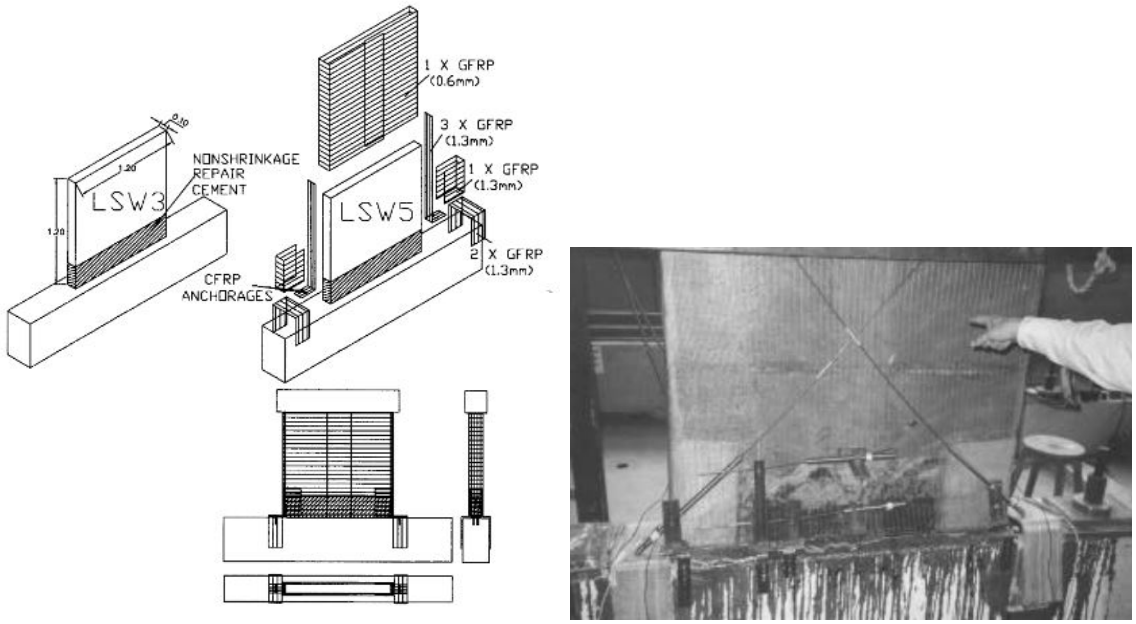

(a) Plan of Retrofit Strategy (b) Photo of Retrofit Specimen at Failure

Figure 2.14: Experimental Tests from Antoniades et al. (2005)

successful in improving the ductility, while web shear FRP strengthening controlled cracks and resulted in more energy dissipation.

Layssi et al. (2012) was very similar to Paterson and Mitchell (2003), and both studies were overseen by the same collaborator, Mitchell. They considered non-ductile shear walls with lap splices in the plastic hinge region. The rectangular specimens had an aspect ratio of 2.7 and a width of 0.15 m. The FRP was applied in one layer fully halfway up the specimen, then in strips above that for the remaining height. The fibers were oriented in the shear direction. There were no anchors used, the FRP was simply overlapped 0.3 m at the middle of the wall. The shear wall was tested in the horizontal position. Retrofitting with FRP improved ductility, energy dissipation, and prevented a premature failure due to the inadequate lap splice in a critical region.

El-Sokkary et al. (2013) considered the necessity of additional reinforcement on current

designed RC walls in the case of which they see larger demands than expected. The first phase of their research involved two 8-story shear wall tests, designed to current standards, and tested to failure. See Figure 2.15 for photos of their experimental setup. The ground and sixth floors exhibited inelastic behavior, and so they were subsequently repaired with the goal of improving the flexural and shear capacity of the walls at the mid-height floor that developed the plastic hinge, and then to increase the rotation capacity at the base of the wall with CFRP without increasing the flexural strength. This sixth floor wall was not able to be re-tested to failure on the shake-table, so a specific program was developed to consider the effectiveness of FRP on the flexural and shear strengths of RC shear walls that are subject to increased demands. Their specific experiment is described in the next paragraph.

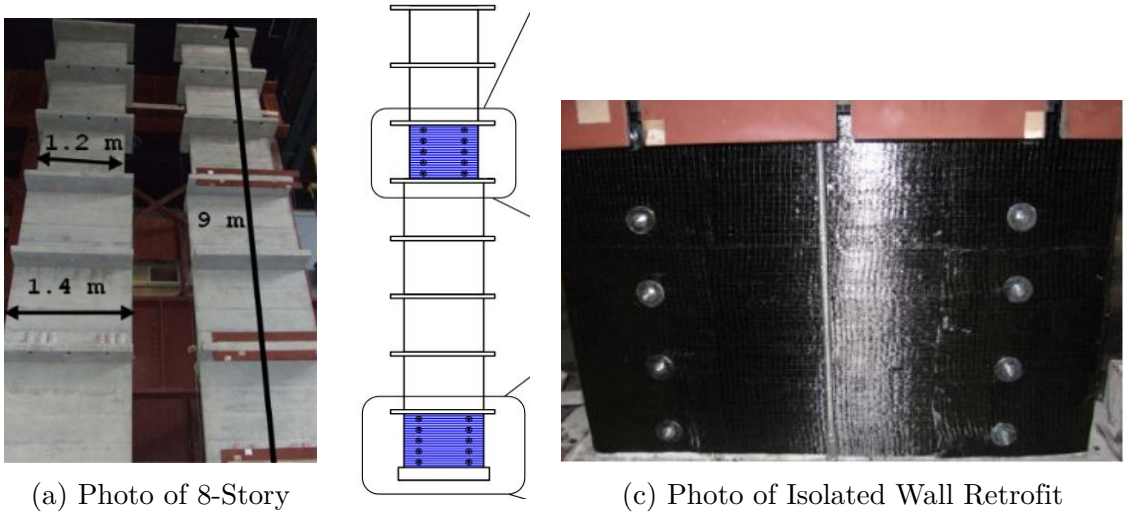

(a) Photo of 8-Story Specimen (b) Retrofit Plan (c) Photo of Isolated Wall Retrofit Specimen

Figure 2.15: Experimental Tests from El-Sokkary et al. (2013)

El-Sokkary and Galal (2013) tested three squat RC shear walls with an aspect ratio of 0.66. The walls were 0.08 m in thickness and rectangular. They considered two FRP retrofit strategies namely 1.) full specimen coverage with horizontal sheets and two additional vertical strips at the boundary regions with FRP anchors into the foundation and head beam. 2.) x bracing across the full height, as well as horizontal strips along the top and the bottom

with vertical anchors into the cap beam and foundation, the same as the first specimen. The walls had a constant axial load and increasing cycles of top moment and lateral load with a moment-to-shear ratio of 2.75. The walls were designed with the current standard of their day, Canadian Standards Association A23.2 (2004) for moderately ductile walls. Both retrofit strategies showed an increase in flexural capacity, but were accompanied by a decrease in the ductility. The plastic hinges were relocated to the foundation wall interface and above the horizontal wrap in specimens one and two respectively.

Altin et al. (2013) strengthened four separate non-ductile specimens with insufficient shear reinforcement. The rectangular walls had an aspect ratio 1.5 and a thickness of 0.10 m. The retrofit schemes were applied to both sides of the wall and they consisted of: (1) 100 mm horizontal FRP strips, spaced at 200 mm apart (2) diagonal strips between the full height struts of the specimen, 200 mm wide (3) diagonal strips along the full height of the concrete strut along with two horizontal 200 mm strips at the top and bottom of the specimen and (4) smaller x-patterns, latticed across the entire specimen, spaced about 270 mm apart and using 100 mm strips with a top and bottom chord of horizontal FRP. See Figure 2.16 for visual depictions of retrofit schemes (3) and (4). The FRP was anchored with 10 mm diameter FRP anchors with a 50 mm splay length. Schemes (1), (3), and (4) were able to effectively alter the failure mechanism of the specimens to be ductile, flexural failures as well as increased the effective ductility from 1% drift to 2% drift without much strength degradation. Plastic hinges were able to effectively develop at the base of these walls. Scheme (2), with just two diagonal sheets of FRP across the full specimen height, failed due to shear before reaching its flexural capacity; the FRP de-bonded and shear diagonal tension cracks propagated.

Le Nguyen et al. (2014) considered two rectangular walls one with aspect ratio of 2.5 and one with aspect ratio of .6, and a thickness of 0.8 m. They were subjected to axial load ratios of 6% for the slender walls and 3 % for the short walls. It appears they used lap

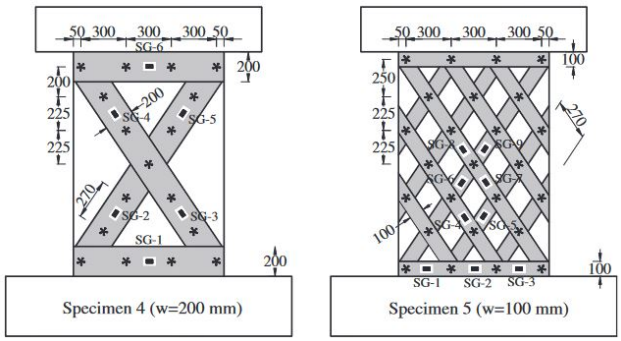

Figure 2.16: Experimental Tests from Altin et al. (2013)

splices for construction, though their test program does not specifically reference this steel configuration. Their retrofitting strategy consisted of 3 vertical strips (with 70% fibers in the longitudinal direction, that is, vertical and 30 % fibers in the horizontal direction per the proprietary CFRP strips) one in the middle of the wall and two at either end. There were also horizontal strips at the base, mid height, and top of the walls. This pattern is repeated on both faces of the walls, with anchors into the foundation, cap beam, and throughout the height of the wall, and through the thickness of the wall, to prevent buckling of the strips. This was a monotonic loading test, no cyclic loading. The slender wall gained strength, but while the control specimen had flexurally-controlled failure, the retrofitted specimen had a combined flexure-shear failure. The FRP strips increased the flexural capacity, and therefore the shear demand, and the higher shear stress led to a degradation in the core of the wall that was not present in the control specimen. The behavior of the short wall improved greatly with the FRP strips, which provided additional strength and much increased ductility, as well as the added benefit of delaying the shear failure and preventing sliding failure at the base of the wall.

Zhang et al. (2016) considered repair of shear walls with FRP retrofits that focused on wall with non rectangular sections; namely L-shaped and T-shaped. The strength and stiffness of the undamaged specimens was recovered, with only a minor decrease in ductility.

Qazi et al. (2015) considered squat RC walls with inadequate shear reinforcement retrofitted with only the faces of the specimens with FRP. They did not provide additional confining FRP wraps around the end regions. The specimens were rectangular with an aspect ratio of 0.67 and a thickness of 0.08 m. The specimens were strengthened with partially bonded CFRP strips, both vertical and horizontal, and anchored them to the foundation. The goal of this investigation was to investigate the ability of CFRP to increase the strength and deformability but without compromising the energy dissipation capacity of the wall. They were tested to failure under a monotonic load. The CFRP was effective in improving the ductility and energy dissipation capacity, as well as altering the failure mode from a shear and brittle failure to a ductile failure mode by limiting the crack propagation in the wall panel.

Qazi et al. (2019) again considered squat RC walls with inadequate shear, but this time the wall was under cyclic lateral load. Again, they wanted to consider the use of 'partially bonded' CFRP strips, especially when the wall boundaries were inaccessible. They attempted two retrofit schemes, 1.) one with horizontal and vertical strips biased towards the edges of the walls, and 2.) one with vertical and diagonal strengthening. The diagonal strengthening extended from the top-center of the wall to the middle center of the edges and another diagonal from the mid center of the wall to the bottom corners. These were all anchored to the wall with fiber anchors. The anchorage effectively limited CFRP debonding, and both strategies improved strength, stiffness, and ductility.

Woods et al. (2016) considered four squat walls designed per ACI318-68. Specimens had an aspect ratio of 1.2 or 0.85 and were rectangular with a thickness of 0.1 m. The two specimens were retrofitted with 1.) one sheet of vertical CFRP and 2.) 3 sheets of CFRP to both faces of the specimen. They wanted to consider the effective improvement of the shear wall behavior if access to the ends of a wall is not available. The retrofit successfully

repressed the premature shear failure, and their results indicated that it is not be necessary to wrap the ends of structures with FRP sheets in order to improve the seismic performance of shear walls, see Figure 2.17 for photo and overall delamination propagation of the FRP.

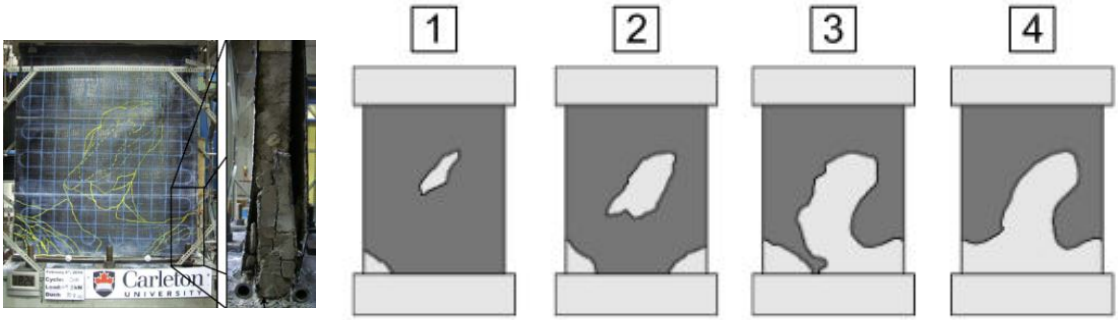

(a) Photo of Retrofit Specimen

(b) FRP Delamination Propagation

Figure 2.17: Experimental Tests from Woods et al. (2016)

Jin et al. (2024b) in 2024 considered the size effect of the reinforced concrete shear wall specimens and the CFRP wrap. The CFRP was shown to effectively alter the failure mode and enhance the seismic resistance of a structure through crack suppression and energy dissipation. However, they also showed that larger sized specimens have a corresponding reduction in strengthening effectiveness. Specifically, the larger specimen size had reduced effects from CFRP on the shear strength, ductility, and energy dissipation. This indicates that the current codes are greatly overestimating the contribution of shear from the FRP strips.

2.5.4 Reinforced Concrete Overlay

The behavior of reinforced concrete, particularly shotcrete, as a strengthening strategy for RC shear walls has been much less extensively tested than FRP. However, concrete collars have been commonly studied and utilized for RC columns, and occasionally beams (Priestley et al., 1996).

"Concrete jacketing" is a common term for fully wrapped concrete elements given an additional 'jacket' of reinforced concrete. This method has been considered and tested extensively, especially around RC columns which may be at risk of damage in high seismic zones (Priestley et al., 1996). It has been shown that providing a simple collar of concrete and steel around the plastic hinge region results in generally shifting the plastic hinge region to above the repair zone. This is something to be cautious of when considering repair and retrofit strategies.

Repair of RC walls was undertaken by Fiorato et al. (1983). They considered a 1/3 scale wall from a 5 story building; the wall was 15 feet tall, 6 feet wide and 4 inches thick. They considered barbell walls. The barbell ends were 12 inches square. They were designed per ACI-77. After testing, the webs were severely damage. The damaged webs were subsequently removed and replaced. One specimen was improved in the replacement with a thicker web section of 6 inches, and in another specimen additional shear steel was added prior to the replacement of the concrete. The columns, though slightly damaged, were not repaired. They only repaired the crushed concrete at the base of the columns which had been marginally damaged. Interestingly, in one specimen, they did add additional diagonal reinforcement, from the foundation at the mid-line of the wall into the boundary elements at a 45 degree angle. The concept was to have tensile ties directly from the boundary elements to help distribute the shear more uniformly across the base of the wall. This is slightly concerning as they had to cut existing web bars to allow this procedure, which were later lap-spliced and welded back to their original length. The initial stiffness of the walls was not able to be fully recovered. Increasing the thickness of the web and adding diagonal reinforcement improved the inelastic response as well.

It is generally well observed that traditional repair, including adequate removal of all damaged elements, can generally get the specimen back to its pre-damage condition for strength

and ductility, if not also stiffness (Vecchio et al., 2002). Although it is important in the repair to pay special attention to the strength of the repair concrete and residual damage in un-repaired zones, which could alter the subsequent behavior of the structural wall, and could even alter the final mode of failure.

Marini and Meda (2009) considered high performance jackets on concrete shear walls and utilized a high strength steel mesh with an ultra high performance fiber reinforced concrete. The experiment was on a 1/3 scale wall of a 3 story building with an aspect ratio of 4 and a thickness of 0.1 m. The jacket and steel mesh were both of higher than typical strength materials and therefore allow the jacket to be much thinner than traditional concrete reinforced jackets. The jacket was 15 mm thick. The wall provided an increase in ultimate resistance, more than twice that of the unretrofitted specimen, and showed increased ductility. The author notes that strengthening of the existing RC walls resulted in a significant increase in the horizontal shear forces into the concrete, which in turn may need additional retrofitting schemes.

Brühwiler and Denarié (2013) considered the addition of ultra-high performance (UHP) concrete jackets to rehabilitate and strengthen concrete structures. The concrete was cast in-place, or 'in situ'. This UHP jacket was shown to improve structural performance and improve durability of the structure.

Raza et al. (2019) considered the seismic strengthening of RC columns with jackets holistically for the past 20 years of experimental data. They summarized that repairs of all kind, including RC jackets, could be effective in strengthening columns and improving the ductility and drift, but the initial stiffness is very hard to recover in an RC column once it's lost.

Nagib et al. (2021) considered an experimental investigation on squat shear-deficient RC

walls, strengthened with UHPRC layers. Four rectangular RC shear walls with an aspect ratio of 1.5, at 1/3 scale were tested with three retrofit strategies: one layer on one side, two layers on both faces, and one jacket, all the way around the wall. Digital image correlation was utilized for detecting the damage mechanism. The wall was 0.1 m thick. The one sided UHPFRC was 0.06 m thick while the double sided and full jacket configurations were 0.04 m thick. The results showed a significant improvement in the lateral load strength, ductility, and energy dissipation capacities, the retrofit strategies and one experimental specimen post test can be seen in Figure 2.18.

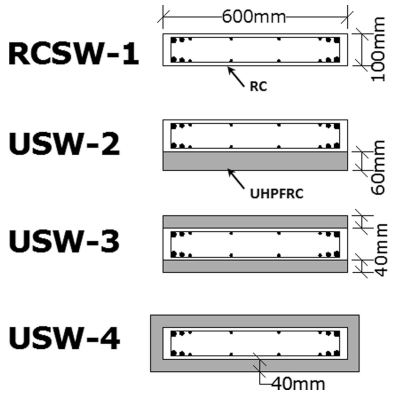

(a) Experimental UHPFRC Retrofit Strategies

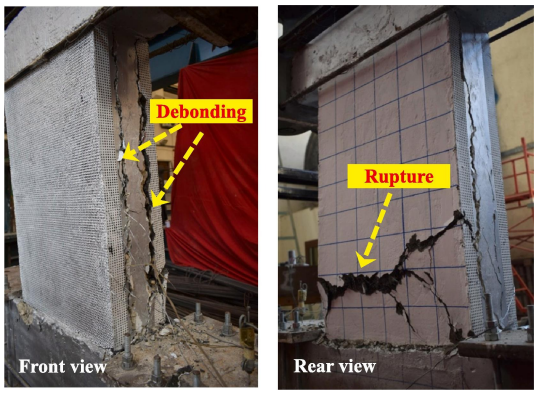

(b) Final Damage State of USW3 Experimental Specimen

Figure 2.18: Experimental tests from Nagib et al. (2021)

Franssen et al. (2021) looked into the use of ultra high performance fiber reinforced concrete (UHPFRC) jackets strengthening of walls and wall-type piers. Their study focused on four large-scale tests of shear critical concrete walls. The walls had an aspect ratio of 1.5 m and a thickness of 9 inches. The experiment removed the cover of concrete to different degrees and replaced it with ultra high performance concrete. This is meant to replicate the condition of corrosion on these 'piers'. Furthermore, one of these specimens was cast at the smaller inner clear cover dimensions, and the jacket was applied externally on this smooth surface, to indicate the affect poor surface prep may have on the results. The walls were loaded

monotonically. The ultimate failure of all of these walls was a sudden shear diagonal crack that localized. Prior to this failure though, the specimens with retrofitting exhibited slightly less initial stiffness as the control, but delayed cracking and ultimately reached higher levels of strength and ductility. The concrete which cast against the un-roughened surface did not reach greater levels of shear resistance than the control, and only had a slight increase in ductility. Additionally, it was not able to distribute the load as effectively as the specimen which had a roughened surface, which you can see in the earlier localization of crack patterns.

Strotmann and Jungwirth (2022) considered an ultra-high performance fiber reinforced shotcrete with the aim of providing a rapid field option for crack control. They found that the fibers in the shotcrete mixture limited the crack widths to 50 micrometers, along with providing a chloride-dense layer which acted as a surface coating.

2.6 Numerical Modeling

2.6.1 General

Typical modeling procedures for finite element analysis can be broken into two general categories: micro models and macro models (Dashti et al., 2014).

2.6.2 Beam or Macro Models

Macro models consider the specimen with global behavior in mind by representing the structure with one element, capable of considering the overall global behavior of a structure. One option to accomplish this is multiple vertical line element models (MVLEM). This was originally created by Massone et al. (2009) and refined by Kolozvari et al. (2015). These can be considered as 'beam models', which are able to account for flexure, shear, and axial loads by use over vertical beam elements, connected by horizontal or vertical springs. This

has been utilized by Orakcal et al. (2004) and Orakcal and Wallace (2006) to successfully capture flexural behavior in slender RC walls. Another option for a macro model could be a rotational spring to represent the plastic hinge region, and a truss or beam element to represent the vertical wall. These models are typically inadequate, and neglect to capture the shear behavior of RC walls due to the common inherent assumption that plane sections remain plane in this model. The strains in the shear-controlled behavior modes of RC walls are highly localized and nonlinear, invalidating the assumption that plane sections remain plane. Macro models have been used by many researchers, some notable studies include work by Kabeyasawa et al. (1983), Vulcano and Bertero (1986), and Linde (1993). These types of models are also currently suggested in ASCE-41 as modeling guidelines of structural walls.

2.6.3 Micro Models

Micro models consist of a discretized mesh of a structure. This can be represented in 2D or 3D. 3D models consist of a 'brick' element with a continuum 3D theoretical space. This is typically a more computationally expensive analysis due to the geometry of the finite element alone. On top of that, the behavior of concrete is difficult to capture as it is relatively unpredictable (Dashti et al., 2017), and it also requires high numbers of elements which result in even higher computational costs.

Micro models in 2D can consist of plane stress, plane strain, shell elements, or truss elements. Palermo and Vecchio (2002), Panagiotou et al. (2021), and Dashti et al. (2014) have attempted models of 2D elements. Furthermore, the explicit or implicit definition of the reinforcing steel as a smeared element, an independent line element, or an embedded element, each result in their own issues such as bond or mesh dependency (Dashti et al., 2017).

There have been many studies dedicated to the difficult task of accurately modeling structural walls (Dashti et al., 2017; Deng et al., 2021; Panneton et al., 2006). A model that has

been shown to capture a wide range of damage patterns in RC shear walls is the nonlinear truss model. The nonlinear truss model by Deng, building on the work of Lu and Panagiotou (2014), has been shown to effectively capture the axial-shear-flexure interaction, diagonal cracking and diagonal compressive failure, as well as strength degradation and out-of-plane plastic hinge buckling as well as bar buckling and rupture.

2.6.4 Modeling of Retrofitted Walls

Understanding and adequately modeling of retrofitting strategies has been undertaken by several researchers (Cortés-Puentes and Palermo, 2012; Li et al., 2005; Mostofinejad and Mohammadi Anaei, 2012; Sakr et al., 2019). The difficulties in this research lie in the adequate capture of behavior of not only the retrofit material (which have historically inconsistent reported behavior), but the behavior at the interface of the existing structure and the overlying retrofit (Dukes and Sattar, 2022a). This is a crucial component of a numerical model because the interface can often be a critical plane of failure for the structure.

Elnady (2008a) proposed an analytical model along with their experimental results. They looked at both macro and micro models. They used a confined concrete model in the end regions where the FRP provided additional confinement of the concrete. The shear strain was incrementally increased at each step, then strain in the ε_x and ε_y were assumed. Then principal strains and stresses were calculated with equations from Mander and Mitchell and Collins (Mander et al., 1988b; Paterson and Mitchell, 2003). The shear force was calculated, and then the axial force was estimated until they were able to achieve equilibrium. They used an idealized tie distribution to simulate the FRP strengthening. The model was able estimate the experimental hysteretic results of their stiffness degradation, strength deterioration within 10%.

Mostofinejad and Mohammadi Anaei (2012) considered FRP confinement on the boundary regions only of squat shear walls. They did this through an Abaqus analysis including a plastic damage model. The FRP was modeled as an 8-note solid element. For appropriately detailed boundary elements, the addition of FRP was insignificant, until you reached a threshold amount of sheets, then it improved ductility. It also added confinement at the boundary elements. The study concluded that it would be sufficient to improve ductility in a specimen by simply applying the retrofit FRP to the plastic hinge region on the boundary.

Le Nguyen et al. (2014) did an in-depth numerical analysis of their experimental results. They considered a smeared fixed crack approach with perfect bond and they use a regularization technique for the softening behavior of the concrete which is based on the classical concepts of fracture energy, modified according to the steel with the tension stiffening effect. They then considered an alternative approach in which they had an interface element between the CFRP and concrete element, associated with a bond-slip model. They were interested in the energy approach, which ensures the global results are not sensitive to mesh size. They use the cracking energy G_f to consider the effect of tension stiffening, as well as the compressive fracture energy to get the ultimate uniaxial strain. Their model overestimated the flexural capacity, until they specifically accounted for the debonding of the FRP. They propose their own equation for FRP strain once the debonding has occurred, but when the anchors are still present, allowing the material to continue carrying tensile load, but no longer compatible with the concrete.

El-Sokkary and Galal (2013) considered a macro-structure model (and he has a very good description of the history of nonlinear wall macro-models). Nonlinear static analysis was performed using Canny. The wall consisted of a multi-axial spring model, with springs representing the flexural and axial tension/compression, and another spring representing the shear deformations. The FRP strips were modeled as rigid links. They were successfully

able to match the parameters in the model to achieve the experimental behavior.

Jin et al. (2023) considered a 3D numerical model which aimed at capturing the effect of strain rate on the separate constitutive components in the steel, concrete, CFRP, and CFRP-concrete interface. They found that the strain rate corresponded to increased damage, as well as an increased ductility coefficient and energy dissipation capacity. Their model showed the CFRP strips were capable to taking high strain rates, increasing the bearing capacity of the shear wall. They summarized their findings with a strain-rate dependent formula which predicts the dynamic shear contribution of CFRP.

El-Kashif et al. (2019) considered a 3D model using the software ANSYS, and attempting to capture the FRP components of the retrofit. They had success with this model, showing good agreement with experimental tests, and showing that an addition of FRP can enhance the flexural strength, stiffness, ductility, and shear capacity of a non-ductile wall.

Jin et al. (2024a) considered the effects of CFRP and the reinforcement ratio of a strengthened shear wall through solid 3D numerical parametric study. They consider the current code which independently separates the shear components of the overall wall strength into the component from the concrete, the steel, and the FRP. They found that an increased reinforcement ratio of the CFRP strips reduced the failure degree of the shear walls, but counter-productively, they also found that an increase in the horizontal shear steel reinforcement ratio weakens the shear-strengthening effects from the CFRP. Subsequently, they developed a coefficient which can more accurately capture the combined effect of the CFRP ratio and the horizontal reinforcement ratio to the overall effectiveness of the CFRP sheets.

A detailed constitutive model of shotcrete concrete as an individual element is described in Schütz et al. (2011). The model accounts for cracking through a smeared model with fracture energy. It also accounts for the cement hydration over time, as well as creep, shrinkage, and

temperature. Another constitutive model was developed by Schädlich and Schweiger (2014) which considers the elasto-plastic strain hardening and softening plasticity. They similarly regularize their strains with a smeared crack and fracture energy assumption. Creep is also considered in this model.

There are many experimental tests with numerical or analytical validation of reinforced concrete jackets around reinforced concrete columns. One such example is by Joseph et al. (2022) where they considered a numerical fiber model to verify the experimental performance of a high performance reinforced concrete (HPRC) jacket for a column. They considered a confined concrete model for the effects of the HPRC jacket, and essentially assumed perfect bond between the existing concrete column and the overlay. This model was only a small part of a larger study on overall retrofit strategies for substandard RC buildings. Another model by Ichikawa et al. (2016) considered ultra HPC with a rotational difference between the overlay and the concrete core, resulting in differing strain values. The sections were then analyzed with the ACI-318-11 approach.

2.6.5 Previous Strain-based Assessment Criteria

Priestley and Kowalsky (1998) suggested serviceability limits of crack width (1.0 mm), concrete strain (0.004) and steel strain (0.015) as well as damage control limits of concrete strain (0.018) and steel strain (0.06). These limits were set with direct displacement based design methodology in place, considering acceptable levels of damage at different displacement limits. Strain-based limits specifically for flexure-controlled walls were previously established for displacement-based design methodologies by Priestley et al. (2008), who suggested the initial limit of yielding due to the strain in the steel, while Panagiotou and Restrepo (2011) set forth specific IO performance levels for steel strain (0.01) and concrete strain (-0.004) and 0.04 maximum steel strain for the LS performance level. There have also been analytical

performance assessment studies for concrete buildings, using stipulated limit strain values for different damage/performance levels (İlker Kazaz et al., 2012; Whitman, 2015; Shendkar et al., 2025).

Strain-based criteria are also indirectly introduced into the New Zealand Code (Zealand, 2017) for assessment of existing structures. The specific document establishes limit curvature values for the hinge regions of wall components, indirectly related to limit strain values in the compressive region and the tension reinforcement of a planar cross-section. Recent work has pursued the formulation of strain-based criteria for the assessment of existing wall buildings. Shegay et al. (2019) proposed changes to the New Zealand code, on the basis of different equations to estimate the limit strains for the concrete and reinforcing steel. The introduction of their criteria was motivated by the fact that the relevant code guidelines were giving component deformation capacities which had significant dispersion and rather limited accuracy when compared against experimental data. Deng et al. (2021) proposed detailed and specific strain criteria for multiple levels of damage for the common IO, LS, and CP limits, and is the basis of this study. The formulation of the criteria was based on the thesis that – contrary to component-level quantities such as hinge rotations or drift ratios - local deformation states in the concrete and reinforcing steel have a direct connection with the level of damage in a structure, and, consequently, with the performance state attained for a specific seismic intensity. A later study by Rajbhandari et al. (2025) proposed strain-based criteria for five distinct categories of damage levels, partially based on qualitative and quantitative descriptions in the Japan Building Disaster Prevention Association (JBDPA) guidelines. The study used relatively simple, lumped-plasticity, beam models to evaluate the applicability of the strain-based criteria to a set of experimentally tested, flexure-controlled walls. Compared to the earlier work of Deng et al. (2021) the specific study was characterized by a number of limitations in the adopted modeling approach and acceptance criteria. First,

the criteria for buckling and rupture were based on merely stipulating limit values of strain, which may not be accurate. More importantly, it is now well-established that using beam elements which neglect the nonlinear flexure-shear interaction is bound to lead to inaccurate results even for flexure-dominated walls (Lowes et al., 2012).

2.7 Summary

In terms of the experimental programs for RC structural walls including retrofit strategies, there is a gap for barbell wall specimens, particularly for reinforced concrete overlay strategies, one sided strategies, and lap splice failures in the end regions of these specimens.

Furthermore the existing guidelines for assessment and retrofit of existing structures, ASCE-41, relies on empirically derived values, and requires further consideration. Particularly, a robust methodology for strain-based assessment of structures is lacking in the literature and the current guidelines. Furthermore, the current guiding document for externally bonded FRP retrofit for RC structures, ACI-440, also relies on empirically derived values, and the design equations should be validated through specific experimental investigation.

Chapter 3

Experimental Setup

3.1 Overview

This chapter describes a set of six experimental non-ductile reinforced concrete structural wall tests, built and tested at the Thomas M. Murray Structural Engineering and Materials Laboratory at Virginia Tech. The details of each specimen's configuration including internal reinforcement and external retrofitting scheme is described, along with the design material properties. The overall setup of the tests is explained, including all instrumentation and loading and restraining mechanisms. The results of the experimental tests are described in detail in Chapter 4.

3.2 Specimen Design

3.2.1 Basis of Design and Retrofit

This test series is designed to examine the behavior of non-ductile structural reinforced concrete (RC) walls built before the 1970s. A general research survey was carried out in collaboration with a panel of professional practicing engineers to determine the specific parameters which would be representative of the practice and detailing methods of mid-1950s to mid-1960s structural walls built in California. The ACI 318-56 (ACI-318, 1956)

code was also consulted to ensure reasonable levels of reinforcement, configuration, and lap splice length were selected.

As this experiment was naturally going to be restricted by the physical parameters of the testing facility, it was necessary to select an appropriate height and size for the specimens. A common approximation for an experimental specimen's height is what is known in literature as an 'effective height'. To determine the effective height for this project, a prototype structure of 8-stories is selected, which is typical for structures built in California in the mid-1950s. To determine an effective height generally, one considers an assumed lateral load distribution caused by dynamic forces, where a single force is applied at each story height, as illustrated in Figure 3.1. These multiple lateral loads may be defined by one equivalent lateral force, $V_{equivalent}$, which acts at a single location. The location of this resultant lateral load is what is known as the effective height, h_{eff}. Therefore, structural walls that are full-height and dynamically loaded can be modeled as shorter walls with an equivalent lateral point load applied at their top effective height, which is depicted in Figure 3.1. Note that an equivalent calculation for the effective height is the ratio of the system base moment to the total system base shear, also known as the system moment-to-shear ratio.

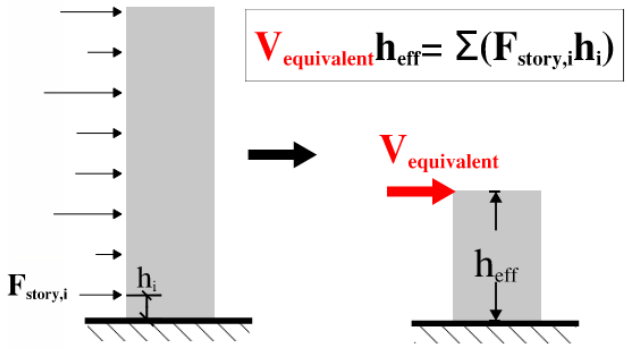

Figure 3.1: Representation of a Structure's Effective Height

During dynamic loading (i.e. an earthquake) the lateral loads at each floor will change, resulting in a dynamic effective height of the structure. Therefore, any attempt to approximate

a static height for quasi-static experimental testing is bound to be restricted in accuracy. It is noteworthy that there have been several experimental tests which aimed to provide a constant moment-to-shear ratio to a partial-height structure (Elnady, 2008b; Birely et al., 2010; Brueggen et al., 2017). Birely et al. (2010) found that a reduction in effective height resulted in a reduction in drift capacity and more rapid strength loss. Elnady (2008a) found that a lower effective height resulted in a more shear-dominated response. Brueggen et al. (2017) found that utilizing a constant moment-to-shear ratio in a 4-story partial height structure versus a 2-story partial height structure (both emulating the same full height 6-story structure), resulted in equivalent plastic hinge behavior. These experimental tests were still simplified methods of consideration for the selected effective height (i.e. constant values). Therefore, these experimental test set-ups are not necessarily more accurate than a setup which does not apply a moment to the top of an experimental wall structure (i.e. the setup used in this study).

The effective height selected for this experimental program was conservatively chosen to constitute a 'worst-case' scenario effective height, which occurs at a minimum value. An experimental investigation on a 7-story structure was undertaken by Panagiotou et al. (2011), which considered the higher mode effects for taller structures. Their findings indicated that the effective height could be as low as 0.25% of a structure's height. Hence, the prototype 8-story structure for this project has an effective height of 2-stories, or 24 feet. The aspect ratio of 2.0 was selected to consider walls which may be both shear and flexure controlled.

The experimental program consisted of six half-scale cantilever specimens, representing the bottom two stories of an eight-story prototype wall building. The general form and nomenclature adopted in this study are shown in Figure 3.2. The specimens are comprised of three parts: the foundation, the wall, and the top transfer beam (also called the cap beam), which can be seen in Figure 3.2a. The wall cross-section, also referred to as a barbell section, was

common before the 1970s. It consists of a thin rectangular web region and two end regions known as "barbells" (also called "pilasters" or "columns").

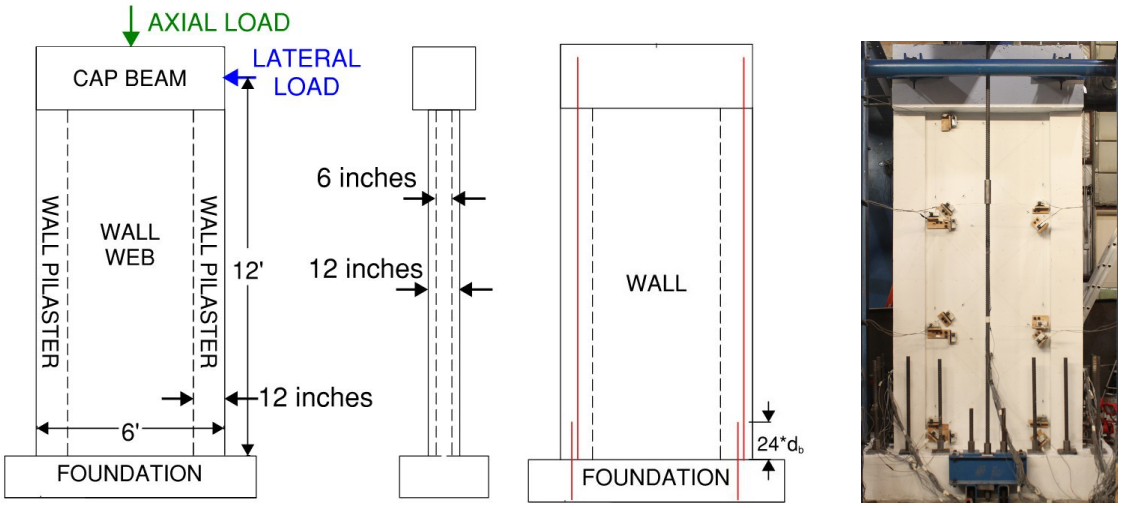

(a) General Specimen Dimensions and Nomenclature

(b) Lap Splice Condition

(c) Un-retrofitted Specimen Prior to Testing

Figure 3.2: General Specimen Details

The specimens are divided into two groups: Group One, consisting of walls *without* a lap splice, and Group Two, consisting of walls *with* a lap splice condition. An as-built photograph of specimen an unretrofitted control specimen is shown in Figure 3.2c. Specific details of the specimen design are provided in Section 3.2.2.1. Only the first specimen will be described in detail, as the internal geometries and layout of the reinforcing steel are nearly identical for all six specimens. The lap splice in the plastic hinge region for group two specimens can be seen in Figure 3.2b.

The detailing and arrangement of these retrofit strategies, particularly the FRP overlay strategies, were determined in consultation with professionals from the design, manufacturing, and structural analysis sectors as well as guided by the ACI 440-17 standards (ACI 440 Committee, 2017). The selection of retrofit methods prioritized techniques commonly used in the field today, ensuring that the research findings are directly applicable to modern

retrofit scenarios. It was identified that, in practice, accessing the full range of a wall, particularly the end regions or the "back face", is often challenging. These areas may intersect with other walls or be located at the bottom of an elevator shaft, making access difficult, if not impossible. Therefore, to address this practical limitation, a single-sided retrofit overlay configuration was selected for S1 specimens. Two primary methods were adopted for investigation: (1) shotcrete and (2) FRP overlay. These can be seen in Figures 3.3b and 3.3c.

The failure modes of the single sided wrap retrofit S1 specimens informed the retrofit for the final S1 specimen, which was designed to have bar buckling FRP wrapping confinement in the pilasters in addition to the single-sided FRP web strengthening. The retrofitted S2 specimen was designed to prevent the anticipated lap splice failure through FRP end-wrapped confinement. The full testing matrix outlining these retrofit strategies is presented in Table 3.1.

Table 3.1: Experimental Program Test Matrix

Specimen Label	Lap Splice?	Retrofit Strategy
S1	No	None
S1-CW	No	Concrete, 1-sided, Web shear strengthening
S1-FW	No	FRP, 1-sided, Web shear strengthening
S1-FP	No	FRP, 1-sided web and Pilaster bar buckling prevention
S2	Yes	None
S2-FL	Yes	FRP, Lap splice clamping

Photographs of each specimen prior to testing, with all applicable retrofit strategies installed, are shown in Figures 3.3 and 3.4.

(a) S1

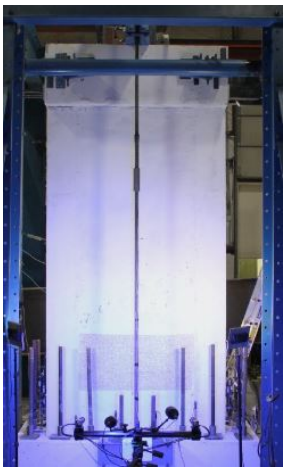

(b) S1CW: Concrete Shear Web Overlay

(c) S1FW: FRP Shear Web Overlay

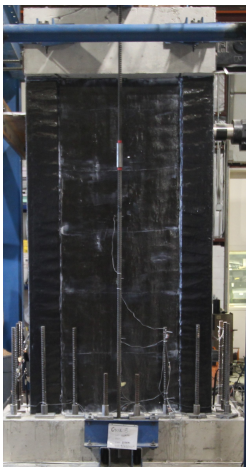

(d) S1FP: FRP Shear Web and Pilaster Buckling Confinement

Figure 3.3: As-built Specimen Group One with No Lap Splice

3.2.2 Unretrofitted Specimen Design

3.2.2.1 S1 - Control

Specimen S1 is detailed comprehensively, as it epitomizes the geometry and steel reinforcement configuration of all six specimens. The foundation dimensions are 2 feet and 10 inches in width, 16 inches in height, and 8 feet in length, as depicted in Figures 3.5 and 3.6. The foundation has 14 cylindrical channels that run vertically through the concrete, facilitating the post-tensioning of the cured specimen to the strong floor via fourteen Dywidag© bars. These bars, possessing a diameter of 1.5 inches and composed of grade 160 steel, are post-tensioned with a force of 80,000 pounds each. This configuration secures the specimen to the strong floor, thereby mitigating the risk of sliding failure during the application of lateral loads.

The wall's geometry is shown in Figure 3.6. The pilasters are 12 inches square, while the web is 6 inches thick and 48 inches long. The longitudinal reinforcement in the pilasters

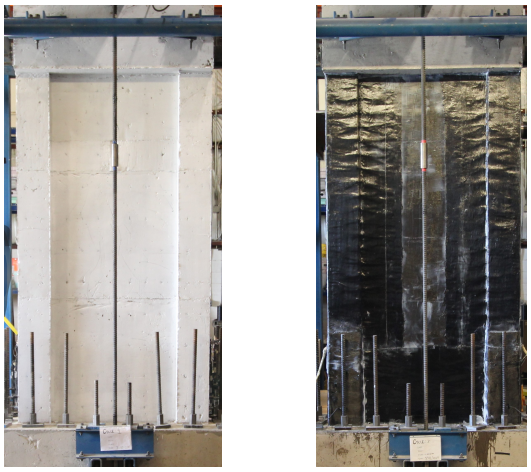

(a) S2

(b) S2FL: FRP Shear Web and Lap Splice Confinement

Figure 3.4: As-built Specimen Group Two with Lap Splice

consists of grade 60 steel, arranged as seen in Figure 3.6. The web's vertical and horizontal reinforcement, as well as the shear stirrups in the pilasters, are D5 bars, which are 5 mm in diameter and equivalent to a #2 bar; they are grade 80 steel.

Acquiring reinforcement materials consistent with pre-1970 methodologies, specifically grade 40 steel, proved impracticable for this project. To reconcile this inconsistency between traditional techniques and the contemporary availability of materials, a constant target value was maintained for the reinforcement ratio multiplied by the steel grade, as delineated in Equation 3.1. This approach serves to bridge the divergence between historical practices and available materials today. The reinforcement ratio employed in the specimens is calculated according to Equation 3.2, utilizing the expected or actually measured reinforcement material properties (see Section 3.2.4.2). The target steel ratio corresponding to a pre-1970s wall, per the research survey described at the beginning of this chapter, is selected as follows for the longitudinal and transverse steel in both the pilasters and web: transverse reinforcement in the pilasters and web, as follows: $\rho_{lp} = 3\%, \rho_{tp} = 0.5\%, \rho_{lw} = \rho_{tw} = 0.25\%$. The subscripts

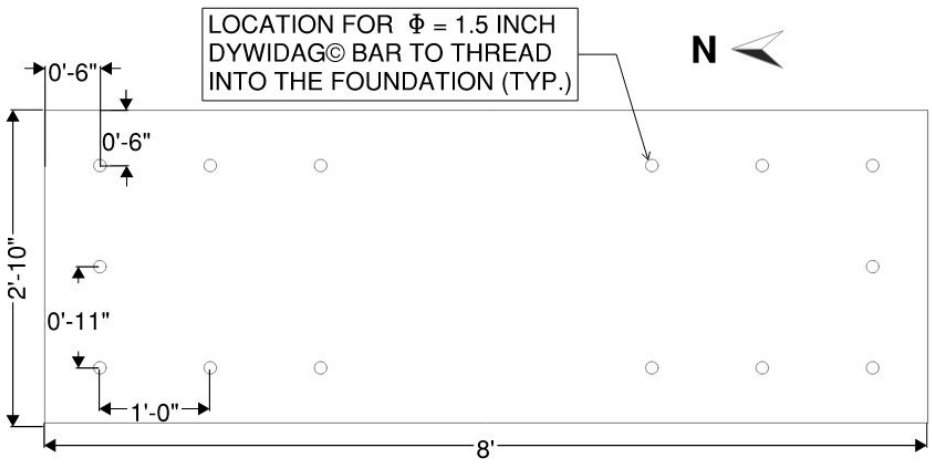

Figure 3.5: Foundation Plan View, Concrete Dimensions and Dywidag© Bar Locations for Foundation Tie Down

correspond to either longitudinal, 'l', transverse, 't', pilaster, 'p', and web, 'w'.

$$\rho_{target} f_{y,Gr40} = \rho_{actual} f_y \quad \text{(Eq. 3.1)}$$

$$\rho = \frac{A_{steel}}{A_{concrete}} 100\% \quad \text{(Eq. 3.2)}$$

The wall reinforcement is arranged as shown in Figure 3.6. #5 bars and #4 bars are used for longitudinal reinforcement in the pilasters, while remaining reinforcement is comprised of D5 bars. D5 bars are the equivalent to a #2 bar in diameter and area.

The cap beam has dimensions of 2 feet wide, 2 feet high, and 6 feet in length. There are four hollow cylinders running horizontally to allow the specimen to be attached to the hydraulic loading actuator via threaded rods. The steel reinforcement in the cap beam consists of #6 stirrups, with #6 longitudinal steel in the stirrup corners.

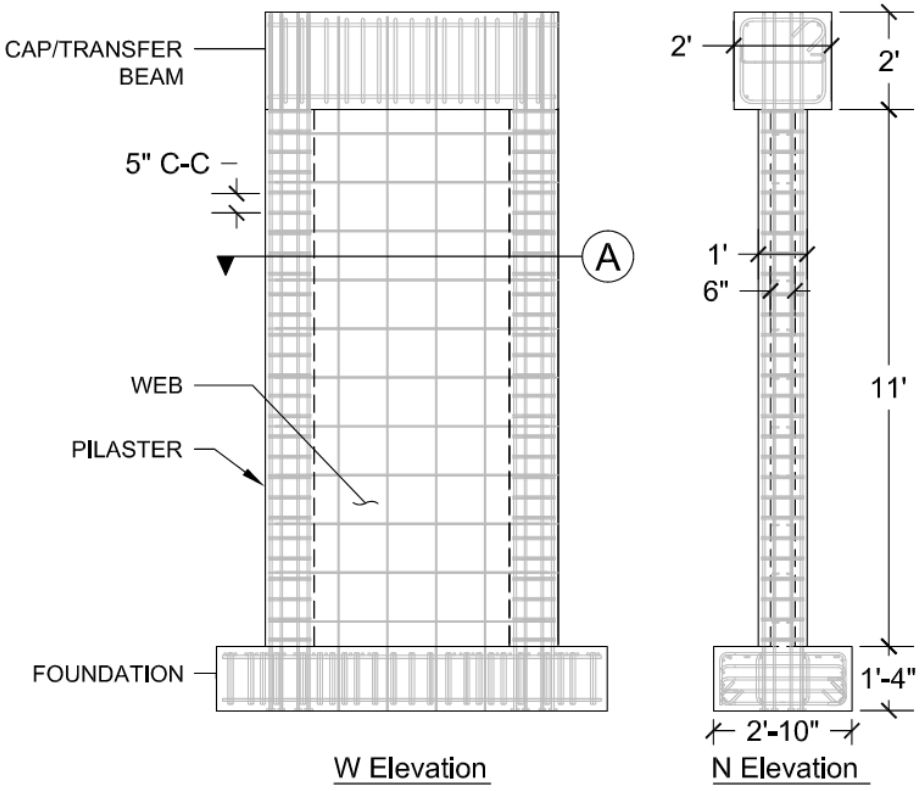

(a) Elevation Views of Specimen Steel Configuration

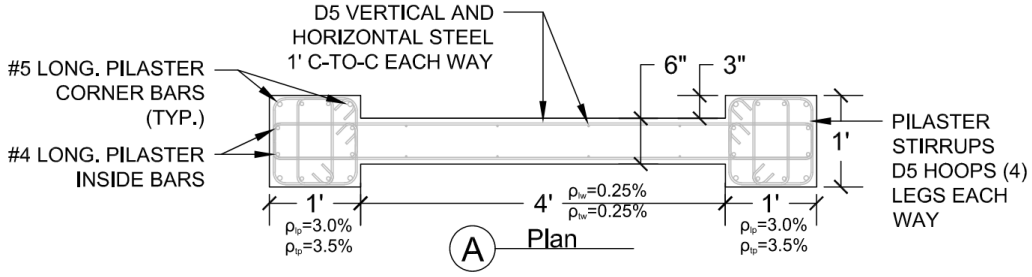

(b) Plan View Through Section A

Figure 3.6: Specimen Geometry and Reinforcement Configuration

3.2.2.2 S2 – Control with Lap Splice

Specimen S2 is an unretrofitted control specimen with identical detailing and geometry as specimen S1 (see Section 3.2.2.1). It has a lap splice in the plastic hinge region equal to a length of $24d_b$ per the ACI 318-56 code requirements (Note the corresponding retrofitted specimen is S2FL, detailed in Section 3.2.3.4). This results lap splice lengths for each bar size as noted in Table 3.2. This lap splice is utilized for all vertical steel from the foundation to the vertical steel in the wall. Figure 3.7a shows the lap splice reinforcement extending the appropriate lap splice length vertically from the foundation; note, the majority of the wall steel is not yet in place. Figure 3.2c shows the final constructed specimen. The expected and desired failure mode of this specimen is through lap-splice slip.

(a) S2 Foundation Lap Splice Photo

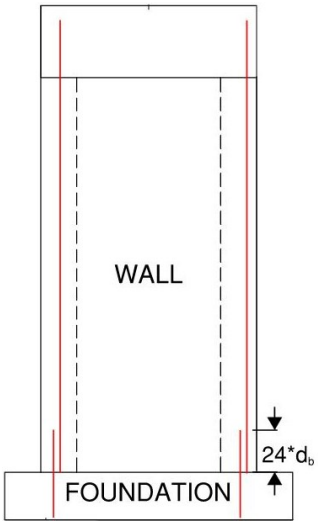

(b) S2 Foundation Lap Splice

(c) S2 Pre-Testing

Figure 3.7: Specimen S2 Photos

Table 3.2: S2 Lap Splice Length in Plastic Hinge Region

Rebar Size (#)	Lap Splice length $24d_b$ (inches)
6	15
5	12
D5	6

3.2.3 Retrofit Specimen Design

3.2.3.1 S1CW - Concrete Web

Specimen S1CW received a retrofit strategy of shotcrete applied to the web of the specimen, with the intent to increase the shear capacity of the web to a degree that will sufficiently preclude a shear web damage pattern. In other words, the flexural inelastic damage, also known as flexural hinging, is intended to precede other damage in the specimen. In order to accomplish this, the ultimate flexural capacity, M_{MCultE}, of the section is calculated in accordance with ACI 318 chapter 22, at an ultimate compressive fiber strain of -.003. The shear capacity associated with the ultimate flexural capacity, V_{MCultE}, is calculated by dividing M_{MCultE} by the shear span per Equation 3.3b. The shear span in this case is the height of the specimen, or 12 feet. To prevent inelastic deformations in shear, the shear strength of the wall $V_{CWall318E}$ must *exceed* the shear demand associated with the ultimate flexural capacity (Equation 3.3d). The shear strength is calculated per ACI-318 and repeated here as Equation 3.3c.

[h]

$$M_{MCultE} = 1848kip - ft \tag{Eq. 3.3a}$$

$$V_{MCultE} = \frac{M_{MCultE}}{height} = \frac{1848kip - ft}{12ft} = 154kip \tag{Eq. 3.3b}$$

$$V_{CWall318E} = (\alpha_c \sqrt{f'_c} + \rho_{t,w} f_{yt,we} + \rho_{t,o} f_{yt,oe}) A_{cv} = 186.8kip \tag{Eq. 3.3c}$$

where $\rho_{t,o}$ is the reinforcement ratio of the concrete overlay, and $f_{yt,oe}$ is the yield strength of the external # 3 reinforcement in the overlay, taken as 60 ksi.

$$V_{CWall318E} > V_{MCultE} \tag{Eq. 3.3d}$$

The interface shear strength was calculated per the Hilti method (Hilti, 2025), founded from Palieraki et al. (2014). It is relevant to note that the dowel bars are not expected to reach yielding during loading, and therefore the ACI 318 shear friction provision is not applicable for this calculation. The dowels are D5 hooks, designed to provide sufficient shear strength at the interface between the existing specimen and the additional retrofit shotcrete. The Hilti method calculates a nominal shear strength, V_n, acting over a concrete interface area, A_c as seen in Equation 3.4a. It considers the parameters for 'friction' as $\beta_f * \tau_f$ and for 'dowel action' as $\beta_d * \tau_d$. The factor of β_f is taken as 0.2 per Hilti, corresponding to a mechanically roughened surface with normal strength concrete.

[h]

$$V_n = A_c(\beta_f \tau_f + \beta_d \tau_d) \tag{Eq. 3.4a}$$

$$\tau_f = 0.33((f'_c)^2(f_{c,vf} + f_{ext}))^{1/3} \tag{Eq. 3.4b}$$

where

$$f_{c,vf} = minimum \left\{ \frac{f_y A_{vf}}{A_c}, \frac{5 f_{bu} l_e A_{vf}}{d_b A_c} \right\} \tag{Eq. 3.4c}$$

Where f_y is the yield strength of the bar, which in this case was reduced due to inadequate development length such that $f_{y,effective} = f_y * l_{embedment}/l_{dh}$, $l_{dh} = 6 inches$, $l_{embedment} = 2.25 inches$. A_{vf} is the nominal bar area, taken as equivalent to a #2 bar. f_{bu} is the bond stress, corresponding to a characteristic bond stress

The shotcrete overlay fills a depth of 3 inches, encompassing the space between the pilaster

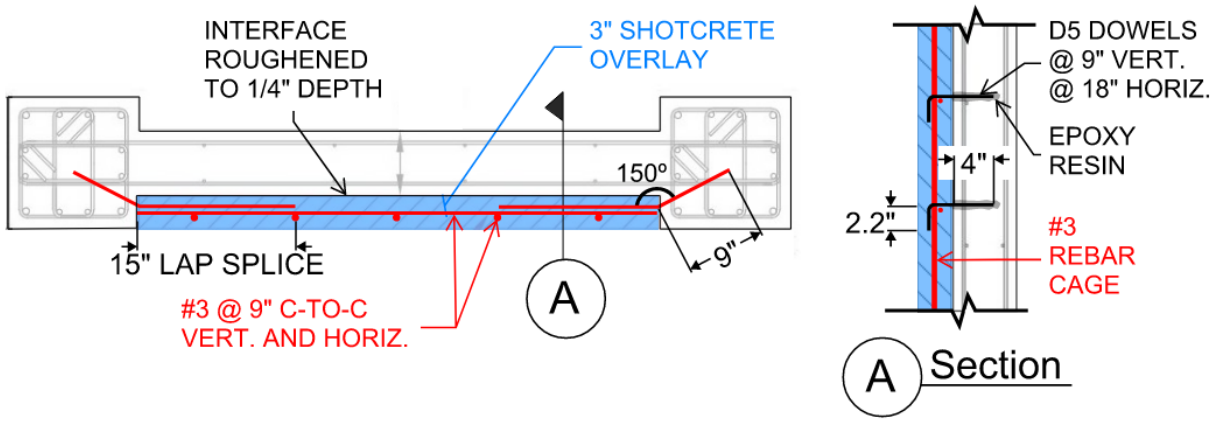

Figure 3.8: S1CW Overlay Reinforcement and Embedment Details

edges and the web as can be seen in Figure 3.8. The required reinforcement to achieve the $V_{CWall318E}$ shear strength is shown in the details of Figure 3.8. A grid of #3 bars was added to the existing specimen, with 9-inch horizontal embedment to the pilasters. Additional dowel anchors were placed at intersections of the vertical and horizontal rebar, embedded 4 inches in the face of the web, spaced at 18 inches horizontally and 9 inches vertically. All embedded rebar from the external cage in the existing specimen were installed with the Hilti HIT-RE 500 V3 2-part epoxy adhesive anchoring system. This epoxy is NSF/ANSI Std 61 approved with a tensile strength per ASTM D638-14 of 7,150 psi and compressive strength per ASTM D695-10 of 12,000 psi.

The web of specimen S1CW is initially prepared with surface roughening, achieved using a hammer bush drill with an attachment designed to impact the concrete to a depth of 1/4 inch. Figure 3.9a shows the result of the surface preparation on the web. It is clear from the figure the difference between the smooth pilaster and the roughened web. The external rebar grid necessitated pre-drilled holes for both the horizontal embedment and the anchors. The shotcrete was then sprayed through a hose, as seen in Figure 3.9c. The force with which the concrete is projected out from the hose forces the shotcrete to self-compact, and the external rebar cage provides additional support prior to concrete curing. The shotcrete was sprayed

with water daily for 3 days and covered with plastic. The final configuration of the concrete overlay retrofit can be seen in Figure 3.9d.

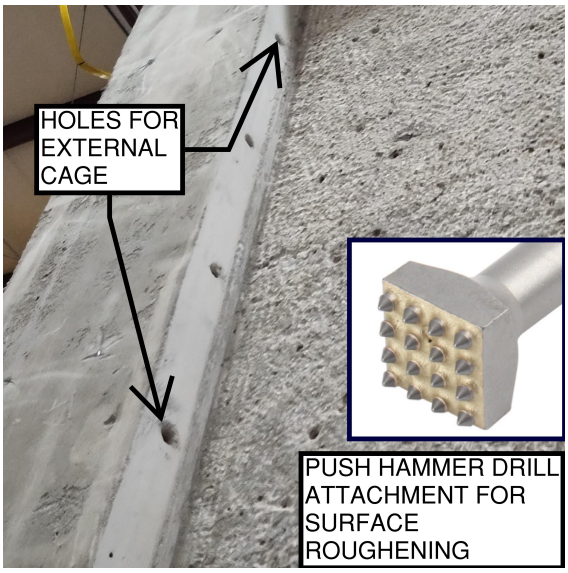

(a) Shotcrete Surface Preparation

(b) Shotcrete External Cage

(c) Installation of Sprayed Shotcrete

(d) Final Shotcrete Installed

Figure 3.9: Shotcrete Installation Process, Specimen S1CW

3.2.3.2 S1FW – FRP Web

The retrofit strategy for the shear strengthening of this specimen followed the same design motivation as the concrete overlay. The shear strength of the specimen must be stronger than the shear associated with the ultimate flexural demand in order to prevent shear inelastic deformation. The required strength is therefore the same calculated per Equation 3.3c. The contribution of the FRP to the specimen can be calculated using the design equation from ACI 440-17(ACI 440 Committee, 2017), written here as Equation 3.5a. The nominal strength of the specimen can then be considered by adding the contributions of the shear reinforcement and concrete to that of the FRP, as seen in Equation 3.6.

$$V_f = \frac{A_{fv} f_{fe} (sin\alpha + cos\alpha) d_{fv}}{s_f} \quad \text{(Eq. 3.5a)}$$

$$A_{fv} = n_f t_f w_f \quad \text{(Eq. 3.5b)}$$

$$f_{fe} = \varepsilon_{fe} E_f \quad \text{(Eq. 3.5c)}$$

$$\varepsilon_{fe} = k_v \varepsilon_{fu} \quad \text{(Eq. 3.5d)}$$

$$k_v = \left(\frac{f'_c}{4000}\right)^{2/3} \left(1 - \frac{2L_e}{d_{fv}}\right) \frac{L_e}{468\varepsilon_{fu}} \quad \text{(Eq. 3.5e)}$$

$$L_e = \frac{2500}{(n_f t_f E_f)^{0.58}} \quad \text{(Eq. 3.5f)}$$

$$V_n = V_s + V_c + \psi_f V_f \quad \text{(Eq. 3.6)}$$

where A_{fv} is the cross sectional area of the FRP wrap, the effective stress of the FRP, f_{fe}, is the effective design strain of the FRP, ε_{fe}, multiplied by the design ultimate tensile strain ε_{fu}, multiplied by the modulus of elasticity of the FRP, E_f. d_{fv} is the effective depth of

the FRP sheet in the direction of the load being resisted, taken as 0.8 times the full length of the FRP sheet of 48 inches, (this accounts for the transfer length between the substrate and the FRP), s_f is the centerline spacing between FRP sheets in this case taken as the width of the fabric sheet, 'n_f' is the number of plies of fabric, and an extra factor of 0.75 is applied with a one-sided overlay strategy, 't_f' is the thickness of the FRP sheet (C100HM has a thickness of 0.02 inches), 'w_f' is the width of the FRP sheet, α is the angle of the fiber orientation relative to the direction of the shear load being resisted, in this case it is taken as zero. k_v a function of the concrete compressive strength, f'_c, the effective shear depth, d_{fv}, the ultimate design strain ε_{fu}, and the effective length, L_e. The effective shear depth of the retrofit strategy is taken as 80% of the total length of the FRP sheet in the direction of the applied loading, the ultimate design FRP strain is taken as the design value provided in the Simpson Strong-Tie technical datasheet (0.011 for C100HM), and the modulus of elasticity of the FRP, E_f, is taken as the Simpson Strong-Tie design value of 15,000 ksi.

The required thickness of FRP oriented in the horizontal (shear) direction to achieve this shear strength is 0.04 inches. This is achieved through two layers of uni-directional carbon fiber wrap, each 0.02 inches thick. See Section 3.2.4.3 for details on the FRP material. The specimen utilized 1/2 inch diameter anchors. The anchors were sandwiched between the two layers of fabric, and embedded 6 inches into the pilaster, with a tail splay of 12 inches long. The estimated peak laminate tensile strain Per ACI 440 is 0.23%, and the estimated contribution to shear strength is $\psi_f V_f = 50$ kips, calculated per Equation 3.5a. The increased shear capacity is anticipated to preclude initial inelastic behavior in shear. This should result in a flexurally controlled failure. Furthermore, to prevent a premature failure through anchor pullout, the total area of the FRP anchors was designed such that the total area on each vertical edge was at least 1.5 times greater than the total area of the flat fabric. The layout of this retrofit strategy can be seen in Figure 3.10. The FRP wrap,

epoxy, and anchors are donated by Simpson Strong Tie. The CSS V-Wrap C100HM series is used for the fabric.

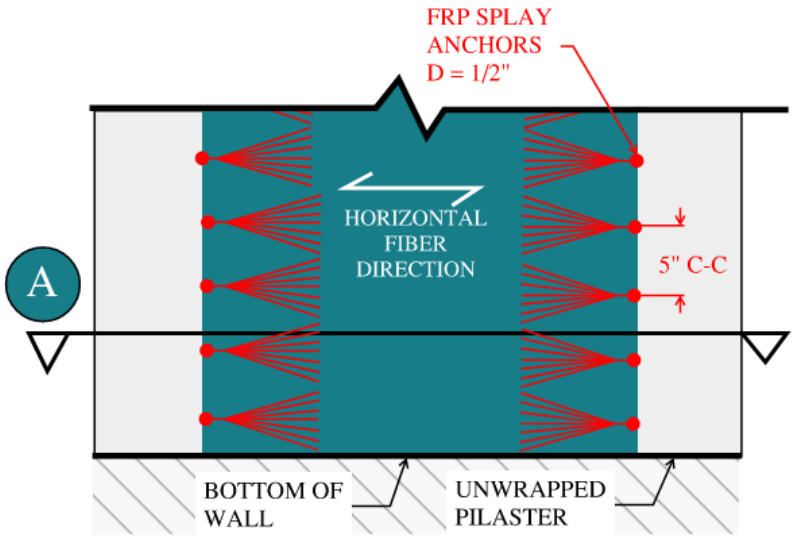

(a) Anchor Elevation Details

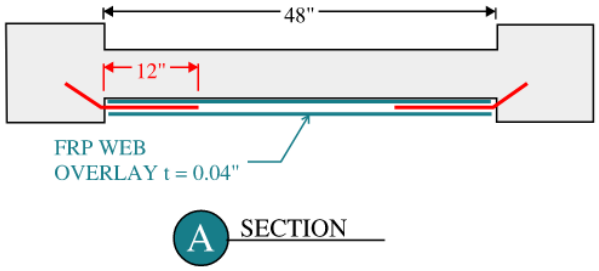

(b) Fabric and Anchor Plan View

Figure 3.10: S1FW FRP Retrofit Configuration

The surface preparation for the FRP installation was done using a diamond grinder in concrete surface. The surface was ground such that the top layer of concrete was removed and the internal pores were exposed. Furthermore, initial holes in the pilaster were needed before anchor installation could occur as seen in Figure 3.11. Finally, the corners of the concrete structure, where applicable, must be rounded to a 1/4 inch radius to ensure there is no localization of strains in the FRP around the corners. Once the structure is adequately prepared and thoroughly vacuumed, the FRP strips are cut to length.

Figure 3.11: FRP Surface Preparation Photo

The surface is prepared with a two-part liquid epoxy, the CSS V-Wrap 770 Epoxy Primer and Saturant, donated from Simpson Strong Tie. The epoxy, when initially mixed is liquid in consistency, and can be rolled onto the specimen, similar to paint, see Figure 3.12a. Then the fabric, CSS V-Wrap C100HM per Simpson Strong Tie, is saturated with this liquid then adhered to the wall, see Figure 3.12b. The epoxy is further mixed with fumed silica, thickening the solution into a paste, akin to a cake icing consistency. The fabric is smoothed onto the surface with paint spreaders, see Figure 3.12c, ensuring a complete bond

and removal of all of the air bubbles. The anchors are then added, ensuring a thick coating of the epoxy is fully saturated into the fibers. Finally, the top layer of fabric is added to ensure the anchors are fully bonded and locked in place. This top fabric is covered with a thicker epoxy, and left to cure and dry. The final specimen with the FRP installed is shown in Figure 3.13.

(a) Initial Epoxy Coat (b) FRP Fabric Wrap (c) Epoxy Paste on Anchors

Figure 3.12: S1FW - FRP Installation

Figure 3.13: Specimen S1FW: Finished FRP Installation

3.2.3.3 S1FP – Pilaster Wrap for Bar Buckling Prevention

The successful implementation of the shear web strengthening through specimen S1FW resulted in inelastic deformation in the pilaster toes due to bar buckling and concrete crushing. The retrofit strategy for specimen S1FP is an attempt to further enhance the inelastic deformability by delaying the occurrence of vertical bar buckling. Subsequently, the ACI 440-23 code equations for bar buckling prevention were utilized for this design, Equation 3.7a. The parameter 'D' is an equivalent circular diameter for the wrapped end pilasters. Other variables in the design equations are b and h are the dimensions of the width and length of the pilaster, taken as 12 inches, ρ_l is the reinforcement ratio of the longitudinal bars, d_{bl} is the diameter of the longitudinal bars, f_y is the yield stress of the steel, and f_{fe} effective design stress. The design values per the manufacturer were used for the ultimate strain, $\varepsilon_{fu} = 1.1\%$, and the modulus of elasticity, $E_f = 15{,}000$ ksi. The value of $\kappa_\varepsilon = 0.5$ comes from experimentally reported values in the literature. The final retrofit configuration has both the shear web strengthening, provided by the horizontally oriented sheets (identical to S1FW), and end pilaster confinement required per code to prevent flexural bar buckling. The confinement of the pilasters with the FRP wrap is not considered for increased concrete compressive strength. Therefore, the expected strength of this specimen is calculated similarly to S1FW, resulting in 50 kips of additional shear capacity in the specimen due to the FRP overlay. The behavior of the specimen should be flexurally dominant in terms of inelastic deformation.

Designing per the code equations allows an interesting investigation of the adequacy of these design equations. The required thickness of FRP fabric required to resist bar buckling was found to be 0.008 inches per the ACI-440 code equation. This was achieved with a single layer of ply, measuring 0.02 inches, which is the thinnest fabric available from Simpson Strong-Tie, named CSS V-Wrap C100HM. The retrofit strategy required the same anchorage scheme as

for S1FW. The details of this design can be seen in the elevation and plan views in Figure 3.14.

$$\rho_f = 2n_f t_f \left(\frac{b+h}{bh}\right) \frac{w_f}{s_f} \quad \text{(Eq. 3.7a)}$$

$$\rho_f \geq \frac{0.0052\rho_t D}{d_{bl}} \frac{f_y}{f_{fe}} \quad \text{(Eq. 3.7b)}$$

$$f_{fe} = \varepsilon_{fe} E_f \quad \text{(Eq. 3.7c)}$$

$$\varepsilon_{fe} = min(0.004, \kappa_\varepsilon \varepsilon_{fu}) = 0.004 \quad \text{(Eq. 3.7d)}$$

(Eq. 3.7e)

The surface preparation and FRP installation followed the same process as specimen S1FW, see Section 3.2.3.2.Figure 3.15 shows the retrofitted West face as well as the un-retrofitted east face of specimen S1FP, along with the FRP wrapped pilasters.

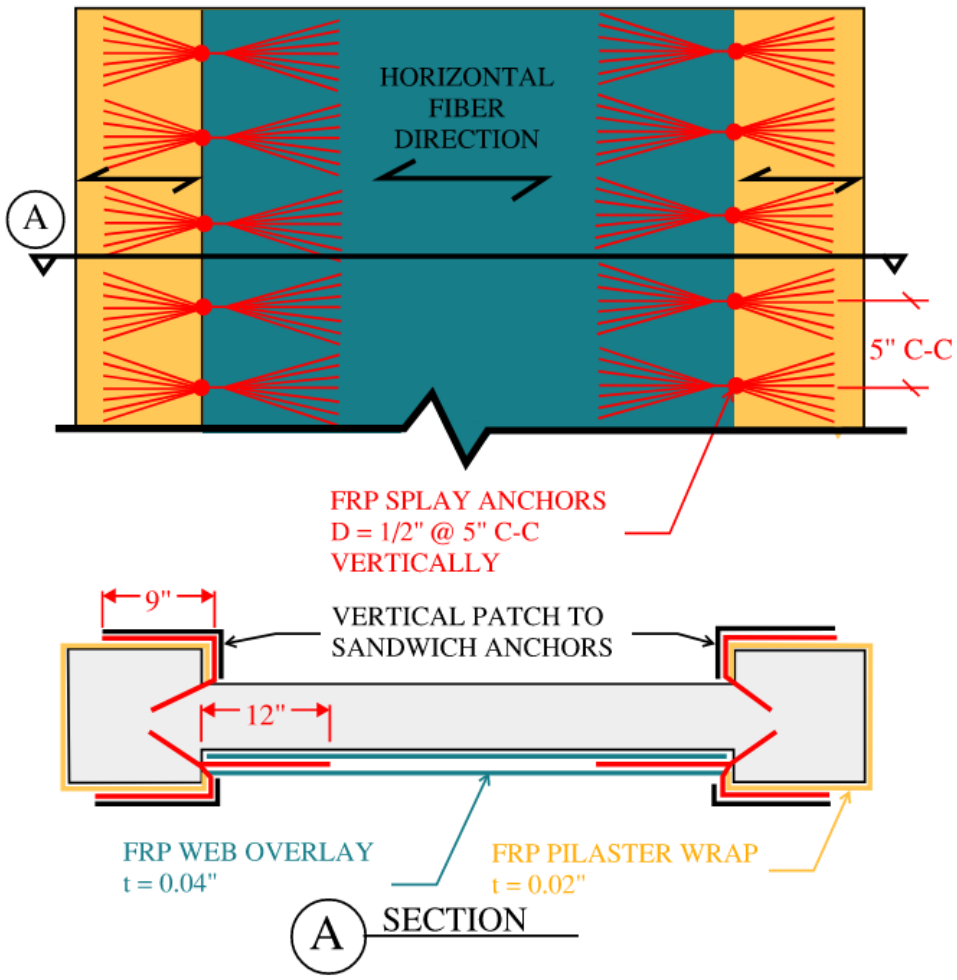

Figure 3.14: Elevation and Plan View of S1FP FRP Retrofit Details

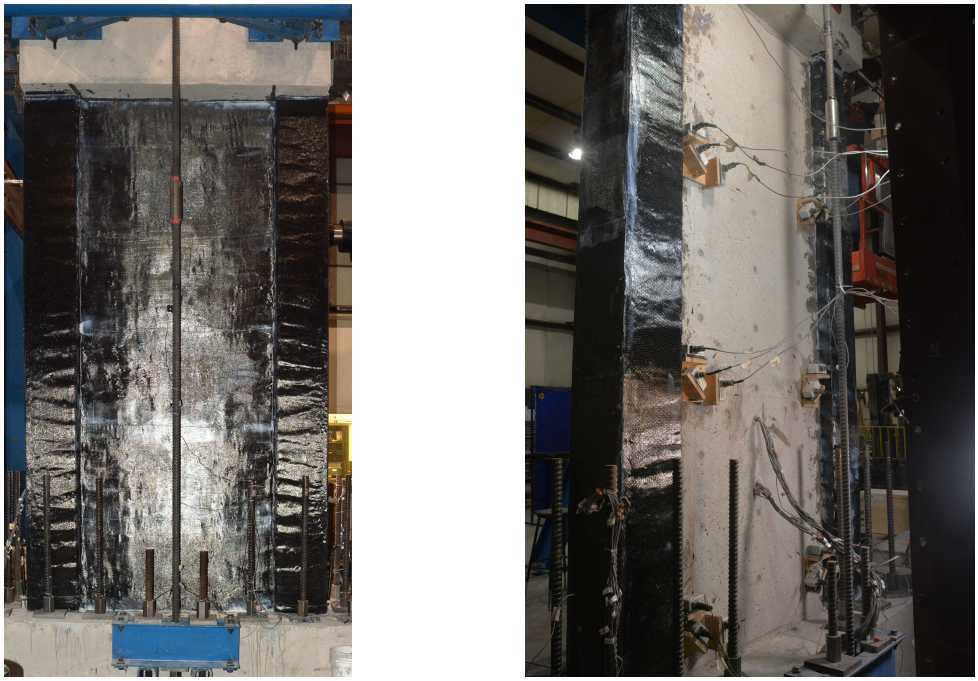

(a) S1FP West Face (b) S1FP East Face

Figure 3.15: S1FP - Pre Test Layout

3.2.3.4 S2FL – FRP Full Wrap

Specimen S2FL has the same lap splice as specimen S2, see Section 3.2.2.2 for details of this design. The specimen was retrofitted in such a way to preclude the expected lap splice slip present in the control specimen. The ACI 440-17 guidelines stipulate the minimum thickness of FRP required to effectively clamp the lap splice and subsequently induce a flexural failure. This equation is reproduced here for a rectangular section in Equation 3.8, using the manufacturer's *design value* for the fiber's modulus of elasticity. The required thickness of FRP to confine the lap splice is 0.20 inches. This is accomplished through two layers of Simpson Strong-Tie CSS V-Wrap C400HM wrap and one layer of CSS V-Wrap C220HM. This confining strategy extends vertically 30 inches from the base of the wall, which is two times the longest lap splice length of the #5 bars. The fabric is anchored with 1-1/8 inch diameter through-thickness anchors spaced at 5 inches center-to-center spacing, as can be seen in Figure 3.16. This structure is also strengthened against shear failure, identically to specimens S1FW and S1FP, through two layers of CSS V-Wrap C100HM and anchored with 1/2 inch diameter anchors at 5 inches center-to-center spacing. The layout, orientation, thickness of FRP sheets, and anchor size are noted in Figure 3.16.

$$Nt_f = 218\frac{D}{E_f} \qquad \text{(Eq. 3.8)}$$

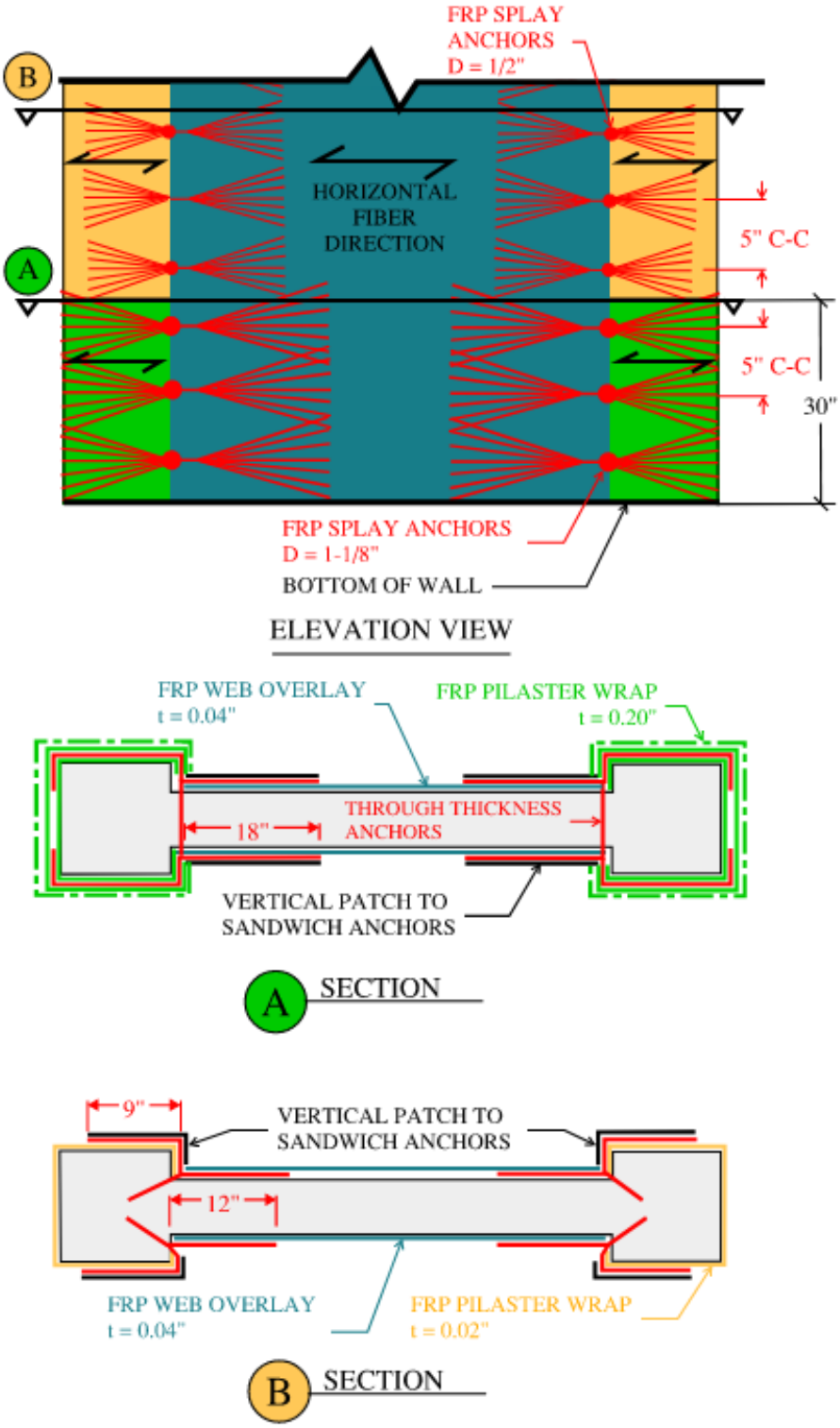

Figure 3.16: Elevation and Plan View of S2FL FRP Retrofit Details

3.2.4 As-Built Material Properties

3.2.4.1 Concrete

The specified concrete compressive strength of the specimens was targeted as follows: 6000 psi for the foundation and cap beam, and 4000 psi for the wall. The specimens were placed in three separate pours, one for the foundation, one for the main wall, and one for cap beam. Three concrete cylinders, measuring 6 inches in diameter and 12 inches in height, were tested on the day of each experiment, per the testing procedure described in the ASTM C39 standard. The average concrete compressive strength on the day of the experimental test is listed in Table 3.3. The exception is the concrete of specimen S2, which came from the same concrete truck as S2FL, and erroneously did not have its compressive strength tested on the day of the test; the noted concrete compressive strength in Table 3.3 is that of S2FL instead.

Table 3.3: Concrete Compressive Strengths

Specimen	$f'_{c,avg}$ (psi)	Age of Concrete (days)
S1	4,220	90
S1-CW	4,160	134
S1-FW	3,970	73
S1-FP	3,750	113
S2	5,505	77
S2-FL	5,505	77

3.2.4.2 Reinforcing Steel

Two types of reinforcing steel were used for this specimen, grade 60 and grade 80. This program used grade 80 bars in the web, as well as for the hoops in the pilasters; namely, grade 80 reinforcement was used for all locations with D5 bars. See Section 3.2.2.1 for more

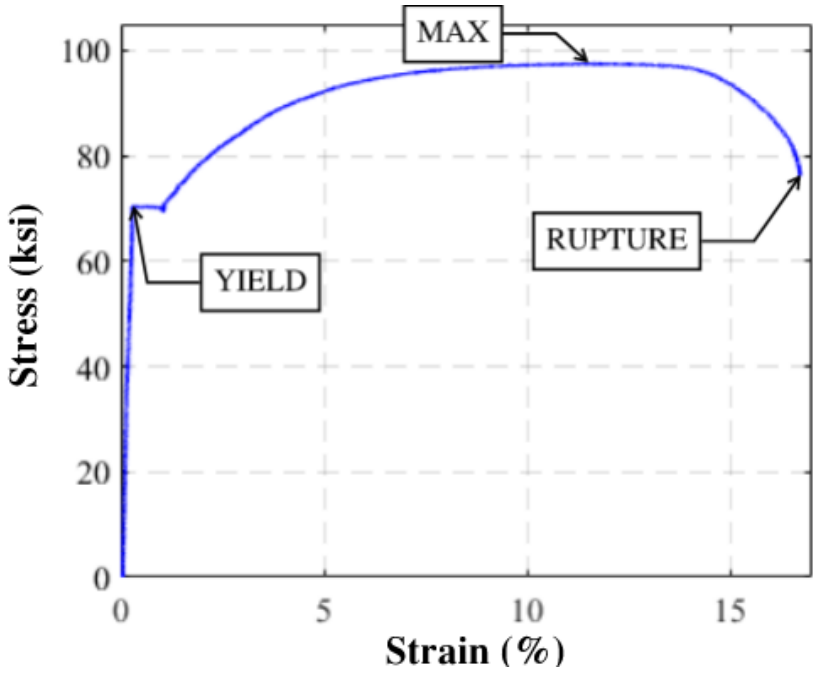

Figure 3.17: Experimentally Obtained Stress-Strain Plot of #5 Rebar

details. The D5 bars have a diameter equivalent to a number 2 bars. Grade 60 steel was used for all other steel.

At least three bars of each size were tested with the Satec Tensile Testing Machine, per ASTM E8/E8M − 13a using an 8-inch gauge length. This produced an overall stress-strain response of the material. A sample graph from one tensile test of a #5 bar is shown in Figure 3.17. The yield strength was determined through the 0.2% offset method.

The tested material properties for the three types of rebar, #4 GR 60, #5 GR 60 and D5 GR 80 are shown in Table 3.4, Table 3.5, and Table 3.6 respectively.

Table 3.4: Mechanical Properties of #4 Bars

Test #	Yield		Maximum		Rupture		Modulus of Elasticity
	ε_y	σ_y (ksi)	$\varepsilon_{\max}$	$\sigma_{\max}$ (ksi)	$\varepsilon_{\text{rupture}}$	σ_{rupture} (ksi)	E (ksi)
1	0.0026	71.8	0.126	98.8	0.169	76.7	27519
2	0.0024	69.6	0.119	98.4	0.178	79.6	29226
3	0.0026	72.0	0.113	98.4	0.172	79.6	28112
4	0.0021	71.6	0.113	98.8	0.162	84.3	33389
Average	**0.0024**	**71.2**	**0.122**	**98.7**	**0.171**	**80.0**	**29561**

Table 3.5: Mechanical Properties of #5 Bars

Test #	Yield		Maximum		Rupture		Modulus of Elasticity
	ε_y	σ_y (ksi)	$\varepsilon_{\max}$	$\sigma_{\max}$ (ksi)	$\varepsilon_{\text{rupture}}$	σ_{rupture} (ksi)	E (ksi)
1	0.0028	70.3	0.115	97.5	0.167	76.5	25227
2	0.0025	70.5	0.102	98.1	0.161	80.3	28595
3	0.0024	69.7	0.109	97.5	0.160	80.3	28815
Average	**0.0026**	**70.2**	**0.109**	**97.7**	**0.163**	**79.0**	**27546**

Table 3.6: Mechanical Properties of D5 Bars

Test #	Yield		Maximum		Rupture		Modulus of Elasticity
	ε_y	σ_y (ksi)	$\varepsilon_{\max}$	$\sigma_{\max}$ (ksi)	$\varepsilon_{\text{rupture}}$	σ_{rupture} (ksi)	E (ksi)
1	0.0050	78.0	0.005	77.9	0.005	68.3	15729
2	0.0045	82.6	0.024	83.9	0.025	65.0	18295
3	0.0043	76.9	0.003	75.8	0.003	60.6	17848
4	0.0036	78.2	0.004	78.4	0.003	59.4	21671
5	0.0039	77.0	0.003	76.2	0.003	59.9	19521
6	0.0051	81.3	0.014	83.3	0.013	54.3	16006
Average	**0.0044**	**79.0**	**0.008**	**78.8**	**0.008**	**61.1**	**17945**

3.2.4.3 FRP

There are three components of the FRP system selected for this project. That is, (1) the fabric, also referred to as 'sheets', (2) the carbon fiber polymer anchors, and (3) the epoxy. These components are shown in Figure 3.18. The epoxy saturates the sheets and the fibers prior to placement, and the product is applied to the specimens as a wet-layup. The finished product is left to cure for at least seven days prior to testing.

There are three types of fabric woven sheet used throughout the project, refer to Sections 3.2.3.2, 3.2.3.3 and 3.2.3.4 for more details on where each type of fiber was used. The *cured design value* for each fabric type, per the manufactures technical specifications, are listed in Table 3.7 and utilized for all strength calculations and determinations of required FRP fabric thickness. All fabrics are unidirectional carbon fiber. The installation of the FRP was done by Structural Technology Solutions, Inc. a partner in the field with Simpson Strong-Tie.

Table 3.7: Mechanical Properties of Different CFRP Materials

Name	Thickness (in)	Strain at fracture ($\varepsilon\_\{fu\}$)	Elastic Modulus (ksi)
CSS V-Wrap C100HM	0.02	1.1%	15,000
CSS V-Wrap C200HM	0.04	0.9%	14,000
CSS V-Wrap C400HM	0.08	1.1%	14,000

The epoxy is Simpson Strong-Tie's CSS V-Wrap 770 2-part Epoxy Primer and Saturant. Initially, this epoxy when mixed is liquid and is applied to the prepared concrete surface. The concrete surface prep is noted in Section 3.2.3.2. The FRP fabric and anchors are subsequently saturated in the epoxy and applied to the concrete surface or into pre-drilled holes, respectively. The epoxy may then be thickened with silica fume and subsequently utilized as a paste to ensure full adherence of the fabric and anchors to the concrete substrate.

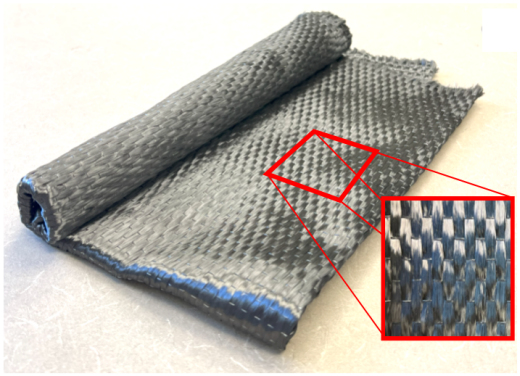

(a) Fiber Reinforced Polymer Sheets, CSS V-Wrap C100HM

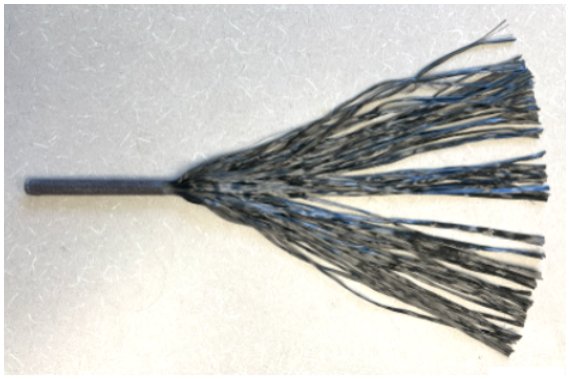

(b) Fiber Reinforced Polymer Anchor, 1/2-inch Diameter

(c) Two part CSS V-Wrap 770 (Figure Retrieved From www.strongtie.com)

Figure 3.18: FRP Component Photographic Details

3.2.4.4 Shotcrete

The design components of the shotcrete are given in Table 3.8. The shotcrete had a compressive targeted strength of 4500 psi with a 0.4 water to cement ratio. The shotcrete was unable to be experimentally tested for actual material properties. Estimated values are used for numerical modeling.

Table 3.8: Shotcrete Specification

Component	lb/yd^3
Coarse Aggregate	1,011
Coarse Sand	627
Fine Sand	1,146
Cement	548
Fly Ash	169
Water	287
Water Reducer	26 $fl.oz./yd^3$

3.3 Experimental Setup

This section describes the physical accessories required to facilitate the experimental test, from the loading actuators to the measurement devices. The experimental lateral loading setup consists of two moment frames, one for in-plane loading, and one for out-of-plane loading. The in-plane moment frame resists the lateral loading action from an MTS Actuator, which is driving the overall displacement of interest for the structure. The in-plane frame is attached to the specimen through four threaded rods that are post-tensioned to the specimen. The control node of the experimental program is shown in Figure 3.19, along with the in-plane frame. The axial loading setup can also be seen in this figure. Two independent loads are applied through two separate hydraulic pumps. The force exerted by the pumps is measured by an external load cell and a pressure transducer.

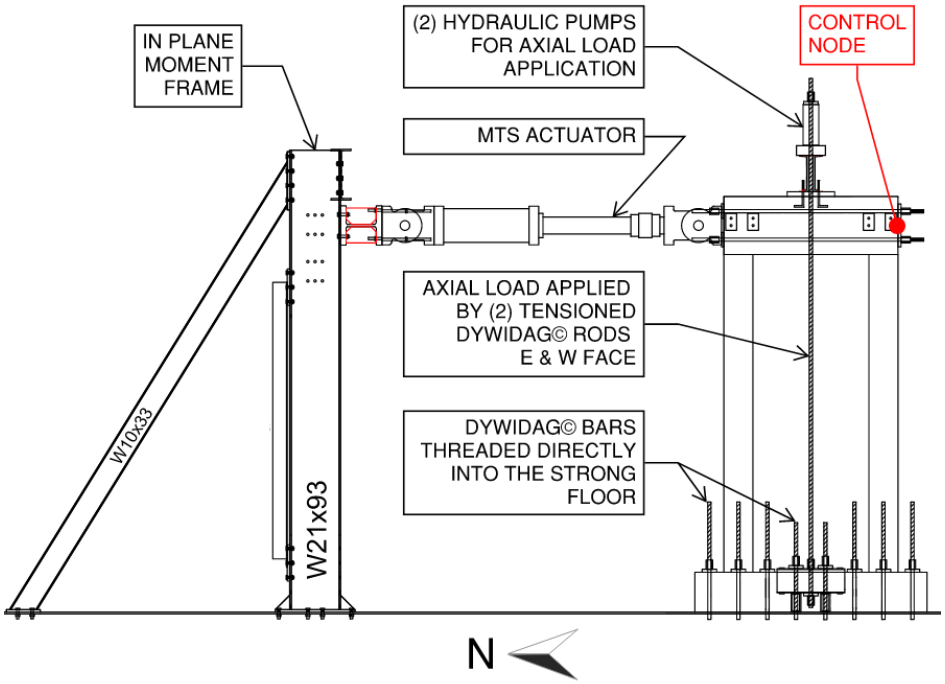

Figure 3.19: Experimental In-Plane Frame and Loading Setup

The out-of-plane frame resists any out-of-plane wall movement brought about by geometric and loading eccentricities. The loading setup for the out-of-plane frame can be seen in Figure 3.20. The out-of plane reaction frame is connected to the specimen through eight grade 160 #5 Dywidag bars and a triangular configuration of HSS sections, as can be seen in Figure 3.21. This configuration allows for rotation at the top of the specimen, ensuring a roller-type connection. The specimen is able to move freely parallel to the MTS machine by virtue of a circular HSS tube which sits inside of a larger circular HSS section connected to the out-of-plane frame.

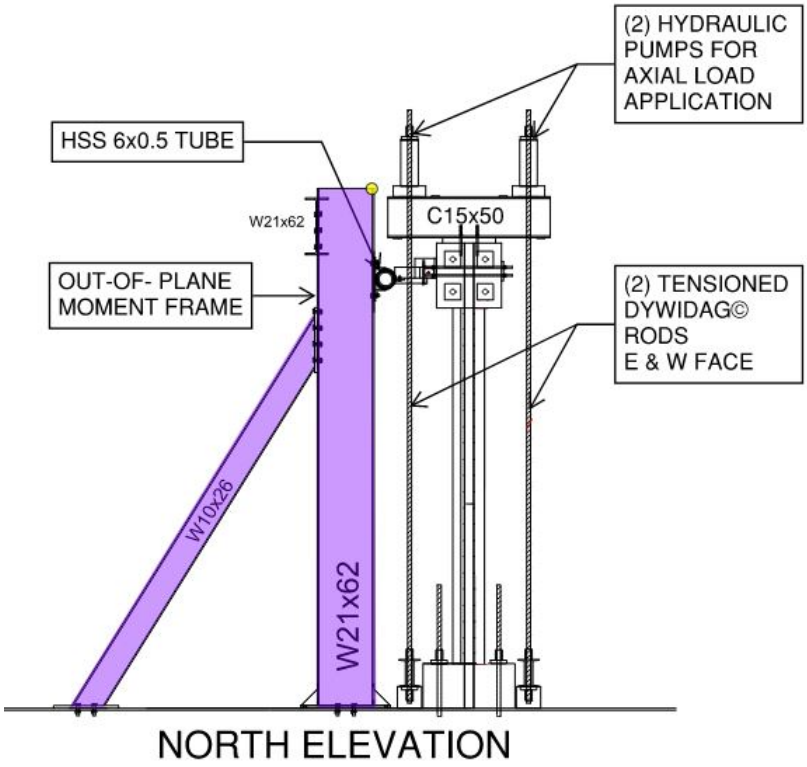

Figure 3.20: Out of Plane Reaction and Axial Loading Setup

The specimens with no lap splice (S1 specimens) are subjected to an axial load of 200 kips, corresponding to an axial load ratio of 10%. Axial load ratios (ALRs) are calculated per Equation 3.9, where P is the axial load, A_c is the gross cross sectional area, and f'_c is the peak concrete compressive strength. The specimens with a lap splice (S2 specimens) are

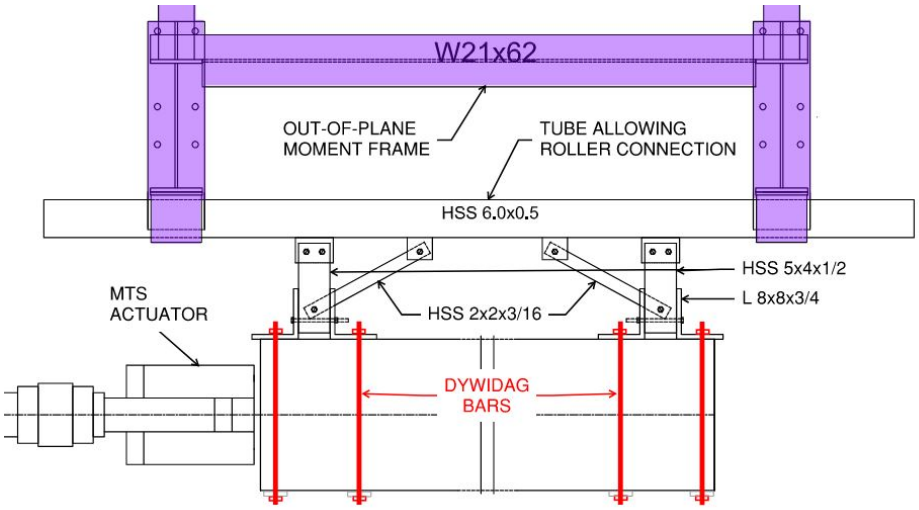

Figure 3.21: Plan View of the Out of Plane Frame Connection

subjected to an axial load of 100 kips, corresponding to an axial load ratio of 5%. The lower ALR is to ensure that the desired failure mode of a lap-splice slip is met, while still being within reasonable ranges of actual axial load magnitudes. The load is applied to the top of the specimen through a spreader beam consisting of two C-channels, which distributes the load from two external Dywidag rods. The Dywidag rods are tensioned to the appropriate load with two hydraulic jacks. See the setup shown in Figure 3.20 for the axial loading setup.

$$ALR = \frac{P}{A_c f'_c} \qquad \text{(Eq. 3.9)}$$

3.3.1 Loading Protocol

The specimens are loaded in both a 'push' and a 'pull' direction, one complete cycle consisting of both directions. Each cycle is repeated twice. The displacement of each specimen is measured at the centroid of the cap beam. Specimens with no lap splice (S1 specimens) are loaded in a slightly different protocol from the specimens with a lap splice (S2 Specimens). The loading protocol was changed for the S2 specimens, which had an anticipated peak drift ratio of 0.8% drift, to ensure the force-controlled cycles did not exceed the anticipated peak displacement. The protocol can be seen in Table 3.9, and Figure 3.22. The end point for each experimental test is noted on Figure 3.22. This point was after the specimen had reached its peak strength and significant degradation was seen. For further discussion of the experimental results, see Chapter 4.

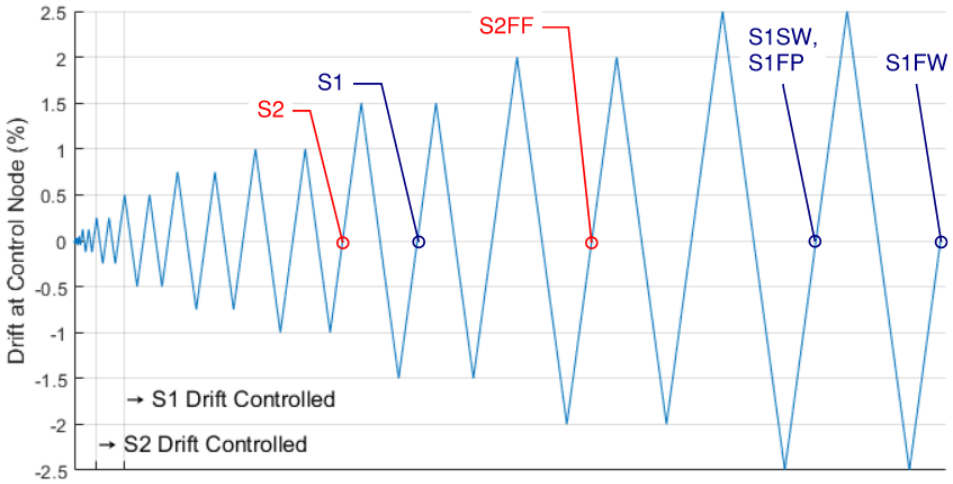

Figure 3.22: Loading Protocol with Test Ends Labeled

3.3.2 Instrumentation

All instrumentation used in the experimental setup was calibrated and connected to a National Instruments© Data Acquisition System.

Table 3.9: Loading Protocol

S1		S2	
Displacement/ Force Controlled	Drift (%)/ Load(kip)	Displacement/ Force Controlled	Drift (%)/ Load(kip)
F	25	F	20
F	50	F	40
F	75	F	60
F	100	D	0.25%
D	0.50%	D	0.50%
D	0.75%	D	0.75%
D	1.00%	D	1.00%
D	1.50%	D	1.50%
D	2.00%	D	2.00%
D	2.50%	D	2.50%

The strain gauges used in this project were from Tokyo Measuring Instruments Laboratory Co., Ltd, their YEF series for post-yield strain gauges. The strain gauges had a resistance of 120 ohms and a gauge factor of 2.11. Steel reinforcement surfaces were prepared, and the strain gauges were installed, in accordance with the Instruction Bulletin B-127 from Micro Measurements. An intermediate step in the strain gauge installation process is shown in Figure 3.23 showcasing the bond between the gauge and the reinforcement. The strain gauge is subsequently protected with several layers of tape, cushion, and epoxy, per the installation procedure. The D5 bars were installed with 2 mm gauge length strain gauges, YEFLAB-2-ILJCTF. All other bars, as well as the FRP (when applicable) were measured with uni-axial strain gauges with a gauge length of 5 mm. Each specimen was outfitted with 80 strain gauges. The locations and label of each strain gauge can be found in Appendix A, but a general overview for useful context is shown in Figure 3.24. There were two strain gauges applied to the SG1 locations, and one strain gauge applied to all other locations.

The fiber reinforced polymer (FRP) overlay was also instrumented with strain gauges when applicable, always in the fiber orientation direction, which means all strain gauges on the

Figure 3.23: Strain Gauge on Reinforcement

FRP were orientated horizontally. Each specimen had a slightly different configuration of strain gauges which can be seen in Figure 3.25

The string potentiometers, also called 'string pots', used in this experimental test are from Measurement Specialties©. They are linear position potentiometers which utilize a voltage feedback signal linearly proportional to the position of a traveling stainless steel measuring cable. The string pots in this experiment had a stroke length of 10 inches. Refer to Figure 3.26a for a photo of one of the string pots. There were 16 string pots arranged in a 40-inch square grid pattern on the wall to measure the vertical, horizontal, and diagonal displacements. Refer to Figure 3.26b for the overall layout and labels. String pot 17 acted as the overall displacement measurement for the control node. It was anchored to the centroid of the cap beam cross section.

In addition to string pots and strain gauges, linear variable differential transformer (LVDT) displacement transducers are used. They use a spring loaded armature to measure displacement through the resistance of the electrical signal. The LVDTs used in this experiment

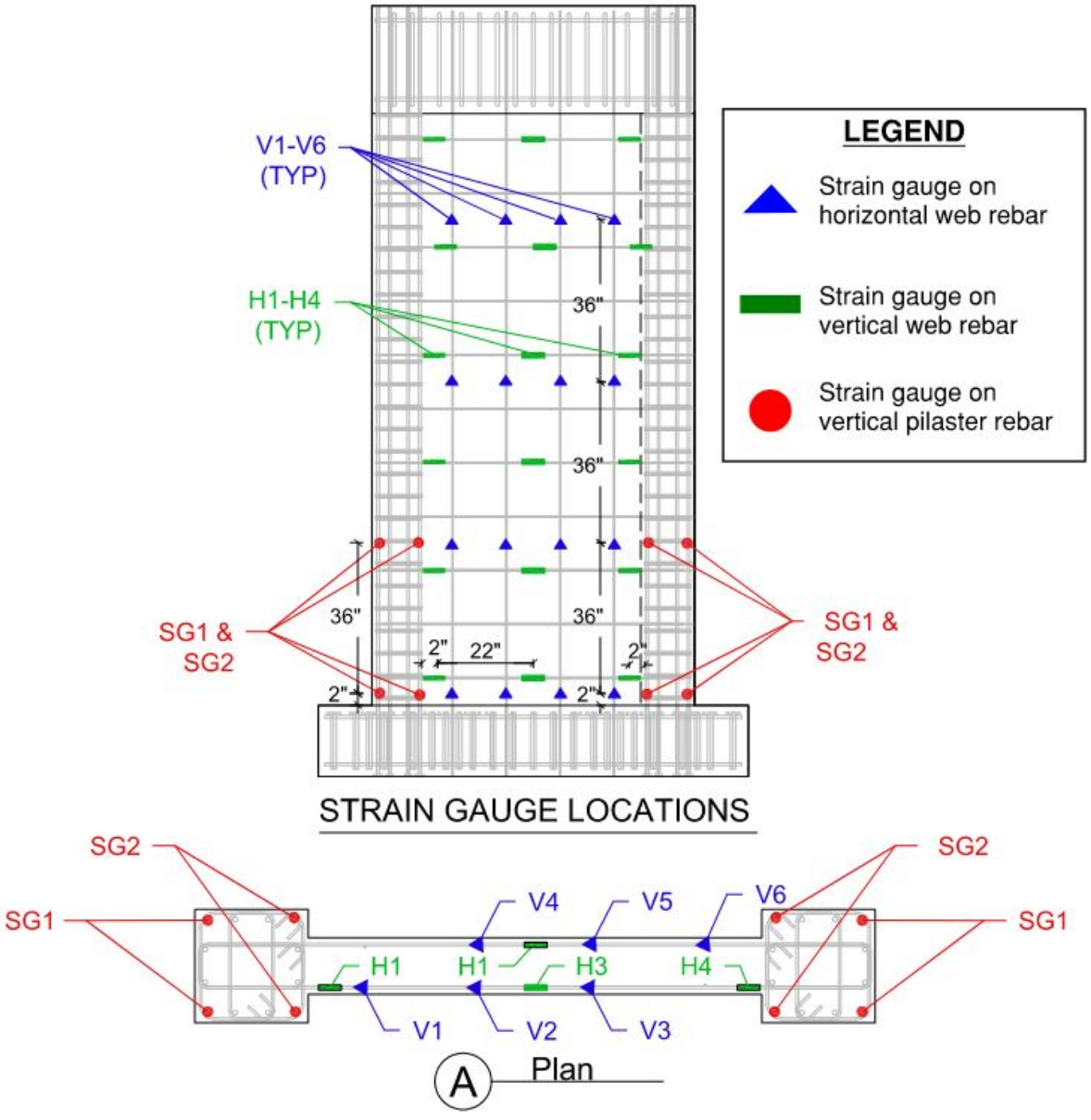

Figure 3.24: Strain Gauge Locations

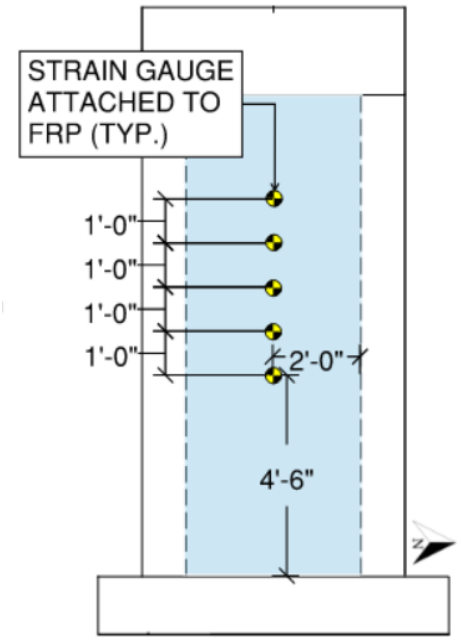

(a) Specimen S1FW

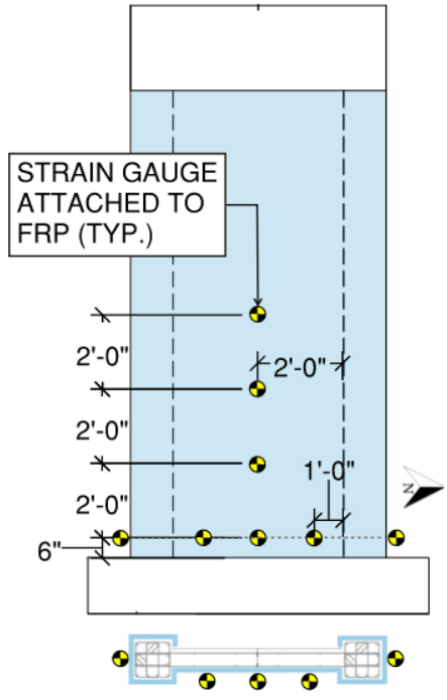

(b) Specimen S1FP

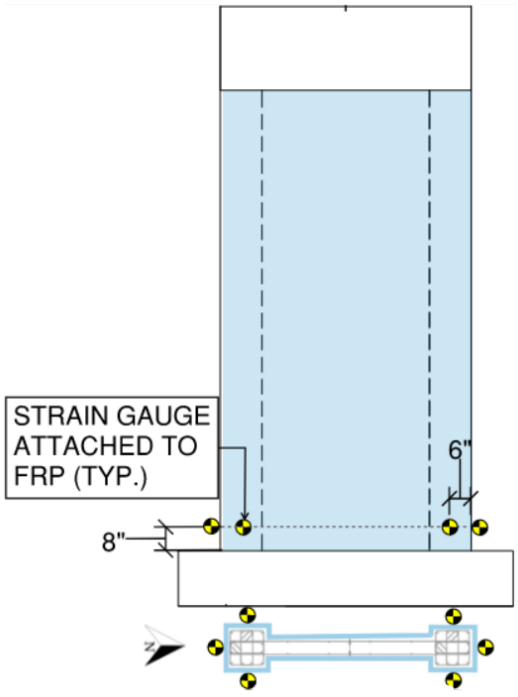

(c) Specimen S2FL

Figure 3.25: FRP Strain Gauge Locations

(a) String Pot Diagram per Measurement Specialties Technical Specification Sheet for PT 101

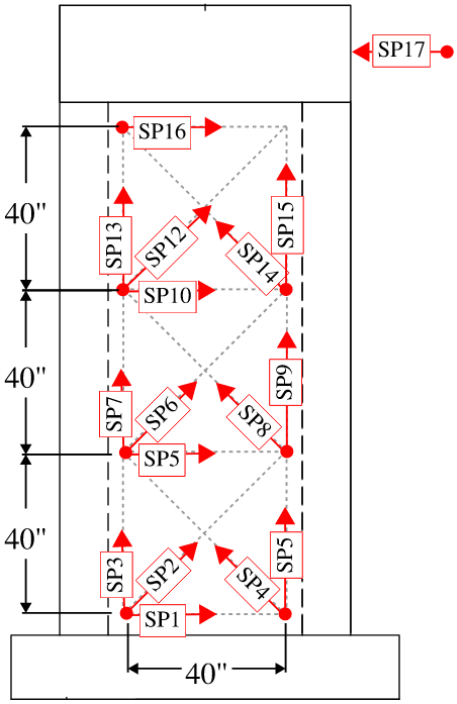

(b) String Pot Layout

Figure 3.26: String Pot Details

have a stroke length of anywhere from 1 inch to 4 inches. The LVDTs were arranged on the specimen to isolate the plastic hinge deformation. A photograph of the north face of the specimen with the LVDTs installed can be seen in Figure 3.27a. They were meant to capture a discreet and specific displacement pattern, from the base of the wall to 14 inches up, as can be seen in Figure 3.27b. The numbering scheme and subsequent labels for the LVDTs can also be seen in this figure. Three LVDTs were also utilized during the experiment in order to monitor the uplift of the specimen, as well as the out-of-plane displacement.

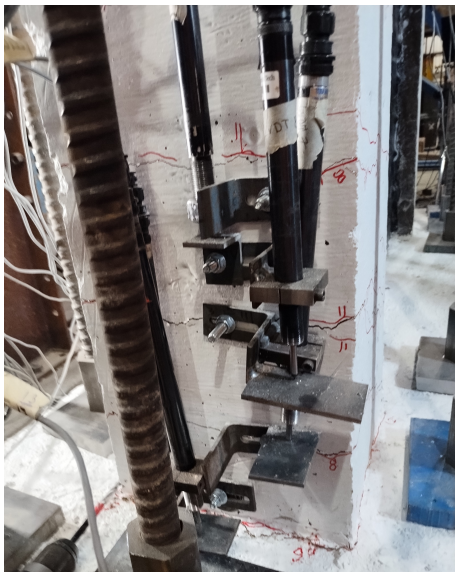

(a) Photo of South End Installed Instrumentation

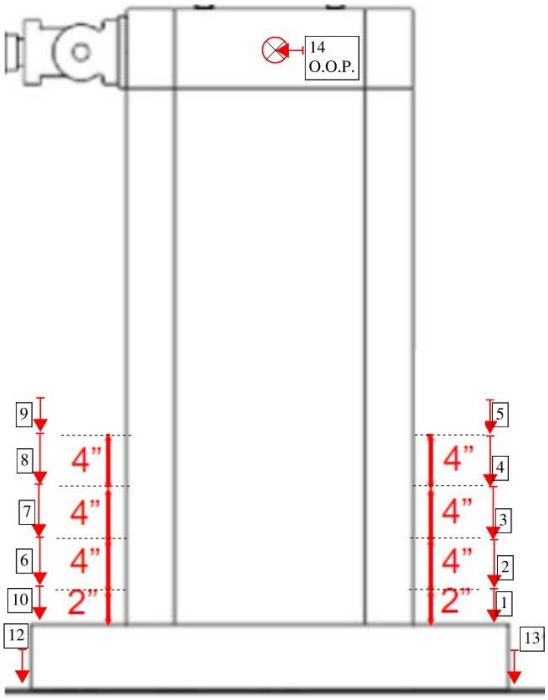

(b) Location on Specimen - Not To Scale

Figure 3.27: LVDT Configuration

Chapter 4

Experimental Results and Discussion

4.1 General

This chapter examines the experimental behaviors of six test specimens described in Chapter 3. The specimen results are divided into two groups: group one (walls without a lap splice) and group two (walls with a lap splice). For each group, the chapter provides a detailed description of the experiments, including force-displacement responses, instrumentation results and analysis, test images, damage accumulation, and final failure patterns.

4.2 Results for Test Group One

Group one constitutes all of the specimens in the experimental program that did not have a lap splice condition. The group includes specimens S1, S1CW, S1FW, and S1FP.

4.2.1 Specimen S1 - Control

Specimen S1 is the unretrofitted control sample for the non-lap splice samples. This specimen exhibited a brittle damage pattern due to a large localized crack in the web and rapid, severe strength loss coincident with toe crushing. Visuals of the specimen before and after testing are shown in Figure 4.1.

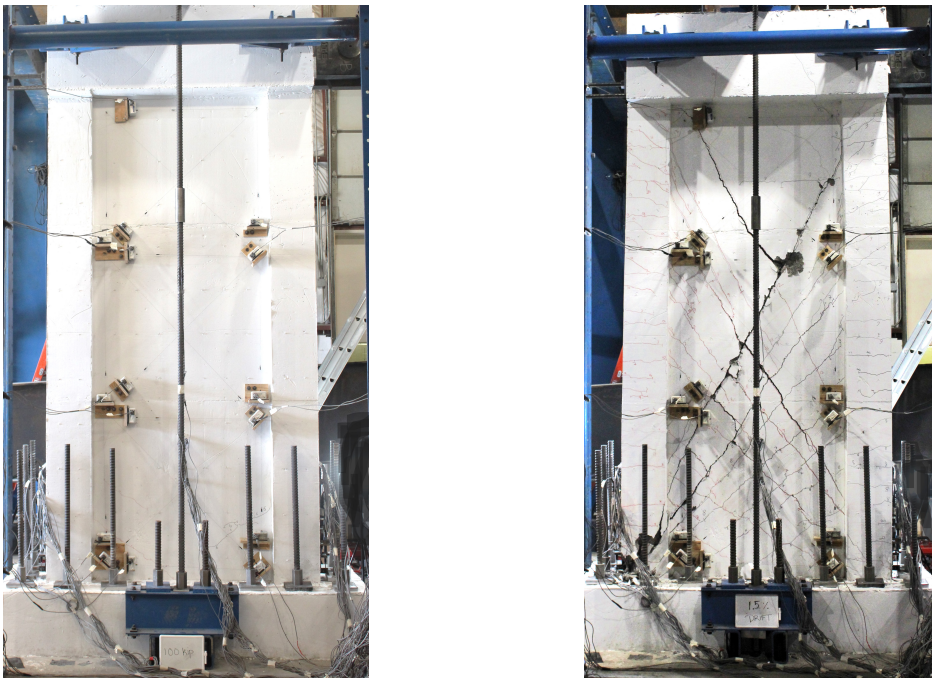

(a) Pre-Test (b) Post-Test

Figure 4.1: Specimen S1 State Conditions

The hysteretic force-drift response is seen in Figure 4.2. The specimen exhibited a slight loss of stiffness in the initial cycles, consistent with the general strength degradation behavior of reinforced concrete specimens. The specimen reached a peak strength of 154 kips during the first stage of loading at 1.0% drift in the positive direction and -148 kips in the negative direction of the same cycle. Yielding of the vertical rebar in the pilasters occurred during the 0.5% drift cycle, see Figure 4.3. At 1.3% drift, the specimen exhibited a sudden drop in strength from 146 kips to 61 kips due to an explosive and brittle toe concrete crushing failure in the pilaster. The test was ended after the first full cycle at 1.5% drift. Table 4.1 shows the peak strains exhibited each cycle by the vertical pilaster steel and the horizontal web steel. It was seen that the demand in the shear steel in the web continued to increase in the latest drift cycles, while the longitudinal steel in the pilasters plateaued, indicating a higher demand in the web of the specimen. This resulted in brittle failure through diagonal

tension web damage and ultimate rupture of the rebar in the web.

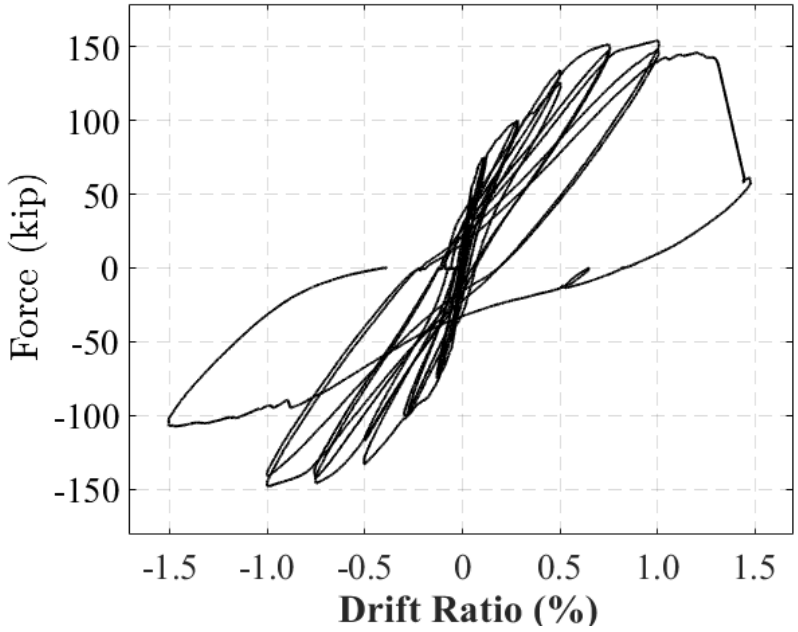

Figure 4.2: Hysteretic Force vs. Drift Response for Specimen S1

Table 4.1: Reinforcement Strains for Specimen 1

Load/Drift	Peak Vert. Pilaster Strain	Peak Horz. Web Strain
100 k	0.002	0.004
0.50%	0.004	0.013
0.75%	0.013	0.018
1.00%	0.014	0.022
1.50%	0.007	N.A.*

*Unreliable strain gauge data

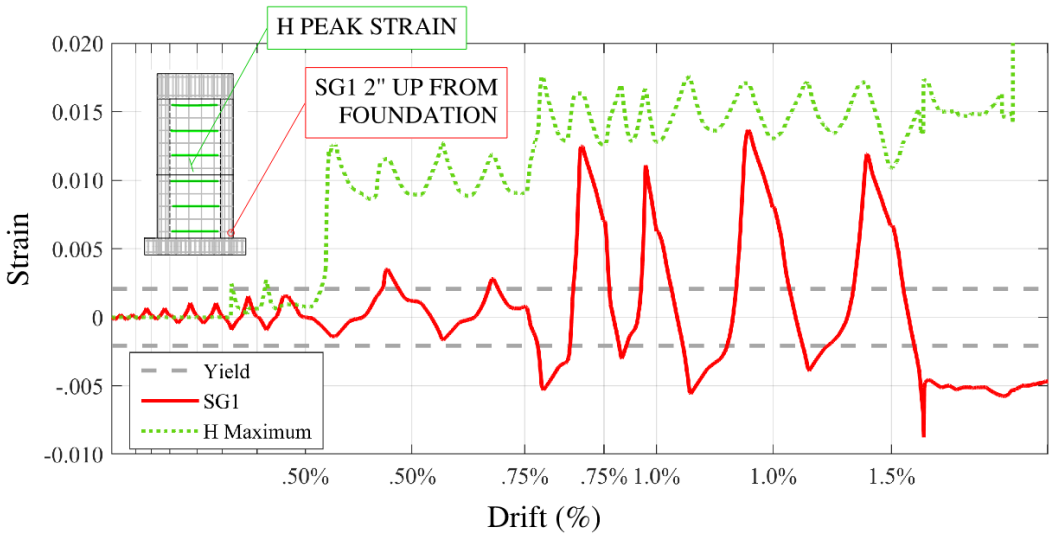

Figure 4.3: Vertical Pilaster Strain Gauge Data for Specimen S1

Figure 4.4 showcases the cracking pattern throughout the duration of the test for specimen S1, the unretrofitted specimen for group one with no lap splice. Initial cracking was observed during the 75 kip force-controlled cycle. These initial cracks manifested in the web of the specimen, near the base, with a slight inclination from the horizontal. During the 100 kip force-controlled cycle, crack propagation persisted, moving up the wall, with an increasingly vertical inclination in the web and the development of horizontal cracks in the pilaster. At 0.5% drift, the diagonal crack in the web had entirely extended over the structure's height, effectively spanning across the diagonal strut of the web. In the 1.0% cycle, the crack further localized, with its width expanding over one-half inch, as noted in Table 4.2, and was accompanied by several rebar fractures. During the 1.5% drift cycle, the specimen experienced several additional rebar fractures within the web, concurrent with a maximum crack opening of 1.8 inches, along with spalled concrete. Ultimately, the specimen demonstrated a shear-crushing failure at the toe of the pilaster, as illustrated in Figure 4.8. The progression of the crack is graphically depicted in Figure 4.4. A table indicating the largest measured crack openings (using the diagonal string pot measurements described in Section 3.3.2) is

presented in Table 4.2. Additional close-up photographs post-loading are provided in Figures 4.5 through 4.8.

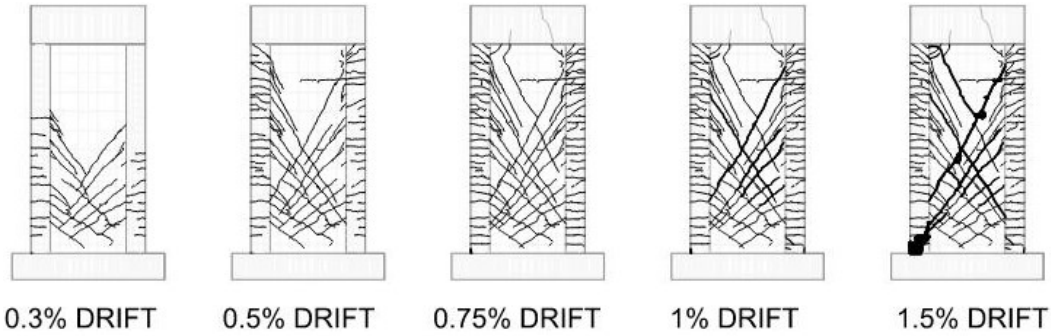

Figure 4.4: Crack Propagation for Specimen 1

Table 4.2: Maximum Measured Diagonal Crack Width for Specimen S1

Drift (%)	Max Crack Width Opening (in)
0.50%	0.20
0.75%	0.34
1.00%	0.53
1.50%	1.80

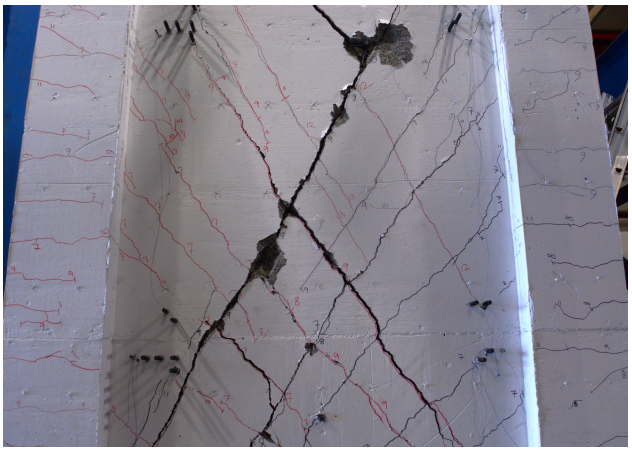

Figure 4.5: S1 Final Upper Wall Close Up

Figure 4.6: S1 Final Lower Wall Close Up

Figure 4.7: S1 Back Wall Final Close Up

Figure 4.8: S1 Crushed Toe Close Up

4.2.2 Specimen S1CW

The results of the reinforced concrete overlay retrofit strategy are discussed below. For details of the design of this specimen, see Section 3.2.3.1. A view of the specimen pre-test and post-test is shown in Figure 4.9.

(a) S1CW Pre-Test (b) S1CW Post-Test

Figure 4.9: S1CW Specimen Initial (Pre-Loading) and Final (Post-Loading) Conditions

The hysteretic force-drift curve is seen in Figure 4.10. The specimen exhibited a much different damage propagation than the control specimen, S1. This specimen had negligible strength loss until the 2.5% drift cycle and showed good ductility through large hysteretic loops. The phenomenon known as 'pinching' is a common observation in hysteretic force-deformation response curves, evidenced in the 'pinching' of the curve towards the origin. This is the opposite of large, wide, round loops in a response. The presence of 'pinching' indicates a reduction in energy dissipation. Pinching was minimally observed in this retrofitted

specimen, thus it was a good indicator of effective energy dissipation. The specimen reached a peak strength of 165 kips during the first stage of loading at 1.5% drift in the positive direction and -160 kips in the negative direction of the same cycle. The specimen's residual strength at subsequent drift ratios was calculated per Equation 4.1, which took the maximum load reached during the first cycle of the subsequent drift ratio and divided it by the overall maximum load from the test. These residual strengths are noted in Table 4.3. The specimen retained most of its post-peak strength until the 2.5% drift ratio, at which point it had lost 26% or 36% of its strength, depending on which direction was considered.

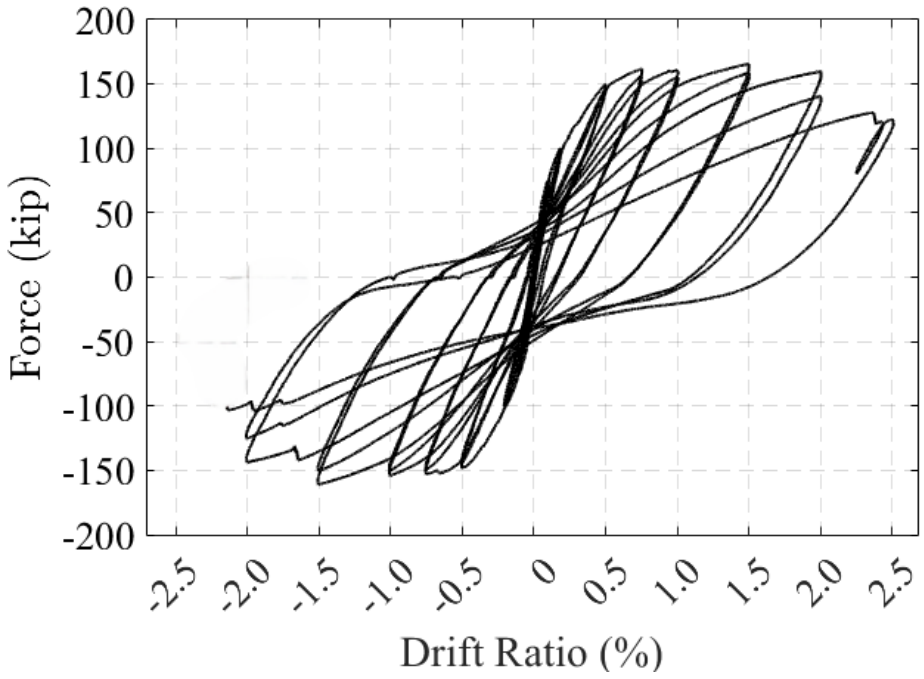

Figure 4.10: S1CW Force-Drift Curve

$$\text{Residual Strength}_i = (P_{max})_{\text{Drift Ratio},i}/(P_{max})_{\text{Test}} \qquad \text{(Eq. 4.1)}$$

Minor cracking was seen on the face of the shotcrete overlay during the initial loading stages. This was attributed to shrinkage cracking and the very low cover due to the 1/2

Table 4.3: S1CW Strength at Critical Drift Ratios

Peak Load @ 1.5% Drift	Residual Strength @ 2% Drift	Residual Strength @ 2.5% Drift
165 kip	96%	77%
-160 kip	89%	64%

scale specimen. Initial cracking due to lateral loading occurred during the 0.5% drift cycle diagonally in the web of the specimen, nearly spanning the entire diagonal strut of the section. Horizontal cracking in the pilaster was also observed at this stage, along with cracking at the vertical joint between the shotcrete overlay and the pilasters. At 0.75% drift, a large crack at the interface of the base of the wall and the foundation began to localize. The cover at the toes of the pilasters began to spall off. At 1.0% drift, the cover at the toes was significantly spalling off, and the crack propagation on the wall became more diffuse across the web without localization, which can clearly be seen in Figure 4.11. At the 1.5% drift cycle, the interface between the wall and the foundation became highly localized, opening to approximately 0.25 inches. At 2% drift, the first rebar fracture occurred in the pilaster. The interface between the pilasters and the shotcrete overlay grew to 0.012 inches. The specimen exhibited further rebar fracture during the final stage of loading in the 2.5% drift cycle, along with heavy damage in the pilaster toes. The crack propagation and toe damage is shown graphically in Figure 4.11, and the measured crack widths from the diagonal string pots are shown in Table 4.4. The crack widths never exceeded 0.30 inches. This was much different from the control specimen, which exhibited the majority of inelastic deformation in the web at the 1% and 1.5% drift ratios and crack widths over 1 inch. The reinforced concrete retrofit overlay was effective in preventing this kind of inelastic deformation and resulted in a ductile, gradual loss of strength through rebar strain and fracture. Damage after the loading was completed was shown in Figures 4.12 through 4.15.

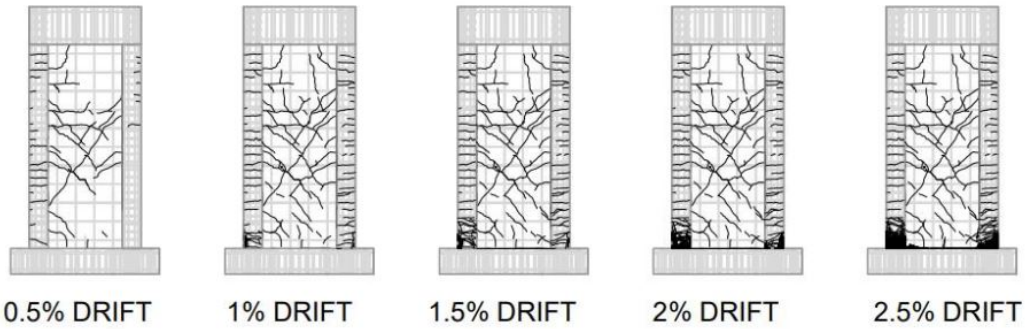

Figure 4.11: Crack Propagation of Specimen S1CW

Table 4.4: Maximum Measured Crack Width for Specimen S1CW

Drift (%)	Max Diagonal Crack Width Opening (in)
0.50%	0.10
0.75%	0.13
1.00%	0.17
1.50%	0.26
2.00%	0.30
2.50%	0.22

Table 4.5 shows the peak strains exhibited each cycle by the vertical pilaster steel and the horizontal web steel. Initial yielding of the vertical rebar in the pilasters occurred during the 75 kip force-controlled cycle. It can be seen that the strain in the longitudinal steel in the pilasters was much greater than the shear steel, indicating a higher demand in the pilasters. This was clearly seen by the high strains in the rebar, up to 4.5% at the 2% drift ratio, and followed by fracture of the vertical pilaster rebar. This was a much more ductile failure mode than the control specimen, which exhibited a brittle concrete crushing failure. The gradual increased strain in the rebar, as well as the fracture, provided for a larger retention of strength at higher drifts than the unretrofitted specimen. Ultimately, this specimen failed through a ductile mechanism governed by end region vertical rebar yielding and fracturing.

Table 4.5: S1CW Peak Reinforcement Strains Per Cycle

Drift	Peak Vert. Pilaster Strain	Peak Horz. Web Strain
0.50%	0.013	0.002
0.75%	0.021	0.003
1.00%	0.039	0.003
1.50%	0.048	0.004
2.00%	[3]*	0.007
2.50%	[4]*	0.006

*Number of Cumulative Ruptured Rebar

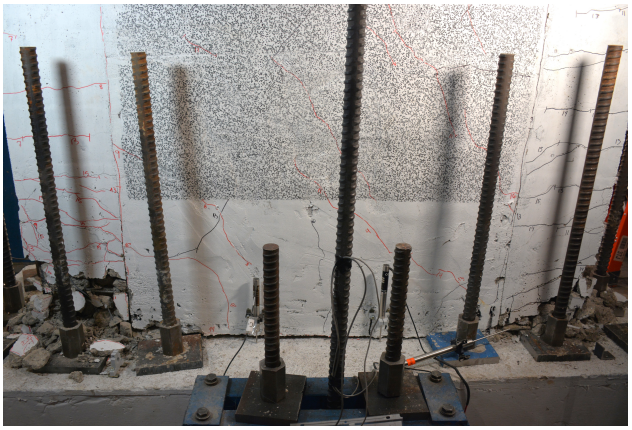

Figure 4.12: Lower Wall of Specimen S1CW

Figure 4.13: Web Crushing of Specimen S1CW

Figure 4.14: North Toe Final State of Specimen S1CW - Bar Buckling

Figure 4.15: South Toe Final of Specimen S1CW

4.2.3 Specimen S1FW

S1FW is a retrofitted copy of the S1 specimen with a one-sided web-only FRP shear strengthening scheme, along with FRP fiber anchors to prevent premature delamination. A view of the specimen pre-test and post-test is shown in Figure 4.16.

(a) S1FW Pre-Test

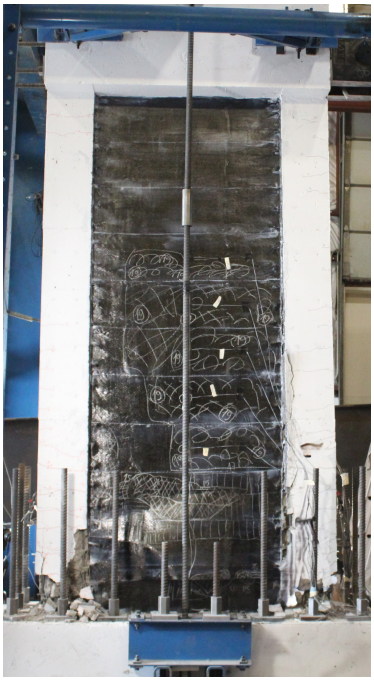

(b) S1FW Post-Test

Figure 4.16: S1FW Specimen Initial (Pre-Loading) and Final (Post-Loading) Conditions

The force-drift curve is seen in Figure 4.17. The specimen reached a peak strength of 166 kips during the first stage of loading at 1.5% drift in the positive loading cycle and -167 kips at the first -1.5% drift cycle. The specimen's residual strength at subsequent drift cycles was calculated per Equation 4.1 and is noted in Table 4.6. The specimen exhibited minimal degradation of strength until the drift ratio of 2.5%.

Initial cracking occurred in the web during the 75 kip force-controlled cycle, which was seen on the un-retrofitted back face of the web. The first cracks in the pilaster appeared during

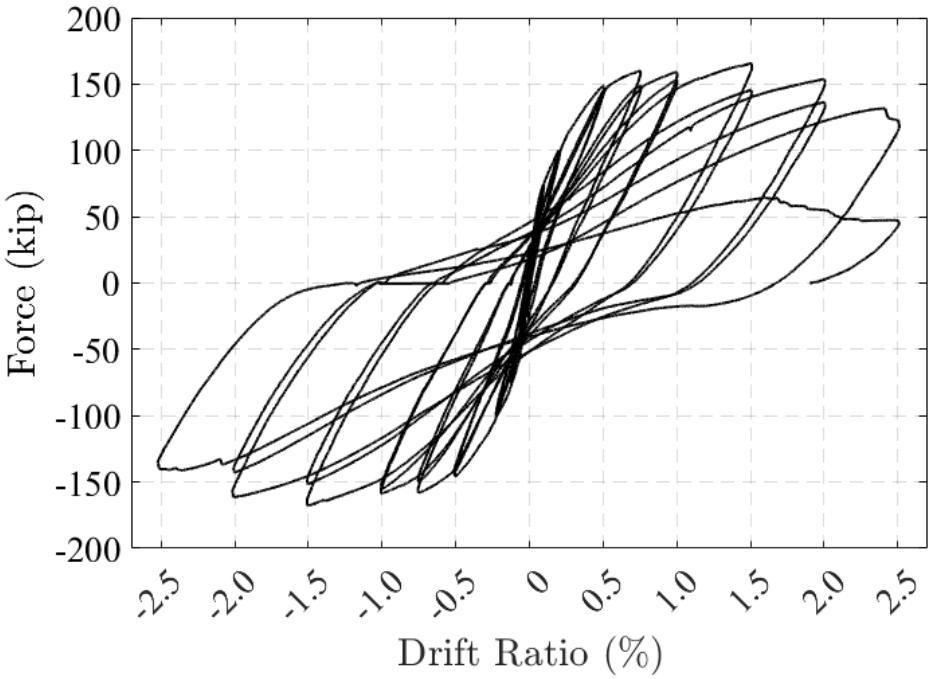

Figure 4.17: S1FW Force-Drift Curve

Table 4.6: S1FW Strength at Critical Drift Ratios

Peak Load (kip)	Residual Strength @ 2% Drift	Residual Strength @ 2.5% Drift
166 kip	93%	80%
-167 kip	96%	83%

*Number of cumulative ruptured rebar

the 100 kip loading stage, at which point more web cracks appeared and propagated as well. At the 0.5% drift ratio, initial cracking from the FRP epoxy was heard. The horizontal cracks in the pilaster propagated about halfway up the pilasters this cycle. At 0.75% drift, the FRP began to delaminate slightly, near the base of the wall close to the foundation. An initial crack of width 0.04 inches was seen at the interface of the foundation and the wall measured with a crack-card. At 1.0% drift, the cracks in the pilaster localized more, to about 0.02 inches.

At the 1.5% drift cycle, the FRP delaminated in a small but noteworthy pattern, spanning

nearly the full width of the wall at a height of three feet, but still maintained a good bond above and generally below this height, as seen in Figure 4.18a. The toes of the pilasters had vertical cracks in the concrete, as well as some spalling, likely due to bar buckling in this region. The interface at the wall and the foundation also highly localized, opening to about 0.25 inches. At 2% drift, there was the first rebar fracture in the pilaster. The inside corners of the pilasters (the corners closest to the web) had significantly spalled concrete, occurring while the pilaster was in compression, which was likely due to rebar buckling. The FRP had not delaminated much further at this stage and the FRP above the 3 delaminated zone was still well bonded to the concrete substrate. The damage pattern obtained after the application of this loading cycle is shown in Figure 4.18b.

At the final drift ratio of 2.5%, the toes of the pilasters were extremely damaged and the rebar had severely buckled. Furthermore, the FRP debonded across the majority of the web, concurrently with large localization of cracks on the back face of the specimen, see Figures 4.18c and 4.19 and Table 4.7 for details of this damage state. Figures 4.20, 4.21, and 4.22 further showcase the overall final damage state of the specimen.

Table 4.7: Maximum Measured Crack Width for Specimen S1FW

Drift (%)	Max Diagonal Crack Width Opening (in)
0.75%	0.11
1.00%	0.13
1.50%	0.21
2.00%	0.30
2.50%	0.58

Table 4.8 provides a detailed account of the peak strains observed in each cycle in the vertical pilaster steel, the horizontal web steel, and the FRP overlay. Yielding of the vertical rebar in the pilasters occurred during the 100 kip force-controlled cycle. It was evident that the demand in the longitudinal steel within the pilasters considerably exceeded that in

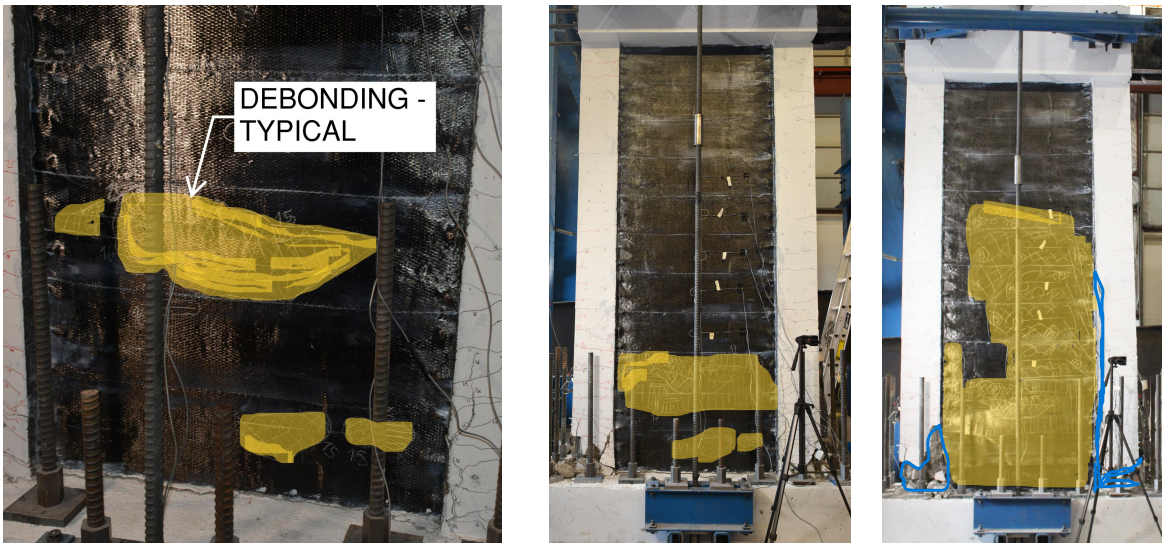

(a) S1FW 1.5% (b) S1FW 2.0% (c) S1FW 2.5%

Figure 4.18: FRP Delamination Propagation for Specimen S1FW

Figure 4.19: Back Lower Wall Final State of Specimen S1FW

the horizontal shear steel; the maximum measured strain in the vertical rebar was observed during the 2% drift ratio, attaining a strain of 4.5%. The strain in the FRP was evaluated in

Figure 4.20: Final Damage State of S1FW - Anchor Pullout and Pilaster Vertical Crack

the horizontal or fiber direction. The highest strain in the FRP was recorded at the lowest gauge on the wall, positioned at 4.5 feet above the foundation, just above the initial FRP delamination point.

The FRP exhibited gradual delamination beyond the 1.5% cycle, eventually achieving strains of 0.003. A graph of the different FRP strains at each height and for each drift ratio is presented in Figure 4.23, and aligns with the visual observation of delamination emanating

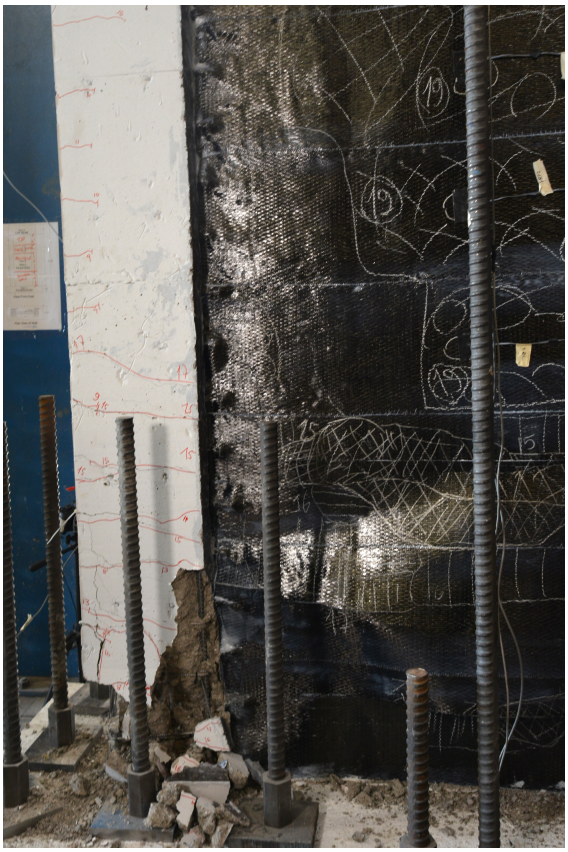

Figure 4.21: South Toe and FRP Delamination Photo of Specimen S1FW - Final Damage State

Figure 4.22: South Toe of Specimen S1FW Final State Photo - Bar buckling

from the lower portion of the wall. The effective design strain, ε_{fe}, for this specimen was determined to be 0.002 which is slightly lower than the strains obtained during the test. The strains in the vertical pilaster rebar indicated yielding, followed by strain hardening followed by vertical rebar fracture. The toe regions of the specimens exhibited bar buckling and ultimately rupture.

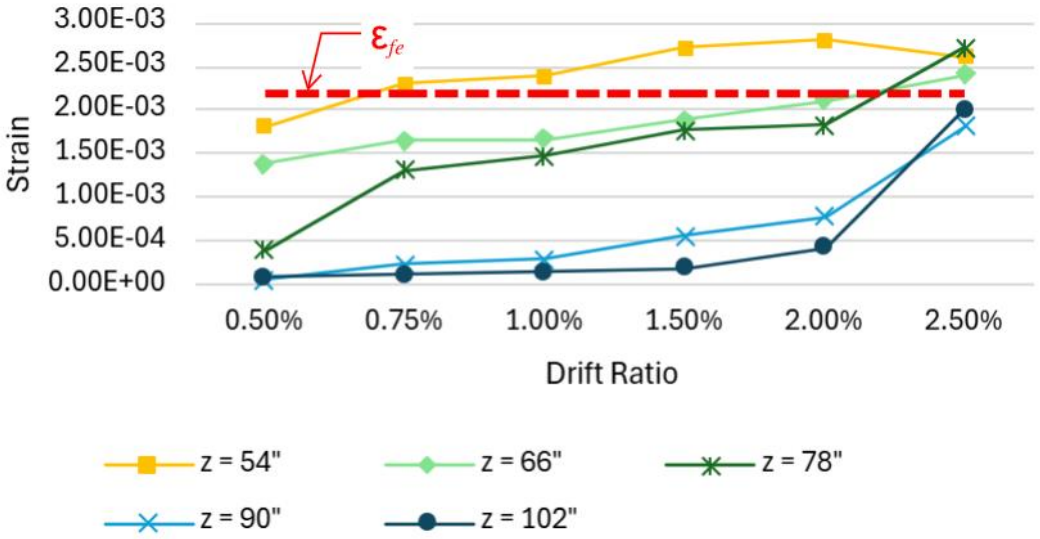

Figure 4.23: FRP Horizontal Strains at Different Locations Along the Height for Specimen S1FW

Table 4.8: S1FW Peak Strains Per Cycle

Drift	Peak Vert. Pilaster Rebar	Peak Horz. Web Rebar	FRP Strain
0.50%	0.013	0.003	0.002
0.75%	0.018	0.004	0.002
1.00%	0.026	0.005	0.002
1.50%	0.037	0.013	0.003
2.00%	0.045	0.018	0.003
2.50%	[4]*	0.014	0.003

*Number of Cumulative Ruptured Rebar

4.2.4 Specimen S1FP

Specimen S1FP was retrofitted based on the results of specimen S1FW and had a shear web strengthening strategy, along with bar buckling confinement at the pilaster ends. A view of the specimen pre-test and post-test is shown in Figure 4.24.

(a) S1FP Pre-Test (b) S1FP Post-Test

Figure 4.24: S1FP Specimen Initial (Pre-Loading) and Final (Post-Loading) Conditions

The force-drift curve can be seen in Figure 4.25. The specimen reached a peak strength of 171 kips during the first stage of loading at 1.5% drift in the positive direction, and -172 kips in the negative direction of the same cycle. The specimen's residual strength at subsequent drift levels was listed in Table 4.9. Note that the first cycle of each drift level was used for the residual strength at a specified drift. The 1.5% drift ratio was characterized by the fracture of the vertical rebar in the pilaster. The specimen showed consistent strength capacity until the 2.5% drift ratio, during which it exhibited a rapid degradation in strength. This specimen

had a rapid decline in strength at the 2.5% drift ratio, only retaining approximately 50% of the maximum strength. The loading in the final drift ratio was also interrupted due to equipment malfunction, as can be seen in the rapid drop at 0.8% drift. The test was quickly resumed and the specimen was successfully pushed to the 2.5% drift ratio.

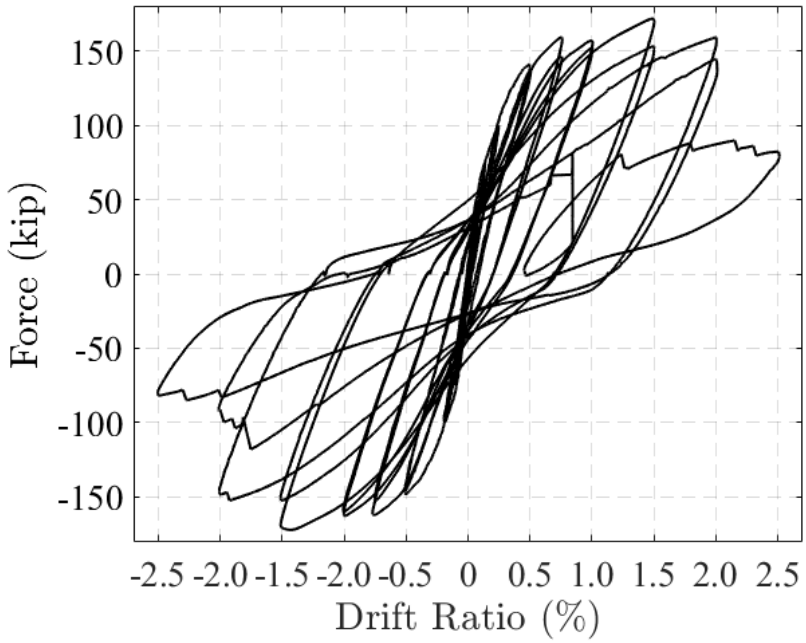

Figure 4.25: S1FP Force-Drift Curve

Table 4.9: S1FP Strength at Critical Drift Ratios

Peak Load (kip) @ 1.5% Drift	Residual Strength @ 2% Drift	Residual Strength @ 2.5% Drift
171 kip	89%	48%
-172 kip	88%	47%

The initial diagonal cracking in the web occurred during the 100 kip force-controlled cycle. At 0.5% drift, there were small diagonal cracks (<0.01 inches) in the web that extended almost the entire strut of the specimen, but no FRP delamination was found in this cycle. At 0.75% drift, the base of the wall and the foundation exhibited a large crack of about 0.20 inches, as well as slightly widening diagonal cracks in the web. At 1.0% drift, there was

initial spalling and some slight concrete crushing at the toes of the specimen. The crack at the foundation-wall interface also grew this cycle, while the web cracks remained essentially the same width, as was shown in Table 4.10. At 1.5% drift, the FRP at the toes ruptured due to confined concrete crushing, and the web toe also experienced crushing, which is shown in Figure 4.27. The foundation crack grew as well during this cycle. During the second cycle of 1.5% drift, the FRP delaminated further, up 15 inches from the foundation into the pilaster. There was also additional spalling and crushing at the toes of the web. At 2% drift, the FRP continued to delaminate, all the way around the three faces of the pilaster, and about 20 inches up from the foundation, shown in Figure 4.28. There was major concrete spalling and likely rebar buckling at this point. The foundation-wall crack was 0.75 inches. At 2.5% drift, the damage in the specimen was characterized by additional FRP delamination on the pilasters and concrete crushing. There was no delamination in the web FRP. The damage propagation is shown in Figures 4.26, 4.27, 4.28, and 4.29. Figures 4.30, 4.31, 4.32, and 4.33 showcases the overall final damage state of the specimen at the end of the test.

Table 4.10: Maximum Measured Crack Width for Specimen S1FP

Drift (%)	Max Diagonal Crack Width Opening (in)
0.75%	0.10
1.00%	0.11
1.50%	0.13
2.00%	0.13
2.50%	0.06

Table 4.11 shows the peak strains exhibited each cycle by the vertical pilaster steel, the horizontal web steel, and the maximum strain in the FRP for each cycle. The FRP strain time histories can be further seen in Figure 4.34, which showcases the different strains exhibited in the web versus the pilaster. The web overall saw very small strain values, particularly when compared to the pilaster strains. The effective design strain, ε_{fe}, for the pilaster bar buckling

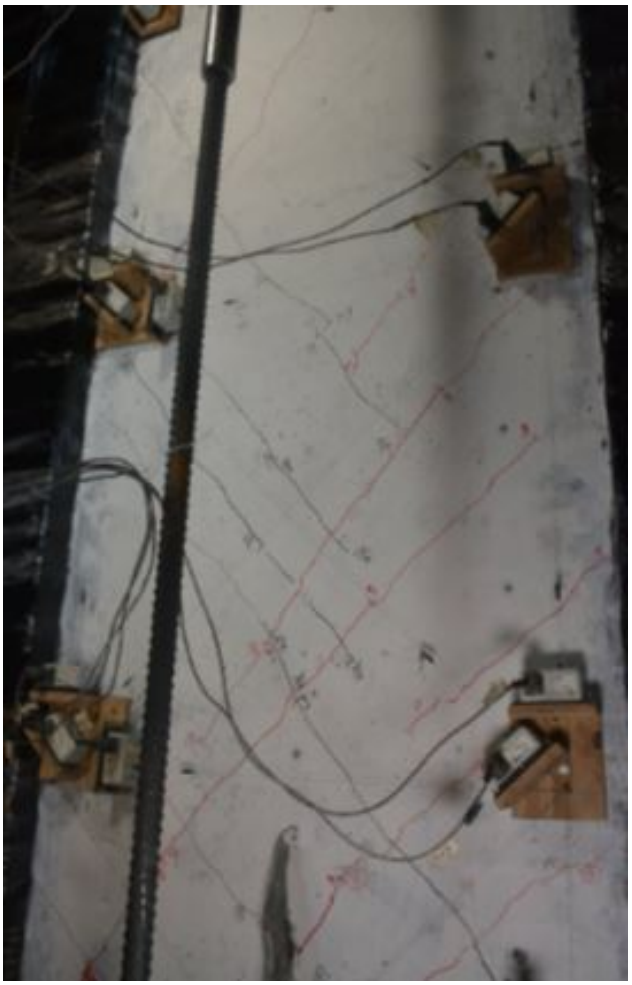

Figure 4.26: Wall of Specimen S1FP at 1.0% Drift

consideration is shown as a red dashed line at 0.004 strain in the figure. The effective design strain in the web FRP was 0.0022, but it is not shown for clarity. The strains in the web stay below their respective effective strain value nearly the entire duration of the test.

The strains induced in the longitudinal steel provide quantifiable justification of the visual damage in the specimen, specifically the localized inelastic deformation of the toes and subsequent rupture of the longitudinal steel. Beyond the 1% drift ratio, the specimen exhibited rupture of the vertical rebar. It is interesting to note that the rupture of the vertical bars occurred at a lower drift ratio than either of the other S1 retrofitted specimens, and that

(a) FRP Initial Rupture

(b) Web Crushing

Figure 4.27: Wall State of Specimen S1FP at 1.5%

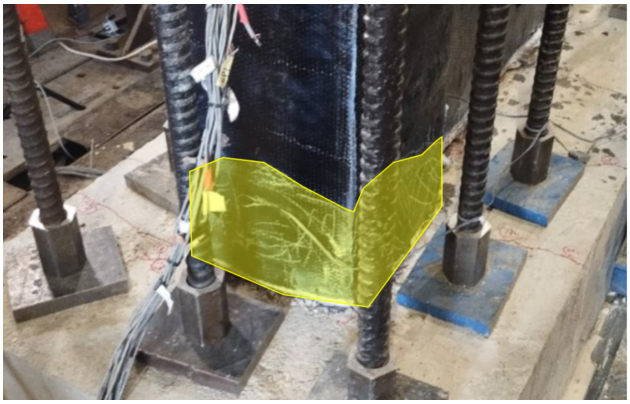

Figure 4.28: Toe Delamination of Specimen S1FP at 2.0%

this specimen, S1FP, had a larger cumulative number of fractured bars by the end of the test.

The peak strains exhibited per cycle in the web of the specimen's FRP overlay are shown in Figure 4.35a and showcase that the highest strains exhibited in the horizontal FRP occur at a height of 54 inches. The graph in Figure 4.35b shows the peak strains in the FRP pilaster wrap for both the north and south pilasters. These figures show graphically how the strains change over time and how the demand in the pilaster FRP is much higher than the demand in the web FRP.

(a) Bar Rupture (b) Concrete Crushing, FRP Rupture

Figure 4.29: Wall State of Specimen S1FP at 2.5%

Table 4.11: S1FP Peak Strains Per Cycle

Drift	Peak Vert. Pilaster Peak Reinf.	Peak Horz. Web Reinf.	FRP Web Overlay	FRP Pilaster Overlay
0.50%	0.011	0.002	0.002	0.002
0.75%	0.021	0.002	0.002	0.002
1.00%	0.037	0.002	0.002	0.004
1.50%	[1]*	0.003	0.002	0.006
2.00%	[5]*	0.003	0.002	0.006
2.50%	[12]*	0.002	0.001	0.006

*Number of cumulative ruptured rebar

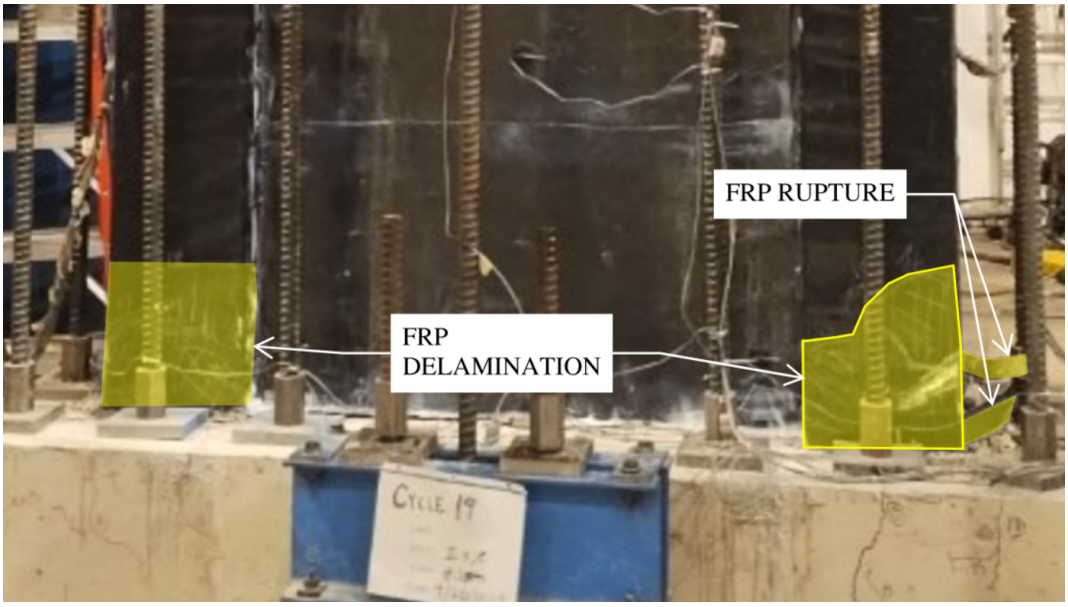

Figure 4.30: Final state of Specimen S1FP - FRP Delamination

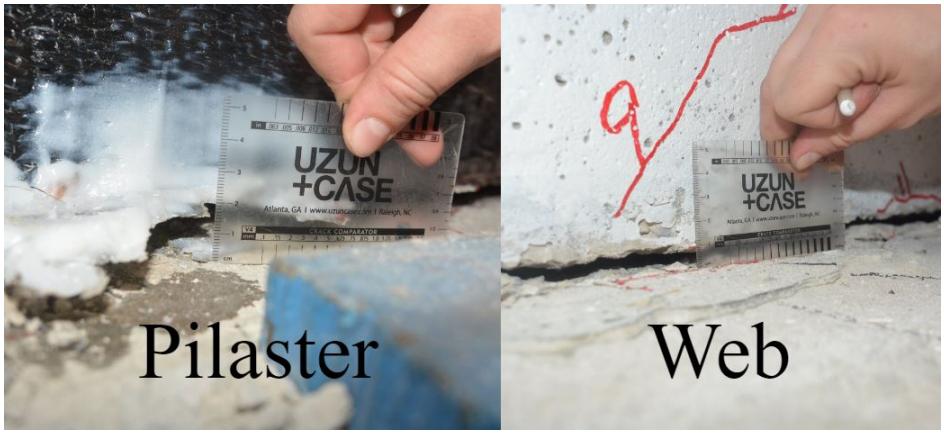

Figure 4.31: Final Base Crack of Specimen S1FP

Figure 4.32: South Pilaster- Final Condition of Specimen S1FP

Figure 4.33: North Pilaster- Final Condition of Specimen S1FP

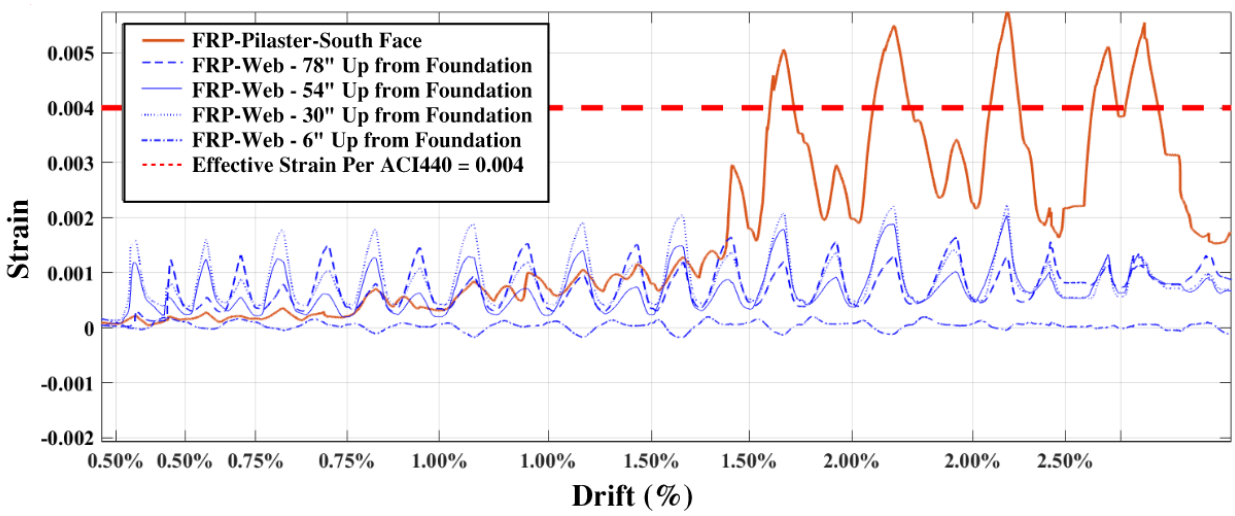

Figure 4.34: FRP Strains Over Time for Specimen S1FP

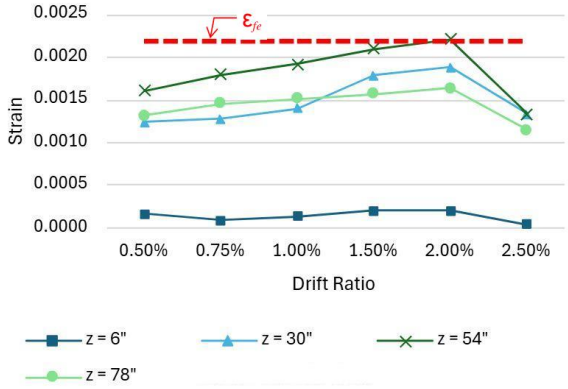

(a) Web Overlay

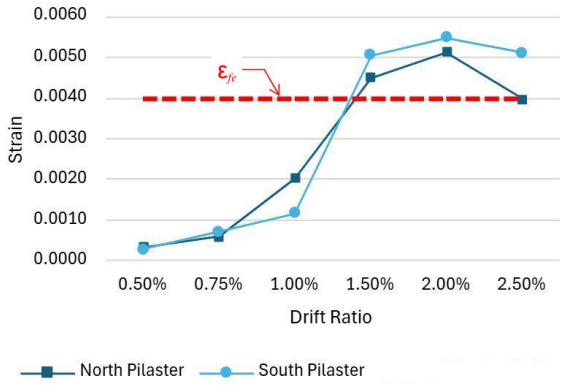

(b) Pilaster Wrap

Figure 4.35: Horizontal Strain Values for FRP on Specimen S1FP

4.2.5 Comparison of Shear Web Strengthening Strategies: Concrete Overlay vs. FRP

Specimens S1CW and S1FW had been retrofitted with shotcrete and fiber reinforced polymer (FRP), respectively, on one side of the web only. They were both designed to achieve the same target shear strength, which had resulted in a flexurally controlled failure. The force-drift comparison graph between all of the group one specimens is shown in Figure 4.36. Residual strengths for each strategy are listed in Table 4.12 for the positive direction of loading only. The strategies had been similarly effective at delaying the shear failure observed in the control specimen, resulting in initial inelastic flexural deformations. This was obvious in both retrofitted specimens through bar buckling and reinforcement rupture at the toes and the lack of crack localization in the webs. Ultimately, both retrofit strategies failed after post-peak behavior associated with flexural yielding, and the final behavior of the specimens was localized shear crack formation in the web. As noted in Table 4.12, the FRP retrofit retained more residual strength than the shotcrete during the final drift ratio.

Table 4.12: Web Shear Strengthening Retrofit Comparison

Specimen	Peak Strength		Residual Strength @ first cycle of max drift		$\frac{Residual}{Peak}$	Preceding Failure Mode
	Drift (%)	Load (kip)	Drift (%)	Load (kip)	(%)	
S1	1	154	1.5	61	39%	Shear Diagonal Tension
S1CW	1.5	165	2.5	122	74%	Flexure
S1FW	1.5	166	2.5	123	75%	Flexure

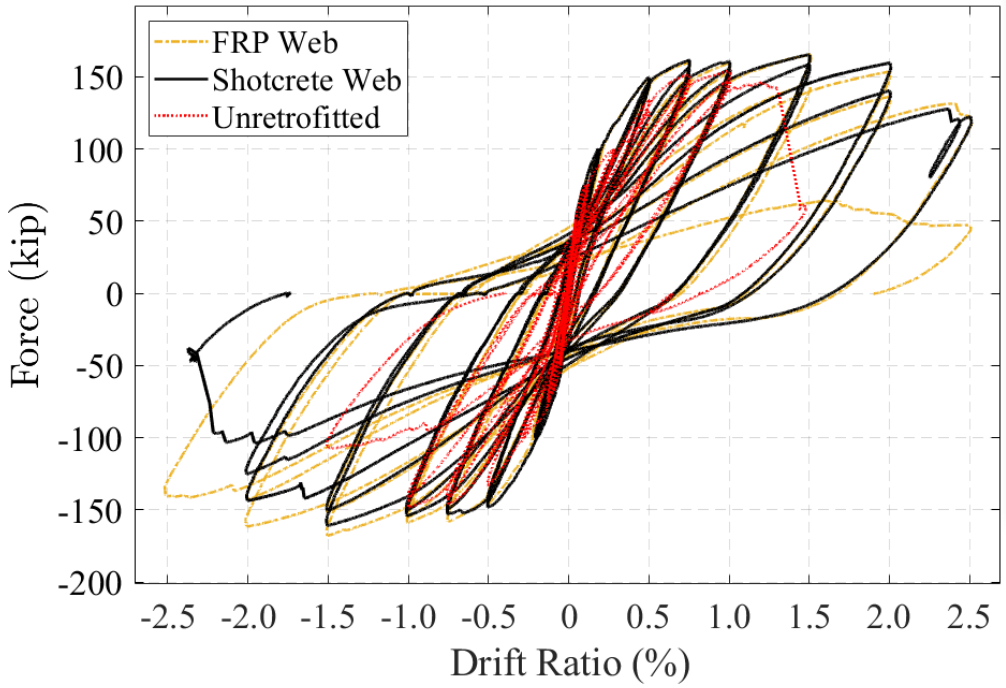

Figure 4.36: Web Retrofit Strategy Comparison

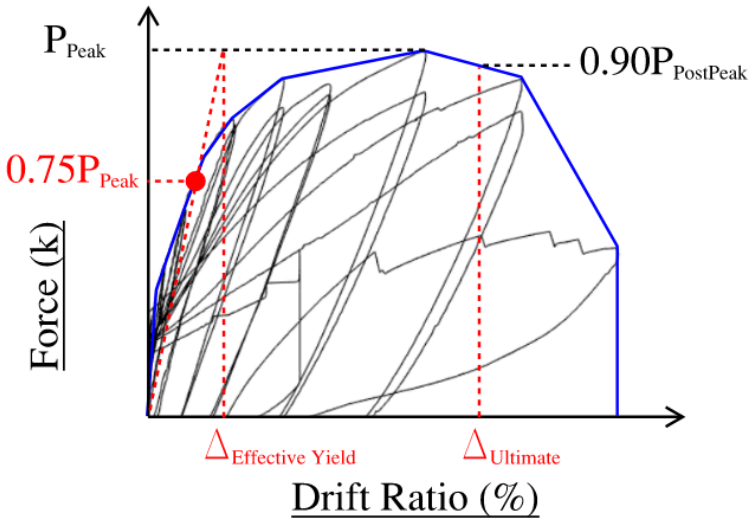

Figure 4.37: Ductility Calculation per Park (1989)

The ductility of each specimen was calculated through the method proposed by Park (1989), and illustrated in Figure 4.37. The effective yield displacement was determined from the experimental hysteretic behavior by determining the intersection of two linear lines that corresponded to a horizontal line passing through the maximum strength and a line passing through the origin and 75% of the maximum strength. The deformation associated with a minor loss of strength in the post-peak behavior, in this case 90% was selected, was defined as the ultimate displacement. The ductility, μ, was the ratio between the ultimate displacement and the effective yield displacement, as seen in Equation 4.2.

$$\mu = \frac{\Delta_{Ultimate}}{\Delta_{Effective\ Yield}} \qquad \text{(Eq. 4.2)}$$

The ductility of each of the specimens is listed in Table 4.13. The retrofit strategies provide nearly identical improvement to the ductility of the specimen.

Furthermore, the contribution of shear to each specimen's overall drift is calculated through details listed in Appendix B. The maximum shear strains exhibited by each of the specimens

Table 4.13: Ductility Comparison of Shear Web Strengthened Specimens and Control

Specimen	Ductility, μ
S1	2.53
S1CW	4.63
S1FW	4.42

for each drift ratio can be seen in Table 4.14. The shear demand was the highest in the control specimen, during the farthest drift ratio of that specimen, 1.5% drift ratio. The shear strengthening strategies successfully reduced the shear strains in the web of the specimen, which was also evident through visual inspection, but which is validated here.

Table 4.14: Shear Strain, γ, Comparison For Shear Web Strengthening Specimens and Control

Drift Ratio	S1	S1CW	S1FW
0.50%	0.007	0.003	N.A.
0.75%	0.011	0.005	0.005
1.00%	0.016	0.014	0.007
1.50%	0.049	0.015	0.011
2.00%	N.A.	0.016	0.015
2.50%	N.A.	0.015	0.026

4.2.6 Comparison of FRP Web and FRP Web & Pilaster Overlay

Specimens S1FW and S1FP both strengthened with one-sided FRP overlay for shear strength in the web, however, S1FP had an additional wrap around the pilasters for bar buckling prevention. The force-drift comparison plot can be seen in Figure 4.38. The strategies were both effective in delaying the shear damage exhibited in the control specimen in the web at 1.0% drift, and they have nearly identical residual strength values until the 2.5% drift cycle, where their residual strengths vary greatly. Table 4.15 shows that at the 2.0% drift cycle, both specimens have a residual strength of about 90%, but at the 2.5% drift cycle, S1FP has only 48% while S1FW still maintains 79%. This is a significant difference and should be considered. This is likely due to the excessive confinement of the FRP in the pilasters, intended to delay bar buckling, but which unintentionally caused concentrated strain in the rebar at the base of the specimen. This is in contrast to the exposed pilasters in specimen S1FW, which allowed strain to distribute more evenly throughout the vertical rebar, and therefore allowed gradual rupture of the rebar and a less severe strength degradation.

Furthermore, the FRP on the web of specimen S1FW reached a measured maximum strain of 0.003 during the 2.0% drift ratio, while the strain in the web FRP of S1FP never exceeded 0.002. The FRP on the pilasters of specimen S1FP reached a maximum measured strain of 0.006, and ultimately ruptured at the toes of the specimen. It appears that if the main goal of the retrofit strategy is to simply enhance the shear strength of the specimen, to preclude inelastic shear deformations, a one-sided retrofit overlay of FRP will sufficiently accomplish this goal. However, if the goal is to delay bar buckling, this did not appear to be advantageous, and resulted in a more rapid loss of strength during the same drift cycles. At the 2.5% drift ratio, S1FP retained approximately 50% of the maximum strength, while the other S1 retrofit specimens had approximately 75% 80% of residual strength at this same drift ratio. Specimen S1FP was ultimately less ductile than specimen S1FW, as can be seen

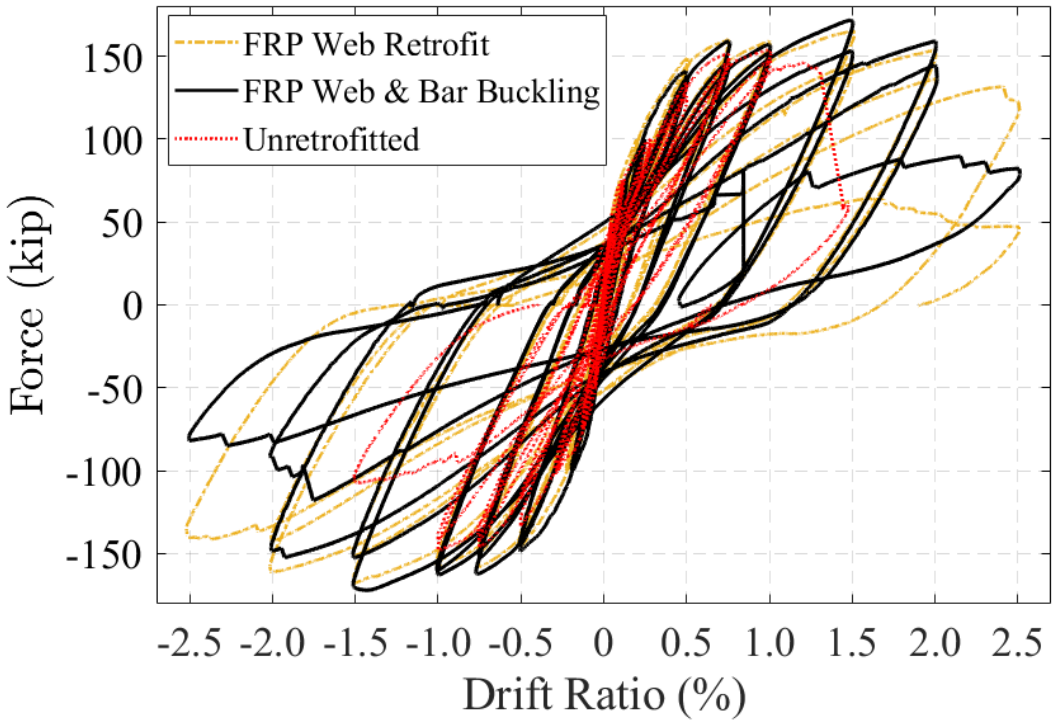

Figure 4.38: FRP Retrofit F-d Comparison: Web vs. Web & Pilasters

in Table 4.16.

Some of the key results for the FRP group one retrofitted specimens are summarized in Table 4.15.

Table 4.15: Summary of Group 1 Specimen Test Results

Specimen	Peak Strength		Residual Strength @ first cycle of max drift		$\frac{Residual}{Peak}$	Preceding Failure Mode
	Drift (%)	Load (kip)	Drift (%)	Load (kip)	(%)	
S1	1	154	1.5	61	39%	Diagonal Tension
S1FW	1.5	166	2.5	123	75%	Flexure
S1FP	1.5	170	2.5	79	47%	Flexure

Table 4.16 presents the ductility measurements of the specimens: unretrofitted, retrofitted with FRP for shear strengthening, and retrofitted to prevent bar buckling. It was observed

that the specimen with pilaster wrapping underwent quicker strength deterioration, leading to reduced ductility for this specimen.

Table 4.16: Ductility Comparison of FRP Retrofitted Group One Specimens

Specimen	Ductility, μ
S1	2.53
S1FW	4.42
S1FP	3.77

The shear strains exhibited by the webs of the specimens are shown in Table 4.17. Specimen S1FP had slightly lower strains in the web than S1FW, but both retrofitted specimens had minimal levels of shear strain compared with the unretrofitted specimen. The final drift ratio, 2.5%, was coincident with FRP delamination on only specimen S1FW, so the shear strains reaching 2.6% further validate the observed web panel damage of this specimen. The FRP on specimen S1FP did not delaminate in the web even at the highest drift ratio.

Table 4.17: Shear Strain, γ, Comparison For FRP Shear Strengthening and Bar Buckling Retrofits

Drift Ratio	S1	S1FW	S1FP
0.50%	0.007	N.A.	0.004
0.75%	0.011	0.005	0.006
1.00%	0.016	0.007	0.006
1.50%	0.049	0.011	0.008
2.00%	N.A.	0.015	0.008
2.50%	N.A.	0.026	0.005

4.3 Results for Test Group Two

The results of test group two are discussed in this section. These specimen contained a lap splice in the plastic hinge region. S2FL was retrofitted with FRP, while S2 acted as the control for this group.

4.3.1 Specimen S2 - Control

Specimen S2 was the unretrofitted control specimen for group two specimens. A view of the specimen pre-test and post-test is shown in Figure 4.39.

(a) S2 Pre-Test (b) S2 Post-Test

Figure 4.39: S2 Specimen Initial (Pre-Loading) and Final (Post-Loading) Conditions

The force-drift curve can be seen in Figure 4.40. The specimen exhibited a clear loss of stiffness initially, which can be attributed to cracking, at about 0.11% drift. The specimen

reached a peak strength of 123 kips during the first stage of loading at 1.0% drift in the positive direction. Note that this peak strength occurred at about 0.65% drift. It reached a peak strength in the negative direction during the same cycle of loading at -118 kips at -0.60% drift. Yielding of the vertical rebar in the pilasters occurred during the 0.5% drift cycle, but the strain demand in the steel did not go higher than 0.015. This is due to the fact that the steel started slipping, rather than engaging with the concrete surrounding it. As the steel slipped, it could not provide adequate resistance to develop the yield strength in the reinforcement. During the second cycle of the same drift, the specimen exhibited a drastic decrease in strength. Table 4.18 shows the peak strains exhibited each cycle by the vertical pilaster steel and the horizontal web steel. The test was ended after the 1.0% drift ratio.

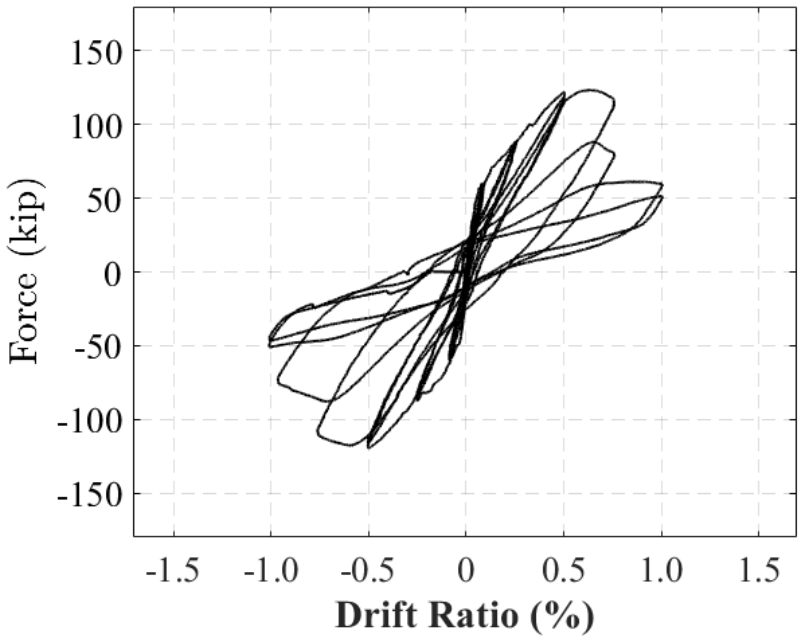

Figure 4.40: S2 Force-Drift Curve

Initial cracking occurred during the 60k force-controlled cycle. The initial cracks occurred in the web of the specimen near the base, with slight inclines, and in the pilasters. At the

Table 4.18: S2 Peak Reinforcement Strains Per Cycle

Drift	Peak Vert Pilaster Strain	Peak Horz Web Strain
0.5%	0.002	0.006
0.75%	0.011	0.008
1.0%	0.007	0.006

0.25% drift cycle, the cracks extended up nearly the full strut of the wall. At 0.5% drift, the damage in the specimen started to localize at the toes, specifically in the lap splice region, within 15 inches of the foundation where vertical cracks occur. The damage was more severe at 0.75% drift, which is also the cycle in which the specimen reached its peak load. The concrete was bulging at the toes of the pilasters, and the vertical cracks were 0.06 inches wide. Note that the specimen was accidentally pushed to -1.0% drift during the second cycle of the intended -0.75% drift. The final loading stage of 1.0% was characterized by more concrete spalling at the toes and very wide localized cracks. The concrete at the toes of the pilasters was removed after the test to observe the slippage, see Figure 4.43b. The damage propagation is shown graphically in Figure 4.41. Figures 4.43b and 4.43 show the extent of damage after the experiment was completed.

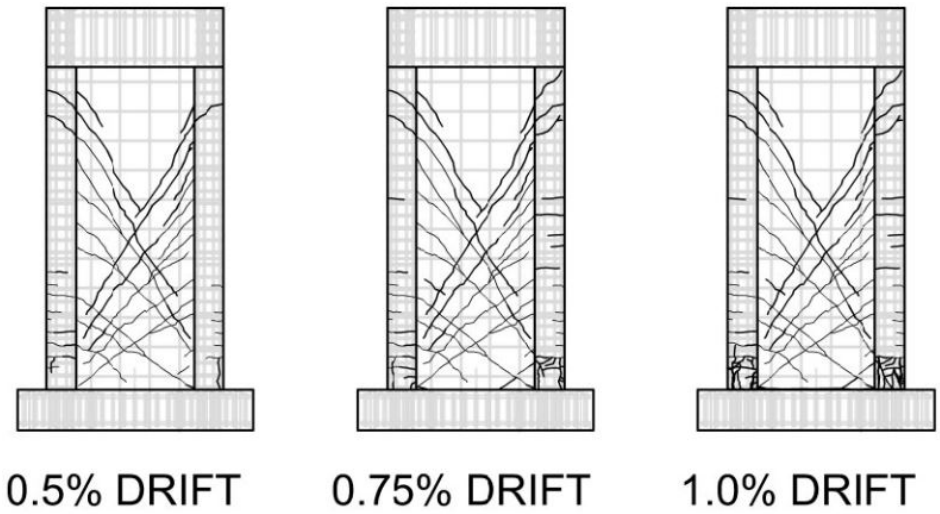

Figure 4.41: Crack Evolution for Specimen S2

Figure 4.42: Lap Splice Region of Specimen S2- Final Condition

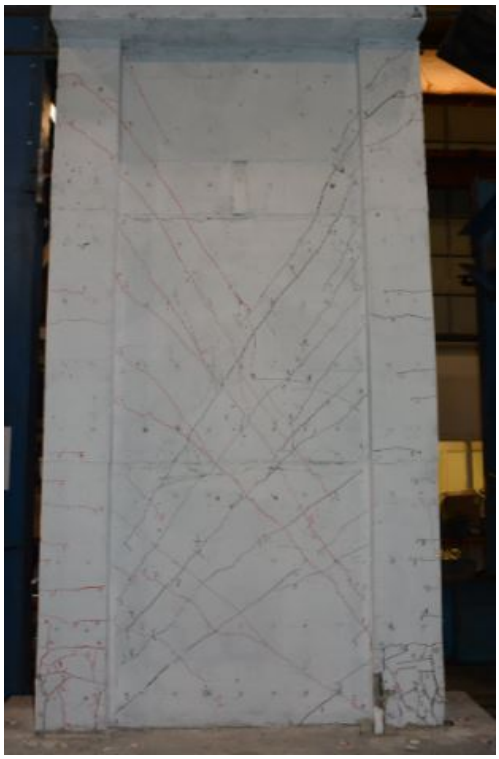

(a) Full Front Overview

(b) Lap Splice Slip Uncovered

Figure 4.43: Final Damage State of Specimen S2 with Lap Splice

4.3.2 Specimen S2FL

S2FL was the same design as specimen S2, but with a full FRP wrap. This FRP wrap encompassed both webs and the pilasters. FRP anchors were embedded through or into the pilasters and wrapped around both the web and the pilasters.

The force-drift curve can be seen in Figure 4.44. The specimen exhibited good ductility and showed only slight loss in stiffness degradation until the 1.5% drift cycle. The specimen reached a peak load of 152 kips during the first cycle of 1.5% drift in the positive direction. It reached a peak strength in the negative direction during the 1.0% drift cycle at -140 kips. This difference in which cycle the maximum load occurred between positive and negative loading could be attributed to the axial load, which was 120 kips during the 1.0% loading cycle but was subsequently reduced to the original 100 kips during the 1.5% cycle. Initial yielding of the vertical rebar in the pilasters occurred during the 0.5% drift cycle. Table 4.19 shows the peak strains exhibited each cycle by the vertical pilaster steel and the horizontal web steel. The test was ended after the first 2.0% drift cycle.

Table 4.19: S2FL Peak Reinforcement Strains Per Cycle

Drift	Peak Vert. Pilaster Strain	Peak Horz. Web Strain	Peak FRP Strain
0.50%	0.012	0.001	1.9E-4
0.75%	0.030	0.001	2.4E-4
1.00%	0.044	0.002	5.9E-4
1.50%	0.074	0.002	8.2E-4
2.00%	[5]*	0.002	8.5E-4

*Cumulative number of fractured rebar

At 0.5% drift, there was minor cracking at the foundation-wall interface. At 1.0% drift, the foundation-wall interface had widened to 0.25 inches. At 1.5% drift, the foundation-wall interface crack had widened to 0.35 inches, and there was some crushing of the concrete at the base of the pilasters, which could be seen due to the large foundation-wall crack. At

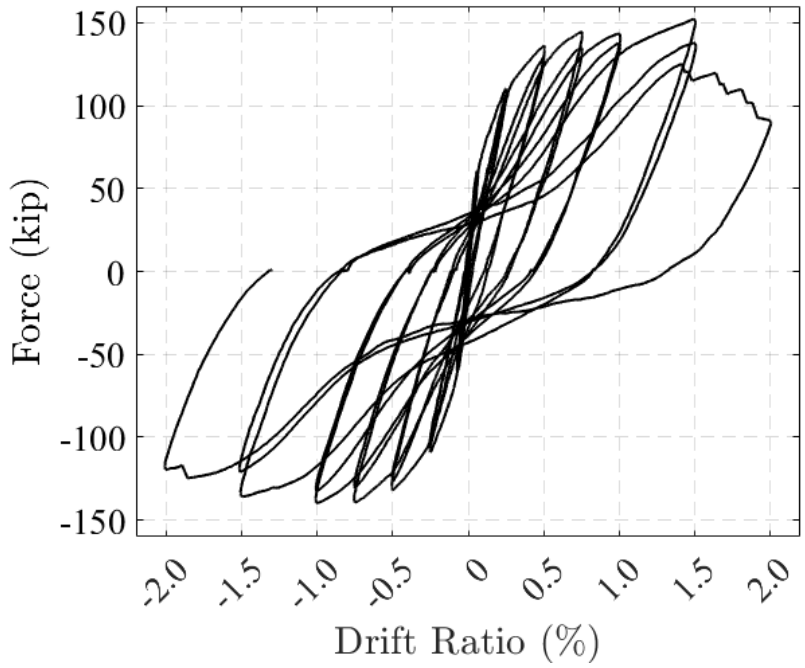

Figure 4.44: S2FL Force-Drift Curve

2.0% drift, the crack width for the foundation-wall interface was 0.80 inches. There was no delamination in the FRP.

A view of the specimen pre-test and post-test is shown in Figure 4.45.

Figures 4.46, 4.47, and 4.48 show the extent of damage after the experiment was completed.

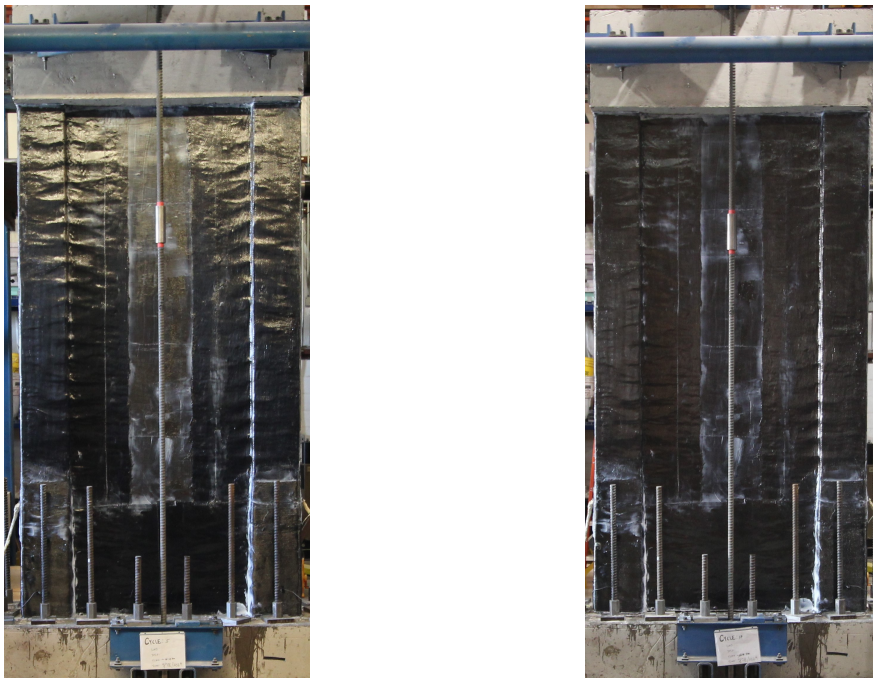

(a) Pre-Test (b) Post-Test

Figure 4.45: S2FL Specimen Initial and Final Conditions

Figure 4.46: Close up of Final Base Crack of Specimen S2FL

Figure 4.47: Final Condition S2FL Base Crack

Figure 4.48: Final Toe Concrete Condition of Specimen S2FL

4.3.3 Discussion on Effectiveness of Lap Splice Prevention

Specimens S2 and S2FL were similar except that S2FL had the addition of FRP wrapped around the entire structure. The force-drift comparison plot is shown in Figure 4.49. The addition of the FRP not only delayed the lap-splice failure but also completely eliminated it as a possibility. The amount of FRP wrapped around the plastic hinge region was cohesive and strong enough with the concrete to the point that it provided full confinement and enabled rebar rupture in the vertical pilaster steel. Table 4.20 showcases how effective the FRP wrap is at improving the ductility of the control specimen, reaching a drift of 2.0% while maintaining 60% of residual strength. The ductility is compared in Table 4.21 for the group two specimens. The retrofitted specimen exhibited a significant improvement in ductility, reaching a level of 5.63, compared to the unretrofitted specimen's ductility of 1.99. The conclusion can be drawn that the effectiveness of FRP, when designed appropriately and installed accurately, prevents lap-splice failures by providing adequate confinement in the plastic hinge region.

Furthermore, the strength of the specimen was also enhanced due to the lap-splice prevention wrap. The specimen achieved nearly 24% more strength due to the retrofit strategy. The lap splice in the plastic hinge region failed prior to the specimen reaching its full flexural capacity.

Table 4.20: Summary of Group Two Test Results

Specimen	Peak Strength		Residual Strength @ first cycle of max drift		$\frac{Residual}{Peak}$	Preceding Failure Mode
	Drift (%)	Load (kip)	Drift (%)	Load (kip)	(%)	
S2	0.75	123	1.0	61	50%	Lap Splice Slip
S2FL	1.5	152	2.0	125	82%	Flexure

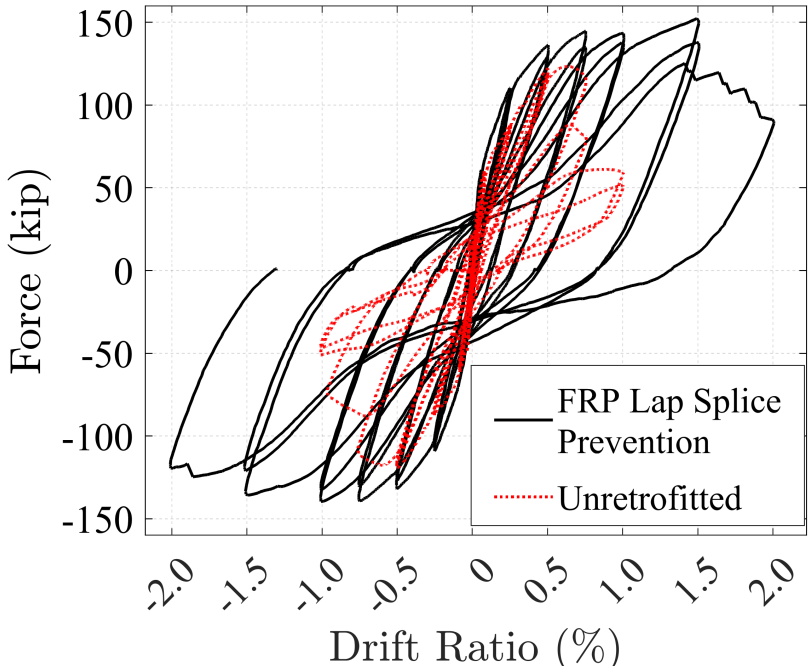

Figure 4.49: FRP Lap Splice Prevention Hysteretic Comparison: S2 vs S2FL

Table 4.21: Ductility Comparison of Group Two Specimens

Specimen	Ductility, μ
S2	1.99
S2FL	5.63

4.4 Conclusions for Experimental Program

The following bullet points summarize the conclusions based on the experimental data described in this chapter. The conclusions drawn rely on the assumption that the overlay strategy is designed in accordance with current guidelines and standards from ACI 440 (ACI 440 Committee, 2023). Furthermore, it is assumed that the installation is undertaken by qualified individuals.

- Shotcrete and fiber reinforced polymer (FRP) are capable of providing similar levels of shear enhancement to a non-ductile RC shear wall, with both increasing the deformation capacity by 66%. This shear enhancement is capable of delaying, but not preventing, diagonal shear deformations under seismic loading.
- FRP used for strengthening a shear-critical RC wall can be effective as a shear strengthening strategy by applying the retrofit to only one side of the web.
- ACI 440 design guidelines for flexural steel reinforcement bar buckling prevention results in a configuration of FRP wrap which may result in highly localized development of strain due to unintended vertical strengthening of the boundary region, thus reducing the ductility of the structure.
- FRP designed per ACI 440 can adequately eliminate the concern of lap splice failure, due to the confinement of the plastic hinge region and precluding a preliminary anchorage pullout. The retrofit strategy enhanced the strength by 24%, enhanced the ductility by a factor of 2.8, and altered the failure mode to be flexurally-controlled.
- The anchors designed for this specimen adequately anchored the FRP retrofit to the specimen in every case; there was no premature failure due to anchorage pullout.

- The design effective strains for the FRP overlays were close to measured strain values. The peak measured strain in the shear strengthening overlay which ultimately debonded was within 10% of the design effective strain of 0.0022, while the peak measured strain in the pilaster wrap for bar buckling was within 50% of the design effective strain of 0.004.

Chapter 5

Truss Modeling Approach for Unretrofitted and Retrofitted Walls

5.1 Introduction

This chapter elucidates the modeling methodology adopted for the numerical analysis conducted in the current study. This methodology is pertinent to this chapter as well as to Chapter 6. The nonlinear truss analogy is adopted herein and it is implemented through the research code, FE-MultiPhys (Koutromanos, 2024). The approach for this study incorporates a conceptual, user-friendly shell macroelement designed to simulate planar non-ductile reinforced concrete (RC) structural walls. The method has been demonstrated to accurately and efficiently represent critical failure modes of RC structural walls, while maintaining a relatively straightforward implementation. It relies on uniaxial material definitions and refrains from imposing kinematic constraints, such as plane-section assumptions, which may not be accurate for wall analyses.

A description of the numerical modeling approach, along with pertinent constitutive models, is described first, followed by a description of the enhancements implemented in capture lap-splice slip and retrofit overlays in this particular study. The modeling is then validated through a comparison with the experimental results presented in the previous chapter. The

ability of the model to capture the global force versus deformation response, as well as damage patterns, is evaluated.

The final component of this chapter considers a brief implementation of modern codes to contextualize the experimental program to a broader scope. This is achieved through the supplemental nonlinear truss analysis of a planar RC Special Structural Wall, detailed with modern code requirements and targeting the same flexural strength as the experimental specimens. Building on the experimental and analytical results, a comparison of the behavior of the modern structure is compared with the response of the non-ductile unretrofitted and non-ductile retrofitted specimens from the experimental program.

5.1.1 Finite Element Modeling Framework

The modeling scheme selected for this analysis is described herein and describes the choice and use of the nonlinear truss analogy. The truss analogy substitutes a finite element of a wall component with an assemblage of two horizontal, two vertical, and two diagonal truss elements, which can be seen in Figure 5.1. The modeled walls in this study are planar walls, and thus it is appropriate to utilize a two-dimensional formulation of the truss assemblage. Each truss relies on a uniaxial stress strain constitutive law, which greatly enhances the efficiency of the truss model as compared with other types of models (refer to the discussion in Chapter 2 for further details of other types of wall models). Previous studies have shown that this method can accurately represent the behavior of walls that exhibit different types of failure, including flexural and shear damage (Deng et al., 2021; Lu and Panagiotou, 2014; Lu et al., 2016; Panagiotou et al., 2021; Alvarez et al., 2020). The nonlinear truss models in this study are based on the modeling strategy for unretrofitted walls described in Deng et al. (2021) and modeled with the software BTM Component (Adstran, 2024). The truss elements may consist of several fibers. The horizontal and vertical elements consist of one fiber of

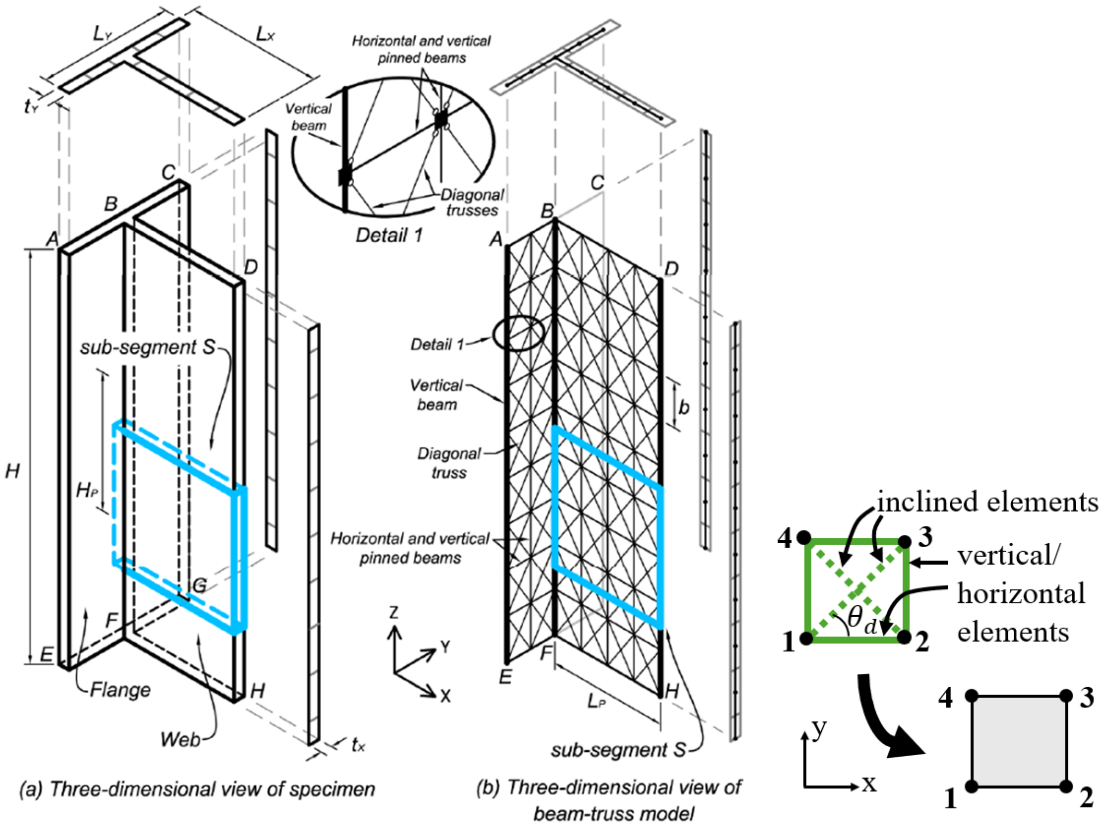

(a) RC Wall Represented with Line Element Assemblage (Figure from Lu et al. (2016))

(b) Formulation of a Truss Standard Panel Assemblage as a Rectangular, Four-node Element

Figure 5.1: Schematic Summary of User-Friendly Implementation of the Truss Model, Representing a Standard Truss Panel Assemblage as a Rectangular Macro-element

concrete material and one fiber of steel reinforcement material, while the diagonal elements consist of only one concrete fiber. The angle between the horizontal and the diagonal truss elements, θ_d, is calculated using the guidelines proposed by Lu and Panagiotou (2014). Analyzes have been performed through FE MultiPhys (Koutromanos, 2024).

The uniaxial material model used in this study for concrete is summarized schematically in Figure 5.2 and was originally formulated by Lu and Panagiotou (2014). The specific material model can account for the strength and stiffness degradation associated with tensile cracking

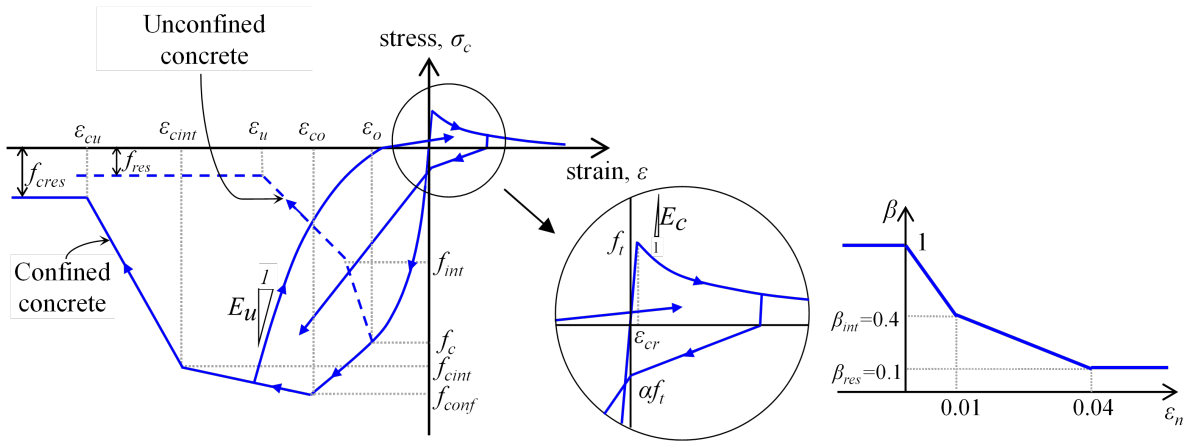

(a) Monotonic and Cyclic Hysteretic Responses

(b) Reduction of Compressive Stress in Inclined Truss Elements due to Transverse Tensile Strain

Figure 5.2: Behavior of Material Model for Concrete

and compressive crushing, as well as unloading and re-loading cyclic behavior. It can also account for the increased compressive strength and deformability of confined concrete. The effects of confining steel in the concrete compression curve are considered using the model proposed by Mander et al. (1988a). For diagonal elements, a reduction coefficient (β) is applied to account for the influence of transverse tensile strains on compressive resistance, on the basis of the modified compression field theory by Vecchio and Collins (1986).

The truss models are equipped with the capability to account for bar buckling and rupture via a uniaxial constitutive law proposed by Kim and Koutromanos (2016). This law represents the hysteretic stress-strain behavior using the equations previously proposed by Dodd and Restrepo-Posada (1995) and a non-iterative stress-update algorithm. In the absence of buckling or rupture, the material model can be fully calibrated if the stress-strain curve in monotonic tension, shown schematically in Figure 5.3a, is known. The constitutive model includes a hysteretic law to capture the cyclic response of the reinforcement steel, as qualitatively shown in Figure 5.3b. The buckling is modeled using a criterion defined in terms of

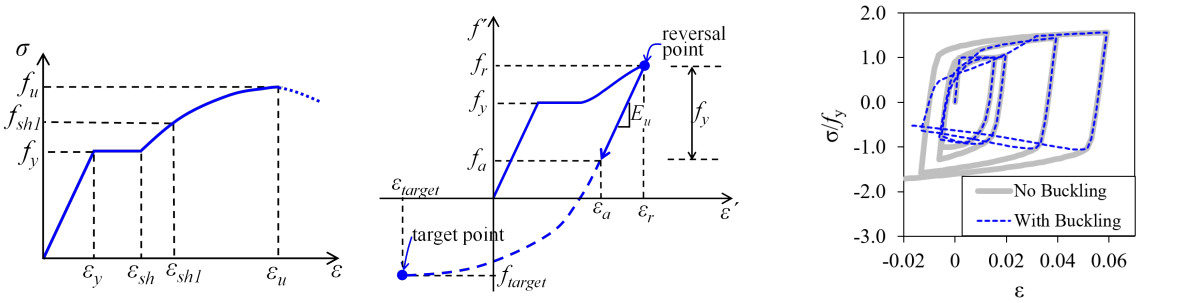

(a) Monotonic Tensile Response

(b) Cyclic Hysteretic Responses

(c) Cyclic Response Considering Buckling

Figure 5.3: Behavior of Material Model for Reinforcing Steel (Figures from Girgin et al. (2018))

axial stress which, when the criterion are met, multiply the stress by a reduction factor, as can be seen schematically in Figure 5.3c through the hysteretic response of a bar exhibiting buckling and a bar exhibiting no buckling (Kim and Koutromanos, 2016). The rupture of the bar under cyclic strain histories is accounted for through a criterion based on the accumulation of a quantity D. Specifically, given the true material stress, f, and the plastic strain rate, $\dot{\varepsilon_p}$, the rate of accumulation of D is governed by the following rate equation, Equation 5.1.

$$\dot{D} = \begin{cases} \left(\frac{f}{f_y}\right)^{2t} \dot{\varepsilon}_p, & \text{if } f > 0 \\ 0 & \text{otherwise} \end{cases} \qquad \text{(Eq. 5.1)}$$

Where f_y is the yield stress and t is a material constant and $\dot{D}$ is the rate of accumulation of the parameter D. Material failure, i.e. rupture, occurs when the value of D becomes equal to D_{cr}, which is also a parameter of the material model. Once the rupture criterion is met at a location of a structure, the material model is rendered incapable of developing any resistance for the remainder of the loading process.

The steel law has been extended to account for potential lap-splice failures. Specifically, the steel resistance in lap-splice regions is assumed to drop to zero once the tensile strain reaches a cap value corresponding to the lap-splice deformation capacity. This strain cap, $\varepsilon_{s,max}$, has been defined based on the lap-splice strength equation proposed in the ASCE/-SEI 41(ASCE/SEI-41, 2023) document and a modified version of the post-yield strain limit proposed by Tarquini et al. (2017), as follows:

$$\varepsilon_{s,\max} = \begin{cases} 1.25\varepsilon_y \left(\frac{l_b}{l_d}\right)^{2/3}, & \text{if } \frac{l_b}{l_d} \leq 0.716 \quad \text{(elastic range)} \\ \varepsilon_y + 0.65\rho_w + 0.005\frac{l_b}{l_d}, & \text{if } \frac{l_b}{l_d} > 0.716 \quad \text{(plastic range)} \end{cases} \qquad \text{(Eq. 5.2)}$$

Where ε_y is the steel yield strain, l_b is the lap-splice length, l_d is the minimum development length required by the ACI 318-19 code and ρ_w is the confinement reinforcement ratio.

The modeled walls were subjected to a cyclic lateral load in accordance with Figure 5.4, as well as a constant axial load. Dynamic effects were not considered. The lateral loading was applied with a displacement-controlled protocol with increasing amplitudes up to a drift ratio of 3.5%, with two cycles at each drift ratio. The walls were fixed at the base and free elsewhere. The lateral and axial loads were applied to the top nodes of the numerical model, at the height of the wall, 24 feet, as illustrated in Figure 5.4a.

The reinforced concrete walls in this project are subsequently modeled in three parts: the web region, the pilaster regions, and the cap-beam transfer region. The web and pilasters are modeled with the appropriate reinforcement ratios and geometry as previously described. The transfer elements are modeled as linearly elastic concrete truss elements. The different regions are called out in Figure 5.4b. Figure 5.4b also shows the loading configuration of the numerical models: the axial load is applied to the top nodes of the transfer beam while the lateral load is applied at the centroid of the transfer beam.

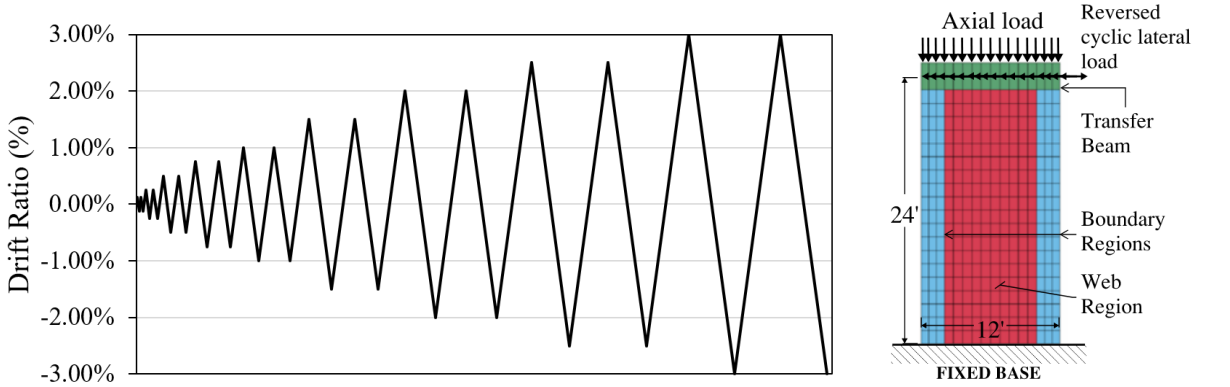

(a) Lateral Loading Protocol (b) Loading Configuration

Figure 5.4: Numerical Model Loading Setup

5.1.2 Mesh Size Effects

To avoid spurious mesh-size sensitivity due to localization, the softening branches of the compression and tension curves are regularized. The value of ε_{cu} is accounting for mesh-size effects based on the notion of concrete fracture energy in compression (Bazant and Planas, 1998), considering a reference length, L_{ref}, which is the weighted length corresponding to each integration point (Coleman and Spacone, 2001). The reference length for the vertical and horizontal web elements is 23.6 inches (600 mm), for the diagonal elements it is 33.5 inches (850 mm) which are reference lengths established by Lu and Panagiotou (2014) based on the side and diagonal lengths used in the unconfined concrete panel study by Vecchio and Collins (1986). The vertical confined concrete reference length is set as 17.7 inches (450 mm) per Deng et al. (2021), which is based on the work done by Mander et al. (1988b) who utilized this gauge length for strain computations of concrete cylinders.

As has already been mentioned, the angle between the horizontal and the diagonal truss elements, θ_d, is calculated using the guidelines proposed by Lu and Panagiotou (2014) and is limited to a range of 45 degrees and 65 degrees. The size of the mesh is determined based on the study done by Deng et al. (2021) which validated several experimental specimens with

the nonlinear truss analogy. They considered numerical modeling ratios of wall length to mesh size ranging from 8 to 20. Two of the experimental cases were explicitly checked for mesh-size sensitivity, and the results showed little to no impact when utilizing a ratio of wall length to element size ratio of 10 versus 20 and another test which utilized ratios 16 to 32.

To ensure mesh-sensitivity would not play a role, and that the strains would be appropriately regularized in the softening regimes, a brief mesh-sensitivity study was performed. Two mesh sizes were considered, motivated by a limiting number of elements spanning a single row along the x-axis of the wall. A value of 18 elements was selected, in keeping with the ranges provided by Deng et al. (2021). A second limiting number of 9 elements along the wall length was selected as the comparison size of half of the original length. The resulting mesh sizes of 16-inches and 8-inches along the x-axis were thus used, which can be seen in Figure 5.5. The comparison of the load-drift curves obtained for the different values of mesh size is provided in Figure 5.6. It can be seen that the load-displacement curves obtained for two different values of mesh size are similar: at 1% drift the peak strengths are within 10% of one another, and at 2% drift, the strength values are within 17% of one another.

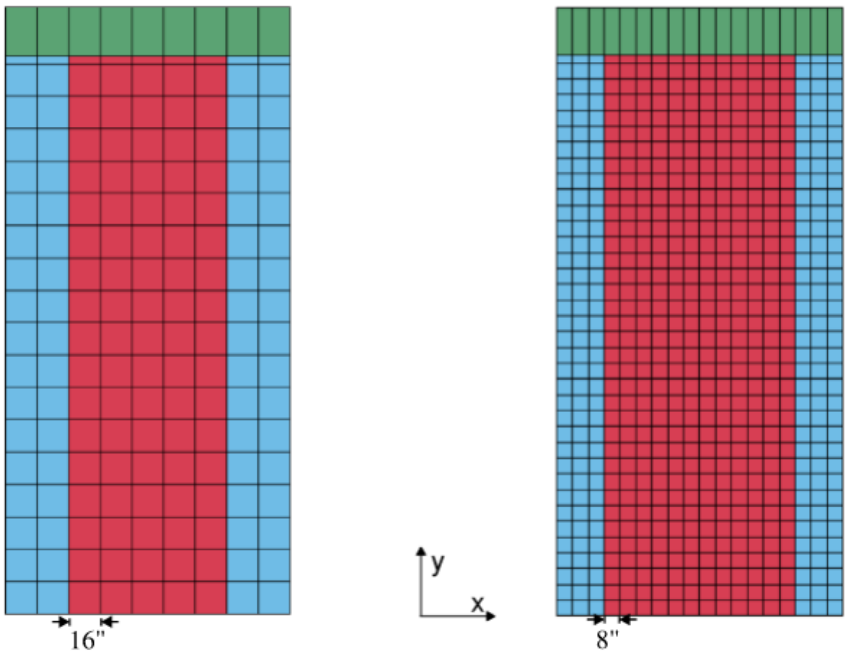

(a) Model with 9 Elements Along X-Axis

(b) Model with 18 Elements Along X-Axis

Figure 5.5: Numerical Models used in a Mesh Size Comparison

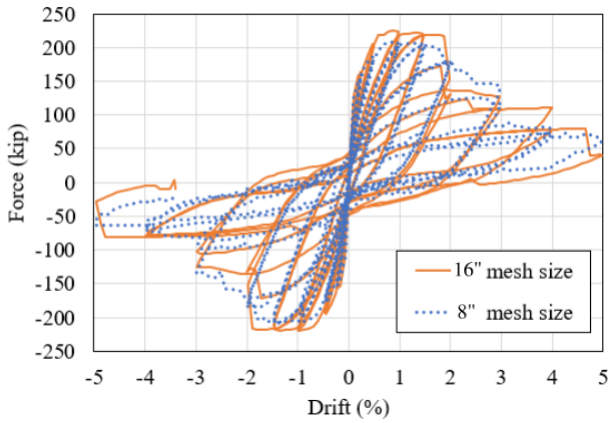

Figure 5.6: Hysteretic Comparison Between the Same Model with Different Mesh Sizes

5.1.3 Modeling of Retrofit Overlays

This section describes the extension of the nonlinear truss modeling approach to incorporate the addition of retrofit overlay strategies for analysis. This is a great advantage of the truss modeling approach in general, that one can adapt it for unique situations with little alteration of the underlying procedure. The extension techniques considered in this project are described below, namely, RC web overlays, and FRP web overlays.

The retrofit techniques applied to the wall are modeled by superposing additional elements representing the RC or FRP overlays, or by modifying the uniaxial concrete or steel properties of the original wall to consider the effect of the FRP jackets. The specific modeling approaches for each retrofit technique are described next.

5.1.3.1 RC Web Overlays

RC overlays are explicitly modeled by superimposing a layer of truss-shell macro-elements on top of the original wall mesh, as can be seen in Figure 5.7. The uniaxial models for concrete and steel used in the overlay are the same as those of the original wall, but they have been calibrated to the specific material properties. Zero-thickness interface elements are used to connect the overlay shell and wall substrate to account for possible slip between the concrete interface. The interface behavior is modeled using a modified version of the constitutive law for concrete interfaces by Palieraki et al. (2014), which considers the adhesive and frictional strength of concrete interfaces as well as the effect of steel anchors. The constitutive law, which is described in detail in Albright et al. (2024), establishes the stress-slip relations in the normal and tangential directions of the interface. The normal stress, σ_n, comprises a stress transferred by the concrete and the stress due to axial resistance generated by steel anchors when the interface dilates. For concrete, a linear tensile softening law is used to represent mode-I, tensile fracture, as shown in Figure 5.8. The tangential shear (bond) stress-slip

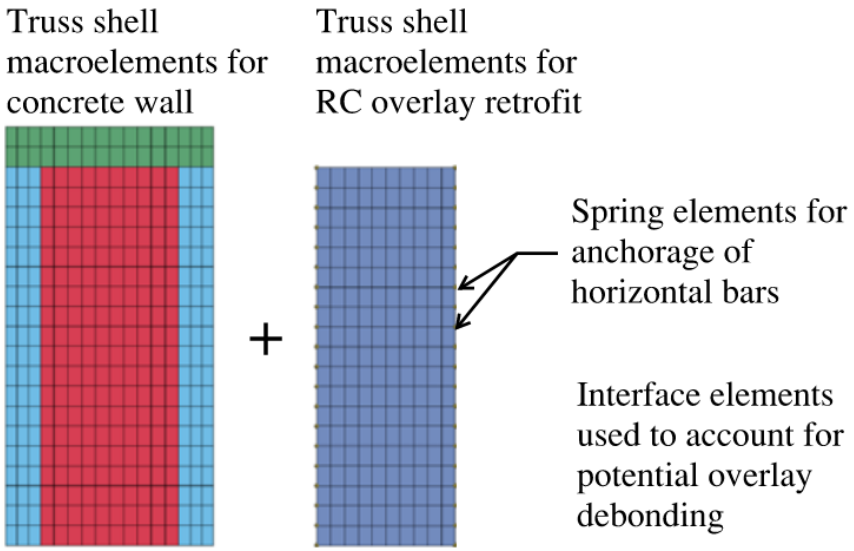

Figure 5.7: RC Shell Overlay Model

response considers the cohesion and frictional resistances of the concrete interface, as well as the shear stress carried by the anchors. The cohesive strength is a degrading function of the tangential plastic displacement, u_t, based on a linear softening law as presented in Figure 5.8. The frictional component is calculated based on the normal stress at the interface multiplied by a friction coefficient μ. Finally, the dilatation of the normal displacement of the interface is defined as a function of the tangential displacement based on the work of Puntel et al. (2006). The interface model is calibrated to the mechanical properties of the concrete and anchoring steel as described in Albright et al. (2024).

In the case of the barbell walls considered in this study, rigid links are provided between the overlay and pilasters at the face where they are in contact. This is done to simulate the bearing of the overlay against the pilaster while in compression, while in tension the connection is also guaranteed by the anchors embedded in the pilaster. The modulus of these rigid links is 29,000 ksi.

The mesh angle of the diagonal element in the truss model of a retrofitted wall is defined

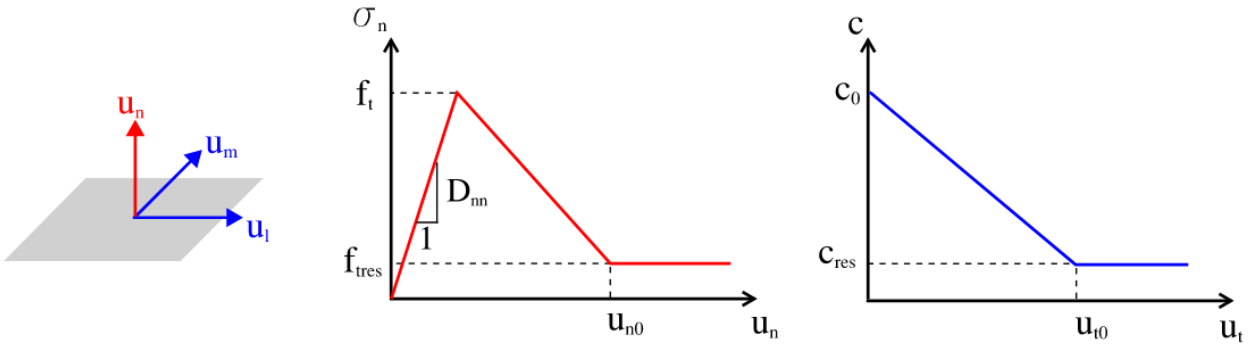

(a) RC Overlay Interface Element Local Axis

(b) Normal Component of Interface Law

(c) Shear Component of Interface Law

Figure 5.8: Softening Laws for Interface Elements (Albright et al., 2024)

using a modified version of the formula proposed by Lu et al. (2016), which considers the contribution of the RC overlay to the shear resistance in Equation 5.3:

$$\theta_d = \tan^{-1}\left(\frac{V_{\max}}{f_{yt}\rho_t t_w L_w + f_{y,to}\rho_{to} t_o L_w}\right) \leq 65^\circ \qquad \text{(Eq. 5.3)}$$

Where V_{max} is the maximum lateral resistance of the retrofitted wall, L_w is the length of the wall, f_{yt} is the yield strength of the shear steel reinforcement, ρ_t is the reinforcement ratio of the shear steel, and t_w is the thickness of the original web, $f_{y,to}$ is the yield strength of steel in the overlay, ρ_{to} is the reinforcement ratio in the thickness of the overlay, and t_o is the thickness of the overlay.

5.1.3.2 FRP Web Overlays

FRP overlays are explicitly modeled by superimposing a layer of shell elements on top of the original wall mesh, which can be seen in Figure 5.9. The shell element representing the FRP comprises an elastic material with low stiffness for the matrix and FRP fibers with a specified orientation. The fibers present an elastic-brittle material response, and its stiffness

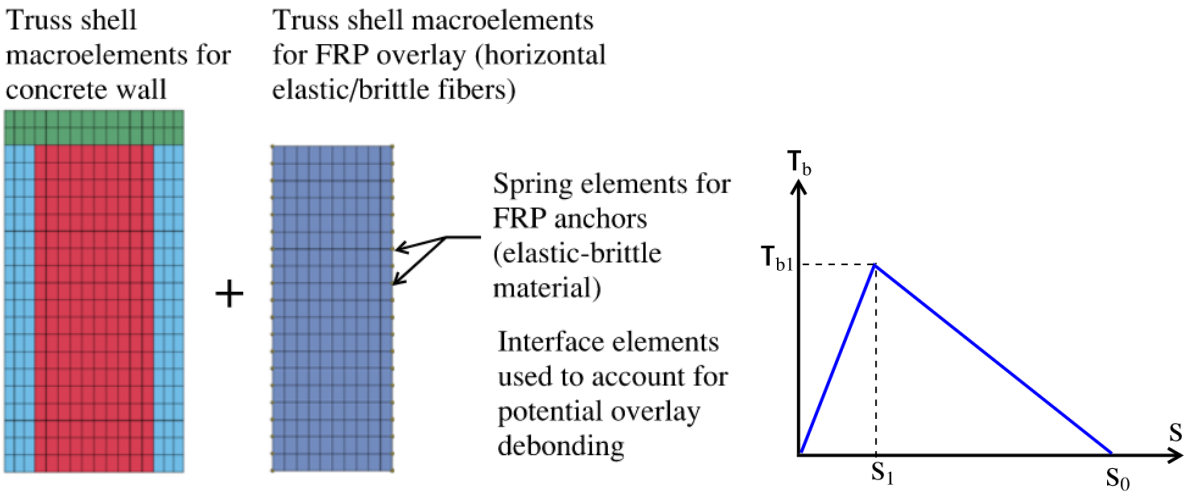

(a) FRP Truss Shell Overlay (Aliasghar-Mamaghani et al., 2024)

(b) FRP Interface Bond fib Bulletin 90 (2019)

Figure 5.9: FRP Overlay Modeling

and ultimate stress are calibrated to match the response of the composite material in the direction of the carbon fibers, per the manufacturer's reported values. For unidirectional FRP composites, the direction perpendicular to the high-strength fibers is also defined as a fiber section but with a lower modulus and lower ultimate stress to represent the tensile response of the epoxy resin alone.

The anchors at the ends of the overlay are simulated through discrete zero-length (spring) elements and are shown in Figure 5.9a. The force-displacement relations that represent the anchors are linear elastic up to failure. The stiffness and ultimate force of the anchors have been determined based on manufacturer data.

Zero-thickness interface elements are used to connect the overlay and wall substrate to account for the potential debonding between the FRP and the concrete substrate. The interface elements are shown in Figure 5.9a for the case of shear web strengthening; the overlay and the interface elements in this case are only shown on the web region. The interface bond-slip response is modeled using the bilinear bond stress-slip law defined in fib Bulletin 90 (fib

Bulletin 90, 2019), which can be seen in Figure 5.9b. The maximum bond strength, τ_{b1}, the slip at the peak, s_1, and the slip after complete bond deterioration, s_0, in Figure 5.9b are determined based on the recommendations of fib Bulletin 90. For carbon FRP (CFRP) sheets, the mean values of these parameters are $\tau_{b1} = 0.72\sqrt{f_{cm} f_{ctm}}$ MPa, $s_1 = 0.0107$ mm, and $s_0 = 0.24$ mm.

The mesh angle of the diagonal component of the truss model of a retrofitted wall is defined using a modified version of the formula proposed by Lu et al. (2016), which considers the contribution of the FRP overlay to the shear resistance in Equation 5.4:

$$\theta_d = \tan^{-1}\left(\frac{V_{\max}}{f_{yt}\rho_t t_w L_w + \Psi_f V_f}\right) \leq 65^\circ \qquad \text{(Eq. 5.4)}$$

where $\Psi_f V_f$ is the shear strength contribution of the FRP overlay calculated using the formula proposed in ACI 440.2R-23 ACI 440 Committee (2023).

5.2 Modeling Comparison for Unretrofitted Walls

Two walls in the experimental study, S1 and S2, were not retrofitted and served as 'control' specimens for subsequent tests. The first unretrofitted specimen, S1, did not contain a lap splice, while the second unretrofitted specimen, S2, did have a lap splice. For more details of the specific geometric configuration and internal steel configuration see Section 3.2.2.1 and Section 3.2.2.2.

5.2.1 Specimen S1

Specimen S1, the unretrofitted control without a lap splice, was modeled twice: once prior to the physical experimental test and another model was modified and run after the experi-

mental test. The pre-test analysis was meant to provide an estimate of the anticipated peak capacity and damage pattern. The peak-capacity prediction was necessary to ensure the adequacy of various test fixtures (reaction frames, base anchorage, etc.). The comparison of the pre-test load-drift curve with the experimental observation is presented in Figure 5.10. The same figure provides the maximum principal strain contour plot at the end of the pre-test analysis, at 1.4% drift ratio. The analysis was satisfactorily capable of predicting the final failure mode and the peak capacity. The latter was underestimated by 10%, due to the fact that the concrete compressive strength and the grade 60 reinforcement yield strength in the actual sample were slightly higher than the values assumed in the analysis.

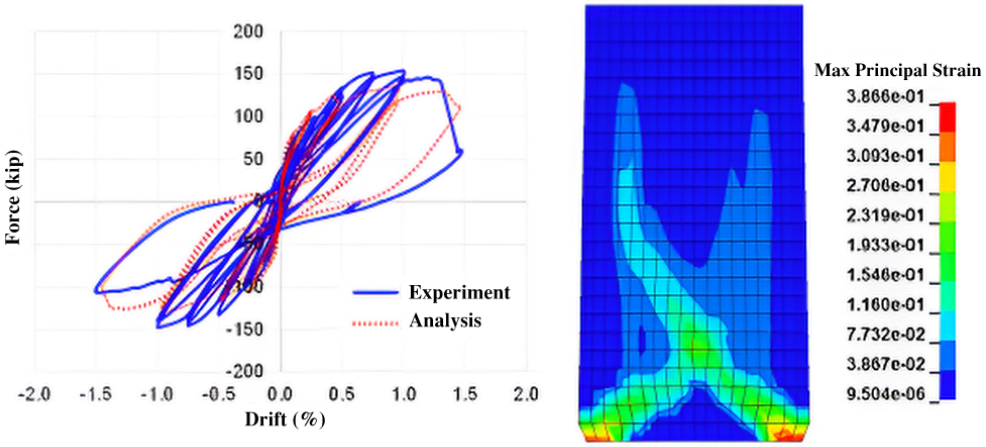

(a) Hysteretic Force vs. Drift Curves from Experimental Results and Analytical Results

(b) Maximum Principal Strain Contour Plot

Figure 5.10: S1 Pre-Experiment Analysis Results

This analysis was repeated after the experimental test with the actual measured material strength values; this analysis gave an extremely faithful match to the damage pattern and the load-displacement curve and was meant to gain further insights into the experimental test. These results can be seen in Figure 5.11, where again the principal strain contour plot

is shown at the peak drift ratio reached in the experiment. The failure mode of this specimen can clearly be seen with the large localized crack and the rupture of several horizontal shear bars along this opening. These results validate the predictive capability and accuracy of the employed analysis approach.

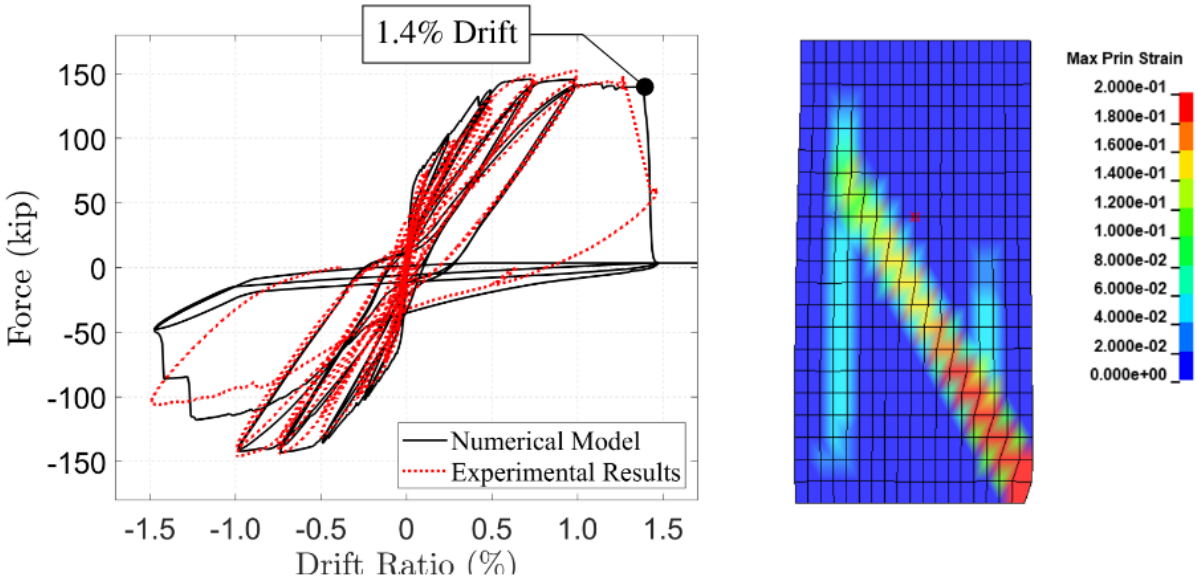

(a) S1 Numerical vs. Experimental Hysteretic Curves: Post-Experiment

(b) S1 Numerical Model principal Strain Contour Plot

Figure 5.11: S1 Numerical and Experimental Results and Contour Plot

It is interesting to compare the measured strains from the experiment with the analytically achieved strain values in the model. For example, the peak horizontal strain from the web shear steel in the experiment, as well as the average strain calculated from the horizontal string pots mounted on the specimen web. The peak strain values from the rebar will be much more localized and are highly dependent on the crack locations. The average strain in the web is a more general parameter which inherently describes an average value across the length of the web. These values are shown in Table 5.1. The peak strains align well for the 0.75% drift ratio, but the alignment diverges beyond that point.

Table 5.1: S1 Horizontal Strains: Experimental and Numerical

Target Drift (%)	Experiment: Peak average horizontal strain	Numerical Model: Peak horizontal strain
0.50%	0.0080	0.0010
0.75%	0.0173	0.0203
1.00%	0.0218	0.0354
1.50%	0.0728	0.3420

The vertical strains are interesting to note in the end regions, where the main contribution of the vertical steel should take most of the flexural demand in the structure. A comparison between the measured peak strains of the vertical pilaster reinforcement and the analytical model peak strains from the same region can be seen in Table 5.2

Table 5.2: Comparison of Experimental and Numerical Model Strain Values at Different Target Drifts for Specimen S1

Target Drift (%)	Experiment: Peak vertical pilaster reinforcement strain	Numerical Model: Peak vertical strain
0.50%	0.005	0.003
0.75%	0.014	0.007
1.00%	0.015	0.010
1.50%	0.008	0.010

The shear strains are calculated per Appendix B, utilizing the string-pot measurements from the web of the wall. The shear strains of the web are the main contributing factor, as the end regions do not exhibit much shear deformation, but rather flexural deformation. A comparison between the measured peak shear strain of the web and shear strain in the analytical model in Table 5.3. The shear strains are in very good agreement at low levels of deformation. The higher levels of shear deformation are not well captured by the experimental analysis which has discrete measurement locations. As the damage localizes, if the measurement devices are not installed in perfect position to capture this inelastic behavior,

Table 5.3: S1 Shear Strains: Experimental and Numerical

Target Drift (%)	Experiment: Peak shear strain in the web	Numerical Model: Peak shear strain
0.50%	0.008	0.008
0.75%	0.018	0.015
1.00%	0.008	0.025
1.50%	0.031	0.194

the resulting measurements are not easily comparable.

5.2.2 Specimen S2

Specimen S2 had a lap splice and the numerical model was able to adequately capture this failure through the definition of a bond-slip law. The numerical specimen failed at a drift ratio of 0.9%, which is slightly higher than the experimental failure which occurred at 0.75% drift. Figure 5.12 shows the hysteretic curves of the experimental specimen and the numerical model. The two curves are generally in good agreement in terms of stiffness degradation. The initial stiffness is also slightly underestimated in the model. This can likely be attributed to the slightly higher concrete and steel material properties than anticipated of the experimental specimen.

The ability of the truss model to capture the lap splice slip is shown through the stress and strain measurements of the toe node in the numerical model, noted in Figure 5.12b as element 17. The stress of the vertical fiber element (representing the reinforcement steel) is shown versus the drift ratio, with the point at which the strain limit for bond slip is exceeded is shown. The similar point of strength degradation is noted on the stress versus strain graph in subfigure b of Figure 5.13. This is compared with the measured strains from the experimental specimen. The strains for the internal bars of the pilasters, SG2, reach levels of 0.012, associated with a sharp jump associated with strength degradation. This is

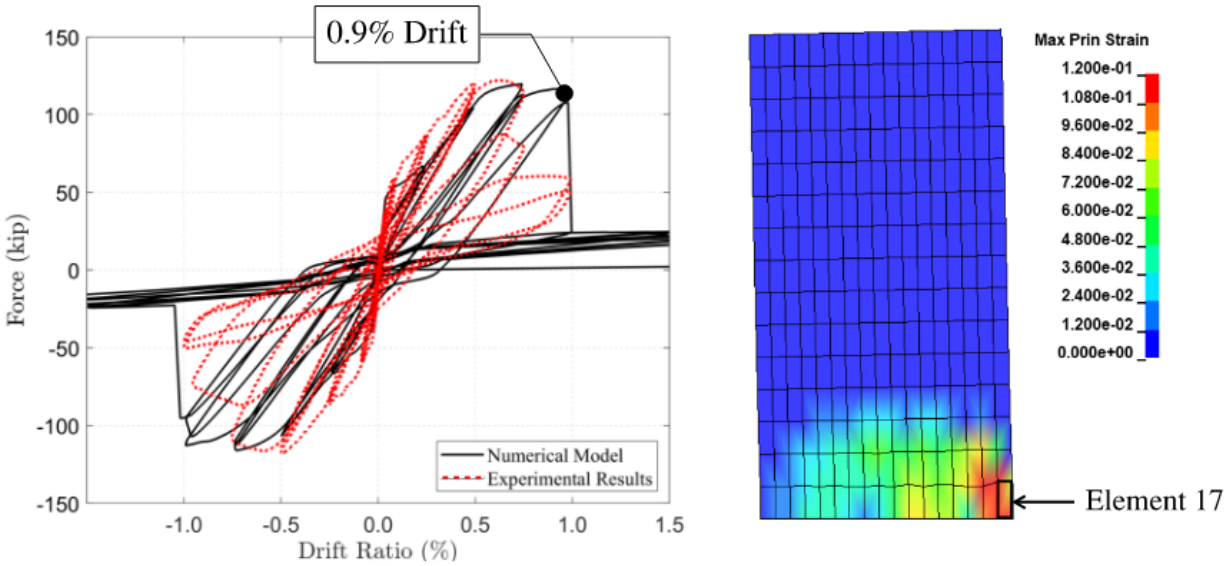

(a) S2 Numerical vs. Experimental Hysteretic Curves

(b) S2 Numerical Model Principal Strain Contour Plot

Figure 5.12: S2 Numerical and Experimental Results and Contour Plot

very close to the assumed value of ultimate strain in the lap splice numerical definition of 0.0127.

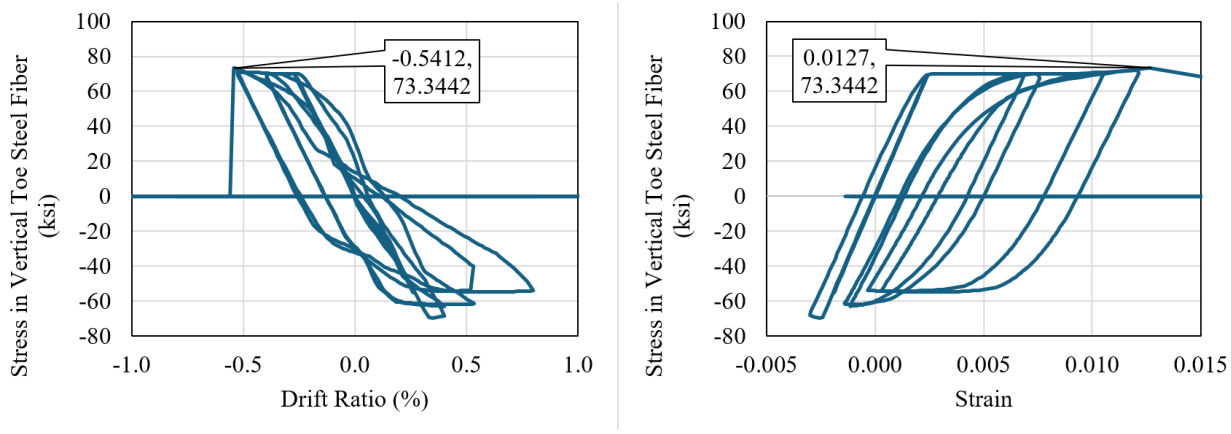

(a) Stress versus Drift Ratio, Loss of Strength Point Called Out

(b) Strain versus Drift Ratio, Loss of Strength Point Called Out

Figure 5.13: Numerical Model Vertical Stress in Steel Fiber for Toe Element for Specimen S2

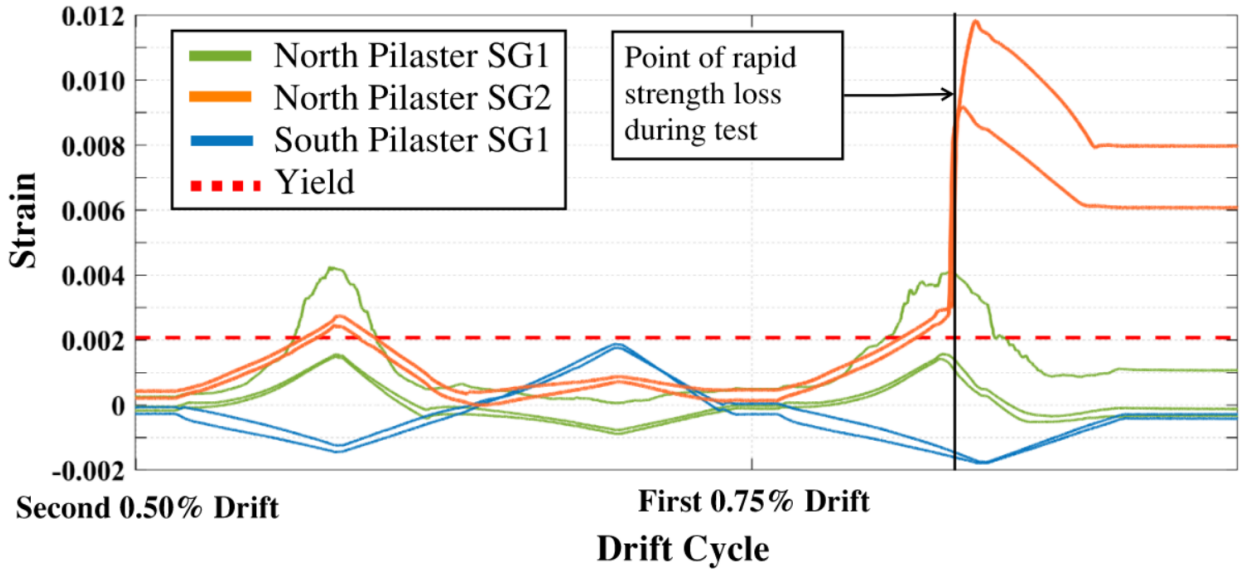

Figure 5.14: Experiment Vertical Pilaster Rebar Strain for Specimen S2

5.3 Modeling Comparison for Walls Retrofitted with Web Shear Strengthening

5.3.1 Specimen S1CW

An analysis was performed using the truss modeling approach, described at the beginning of this chapter, for the retrofitted specimen S1 with the one-sided concrete overlay in the web region. The values for the interface laws used are as follows: $c_o = 1$ MPa (0.290 ksi), $\mu = 0.5$, $f_t = 0.5$ MPa (0.145 ksi). In alignment with the strengthening strategy and the experimental results, this specimen was expected to reach a drift ratio of 2% before exhibiting strength degradation. This was indeed the case, as can be seen in Figure 5.15, which shows the hysteretic curves of both the experimental results and the numerical model. The maximum principal strain contour plot at the instant of a positive drift ratio of 2.5% indicates the ultimate formation of localized diagonal cracks in the center of the web, localized vertical cracks in the vicinity of the web-to-pilaster interfaces, and significant distortion in the vicinity of the toe of the pilaster. The experimental specimen similarly exhibited diagonal web cracking, as well as local toe damage due to bar buckling and concrete crushing web at this point. The strength degradation is well captured by the numerical model.

The discreet springs, which anchor the overlay to the wall substrate at the pilaster interface, exhibit low levels of strain. The maximum values of strain exhibited in the specimen are found at the base of the model, at the bottom two most nodes. A graph of the horizontal strains from these two bottom nodes is shown in Figure 5.16. It can be seen that yielding is barely exceeded for the retrofit shear steel bars at the interface.

The relative slip between the overlay and the underlying substrate can be seen from Figures

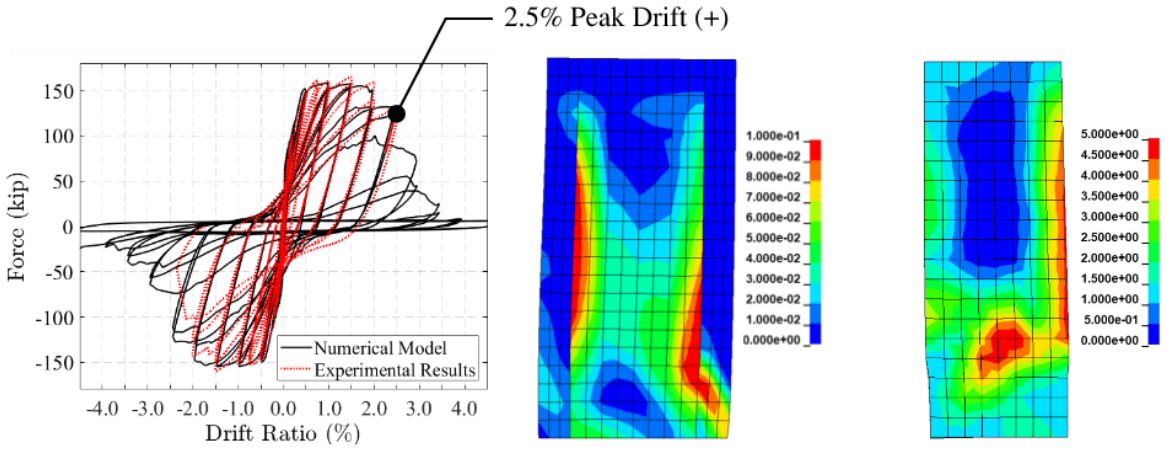

(a) Load-drift Hysteretic Curve, Numerical and Experimental

(b) Maximum Principal Strain Contour at 2.5% drift

(c) Contour of Slip (in mm) Between Overlay and Wall Concrete at 2.5% Drift

Figure 5.15: Analysis Results for Concrete Retrofitted Wall Specimen, S1CW

5.17a and 5.17b by considering their differences. The overlay elements at the base of the model are particularly interesting, as they indicate a difference between the two surfaces, indicating some value of slip. The de-aggregated x and z displacements can be seen in Figure 5.18.

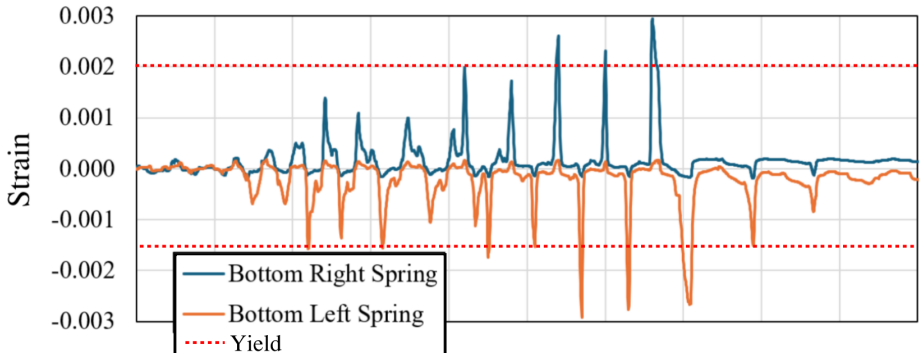

Figure 5.16: Strain Plots Over Time for Horizontal Spring Elements Exhibiting The Highest Demand In Specimen S1CW

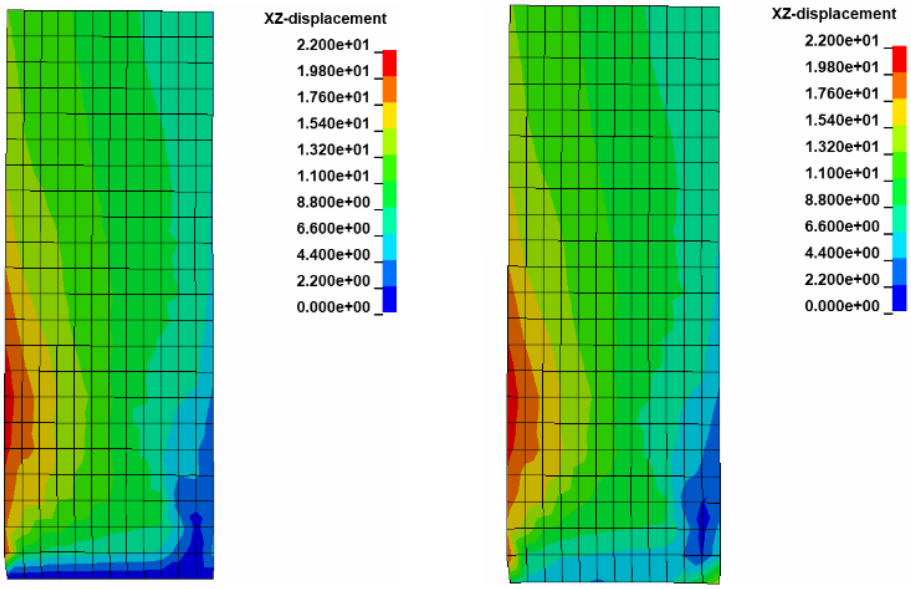

(a) Concrete Substrate in the Web (b) Retrofit Overlay in the Web

Figure 5.17: Numerical Model XZ-Displacement of 0% Drift Immediately After Final 2.5% Loading Cycle of Specimen S1CW

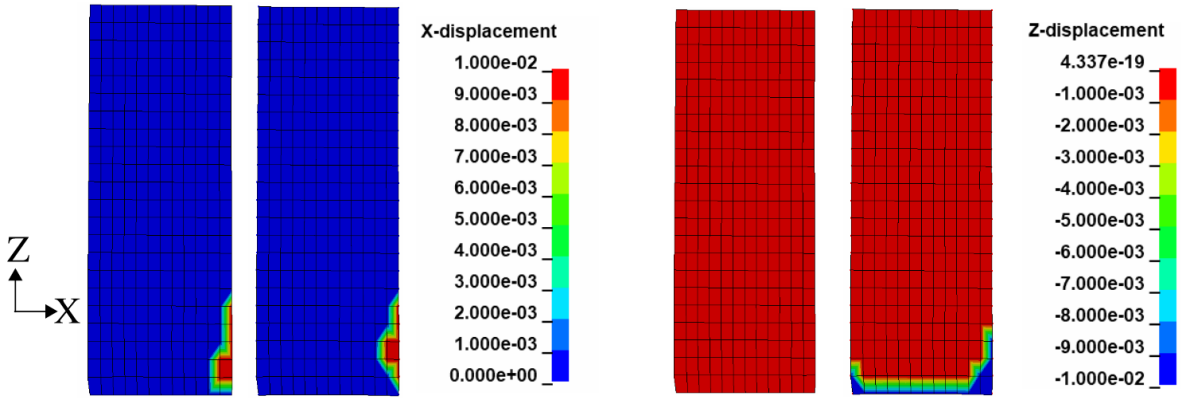

(a) Positive and Negative X-Displacement of Web Substrate (left) and Web Overlay (right)

(b) Positive and Negative Z-Displacement of Web Substrate (left) and Web Overlay (right)

Figure 5.18: De-aggregated Numerical Model Displacement from Figure 5.17

5.3.2 Specimen S1FW

In this section, the numerical analysis of the retrofitted specimen with a one-sided FRP shear strengthening, S1FW, is discussed. The load-displacement curve from the cyclic truss analysis is compared to the experimental hysteretic curve in Figure 5.19. The truss model provided a satisfactory reproduction of the hysteretic response, including the degradation of the strength. The truss model gave an overestimation of the inelastic deformability, as it exhibited degradation during the second load cycle at a drift ratio of 3%, when in reality the experiment experienced significant strength degradation during the second cycle of 2.5% drift. Note the specimens exhibit a residual capacity, consistent with the definition of residual strength described in the concrete model.

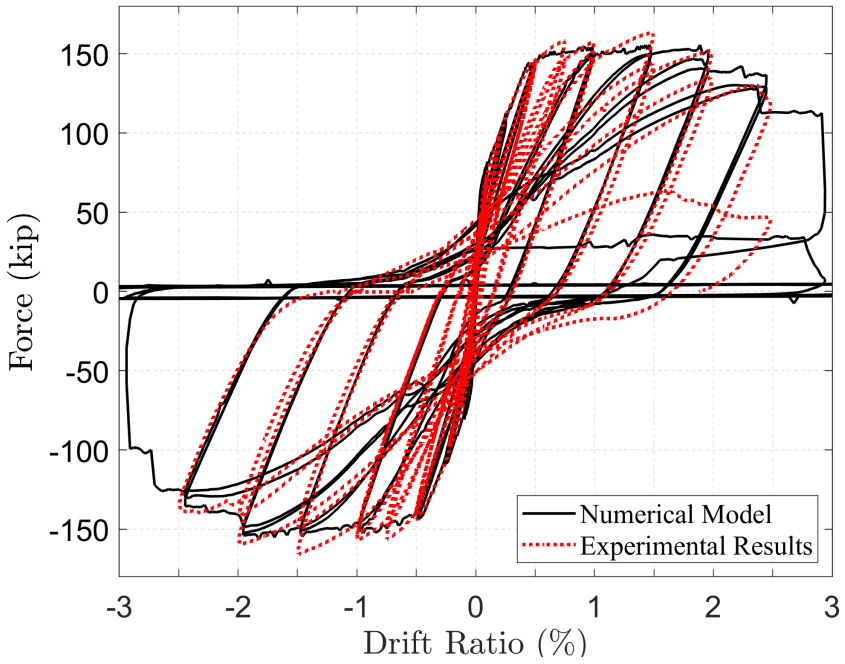

Figure 5.19: S1FW Numerical vs. Experimental Hysteretic Curves

The maximum principal strain contour plots shown in Figure 5.20 indicate the concrete substrate and the associated FRP overlay strain levels at drift ratios of 2% and 2.5%. The plots show an essentially flexure-controlled response due to degradation at the toe of the

specimen at the 2% drift ratio, which is associated with the peak strength in the cycle directly prior to strength degradation. This is consistent with the results of the experimental specimen, which had failure at the 2% drift ratio associated with toe concrete crushing and bar buckling. There was minor delamination of the FRP on the lower web of the specimen during this cycle as well. The same contour plot at 2.5% drift ratio indicates extensive shear-crushing failure at the toes of the pilasters and at the base of the web. This result could likely be improved with further calibration of the interface element. The experimental specimen exhibited major FRP delamination at this drift ratio coincident with anchor pullout. Furthermore, the numerical model failed to capture the localized diagonal cracks at the base of this specimen during this final drift ratio. It is anticipated that the appropriate capture of the strength degradation and the failure mode (i.e. FRP delamination, coincident with additional web shear failure) could be improved in the numerical model with further calibration of the interface and spring elements.

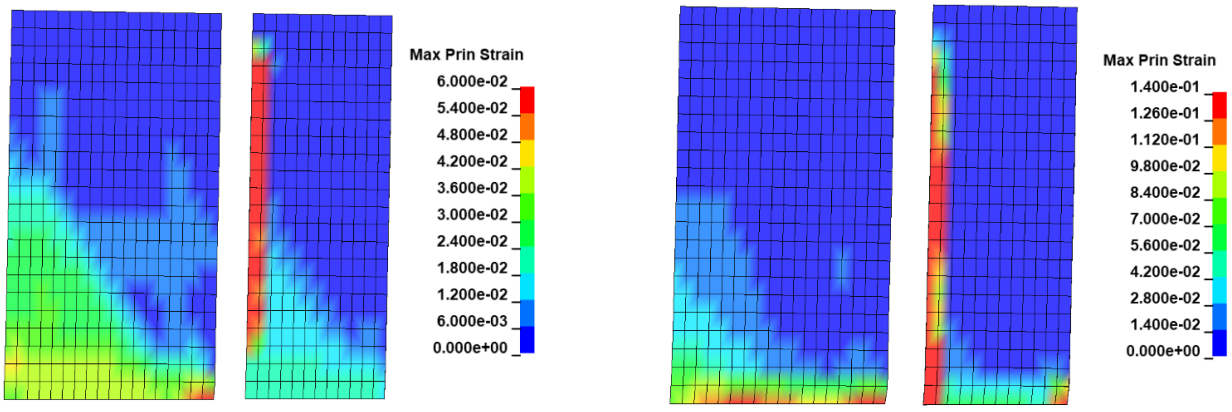

(a) 2.0% Drift (b) 2.5% Drift

Figure 5.20: Numerical Analysis Principal Strain Contour Plots for FRP Overlay and Concrete Substrate, Specimen S1FW

The ability of the model to capture the anchorage of the overlay is shown in Figure 5.21. The highest strains exhibited in the springs are at the base of the wall. The horizontal strain

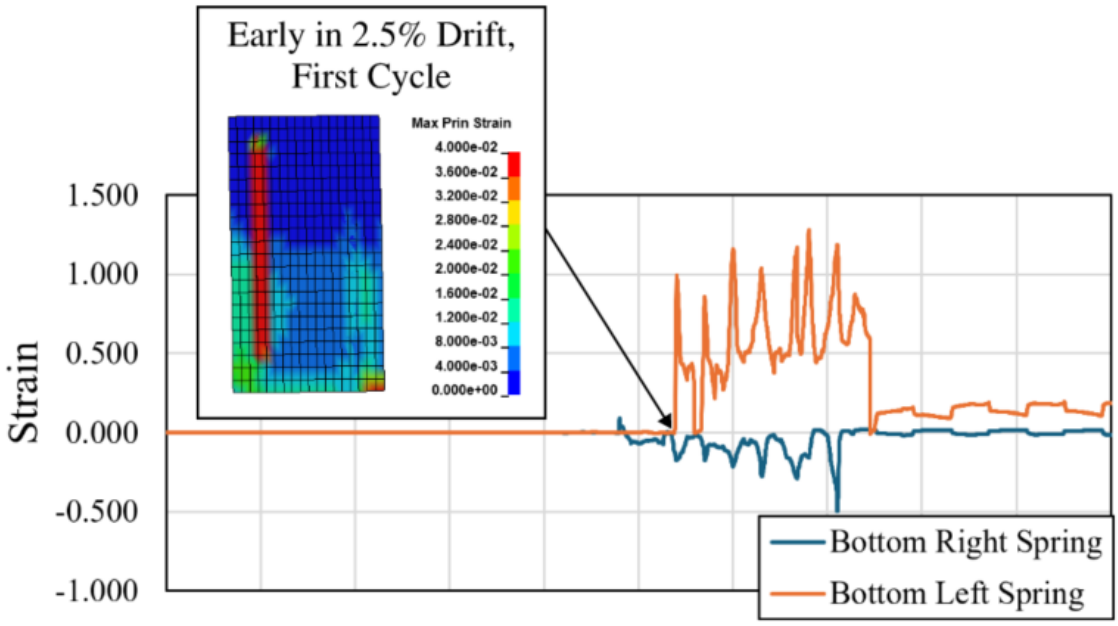

Figure 5.21: Strain Plots Over Time For Horizontal Spring Elements Exhibiting The Highest Demand In Specimen S1FW

has a rapid change in strain during the initiation of the first cycle of the 2.5% drift ratio. The corresponding global behavior in terms of the maximum principal strains are shown in the figure as well, to showcase how the highest demand in the structure is indeed along the intersection of the web and pilaster interface at the point where the strains start to reach maximum levels. The strains remain relatively small (<0.014) up until this point. The corresponding overlay strain and substrate strain can be compared with the strains shown in Figure 5.20b at the peak drift of 2.5%.

The shear stress contour plot for the FRP overlay elements is shown for the progression of 1.5% drift, 2.0% drift and 2.5% drift in Figure 5.22. This progression follows the experimental progress as well, which was ultimately characterized by the lower portion of the web FRP delamination at earlier drifts, followed by the anchor pullout coincident with full FRP web delamination at the 2.5% drift ratio.

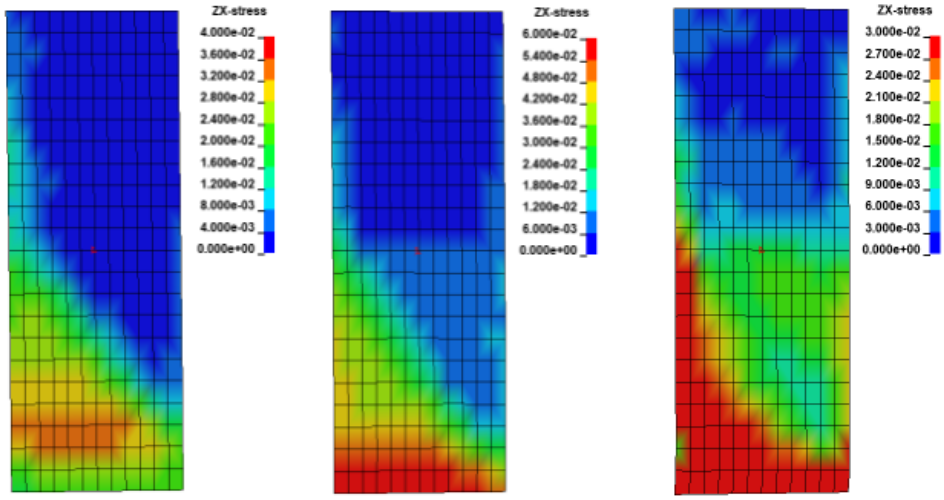

(a) 1.5% Drift (b) 2.0% Drift (c) 2.5% Drift

Figure 5.22: Shear Stress Contour Plot for the FRP Overlay

5.4 Modeling Comparison for Walls with End Wrapped Strategies and Shear Strengthening

5.4.1 Specimen S1FP

The successful implementation of the shear strengthening strategy in S1FW motivated the retrofit strategy of this specimen, S1FP. This specimen was wrapped in the web region identically to specimen S1FW to enhance the shear strength of the web, but the pilasters were wrapped with additional FRP fabric and anchors to delay bar-buckling. The specimen was modeled with the same modeling procedure as described in the beginning of this chapter. The FRP overlay was implemented over the entire specimen, including the web and the pilasters. The bond between the FRP and the end pilasters was assumed to be perfectly bonded because of the quantity of the FRP wrap. The peak strain exhibited during the experimental test by the end-wrapped FRP was 0.006 which occurred at a 2% drift ratio. The design values provided by the manufacturer for the modulus of elasticity were used in the model.

The failure in the model was dominated by the crushing of the diagonal web concrete coincident with the rupture of the vertical bar. This occurred at a drift ratio of 2.5%. The truss model does not capture the localization of vertical steel strains and earlier bar ruptures as seen in the test, which resulted in a delayed strength degradation in the numerical results, which can clearly be seen in Figure 5.23. Note the numerical analysis exhibits residual capacity, consistent with the definition of residual strength described in the concrete model.

The principal strain contour plot at the 2% drift ratio and the 2.5% drift ratio can be seen in Figure 5.24.

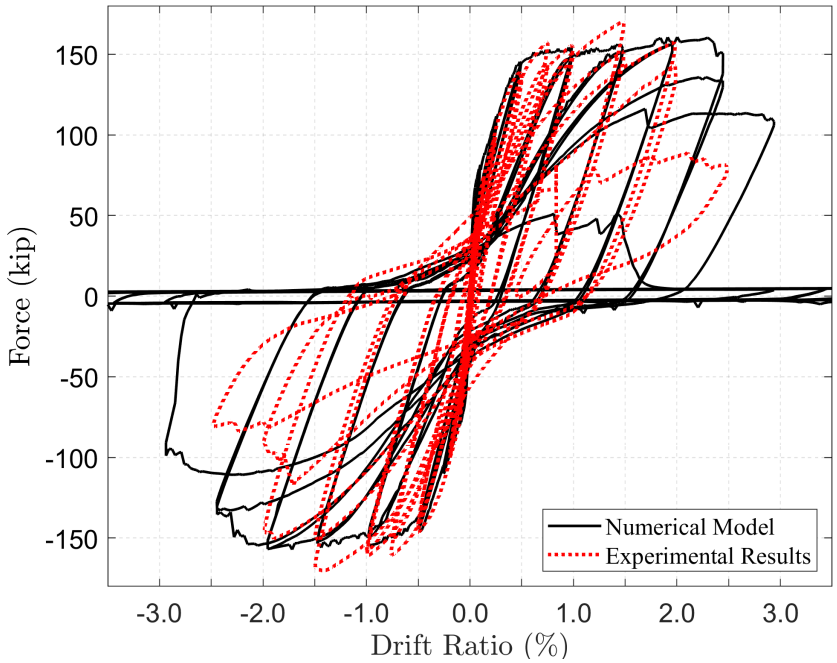

Figure 5.23: S1FP Numerical vs. Experimental Hysteretic Curves

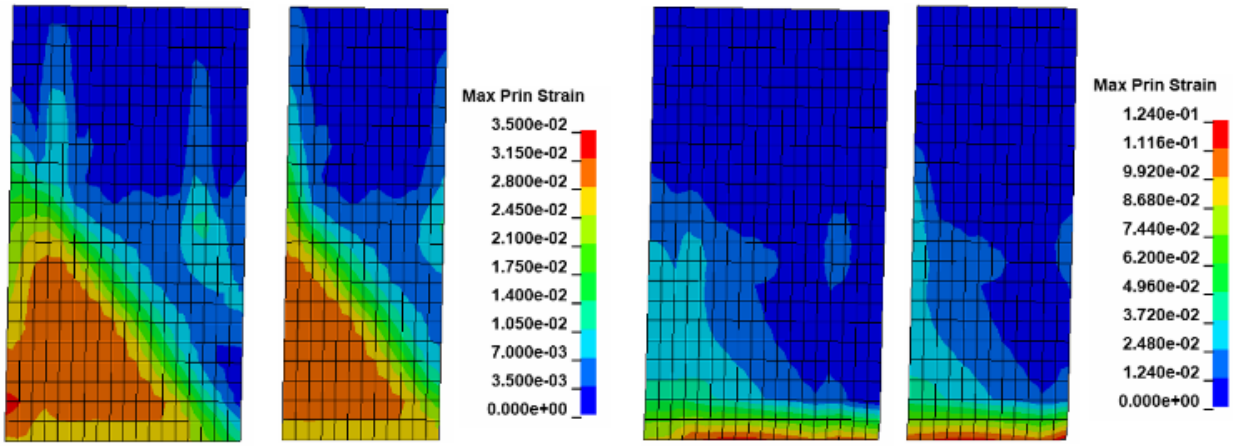

(a) 2.0% Drift (b) 2.5% Drift

Figure 5.24: Numerical Analysis Principal Strain Contour Plots for FRP Overlay and Concrete Substrate, Specimen S1FP

5.4.2 Specimen S2FL

The numerical model of specimen S2FL, which has the FRP retrofit strategy including prevention of lap splice slip and shear web strengthening, is compared with the experimental results as can be seen in Figure 5.25. Once again, this numerical model uses a layer of overlay elements and a layer of zero-length interface elements. The FRP around the end regions was assumed to have perfect bond due to the high levels of wrapping. The peak rupture strain exhibited by the FRP was 0.008. The numerical model was faithfully able to capture the delay of the lap splice slip through an effective clamping of the pilaster, up to a drift of approximately 3%. The failure in the model is initiated by vertical bar rupture, which is also consistent with the experimental results. The numerical model, however, reaches a higher drift ratio than the experimental specimen as can be seen in Figure 5.25. The numerical model does not capture the localized high vertical strains in the pilasters that was observed during the experimental test. This is likely due to the vertical strength due to the epoxy laminating the FRP to the wall, which provides some non-negligible resistance in the vertical direction. Additionally, the 'patch' overlay component meant to sandwich the FRP fiber anchors was installed vertically above 30 inches. This may have had a non-negligible strengthening effect on the longitudinal strength of the end regions, also resulting in higher strains at the base where the crack localized.

The maximum principal strain of the concrete substrate and the FRP overlay are shown in Figures 5.26 and 5.27.

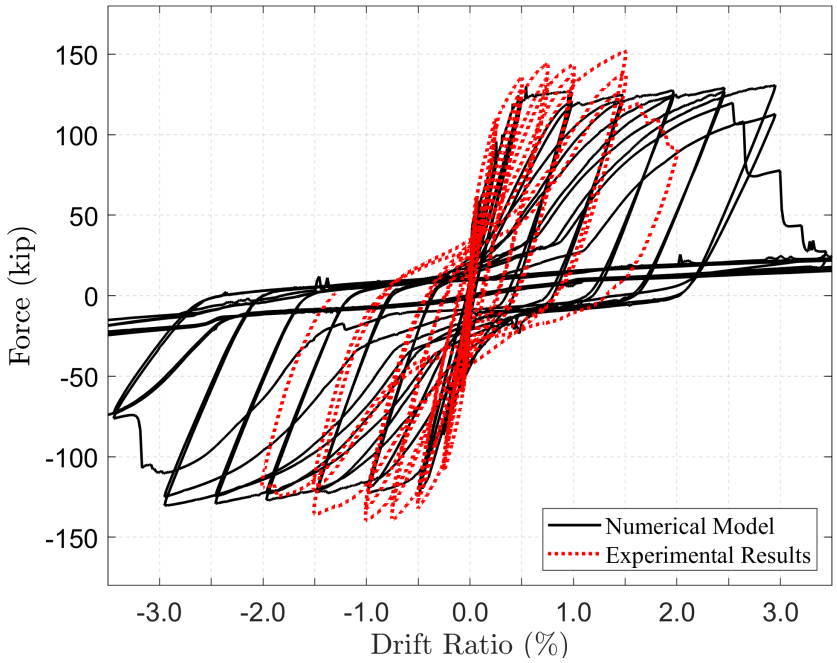

Figure 5.25: S2FL Numerical vs. Experimental Hysteretic Curves

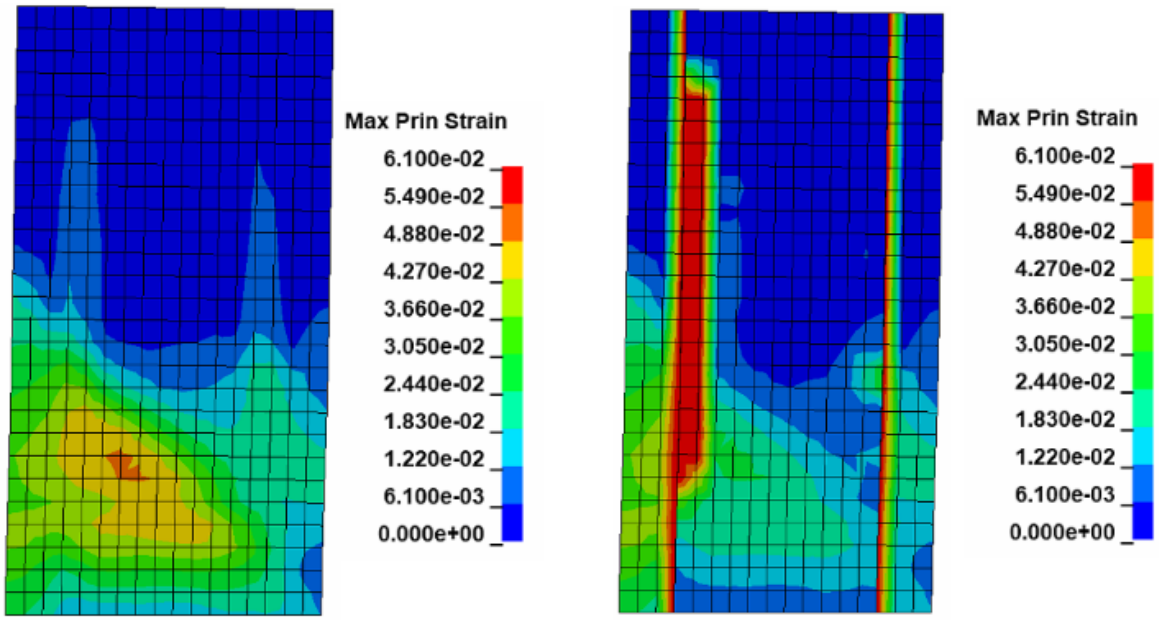

(a) Concrete Substrate (b) FRP overlay

Figure 5.26: Numerical Principal Strain Contour Plot at 2% Drift for Specimen S2FL Bar Buckling Prevention

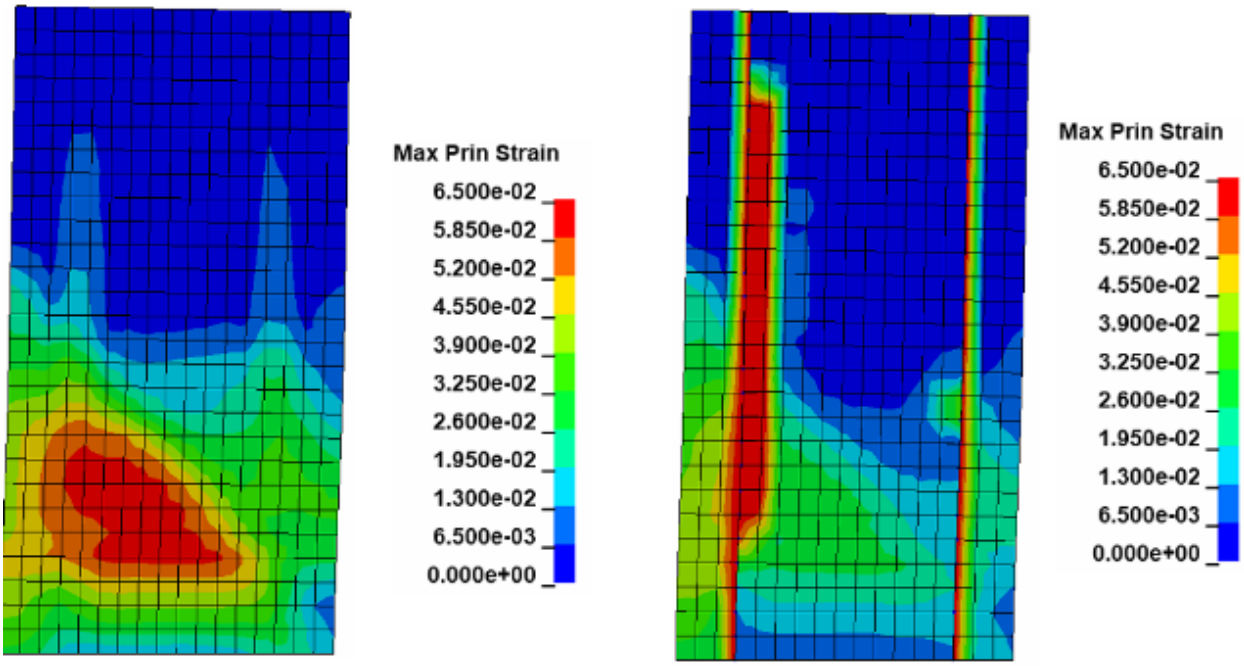

(a) Concrete Substrate (b) FRP Overlay

Figure 5.27: S2FL Numerical Principal Strain Contour Plot at 2.5% Drift

5.5 Modern Design Comparison and Discussion

This section provides an overview of the design and modeling considerations for a comparative study of a modern structural wall to the unretrofitted non-ductile and retrofitted non-ductile experimental results. A prototype RC structural wall was designed with current ACI-318 seismic provisions for special RC structural walls. This structure was designed with a targeted flexural strength equivalent to the flexural over-strength demand observed in the experimental retrofitted specimen.

Three distinct detailing scenarios for the RC structural walls were evaluated: unretrofitted non-ductile walls, non-ductile walls with a web shear retrofit overlay, and ductile special RC structural walls. The special ductile RC wall was designed in accordance with ACI-318 detailing requirements for seismic loads for the associated shear demand. The resulting reinforcement ratios of the boundary elements are as follows: $\rho_l = 1.8\%$ for longitudinal steel and $\rho_t = 0.7\%$ for transverse (confining) steel. The web region requires reinforcement ratios of $\rho_l = \rho_t = 0.4\%$. This can be seen in Figure 5.28. This design was numerically modeled using the nonlinear truss analogy, extensively discussed in this chapter, and a hysteretic curve was established for the ductile special RC wall.

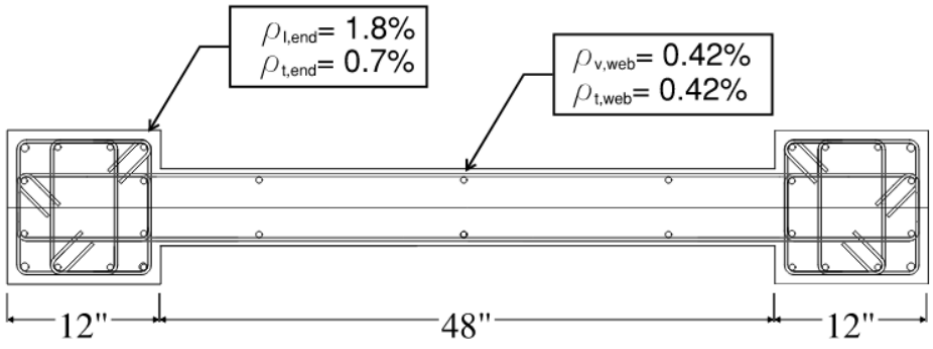

Figure 5.28: Modern Wall Design Details

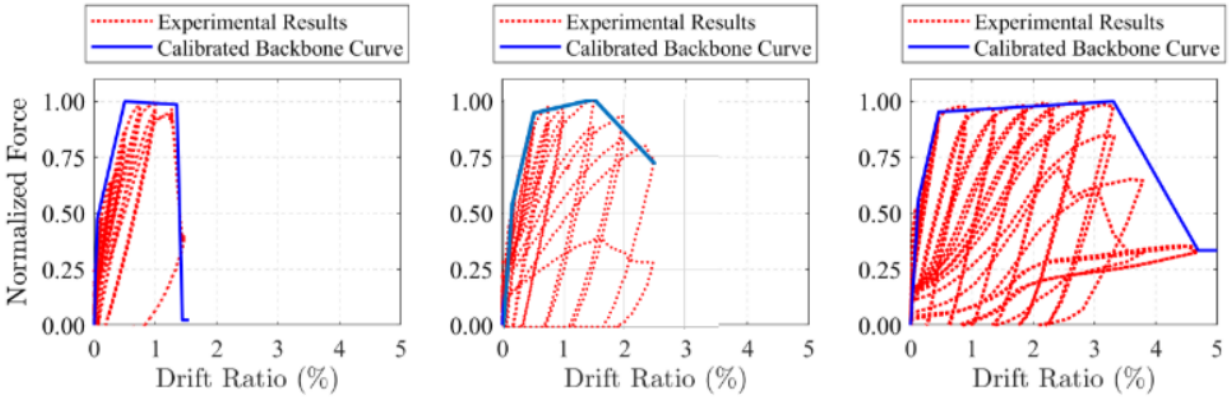

(a) Unretrofitted Specimen (b) Shear Strengthening Retrofit Specimen (c) Modern wall

Figure 5.29: Hysteretic and Associated Backbone Curves in Accordance with ASCE-41

From the three hysteretic curves from the three walls, (experimental unretrofitted non-ductile, experimental retrofitted non-ductile, and numerical ductile special), normalized backbone curves are derived. Figure 5.29 shows the normalized backbone curves for the force-deformation response.

The ductility can be easily evaluated for these specimens, as defined previously in Chapter 4, based on the work by Park (1989). The quotient of the ultimate deformation (associated with 10% strength loss) and the effective yield point gives the ductility. Table 5.4 showcases the ductility comparisons for the three walls, based on their backbone curves. The modern structure is nearly twice as ductile as the retrofitted specimen. Which in turn is nearly twice as ductile as the unretrofitted non-ductile specimen. Note that these comparisons are made for singular components, namely RC structural walls, and may showcase a different outcome when considered as part of a full building system.

Table 5.4: Ductility Comparison for Backbone Curves of Non-Ductile Retrofitted, Non-Ductile Retrofitted, and a Ductile Special Wall

Wall	Ductility, μ
Unretrofitted Non-Ductile Wall	2.53
Retrofitted Non-Ductile Wall	4.63
Ductile Special RC Wall	9.38

Chapter 6

Parametric Study Considering Strain-Based Criteria for Seismic Assessment

6.1 General

This chapter outlines the numerical analysis undertaken as part of this dissertation work. The main motivations of this analysis are twofold: 1) to investigate the ability of a strain-based criteria to consistently capture key points on the envelope force-deformation curve for RC walls and 2) to compare current guidelines provided by ASCE/SEI-41 (2023), hereafter referred to as ASCE-41, for older reinforced concrete (RC) walls with the strain-based criteria, with the intent to propose an acceptable method for analysis of RC walls to be adopted in ASCE-41. To accomplish these goals, a parametric study was conducted to evaluate a wide range of archetypal RC walls built in California pre-1970s. This resulted in the consideration of 200 unique wall configurations, considering variable end-region reinforcement, web-region reinforcement, web thickness, applied axial loads, and end-region stirrup spacing. The results of this parametric analysis showcase the ability of the strain-based assessment to capture the expected degradation of these structures well, with a more generalized approach than what is provided by current guidelines.

The current standard for seismic evaluation and retrofit of existing buildings in the United States is ASCE-41 which incorporates performance-based engineering concepts and methods. This standard establishes a 3-tier evaluation framework, with the various tiers corresponding to increasing levels of scrutiny and accuracy. The Tier 3 procedure relies on linear or nonlinear analysis of a computational model of the structure to determine the capacity and compare it with the seismic demand. The nonlinear static procedure (NSP), which is the focus of the present study, is allowed for all existing structures which do not have significant contributions from higher mode-shapes. The NSP requires developing a detailed numerical model of a structure, including appropriate considerations for expected material properties, mass, stiffness, torsion, soil-structure interaction, and p-delta effects. Furthermore, strength and stiffness degradation of all lateral force-resisting components must be explicitly modeled through distributed or lumped plasticity models with generalized load-deformation curves. Although the peak resistance in these load-deformation relations is defined on the basis of principles of structural mechanics, most of the other curve parameters have been obtained empirically from experimental data. Some of this experimental data is extremely limited.

Once the structure has been appropriately modeled, the NSP dictates the model be subjected to a monotonically increasing lateral load until a target displacement is exceeded, at which point quantitative values of acceptance criteria are used to assess structural and non-structural components. For RC structural walls, the evaluation is differentiated based on parameters related to internal reinforcement detail, applied axial loads, and the expected controlling behavior (flexure, shear, or shear-friction). According to ASCE-41, a flexurally controlled RC wall may be deemed acceptable if the overall plastic hinge rotation is less than a prescribed threshold value for the each performance objective of the structure. ASCE-41 provides acceptance criteria (in the form of deformation limits) for structural components at three performance levels: immediate occupancy (IO), life safety (LS), and collapse pre-

vention (CP). Immediate occupancy is qualitatively designated as a damage state where the structure still essentially retains its pre-earthquake strength and stiffness. The LS performance level correlates to a small amount of damaged components but still retains a margin of safety. The CP performance level is described by damaged components of the structure, while the structure continues to support gravity load; however, it has no margin to resist collapse. The performance thresholds stated for structural walls per ASCE-41 are inherently limited, as they are based on limited empirical data. For walls which differ significantly from the experiments used to derive the idealized force-deformation curves in ASCE-41, this may be an un-representative and inaccurate method of assessment. Furthermore, empirical datasets are bound to inadequately account for all geometric configurations and unique detailing found in practice. Epackachi et al. (2018) has recently proposed updated modeling parameters for rectangular, barbell, and flanged shear-critical walls. Council (2023) has proposed updated parameters for shear controlled walls. Both of these recommendations are based on further empirical databases, and are therefore inherently bound to be inadequate to account for all configurations, and moreover, some of their proposed parameters show large scatter from their datasets.

An alternative assessment procedure, one which utilizes local (material) response, is inherently more robust as it does not rely on the external loading configurations or the internal geometric configuration of individual structures. It is also logical to note that global deformation (and structural component damage) is driven by a unique local stress-strain inelastic behavior. Therefore, establishing limit strain values for concrete and reinforcing steel, for example, would naturally be expected to lead to performance threshold metrics that have good predictive capability for the entire range of wall configurations encountered in engineering practice. Since numerical models can provide a comprehensive level of detail at the material level, this is an easily monitored and applied metric. It should be noted that experimentally

derived acceptance criteria (including strain-based criteria) are currently permitted through ASCE-41, provided that appropriate testing, calibration, and peer review are carried out.

For a more detailed discussion on other researcher's use of a strain-based criteria and other's critiques of the current assessment code and procedure, see Chapter 2.

6.2 Selected Parameters

A general research survey was carried out in collaboration with a panel of professional practicing engineers to determine the specific parameters which would be representative of the practice and detailing methods of mid-1950s to mid-1950s structural walls built in California. This resulted in a set of ranges regarding reinforcement detailing, wall geometries, material parameters, and loading configurations, which are summarized in Figure 6.1. Since the range of parameters selected comes from an investigation into as-built structures, the results are expected to be adequately representative of physical anticipated behavior for structures built from this period. Several variables were kept constant in all models, specifically the concrete strength, f'_c, the steel reinforcement strength, f_y, the wall length, L_w, and the wall height, H, of 24 feet. The height and length correspond to the full-scale values of the experimental specimens described in earlier chapters. This allows the parametric study to supplement the experimental work, while maintaining the same approximate, 'worst-case' scenario assumptions discussed in Section 3.2.1.

The following parameters were varied: rectangular or barbell cross section, web thickness (t_w), web reinforcement ratio (vertical and horizontal ρ_w), end region longitudinal reinforcement ratio (ρ_{end}), the ratio between the spacing of the transverse stirrups in the end region to the longitudinal bar diameter (s/d_b), and the axial load ratio (ALR), which is the axial load divided by the cross sectional area and the compressive strength of the concrete. The

models were subjected to a constant axial load P_{ax}, and a cyclic lateral load P_{lat}, following a displacement protocol of the top node, Δ_{top}.

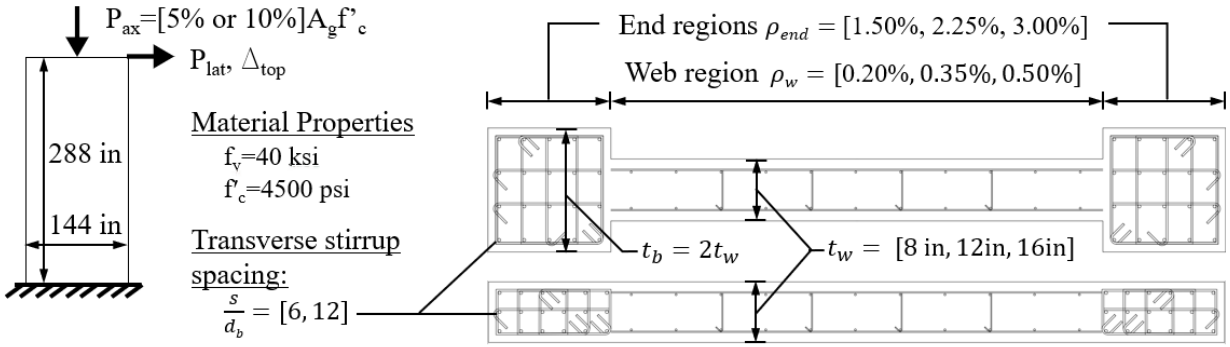

Figure 6.1: Ranges of Parametric Variables Selected for Numerical Models

With all possible combinations of the parameters defined previously, the total number of wall configurations is 216 (108 with rectangular sections and 108 with barbell sections). Every wall configuration was modeled with realistic reinforcement configurations and bar diameters. These design configurations were initially intended to have an insufficient amount of confining steel ($A_{sh,prov}/A_{sh,req} < 0.7$), thus obtaining the ASCE-41 classification of 'non-conforming' reinforced concrete structural walls. 16 of the investigated walls were unintended designed with conforming configurations of confining steel, and thus they are excluded from this analysis. The total number of considered models is 200. This investigation focused on planar structural and their seismic response while subjected to axial and lateral loading. The response was evaluated from a strain-based criteria as well as a global plastic hinge rotation aligned with ASCE-41.

The numerical models were analyzed in accordance with Chapter 5.

6.3 Strain Based Criteria

A more robust method of assessment of existing structures is through the use of a local (strain-like) criteria, which is governed by specific thresholds related to the constitutive material defined in the model.

The strain criteria, proposed initially by Deng et al. (2021), is presented in Table 6.1. This Table presents the list of possible damage conditions of a wall that would result in the exceedance of each performance level. Exceedance of IO corresponds to damage mechanisms associated with a significant loss of lateral stiffness in a wall: large flexural cracking, large shear cracking (exceeding 0.06 inches), and concrete cover spalling. Exceedance of LS is assumed to occur when the wall lateral load resistance starts to deteriorate due to failure in concrete or steel: rupture of vertical or horizontal bars, crushing of confined concrete toes, diagonal crushing of the web, and lap-splice slip (when lap splices are present). Exceedance of CP corresponds to a significant deterioration of the lateral load resistance, due to widespread material failure: rupture of a significant number of vertical or horizontal bars, complete crushing of confined concrete toe or unconfined concrete in the web, and failure of lap splices (when lap splices are present).

The strain-based acceptance criteria corresponding to each of these damage modes are defined in Table 6.1 in terms of steel strain (ε_s), concrete strain (ε_c) and the damage parameter D used to define bar rupture in the steel constitutive law and are based on the results from Deng et al. (2021). A performance level is exceeded when one of the criteria shown in Table 6.1 is met, for any individual element. One advantage of the proposed approach is that there is no need to pre-determine the type of behavior of the wall (flexure vs. shear), and that it can naturally capture mixed-mode responses. Another advantage is that specific criterion

Table 6.1: Acceptance Criteria Based on Material Damage and Strain-related Parameters

Performance level	**Exceedance criteria based on material damage**	**Acceptance criteria**
Immediate Occupancy (IO)	IO-1. Large residual flexural cracking	$\varepsilon_s \leq 1.0\%$
	IO-2. Large diagonal (shear) cracks	$\varepsilon_{c,diag} \leq \frac{w_{cr}}{L_d}$
	IO-3. Concrete cover spalling	$\varepsilon_{c,vert} \leq -\varepsilon_0$
Life Safety (LS)	LS-1. First fracture of vertical or horizontal bar	$D \leq D_{cr}$
	LS-2. Onset of confined concrete crushing	$\varepsilon_{c,vert} \geq -0.75\varepsilon_{cu}$
	LS-3. Onset of diagonal web crushing	$\varepsilon_{c,diag} \geq -\varepsilon_0$
	LS-4. Onset of slip in lap splice (when present)	$\varepsilon_s \leq 0.75\varepsilon_{s,max}$
Collapse Prevention (CP)	CP-1. Fracture of more than 50% of vertical bars in one boundary region or 50% of horizontal bars along a height equal to the wall length	$D \leq D_{cr}$ (in 50% of boundary/ horizontal bars)
	CP-2. Severe confined concrete crushing	$\varepsilon_{c,vert} \geq -\varepsilon_{cu}$
	CP-3. Severe diagonal web crushing	$\varepsilon_{c,diag} \geq -\varepsilon_u$
	CP-4. Failure of lap splice (when present)	$\varepsilon_s \leq \varepsilon_{s,max}$

can easily be supplemented to any of the performance levels, to further characterize the degradation of unique walls configurations. The qualitative definitions of material damage noted in Table 6.1 are general and independent of the modeling approach. Some of the quantitative values for acceptance criteria in Table 6.1 are based on the specific truss model selected for this study (i.e. diagonal strain criteria) and relate to the specific constitutive material model employed in this study. The remainder of the quantitative acceptance criteria relate to the typical performance parameters shown in other research analysis, such as strain in the steel reinforcement and concrete compressive strains. These acceptance criteria can be adapted to different modeling approaches with small changes, as shown in Murcia-Delso et al. (2025) for a continuum finite element model.

The parameters listed in the table are described as follows: ε_s is the strain of vertical steel, $\varepsilon_{c,diag}$ is the concrete strain in diagonal element, $\varepsilon_{c,vert}$ is the vertical concrete strain, D

is the material parameter controlling steel failure in the constitutive model by Kim and Koutromanos (2016), w_{cr} is the critical crack opening taken as 0.06 inches based on the FEMA Council (1998), L_d is the length of the diagonal element, ε_0 is the compressive strain of unconfined concrete at the peak strength, ε_u is the ultimate compressive strain of unconfined concrete, ε_{cu} is the is the ultimate compressive strain of confined concrete, ε_y is the yield strain of steel, D_{cr} is the critical value of D at which bar rupture occurs, $\varepsilon_{s,max}$ is the maximum tensile strain that the lap splice can develop prior to failure.

The limiting value of ε_{cu} is calculated by $\varepsilon_{cu} = (0.012 - 0.002273) * L_{ref}/L_{element} + 0.002273$, and the limiting value of ε_u is calculated by $\varepsilon_u = (0.012 - 0.002) * L_{ref}/L_{element} + 0.002$. The value of D_{cr} is taken as 0.21, the value of $\varepsilon_{s,max}$ is taken as 0.0128.

6.4 Results

The results of the parametric analysis are described in the following section. A force-versus-drift curve was obtained for each of the 216 walls considered in the study. The performance of each wall was evaluated per the strain-based criteria in Section 6.3 for each of the three different performance levels (IO, LS and CP). The drift at which a performance level was exceeded per the strain-based criteria was recorded; these drift will subsequently be referred to as Δ_{IO}, Δ_{LS}, and Δ_{CP}. The backbone curve of each hysteretic plot was collected for the positive drift direction only; they are plotted in Figure 6.2, organized with specific similarities of parameters to provide clarity of the results. There are 18 backbone curves in each plot, 9 for rectangular walls, and 9 for barbell shaped walls. The 18 curves represent the range of internal reinforcement ratios noted in Figure 6.1 for both vertical and horizontal reinforcement in the webs and end regions. Figure 6.2 aims to showcase the scope of the numerical study, as well as showcase the graphical distinctions of the force-versus-drift curves.

The y-axis is a normalized parameter of shear stress, calculated with Equation 6.1. Some expected conclusions are easily observable in Figure 6.2. For example, the highest stress corresponds to the larger web thickness and the barbell sections, which naturally have larger concrete areas in the end region than the rectangular walls. The IO drift and IO force, noted with the black 'X' in Figure 6.2, is clearly seen prior to a plateau in the backbone curve, while the LS and CP values are near the point of strength degradation. The statistics of the IO, LS and CP limits describing the performance of the walls are presented and discussed in this section.

$$\tau = \frac{P}{A_{crosssection}\sqrt{f'_c}} \qquad \text{(Eq. 6.1)}$$

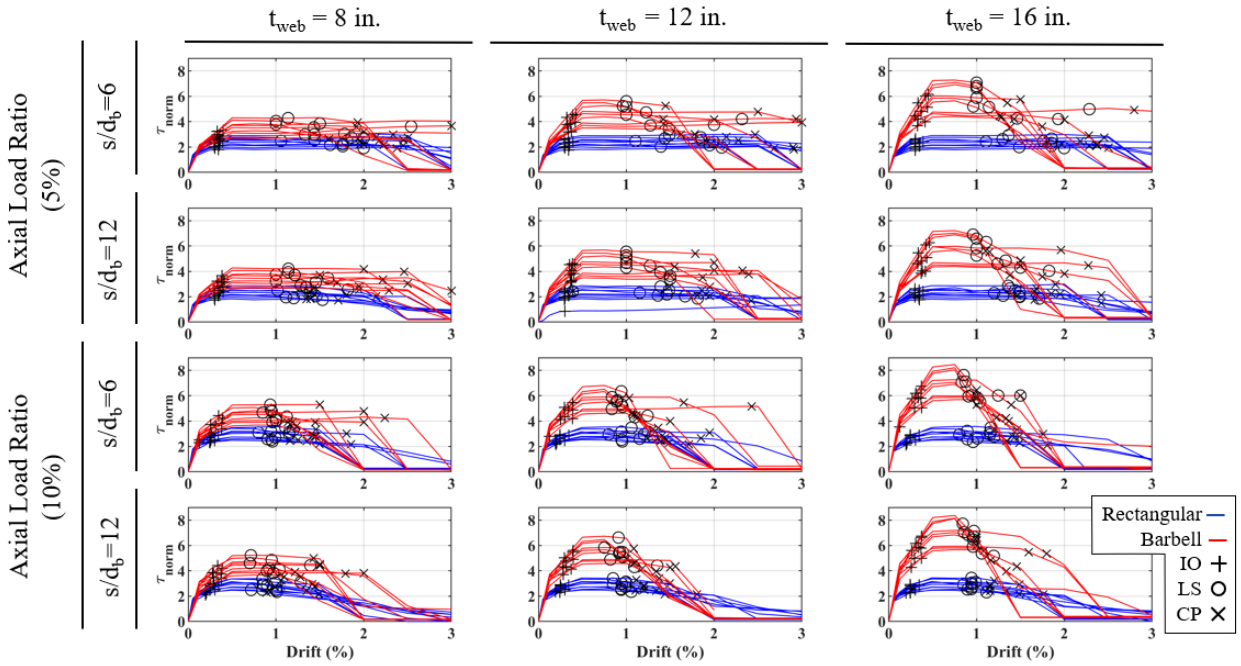

Figure 6.2: Shear Stress Versus Drift Backbone Curves for 216 walls in the Parametric Study, with IO, LS, and CP Performance Limits Noted.

6.4.1 Strain-based Criteria Assessment with Key Points of a Backbone Curve

ASCE 41 allows the use of a peer-reviewed alternative assessment criteria which is based in fundamental principles of engineering mechanics. The majority of this guidance is focused on experimentally motivated justifications, which may have supplemental analytical modeling support. The ASCE-41 guidance given for general acceptance criteria for the IO, LS, and CP performance levels as they relate to the overall normalized force-deformation curves corresponding to nonlinear procedures is shown in Figure 6.3a. The criterion for IO is labeled in the figure and relates to no more than half of the deformation associated with the peak strength, point C, of the idealized curve. The LS parameter is considered at no more than 75% of the deformation associated with residual strength at point F, where point F is defined by 5% of the peak strength or 5% of the effective yield point. Finally, CP shall be taken as the deformation limit at point F. This criterion is incredibly difficult to capture experimentally for structural walls, which are rarely pushed to a level of degradation consistent with this allowable criteria.

The deformation demand is difficult to induce faithfully in a numerical model as well, thus the more reliable strength degradation is utilized to provide meaningful comparisons of the numerical results with targeted levels of performance. Figure 6.3b showcases an example hysteretic curve (positive direction only) for one of the numerically modeled structures. Figure 6.3b shows three limits of performance level, namely IO, LS, and CP which are determined by the strain-based criteria exceedance. Figure 6.3b also shows three reference drift values, associated with more traditional considerations of strength degradation, namely the drift at the effective yield point, $\Delta_{\text{Effective Yield}}$, 90% of the post peak strength, $\Delta_{0.9*\text{Post Peak}}$, and 50% of the post peak strength, $\Delta_{0.5*\text{Post Peak}}$. The effective yield drift is taken as the drift at

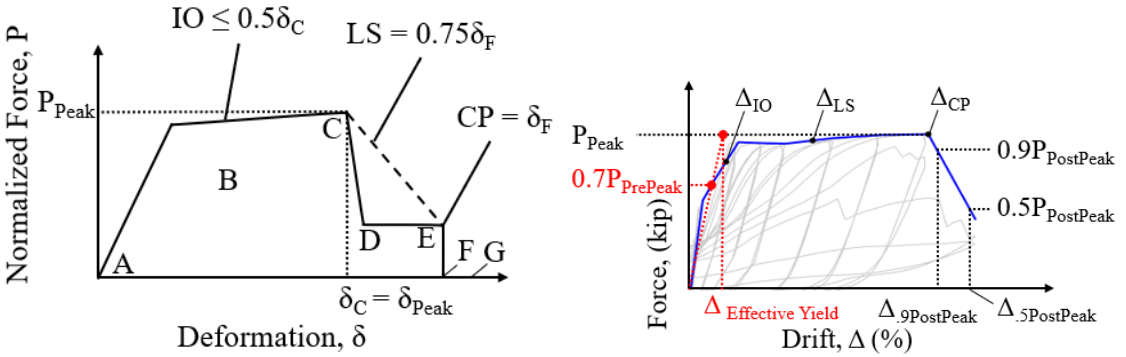

(a) ASCE-41 Acceptance Criteria for Alternative Assessment Nonlinear Procedures

(b) Example Hysteretic Curve from One Numerical Model with Key Points Labeled

Figure 6.3: Assessment Methodologies Based on Values in a Backbone Curve

which a linear line through the origin and a point of 70% pre-peak strength intersects with a horizontal line taken at the peak strength of the structure. The ratios of interest for each performance level are noted in Equations 6.2,6.3, 6.4.

$$\mathrm{IO}_{\mathrm{Ratio}} = \frac{\Delta_{\mathrm{IO}}}{\Delta_{\mathrm{Effective\ Yield}}} \qquad \text{(Eq. 6.2)}$$

$$\mathrm{LS}_{\mathrm{Ratio}} = \frac{\Delta_{\mathrm{LS}}}{\Delta_{0.9^{*}\mathrm{Post\ Peak}}} \qquad \text{(Eq. 6.3)}$$

$$\mathrm{CP}_{\mathrm{Ratio}} = \frac{\Delta_{\mathrm{CP}}}{\Delta_{0.5^{*}\mathrm{Post\ Peak}}} \qquad \text{(Eq. 6.4)}$$

A graph of the cumulative sum for the different performance levels is shown in Figure 6.4. The ratios from Equations 6.2, 6.3, and 6.4 are plotted on the x axis, in subfigures a, b, and c respectively. Figure 6.4a relates to the immediate occupancy ratio, and it indicates that the average ratio between the drift limit associated with the strain-based criteria for IO and the effective yield drift is 1.38. One may conclude that the IO limit obtained from

the strain-based criteria is often slightly above the effective yield point of the structure. Furthermore, 50% of all of the numerical models reached the IO strain-based limit between the effective yield drift or at 1.68 times the effective yield drift. This is reasonable, as the qualitative description of this limit per ASCE-41 is that the structure retains most of its initial strength and initial stiffness. This is also graphically similar to Figure 6.3a which indicates an acceptable deformation at the IO level is some point beyond initial yielding.

The drift associated with the LS limit is related to the drift at 90% of post-peak strength. The average value of 0.77 for this ratio, shown in Figure 6.4b, indicates the LS limit, on average, is determined to occur slightly prior to 10% strength degradation in the structure. The inter-quartile range of this graph is 0.24, indicating that 50% of all specimens exhibited ranges of the LS ratio between 0.67 and 0.91. This is again in qualitative alignment with the allowable criteria offered in ASCE-41, shown in Figure 6.3a, which suggests an LS limit slightly beyond peak strength is reached in the structure. Finally, the average value of the CP graph in Figure 6.4c is 0.79, and the inter-quartile range is 0.11. This is a relatively narrow range, indicating the CP_{ratio} is captured quite effectively and consistently near the 50% strength degradation of the structure. It is interesting to note that the CP ratio never exceeds 1, indicating the strain-based criteria is 100% effective in determining a threshold less than or equal to deformation associated with 50% strength degradation. Again, this is reasonable because the degradation of the specimen should be captured by the CP limit, and it should be associated (per the qualitative description in ASCE-41) with the ability of the structure to withstand only gravity loads.

For further consideration, the graphs of the cumulative sums for the individual studies of the barbell and rectangular walls have been separated in Figures 6.5 and 6.6 respectively. The trend of the data is overall similar to the cumulative graphs of the total dataset in Figure 6.4, but there are some interesting differences. For the IO performance level the inter-quartile

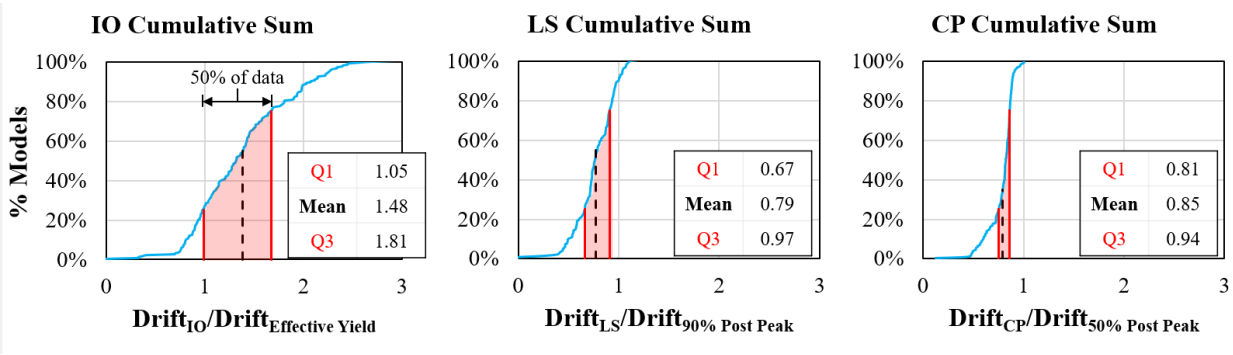

(a) IO_{Ratio} (b) LS_{Ratio} (c) CP_{Ratio}

Figure 6.4: Cumulative Sum Charts of the Ratios from Equations 6.2, 6.3, and 6.4

range is smaller for both of the subsets of the data, meaning that each dataset has a narrower spread of results than when looking at the entire dataset. The rectangular walls have a higher IO_{Ratio} on average than the barbell walls, indicating the barbell walls exceed an IO strain-based threshold earlier than the rectangular walls. This is in contrast to the LS and CP performance levels, where the barbell walls, on average, reach an exceedance strain-based criteria later than the rectangular walls. The LS_{Ratio} for barbell walls has a higher Q3, 0.96, and average value, 0.8, than the rectangular walls, indicating the LS threshold is exceeded slightly later for barbell walls than for rectangular walls, on average. The inter-quartile range of the rectangular walls for the LS limit is very small, 0.11, indicating the data is more predictable in performance. Another interesting note is that the inter-quartile range of the CP_{Ratio} for the barbell walls is very small, just 0.06, indicating that 50% of the data is captured in this narrow window, and showcases how consistently the barbell walls consider the CP_{Ratio}.

Overall, at the IO performance level the rectangular walls exceed the effective yield drift at higher drifts than the barbell walls. In fact, three quarters of the barbell walls have a ratio less than 1.32, while only one quarter of rectangular walls claim this ratio. At the

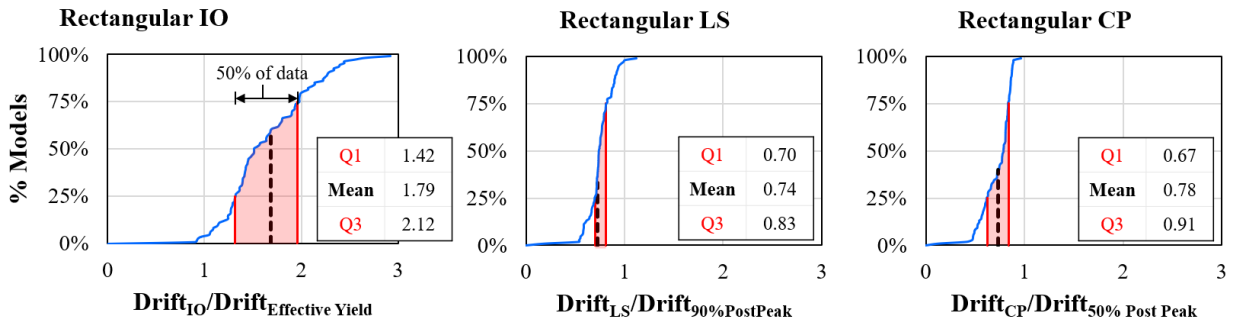

(a) IO_{Ratio} (b) LS_{Ratio} (c) CP_{Ratio}

Figure 6.5: Rectangular Walls Cumulative Sum of the Ratios from Equations 6.2, 6.3, and 6.4

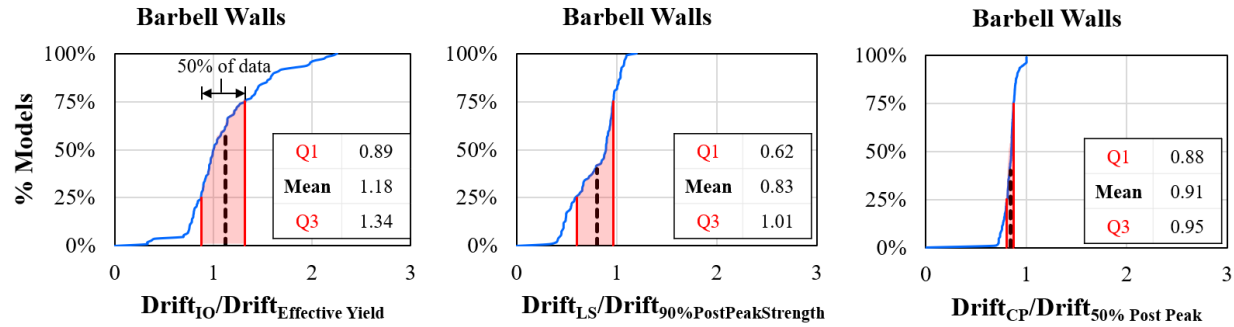

(a) IO_{Ratio} (b) LS_{Ratio} (c) CP_{Ratio}

Figure 6.6: Barbell Walls Cumulative Sum of the Ratios from Equations 6.2, 6.3, and 6.4

higher damage state (LS and CP) barbell walls exhibit a higher ratio than rectangular walls, meaning they tend to over-predict these damage ratios relative to rectangular walls.

6.4.2 ASCE-41 Comparison

6.4.2.1 Rectangular Walls

Out of the 108 rectangular walls considered in the study, 103 would be classified as flexure-controlled according to ASCE-41, while 5 of the walls would classified as shear-controlled.

Additionally, within the 103 flexure-controlled walls, there were 12 walls which would be considered conforming according to ASCE-41 because their $A_{sh,prov}/A_{sh,req}$ was greater than 0.7, unintentionally. Therefore, the analysis results discussed in this section has focused on the remaining 91 flexure-controlled non-conforming walls. The results obtained for the conforming flexure-controlled and shear-controlled walls are not discussed because the number of walls was considered too small to arrive at general findings.

The analysis of the damage modes triggering the performance levels of the 91 non-conforming flexure-controlled walls indicates that the IO limit is associated in most of the cases to concrete cover spalling (98%), while there is only one case related to large residual cracking and one to large diagonal cracking. There were two damage modes triggering the LS criteria: onset of confined concrete crushing (57%) or onset of diagonal web crushing (43%). For CP, the triggering damage modes are similarly characterized by two governing criteria: severe confined concrete crushing (52%) or severe diagonal web crushing (48%). It is interesting to note that the vast majority of the walls (87%) reached the CP criteria in a similar pattern from their LS criteria, i.e. if a wall reached the LS criteria through confined concrete crushing, they likely failed in severe concrete crushing; similarly if they reached the LS criteria through diagonal web crushing, they likely reached the CP criteria through severe diagonal web crushing. Hence, the failure of the walls is ultimately governed by confined concrete crushing or diagonal web crushing, according to the models. The walls failing due to diagonal web crushing had reached their flexural capacity, and their failure can be explained by the shear-flexure interaction.

The response and acceptance criteria of flexure-controlled walls is determined in ASCE-41 based on total hinge rotation. It is useful to be able to compare the truss model results with the ASCE-41 provisions, since the current state of practice relies on the deformation values noted in ASCE-41 for RC structural walls. This comparison can also give an idea of

the level of scatter or the potential benefits or drawbacks of using a new assessment criteria. Subsequently, the drift values at which the performance limits are exceeded via the strain-based criteria have been converted to total hinge rotation. This conversion was undertaken assuming a simple plastic hinge model with effective plastic hinge length of $L_w/2$, through the approach described in Abdullah (2019). Figure 6.7 presents the hinge rotation for IO, LS and CP limits against L_wc/b^2 which is a key parameter to define these performance limits in the ASCE-41 standard. The results of only the rectangular walls are shown in Figure 6.7. Furthermore, the limiting hinge rotation per ASCE-41 criteria are also plotted for RC walls with 10% or less ALR. Note, there are two lines in the IO limit because the criteria is further dependent on the amount of shear steel in the end regions and the spacing of the transverse reinforcement, but both lines follow a similar trend.

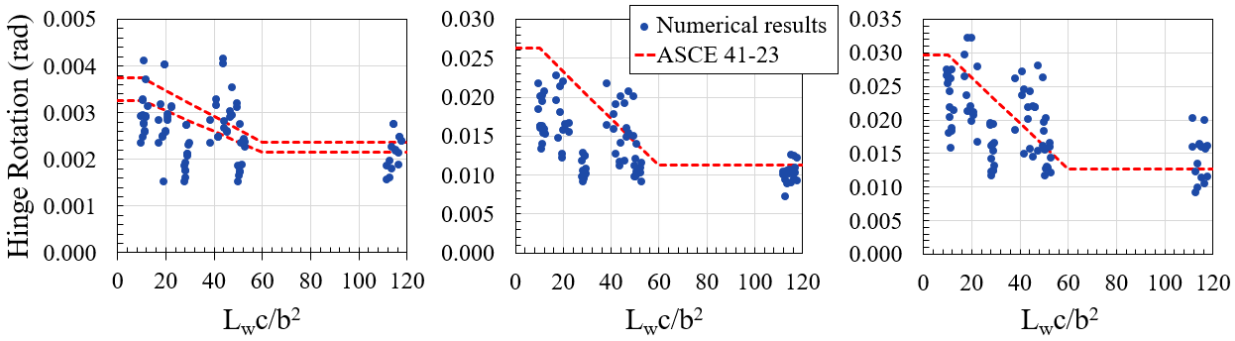

(a) IO limit (b) LS limit (c) CP limit

Figure 6.7: Performance Limits for Rectangular Walls Classified as Nonconforming Flexure-controlled: Influence of Parameter L_wc/b^2

As can be seen in graphically Figure 6.7, ASCE-41 limits hinge rotation with decreasing thresholds for higher L_wc/b^2 values. The numerical results typically follow this trend in the ASCE-41 hinge rotation limits. Higher L_wc/b^2 values in the numerical model coincide with structural walls with smaller cross-sectional areas and higher axial loads, resulting in a larger neutral axis depth. In addition, the numerical results show a slight underestimation as com-

pared to the ASCE-41 curve for all three performance levels, which is noted in the mean value of the ratio of the numerical value to the ASCE-41 determined value for rectangular walls in Table 6.2, which are all slightly below 1. This leads to the conclusion that the ASCE-41 rotation limits for plastic hinge regions of RC structural walls may be slightly un-conservative, as they allow for more rotation than the strain-based criteria assessment would lead to. The use of strain-based criteria for assessment of non-conforming flexurally-controlled walls should lead to generally conservative design on average but should be considered with the ASCE-41 guidelines as a minimum allowable hinge rotation for a given performance limit.

Table 6.2 presents the mean and coefficient of variation for the ratios of numerical-to-code performance limits. The mean value is calculated per Equation 6.5. These values are calculated for the 91 non-conforming flexurally-controlled rectangular walls. As shown, the mean ratios are close to 1 and moderate dispersions are obtained, with coefficients of variation between 0.24 and 0.28. The magnitude of the coefficients of variation is similar to those obtained by Abdullah (2019) when comparing experimental results with expressions proposed to determine wall response parameters. The expressions from Abdullah are adopted in ASCE-41. Hence, it can be concluded through statistical comparison, that the numerical results utilizing a strain-based criteria for rectangular walls are consistent with the performance expected in ASCE-41, and therefore these numerical results provide a comparable result to experimental data. This criteria still has the advantage of determining the degradation of the structure through the actual material level deformation, rather than the global hinge rotation parameter.

$$\mu = \frac{\text{numerical value}}{\text{expected value}} \qquad \text{(Eq. 6.5)}$$

The same data from Figure 6.7 has been plotted a second and third time in Figures 6.8

Table 6.2: Statistics for the Ratio of Numerical-to-code Performance Limits for Non-conforming Flexure-controlled Rectangular Walls

Performance limit	Mean	Coefficient of variation
IO	0.90	0.24
LS	1.37	0.27
CP	1.14	0.28

and 6.9 respectively, to show some of the interesting trends when the data is grouped by web width, axial load ratio (ALR) and the slenderness parameter (s/d_b). Figure 6.8 clearly showcases a recognizable and predictable pattern of the results, namely that the walls with lower web thickness, result in a higher value of $L_w c/b^2$, and generally walls with higher axial load ratios exceed allowable strain-performance levels at lower hinge rotations than their similar counterparts.

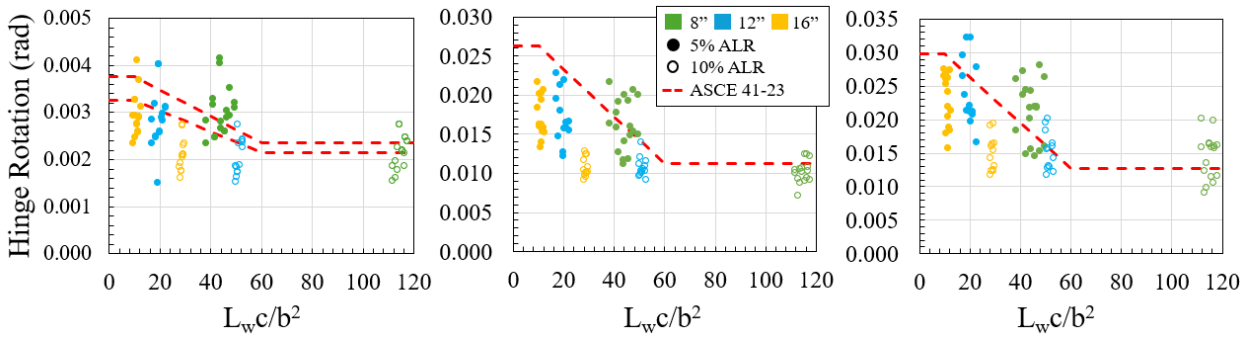

(a) IO limit (b) LS limit (c) CP limit

Figure 6.8: Strain-Based Criteria Performance Levels Wall Web Thickness and Axial Load Ratio (ALR) For Rectangular, Flexurally-Controlled Walls

Figure 6.9 shows an interesting and unexpected phenomenon. The results are not as easily distinguishable between clusters of the data as the results in Figure 6.8; however, interesting conclusions can still be observed. The higher s/d_b value of 12 corresponds to a higher amount of spacing between the end region stirrups, which results in a reinforcing bar which is more prone to buckling. These values are indicated by blue markers, and their linear trend-line is

marked on the graph. There is not a clear demarcation at the IO limit between a slenderness parameter of 6 or 12, but at the LS and CP limits the distinction can clearly be noted. The trend-lines indicate that, in general, a larger s/d_b parameter leads to a reduction in allowable hinge rotation. This is likely due to the propensity of the bars to buckle and subsequently rupture with the larger s/d_b value.

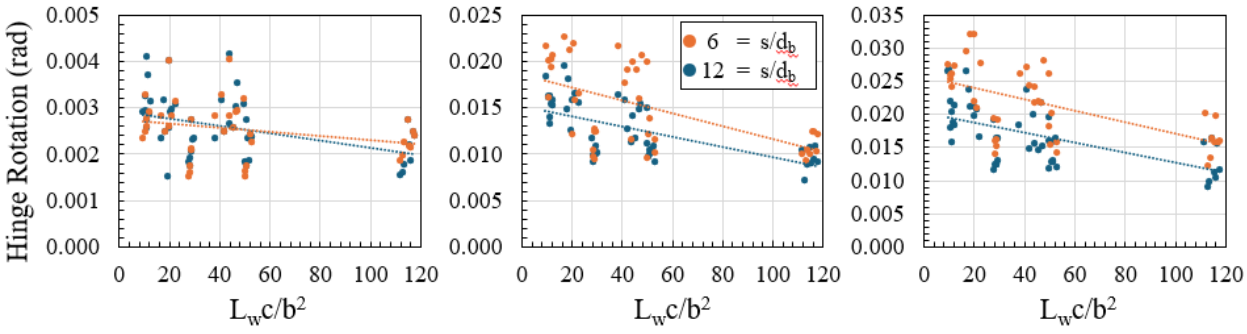

(a) IO limit (b) LS limit (c) CP limit

Figure 6.9: Strain-based Criteria Performance Levels Delineated by Slenderness Parameter (s/d_b) for Rectangular, Flexurally-controlled Walls

6.4.2.2 Barbell Walls

Out of the 108 barbell walls considered in the study, 72 would be classified as non-conforming flexure-controlled walls according to ASCE-41, while 36 would be classified as shear-controlled. The results for these two types of walls (flexure-controlled and shear-controlled) are analyzed separately.

The analysis was carried out for the 72 barbell walls classified as non-conforming flexure-controlled with the same performance criteria for the three performance levels as described in Section 6.3. The damage modes triggering the Immediate Occupancy performance level indicates 24% of the walls exhibited large diagonal shear cracks while 76% experienced concrete cover spalling. 100% of the walls exceeded the Life Safety (LS) threshold by an onset of diagonal web concrete crushing. At the Collapse Prevention (CP) level, walls classified as

flexure-controlled experienced failure in 80% of cases due to severe diagonal web crushing, in 19% due to severe confined concrete crushing, and in 1% due to rupture of multiple vertical bars. Similarly to the rectangular non-conforming flexure-controlled walls, the failure mode from LS to CP was typically consistent (i.e. LS acceptance criteria exceedance of diagonal web crushing resulted in a CP acceptance criteria exceedance of diagonal web crushing.)

The response and acceptance criteria of the flexure-controlled walls is determined in ASCE-41 based on hinge rotation. It is therefore useful to determine the overall hinge rotation associated with each strain-based exceedance for all three performance levels, to be able to use familiar values as a basis for discussion. The overall hinge rotation for the barbell wall simulations was determined through the same protocol as for the rectangular walls. Figure 6.10 presents the hinge rotation for IO, LS and CP limits against $L_w c/b^2$. As shown in the Figure the numerical results do not seem to follow the trend of the equations in ASCE-41 well. ASCE-41 considers a decrease of the hinge rotation capacity with the increase of $L_w c/b^2$, while the numerical results show a consistent trend regardless of $L_w c/b^2$. There is no distinction in the code for barbell or rectangular walls as far as the acceptance criteria for non-conforming flexure-controlled walls, thus the dashed red lines in Figure 6.10 is the same ASCE-41 limit as shown in Figure 6.8. The walls with smaller cross sections of web area tend to have higher $L_w c/b^2$ values. It would make sense that the overall hinge rotation, particularly for the CP limit, is much higher in this wall than the ASCE-41 parameter, because the barbell end regions are contributing much more resistive capacity in compression, and this is not well described by the $L_w c/b^2$ parameter.

Table 6.3 presents the mean and coefficient of variation for the ratios of numerical-to-code performance limits. As shown, the mean ratios are close to 1 but large dispersions are obtained for LS and CP (coefficients of variation of 0.44 and 0.47). Hence, the response of the barbell walls for LS and CP do not seem to align well with the code equations. This

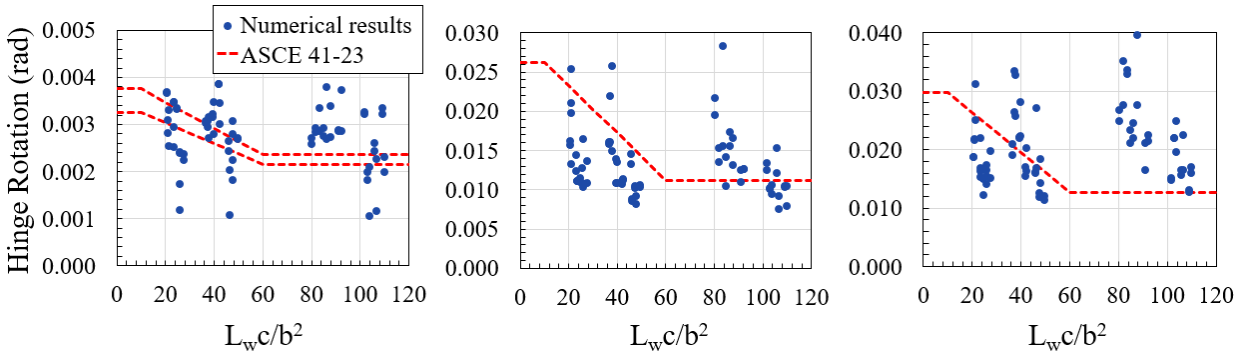

(a) IO limit (b) LS limit (c) CP limit

Figure 6.10: Performance Limits For Barbell Walls Classified As Non-Conforming Flexure-Controlled: Influence Of Parameter $L_w c/b^2$

may be cause for additional or specific consideration to be given to barbell shaped in the current ASCE-41 standard.

Table 6.3: Statistics for the Ratio of Numerical-to-code Performance Limits for Non-conforming Flexure-controlled Barbell Walls

Performance limit	Mean	Coefficient of variation
IO	1.10	0.26
LS	0.91	0.40
CP	1.26	0.45

Another parameter that could influence the performance of the barbell walls is the maximum normalized shear stress. This parameter is considered in ASCE-41 to calculate performance limits in conforming flexure-controlled walls, but it is not used for non-conforming flexure-controlled walls. Figure 6.11 presents the hinge rotation for IO, LS and CP limits against the normalized shear stress. As shown, the numerical results for LS and CP limits present a descending trend with the increase of the normalized shear. This is consistent with the fact that a majority of failures observed in analysis were diagonal compression shear failures. The IO limit does not seem to be correlated with the normalized shear. The results indicate that including the normalized shear stress in the performance limit calculation would improve the

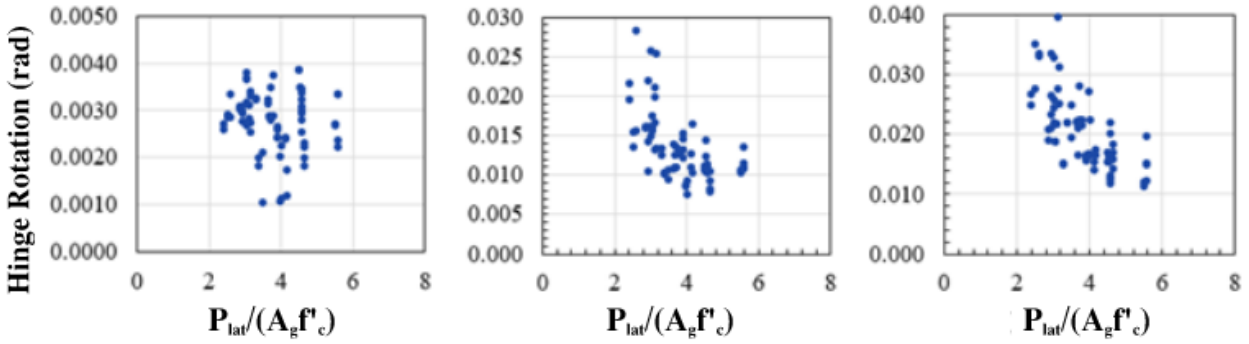

(a) IO limit (b) LS limit (c) CP limit

Figure 6.11: Performance Limits for Barbell Walls Classified as Nonconforming Flexure-controlled: Influence of Normalized Shear Stress

code predictions for LS and CP for barbell non-conforming flexure-controlled walls.

For the 36 walls classified as shear-controlled, IO was exceeded in 39% of the cases due large diagonal shear cracks and in 61% due to concrete cover spalling. In all walls, life safety (LS) performance was compromised by the onset of diagonal web crushing. For walls classified as shear-controlled, CP was exceeded in all cases due to severe diagonal web crushing. Hence, the ultimate failure of the barbell walls was governed by diagonal web crushing, according to the models. These walls a 100% condition of LS diagonal web crushing would result in a CP exceedance failure mode of severe diagonal web crushing.

The performance of the 36 walls classified as shear-controlled is analyzed in terms of drift ratio. This is how ASCE-41 determines wall response and acceptance criteria for shear-controlled walls. Figure 6.12 presents the drift ratio for IO, LS and CP limits against V_n/V_{max} which is a parameter used to define performance limits in ASCE 41. As shown in the figure, the numerical results show a slight decrease of the drift ratio limits with the decrease of V_n/V_{max}, showing a consistent trend with the ASCE-41 equations. However, the numerical results are mostly below the drift capacities obtained with the code. Table 6.4 presents the mean and coefficient of variation for the ratios of numerical-to-code performance limits. As

shown, the coefficients of variation remain small (below 0.20) due to the consistent trends within the numerical data alone, but the mean values are well below 1. This indicates that code equations could allow excessive drift ratios for a given V_n/V_{max}, resulting in potentially unsafe requirements for barbell walls. However, the number of data points available are not sufficient to arrive at a definitive conclusion.

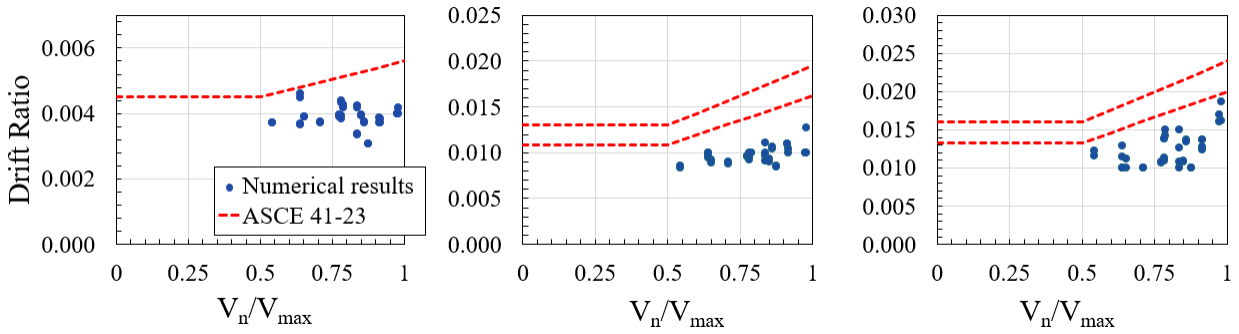

(a) IO limit (b) LS limit (c) CP limit

Figure 6.12: Performance Limits for Shear-Controlled Walls with Barbell Section: Influence of Parameter V_n/V_{max}

Table 6.4: Statistics for the Ratio of Numerical-to-code Performance Limits for Shear-controlled Barbell Walls

Performance limit	Mean	Coefficient of variation
IO	0.76	0.11
LS	0.43	0.13
CP	0.67	0.11

The numerical analyses on 72 barbell walls classified as non-conforming flexure-controlled compare with similar statistical spread to the IO limit established in ASCE 41-23. For LS and CP, the numerically obtained limits have a systematically wider spread than the limits obtained by ASCE 41-23 analysis. The numerically obtained values do not show a clear trend when plotted against the horizontal axis parameter $L_w c/b^2$. This suggests that perhaps the ASCE-41 parameters may not capture the behavior of these types of walls well.

While the means of the numerical-to-code performance limits are close to 1, the coefficients of variation for LS and CP are high (0.44 and 0.47). The deformation capacity for LS and CP obtained in the numerical analyses tends to increase with the maximum normalized shear stress, consistent with the diagonal compression failures obtained in the models, but ASCE-41 does not currently consider the influence of this factor for non-conforming walls.

The numerical analyses on 36 barbell walls classified as shear-controlled show that the drift limits for the different performance levels slightly increased with the increase of the theoretical shear resistance normalized to the flexure resistance, like in code equations. The numerically obtained limits are significantly lower than those established in ASCE-41 for all three performance levels. Still, the number of data points is insufficient to arrive at general conclusions about the level of (un)conservatism of the code equations.

6.4.3 Strain-based Assessment of Experimental Analytical Results

The strain-based criteria as so described in this chapter, was utilized for the numerical models described in Chapter 5 to assess their exceedance of LS, and CP performance limits through the strain-based criteria. The results of this assessment are shown in Figure 6.13. The two limits for LS and CP for the numerical results are shown in blue, and the method of strain-based criteria exceedance is noted through the legends. The experimental results are also plotted in the same figure for comparison. The initial behavior of observed toe crushing, vertical bar rupture, or lap splice slip, is shown in yellow for the experimental results.

Specimen S1 exceeded the strain-based criteria at LS due to diagonal web concrete crushing around 1% drift, and exceeded the CP criteria through diagonal web concrete crushing, as can be seen in Figure 6.13a. The toe crushing observed in the experimental results occurred concurrently with diagonal web concrete crushing, and the loss of strength in the experimental and analytical results is in good agreement, within 10% of one another.

Figure 6.13b shows specimen S1CW exceeded the LS performance limit through vertical bar rupture at a drift of 1%, which is earlier than the initial bar rupture observed in the experiment at 2% drift. The exceedance of Specimen S1CW of the CP performance criteria is through diagonal web crushing, which was also observed in the experimental results at the 2.5% drift ratio.

Specimen S1FW exceeded the strain based criteria by diagonal web crushing at 2% drift for the LS performance limit and 2.7& drift for the CP performance limit, as shown in Figure 6.13c. Note, the vertical bar rupture in the numerical results occurs after the LS threshold has been exceeded. The experimental results were characterized by vertical bar rupture at the 2.5% drift, and subsequent concrete toe crushing and spalling due to buckling of the reinforcement, as well as diagonal web crushing.

Figure 6.13d shows the analytical results of Specimen S1FP, which exceeded the strain based performance criteria through diagonal web crushing for the both the LS and CP limits.

The group two experimental specimens with a lap splice exceed the LS performance limit in the numerical results through lap splice slip, and can be seen in Figures 6.13e and 6.13f. The experimental lap splice slip observed in the control specimen, S2, occurs at a drift within 5% numerical results. The FRP wrapped specimen designed to restrain lap-splice slip, exceeds the CP performance limit through diagonal web crushing, which was not observed in the experimental results. The point at which the first bar rupture was observed in the experimental results is noted in Figure 6.13f.

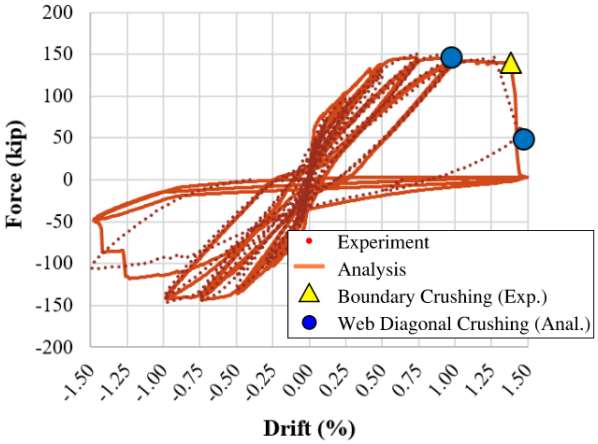

(a) Specimen S1

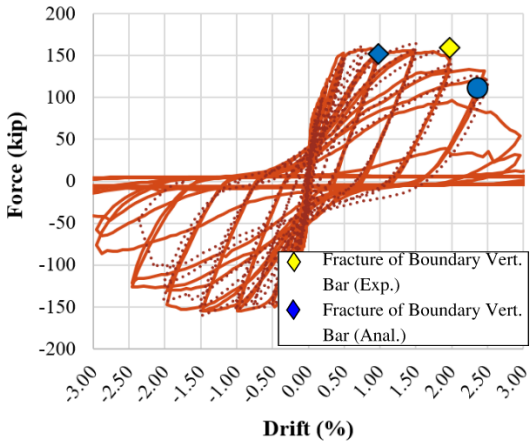

(b) Specimen S1CW: Concrete Overlay

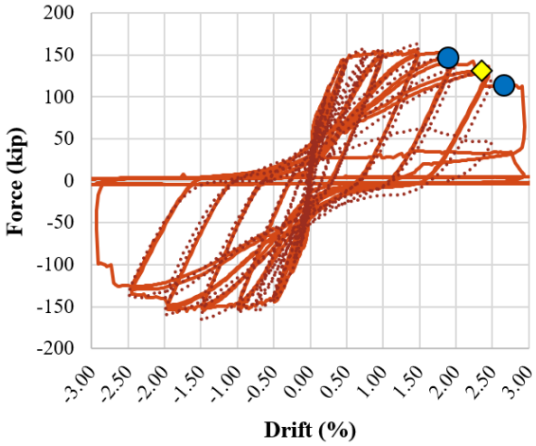

(c) Specimen S1FW: FRP Web Overlay

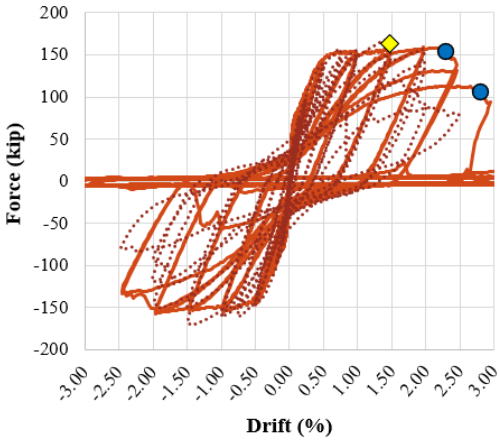

(d) Specimen S1FP: FRP Bar Buckling Wrap

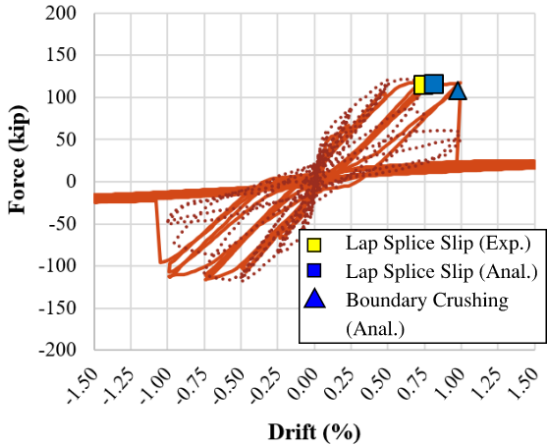

(e) Specimen S2: Lap Splice Control

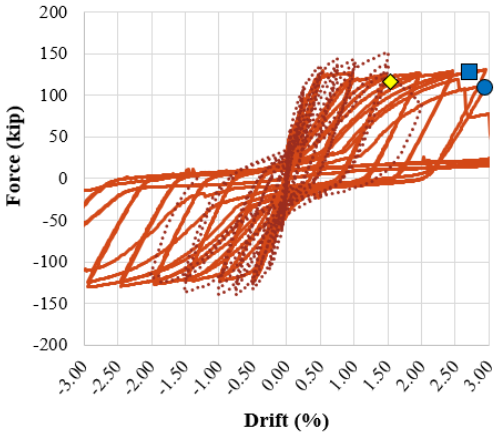

(f) Specimen S2FL: FRP Lap Splice Prevention

Figure 6.13: Strain Based Assessment of Numerical Model Performance with Experimental Results

6.5 Limitations of Methodology

This section details the specific limitations of the parametric study, the use of the strain-based criteria, and the modeling framework utilized in this study.

In the parametric study, the selection of an effective height of 24 feet represents a limitation within this study, which is further elaborated upon in Section 3.2.1. The selected height was intended to represent a 'worst-case' scenario, particularly under the quasi-static loading conditions applied in the parametric study. However, this may not fully reflect accurate conditions. It is recommended that future research be conducted to incorporate dynamic loading for a full scale numerical model to ensure that the correct effects are captured by a shorter structure with an appropriate effective height. It is important to acknowledge that the impact of varying effective heights is partially addressed through the analysis of the normalized shear stress value. In the future, it might be essential to conduct an additional study where the actual effective height value is altered. This would help determine how well the influence of effective height can be entirely represented through changes in the normalized shear stress.

An additional limitation of the parametric study is the omission of variable compressive concrete strengths, f'_c. Although several normalized parameters, such as the axial load ratio and normalized shear stress, partially account for the impacts of variable f'_c, and the actual range of compressive strengths observed in the real-life structural review of the era of interest analysis was relatively narrow, the effects of this parameter are still considered important. Therefore, further investigation into its potential effects on the results is deemed necessary.

The consideration of the strain-based criteria to levels of strength degradation of the global force-deformation curves was an initial correlation of sorts. This correlation appears to have a

degree of conservatism. For instance, the collapse prevention strain limit was exceeded prior to severe degradation in strength. The amount of conservatism (if any) for the specified strain thresholds should be further evaluated on the basis of more detailed studies (e.g., considering bidirectional seismic loading effects).

A mesh sensitivity study was undertaken to compare the results of the strain-based acceptance criteria for the same structure modeled with two different element mesh sizes. Further details of this study and the results of the hysteretic responses are noted in Section 5.1.2. This section will expand the discussion to consider the effect on the strain-based criteria. There were no differences in the description of the models or the performance criteria thresholds (though it is important to note that the limits of strain exceedance for the concrete members are dependent on the size of the mesh and thus the strains were adjusted accordingly to the appropriate mesh size; for more details of how to calculate the appropriate strains for the criteria, see Section 6.3).

The two mesh sizes considered were motivated by a limiting number of elements spanning a single row along the x-axis of the wall, resulting in mesh sizes of 16-inches and 8-inches. For further details of the mesh size study, see Section 5.1.2. The comparison of the load-drift curves obtained for the different values of mesh size is provided in Figure 6.14, along with the exceedance for the three limits of performance levels, IO, LS, and CP. The drift and force values associated with the performance level exceedance are Table 6.5. It can be seen that the strain-based acceptance criteria are exceeded at nearly exactly the same drifts, within 6% of one another. The models exhibited the same exceedance criteria for each performance level, with failure modes governed by concrete crushing of the confined boundary regions. The strengths associated with each performance limit appear to have a large spread due reasonable factors inherent in modeling of different mesh sizes, such as the location of the steel fibers. This discrepancy in strength at each PL exceedance is anticipated to be reduced

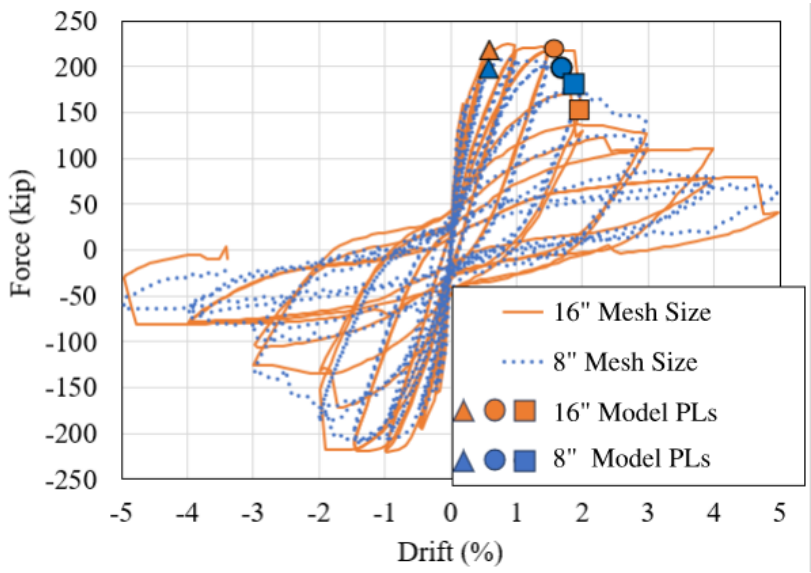

Figure 6.14: Hysteretic Comparison Between the Same Model with Different Mesh Sizes

with a finer mesh analysis.

Table 6.5: Exceedance Criteria and Forces for Different Mesh Sizes

Mesh Size	PL	Exceedance Criteria	Drift (%)	Force (kip)
16” mesh size	IO	Concrete cover spalling	0.59	218
	LS	Confined concrete crushing	1.60	219
	CP	Confined concrete crushing	1.98	152
8” mesh size	IO	Concrete cover spalling	0.59	197
	LS	Confined concrete crushing	1.69	199
	CP	Confined concrete crushing	1.88	180

6.6 Conclusions for Parametric Study

An extensive parametric study was carried out; it aimed to represent structural RC walls archetypical from design and construction practice in the mid 1950's and 1960's in California. The parametric study consisted of a range of variables including wall geometry, internal reinforcement configuration, spacing of the end region stirrups, and axial load ratio. The walls were assessed with a strain-based (local) criteria specific to constitutive properties and material strain, initially presented by Deng et al. (2021), for the three performance levels most often associated with seismic assessment per ASCE-41, namely immediate occupancy (IO), life safety (LS), and collapse prevention (CP). The results of the strain-based assessment were evaluated for their ability to capture critical points on the backbone force-deformation curve consistently. The associated plastic hinge rotation and drift ratio for flexure controlled walls and shear controlled walls respectively, was compared to the current limits provided in ASCE-41 for IO, LS, and CP.

The following conclusions can be drawn from the results of the parametric analysis.

The strain-based criteria used herein tends to systematically bias towards a higher deformation value for the IO limit than a calculated effective yield point. This trend is slightly higher for rectangular walls than for barbell walls, but it still generally over-estimates an IO limit higher than the effective yield point. It is critical to note, however, that the IO limit per the qualitative description in ASCE-41 and the proposed acceptable limit for nonlinear procedures is *beyond* what may be considered a 'yield' point. Therefore, the strain-based criteria is not necessarily out of alignment with generally agreed upon qualitative measures of deformation for the IO limit, rather this comparison showcases that the strain-criteria qualifies structural walls for the IO limit about 1.5 times that of an effective yield point.

The strain based criteria systematically determines the LS deformation limit to be 79% of the deformation associated with 90% strength degradation. This is reasonable, as the life safety level should be obtained while the structure has obtained some damage, but still has a margin against collapse per the ASCE 41 guidelines. The CP deformation limit is determined by the strain criteria to systematically occur prior to the structure achieving 50% strength degradation. This is again a good alignment with the qualitative description provided in ASCE-41 which states that the structure should maintain gravity load carrying capacity, but no margin against collapse at the CP limit.

In terms of the comparison of the strain based results to the current assessment guidelines, the following conclusions can be drawn.

- The assessment of non-conforming flexurally-controlled rectangular structural RC walls can be captured with similar levels of statistical dispersion for IO, LS, and CP by ASCE-41 and the herein utilized strain-based criteria. The damage associated with hinge rotation in ASCE 41-23 for IO, LS, and CP are based on expected levels of acceptable qualitative damage. This damage is inherently captured in the strain in the material, and is therefore, by definition, captured by the strain-criteria.

- Non-conforming flexurally-controlled barbell structural walls are captured with similar statistical spread by the strain-based criteria and ASCE 41-23 for IO. However, non-conforming flexurally-dominated barbell structural walls show a larger dispersion in the statistical analysis for the plastic hinge rotation than may be acceptable between the two methods for LS and CP performance levels. As has been noted numerous times, the strain-based assessment criteria assigns performance limits based on the local material damage levels, and has therefore more robust justification for its conclusions. The deformation capacity for LS and CP obtained in the numerical analyses with

the strain-based criteria tends to decrease with increasing normalized shear stress, consistent with the diagonal compression failures obtained in the models, but ASCE 41-23 does not currently consider the influence of this factor for non-conforming walls. It is therefore recommended that the maximum shear stress be incorporated into the assessment procedures of ASCE 41-23 for these non-conforming flexurally dominated barbell structural walls.

- Non-conforming shear-controlled barbell walls do not show good statistical agreement with the ASCE 41-23 procedures and the strain based criteria for appropriate levels of drift at IO, LS, and CP. However, this dataset was relatively small in this study, and thus further evaluation is necessary to draw conclusions relevant for walls of this type.

- Strain-based damage limits have been established for the performance levels defined in ASCE 41 for Immediate Occupancy (IO), Life Safety (LS) and Collapse Prevention (CP) levels. They are related to concrete cover crushing, flexural and diagonal concrete cracking, diagonal concrete crushing, crushing of confined core concrete, and bar rupture. With respect to demand parameters such as hinge deformation or drift ratio, material strains have the advantage of being directly related to the damage conditions that affect structural performance and are independent of wall configuration or external loading. The strain-based criteria has been shown herein to effectively capture all anticipated failure modes from shear to flexure and bar buckling. The strain-based criteria assessment method has been demonstrated with analyses of wall components exhibiting flexure and shear. The values predicted with strain-based criteria at the IO, LS and CP performance level generally follow traditional reference values of strength degradation and are in qualitative alignment with the proposed peer-based acceptance criteria suggested by ASCE-41. The ability of the strain-based criteria to capture relative strength deformation is in good agreement with the general historical knowledge of

the performance limits and typical strength degradation. The reference to traditional strength degradation values such as 10% strength degradation, shows less spread of the results when the specific wall shapes (rectangular vs barbell) are isolated. The strain criteria is thus further assessed with 216 additional numerical models, and it is shown to be particularly effective for planar structural walls modeled with a nonlinear truss analogy.

Chapter 7

Summary, Conclusions, and Future Work

The work presented in this dissertation is focused on the seismic assessment and retrofit of non-ductile reinforced concrete (RC) structural walls. The main goals of this investigation are to i) understand the seismic performance of older non-ductile RC walls, ii) evaluate the effectiveness of retrofit strategies for typical non-ductile inelastic behavior in conjunction with the current ACI 440 Committee (2023) guideline's ability to adequately prevent target failure modes, iii) determine the capability of the nonlinear truss models to capture the experimental response of retrofitted planar walls, iv) create a supplementary body of numerical models indicative of design and construction in the mid-1950s and 1960s in California to consider parameter sensitivity, and v) compare two assessment strategies for the seismic performance of older walls, namely a set of strain-based criteria and the current ASCE-41 (ASCE/SEI-41, 2023) guidelines.

A literature review of previous experimental studies of retrofitted non-ductile RC walls was undertaken. It was found that there were no experimental studies of barbell sections with a concrete overlay retrofit, and very few studies with barbell sections considered with fiber reinforced polymer (FRP) overlays. Additionally, there were no studies considering the current ACI-440 equations of design for retrofit strategies for barbell walls. A review of the analytical methodologies for RC walls and any associated numerical modeling of retrofit

strategies was also undertaken. The nonlinear truss analogy was deemed to be the most efficient while maintaining accuracy for capturing seismic performance. The model can also easily incorporate unique considerations for any project, such as lap splice slip and retrofit overlays. Finally, the current state of assessment for existing walls was examined, together with an overview of previous critical appraisal of existing methods.

7.1 Conclusions Regarding the Experimental Program

An experimental study was conducted at the Thomas M. Murray Structural Engineering and Materials Laboratory at Virginia Tech. Six cantilever half scale RC structural barbell walls were constructed and tested under constant axial and quasi-static cyclic lateral load. The design of the specimens originated from a survey of existing buildings designed and built in the mid-1950s and 60s in California. This resulted in a design with insufficient shear steel in the web, and inadequate confinement of the boundary region. One specimen acted as the control for three subsequent retrofit strategies: one-sided shear web strengthening with concrete overlay, one-sided shear web strengthening with FRP overlay, and shear and bar buckling prevention with FRP overlay wraps on the web and pilasters. Another set of specimens was designed and built with an inadequate lap splice of $24d_b$, and the retrofit strategy was FRP for shear web strengthening and FRP end region wrap to prevent lap splice slip condition.

The following conclusions can be drawn from this experimental program:

- Walls built in accordance with the building codes of the 1950s and 60s may exhibit brittle failure modes associated with shear or lap splice; these vulnerabilities are associated with the presence of very light reinforcement in the web region.
- Shear strengthening strategies for the web region of non-ductile and shear-critical RC

structural walls can be achieved through one-sided retrofit overlays, which prevent the premature occurrence of localized inclined cracks in the web. Both shear strengthening strategies were effective in precluding this brittle shear deformation as described below:

  - A concrete retrofit overlay designed in accordance with the current ACI-318 (2019) code was effective in precluding diagonal tension behavior. A significant remark to make is that the ACI-318 document does not contain anchor design equations for the case that the anticipated anchor stress is less than the yield stress. The so-called Hilti design equations can be used for this case to establish adequate anchorage of the RC overlay (Hilti, 2025).
  - A FRP shear strengthening overlay designed in accordance with ACI-440 guidelines was found to be effective in delaying diagonal tension failure.

- The observed maximum debonding strain exhibited in the FRP shear strengthening overlay was 0.0028, which was slightly higher than the design effective strain 0.0022. This is a very close observed behavior and suggests the current ACI-440 limits for effective design strain are adequate.

- ACI-440 equations for design of lap splice slip prevention were effective in eliminating the occurrence of lap splice failure by mitigating the inadequate bond through an effective clamping force, such that vertical reinforcement bar fracture occurred.

- When shear failure is precluded, the predominant flexural ductility of such walls is primarily limited by the propensity for vertical bar buckling in the pilaster toe regions.

- When considering both shear web strengthening and bar buckling prevention through an FRP wrap 30 inches high and designed according to the equations in ACI-440, the resulting ductility of a RC wall is reduced, compared to the case of the shear web FRP overlay with unwrapped pilasters. The inclusion of both of these retrofit

strategies subsequently leads to a propensity of the wrapped pilaster to exhibit localized tensile cracking, hence increasing local tensile strain demands in the vertical bar and accelerating bar rupture. The increase in local tensile strain demands is attributed to the presence of vertical FRP patches used in conjunction with FRP anchors embedded in the pilasters. The tensile resistance of the epoxy matrix in the horizontal wraps may also impact the strain demands.

- A potential remedy for the previously stated bullet point issue, is to configure the pilaster wrap as a set of discontinuous strips along the height. This strategy may improve the distribution of strains in the pilasters while also enhancing the flexural ductility by delaying bar buckling; this retrofit configuration remains to be experimentally verified.

7.2 Conclusions Regarding Analyses Supplementing the Experimental Program

A numerical analysis was undertaken to assess the capability of the numerical modeling method of the nonlinear truss analogy presented by Deng et al. (2021) to capture the experimental response of retrofitted structures. The method was expanded in this study to consider retrofit overlay elements and lap splice conditions, which may be critical for older structures. The following conclusions may be drawn from the analysis of the experimental specimens using the nonlinear truss approach for planar RC walls:

- The analyses of the unretrofitted specimens gave very good estimates of the overall hysteretic behavior, and captured both specimen's peak strengths within 4.5% of the experimentally obtained value. The non-lap splice specimen analytical results had a slight overestimation (9%) of the deformation capacity at 10% strength loss. The

numerical analysis for the specimen with the lap splice overestimated the deformation capacity at 10% strength loss by 30%. Strain exhibited by the lap splice was within 5% of the measured value, and the numerical model effectively captured the rapid strength degradation exhibited by the lap splice slip condition.

- The modeled wall with the concrete overlay gave a similar force-deformation curve to the experimental results, capturing the peak demand within 5%, and predicting the deformation capacity associated with 10% strength degradation within 1%. The crack opening between the overlay elements with respect to the underlying surface, as measured between the pilaster and the concrete overlay, shows a similar behavior to the experimental results, displaying a numerical displacement of 0.19 inches versus an experimentally measured result of 0.15 inches. The damage pattern at the 2.5% drift ratio showcases damage at the base of the wall, similar to what was observed in the experimental specimen. The 2D planar model effectively captured the bearing capability of the interface between the web and the pilasters, as well as the slip between the overlay and the substrate.

- The model with the FRP interface on the web attached with discreet springs to the pilasters, was capable of capturing the overall force-versus deformation curve very well, particularly with material properties per the manufacturer's *design* material values. The numerical model estimated the peak strength within 6% and the deformation capacity associated with 10% strength loss within 1%. The failure mode of the FRP delamination coincident with anchor pullout is decently captured through the model and can be seen numerically in the high strains of the anchors at the farthest drift cycle.

- The walls with wrapped end-regions assumed a perfect bond in the end regions between the overlay and the substrate. These numerical models estimated the global

peak strengths within 6% of experimental results. The model with the lap splice FRP prevention wrap overestimated the deformation capacity of the actual specimen at 90% of the post peak strength by 62%; this was likely due to the lack of incorporation of the vertical strengthening of the end regions due to the epoxy overlay and vertical FRP patching. The retrofit wraps around the end regions of a wall can also be accounted for indirectly in a truss model, by favorably adjusting the values of model parameters associated with concrete compressive strength and deformability, bar buckling resistance and lap splice strength.

- A comparative analytical study of a prototype structural ductile special RC wall was considered against the performance of two experimental specimens: a unretrofitted non-ductile specimen and a retrofitted non-ductile specimen. The behavior of the modern wall was found to be twice as ductile as the retrofitted specimen, and more than 3 times as ductile as the unretrofitted specimen. These results should be taken with caution, as this is only a component level performance, and the current seismic assessment of existing structures relies on a system wide analysis.

7.3 Conclusions from the Parametric Analytical Study

A parametric study was conducted on a set of 200 rectangular and barbell walls, configured to align with the design and practice of RC structural walls of the 1950s and 1960s from California. The intent of the parametric study was to investigate the sensitivity of any notable parameters such as axial load, reinforcement ratios in the web or end region, spacing of transverse end region stirrups, and web width. Furthermore, the parametric study was undertaken to investigate the ability of the strain-based criteria proposed by Deng et al. (2021) to consistently capture key points of IO, LS, and CP on the envelope force-deformation

curve for RC walls. The parametric study also served as a basis for a comparison to the current guidelines provided by ASCE-41 for acceptance criteria of non-ductile walls.

The strain-based criteria was selected for the assessment of the structures in the parametric study for several reasons. They are a more fundamental consideration that relies on engineering principles, rather than a global drift or rotation allowance. Material strains have the distinct advantage of associating assessment criteria directly with concerns of damage related to and affecting structural performance. They are independent of geometric configuration or external loading. This makes these criteria directly applicable to modern structures as well. Another useful consideration of the strain-based criteria is the ability of the criteria to adapt to unique configurations (i.e. a retrofit overlay or a lap splice condition) by simply appending the existing criteria. This feature was utilized for the study of the experimental specimens.

Any model can implement the strain based criteria described in this work, provided it is capable of faithfully capturing material level behavior, particularly in a softening regime, which is independent of mesh-size effects, and which de-aggregates element strains into horizontal, diagonal, and vertical components.

The following conclusions can be drawn for the strain-based criteria:

- The method has been demonstrated with analyses of wall components exhibiting flexure, shear and lap-splice failures. The proposed drift limits are shown to provide consistent results at the IO, LS and CP performance levels.
  - The criteria was shown to systematically determine the performance limit of immediate occupancy (IO) at a deformation at about 1.5 times that of an effective yield deformation.
  - The criteria was shown to systematically determine the performance limit of life

safety (LS) at approximately 80% of the deformation associated with 10% strength loss.

  - The criteria was shown to systematically determine the performance limit of collapse prevention (CP) at 85% of the deformation associated with 50% strength degradation.

- Overall the strain-based criteria appear to be slightly conservative when compared with the selected strength degradation parameters of 10% strength loss for LS limit comparison and 50% strength loss for CP limit comparison.

- These criteria can be applied to any finite element model that reliably determines vertical, diagonal, and horizontal strains. As long as the model captures valid behavior, especially in the post-peak degradation phase, the strain-based criteria remain applicable.

- These criteria are adaptable to any failure mode limit deemed appropriate to capture, by merely appending the existing criteria with any desired considerations for associated failure modes, without the need to alter the prevailing criteria.

The following conclusions can be drawn from the parametric study.

- Walls with a smaller web width consistently result in higher values of Lw_c/b^2, typically resulting in lower amounts of hinge rotation for each performance limit. Similarly, walls with higher axial load ratios generally exceed performance limits at smaller hinge rotations.

- At higher performance limits (LS and CP) the slenderness parameter considered, s/d_b, indicates that walls with higher values for this slenderness parameter reach exceedance at lower hinge rotations. This is conceptually understood as the higher the slenderness,

the more propensity the structure has for vertical bar buckling, and hence the less deformation capacity it undergoes prior to exceeding damage limits.

- The results of the parametric study indicate that nonconforming flexure-controlled rectangular structural walls show good statistical agreement with the current limits provided in ASCE-41 at drift ratios of IO, LS, and CP. The mean of the numerical-to-code performance limits are close to 1 and the level of dispersion of the predictions is similar to that obtained with the experimental data used to derive the code limits. This indicates that using the strain-based criteria for assessment of these types of structures may provide similar levels of dispersion in the overall results, and it should be appropriate to use the strain-based criteria for assessment. This result is the same for barbell nonconforming flexure-controlled walls at the IO performance limit.

- Nonconforming flexure-controlled barbell walls for the LS and CP limits show a quite wide statistical difference from the limits set forth in ASCE-41 as compared to the strain-based criteria defined limits. The inherent ability of the strain based criteria to be applicable to any wall configuration suggests that the ASCE-41 criteria is slightly too conservative for the limits placed on barbell walls which are nonconforming and flexure-controlled.

- Shear-controlled barbell walls showed deformation capacities which were significantly lower as determined by the strain-based criteria than the ASCE-41 criteria. Further investigation with a larger dataset should be considered to determine the implications of this result with better statistical significance.

7.4 Recommendations for Future Work

Due to the limitations of the numerical investigation, several proposals for future work are deemed necessary. The contextual discussion can be seen in Section 6.5. The recommendations are reiterated here for conciseness:

- Dynamic loading for a full scale numerical model is deemed important to ensure that the correct effects are captured by a shorter structure with an appropriate effective height.
- Building on the previous item, a study which varies the actual effective height, and the aspect ratio value, would be useful in helping to determine how well the influence of effective height can be represented through changes in the normalized shear stress.
- The effects of altering the concrete compressive strength should be investigated, as this is deemed a important parameter, both historically, and in the results of this study.
- The amount of conservatism in the strain-based limits should be considered through additional numerical investigations and more detailed studies, perhaps considering bidirectional seismic loading effects.
- There are other factors in a structural assessment which may be of interest to stakeholders, such as residual drifts, non structural damage, or global stability. It is suggested that a future study incorporate the modeling guidelines of ASCE-41 for non-structural components, to consider the overall performance of both structural and non structural performance, utilizing a combination of the strain-based criteria for assessment of an RC structural wall, and the ASCE-41 criteria for assessment of the non-structural components.

- Further mesh sensitivity studies may be instituted to showcase any influence mesh-size may have for the strain-based assessment.
- Additional simulations in a larger framework may be useful in drawing statistical comparisons of the strain-based criteria to capture IO, LS, and CP behavior for larger and broader groups of structures.

The experimental investigations provided further fodder for future investigations, some of which have been previously mentioned, and are summarized here for conciseness:

- Additional experimental studies may be undertaken to consider the effectiveness of repair and replacement of retrofit strategies which have been slightly damaged, perhaps to the LS level. It is useful to consider the implications of continued repair rather than wholesale replacement of damaged structures.
- Another interesting experimental study may be the retrofit configuration described in Chapter 5 for an FRP discontinuous horizontal end region wrap. The goal of these dispersed horizontal strips would be to confine buckling in a pilaster, while still allowing the dispersal of vertical strains, hopefully leading to a reduction in the formation of highly localized damage and an increase in overall ductility.
- Anchorage of the FRP to the concrete was not investigated in this study; it may be interesting to consider different amounts of anchorage and lengths of FRP fiber anchors to determine minimum cases and to further refine the acceptance criteria for the strain-limits of this failure mode.

References

Abd-Elhamed, A. and Mahmoud, S. (2016). Nonlinear static analysis of reinforced concrete framed buildings - a case study on Cairo earthquake. *Journal of Engineering Research*, 4:1–23.

Abdullah, S. (2019). *Reinforced Concrete Structural Walls: Test Database and Modeling Parameters*. Phd. dissertation, University of California, Los Angeles.

ACI-318 (1956). *ACI 318-56: Building Code Requirements for Reinforced Concrete*. American Concrete Institute.

ACI-318 (2019). *ACI CODE 318-19: Building Code Requirements and Commentary*. American Concrete Association.

ACI-369 (2022). *ACI CODE 369.1-22: Seismic Evaluation and Retrofit of Existing Concrete Buildings—Code and Commentary*. American Concrete Association.

ACI 440 Committee (2017). *440.2-17 Guide for the Design and Construction of Externally Bonded FRP Systems for Strengthening Concrete Structures - Guide*. American Concrete Institute.

ACI 440 Committee (2023). *440.2-23 Guide for the Design and Construction of Externally Bonded FRP Systems for Strengthening Concrete Structures - Guide*. American Concrete Institute.

ACI Committee 506 (2018). ACI spec-506.2-13 specification for shotcrete. Technical report, American Concrete Institute.

Adstran (2024). BTM component, version 1.0.3. http://www.adstran.com/.

REFERENCES

Albright, A., Koutromanos, I., Murcia-Delso, J., Aliasghar-Mamaghani, M., and Pulido, B. (2024). Experimental and analytical evaluation of RC walls with concrete retrofit overlays. In *Eighteenth World Conference on Earthquake Engineering (WCEE): Milan, Italy*.

Aliasghar-Mamaghani, M., Albright, A., Koutromanos, I., Murcia-Delso, J., Brandetsas, C., and Panagiotou, M. (2024). Experimental testing of non-ductile RC walls with and without FRP retrofit. In *Eighteenth World Conference on Earthquake Engineering (WCEE): Milan, Italy*.

Almeida, J., Prodan, O., Tarquini, D., and Beyer, K. (2017). Influence of lap splices on the deformation capacity of RC walls. I: Database assembly, recent experimental data, and findings for model development. *Journal of Structural Engineering*.

Altin, S., Anil, ., Kopraman, Y., and Kara, M. E. (2013). Hysteretic behavior of RC shear walls strengthened with CFRP strips. *Composites Part B: Engineering*, 44(1):321–329.

Alvarez, R., Restrepo, J., and Panagiotou, M. (2020). Rc wall plastic hinge out-of-plane buckling: analysis using the nonlinear beam-truss model. *Journal of Structural Engineering*, 146:04020274:1–20.

Antoniades, K. K., Salonikios, T. N., and Kappos, A. J. (2005). Tests on seismically damaged reinforced concrete walls repaired and strengthened using fiber-reinforced polymers. *Journal of Composites for Construction*, 9(3):236–246. Publisher: American Society of Civil Engineers.

ASCE/SEI-41 (2023). *Seismic Evaluation and Retrofit of Existing Buildings*. American Society of Civil Engineers.

Balaguru, P., Nanni, A., and Giancaspro, J. (2009). *FRP Composites for Reinforced and*

Prestressed Concrete Structures: A Guide to Fundamentals and Design for Repair and Retrofit (1st ed.). CRC Press.

Bazant, Z. P. and Planas, J. (1998). *Fracture and Size Effect in Concrete and Other Quasibrittle Materials*. Routledge.

Birely, A., Lowes, L., Lehman, D., Marley, K., Hart, C., and Kuchma, D. (2010). Investigation of the seismic response of slender planar concrete walls. In *Proceedings of the 9th U.S. National and 10th Canadian Conference on Earthquake Engineering*.

Brueggen, B. L., French, C. E., and Sritharan, S. (2017). T-shaped rc structural walls subjected to multidirectional loading: Test results and design recommendations. *Journal of Structural Engineering*, 143(7):04017040.

Brühwiler, E. and Denarié, E. (2013). Rehabilitation and strengthening of concrete structures using ultra-high performance fibre reinforced concrete. *Structural Engineering International*, 23.

Buniya, M., Barbosa, A., and Sattar, S. (2017). Assessment of a 12-story reinforced concrete special moment frame building using performance-based seismic engineering standards and guidelines: ASCE 41, tbi, and latbsdc. In *SP-339, performance-based seismic design of concrete buildings: State of the practice*.

Cardenas, A. E., Russell, H. G., and Corley, W. G. (1980). Strength of low-rise structural walls. *ACI Symposium Publication*, 63.

CEN (2005). *Eurocode 8: Design of structures for earthquake resistance - Part 3: Assessment and retrofit of buildings*. CEN.

Chakrabarti, A., Menon, D., and Sengupta, A. (2008). *Handbook on Seismic Retrofit of Buildings*. Alpha Science International.

REFERENCES

Coleman, J. and Spacone, E. (2001). Localization issues in force-based frame elements. *Journal of Structural Engineering*, 127(11):1257–1265.

Cook, D. and Sen, A. e. a. (2023). ASCE/SEI 41 assessment of reinforced concrete buildings: Benchmarking nonlinear dynamic procedures with empirical damage observations. *Earthquake Spectra*, 39:1720–1754.

Cortés-Puentes, W. L. and Palermo, D. (2012). Modeling of RC shear walls retrofitted with steel plates or FRP sheets. *Journal of Structural Engineering*, 138(5):602–612. Publisher: American Society of Civil Engineers.

Council, A. T. (1998). *Evaluation of Earthquake Damaged Concrete and Masory Wall Buildings*.

Council, F. A. T. (2023). Nehrp recommended revisions to asce/sei 41-17, seismic evaluation and retrofit of existing buildings. Technical report, FEMA.

Daei, A. and Zarrin, M. (2023). Assessing seismic performance of code-compliant steel special moment frames using ASCE 41-17. *Structures*, 54:764–784.

Dashti, F., Dhakal, R., and Pampanin, S. (2014). Numerical simulation of shear wall failure mechanisms. In *2014 NZSEE Conference*.

Dashti, F., Dhakal, R., and Pampanin, S. (2017). Numerical modeling of rectangular reinforced concrete structural walls. *Journal of Structural engineering*.

Dazio, A., Beyer, K., and Bachmann, H. (2009). Quasi-static cyclic tests and plastic hinge analysis of rc structural walls. *Engineering Structures*, 31(7):1556–1571.

Demirel, I. O., Yakut, A., and Binici, B. (2022). Seismic performance of mid-rise reinforced concrete buildings in izmir bayrakli after the 2020 samos earthquake. *Engineering Failure Analysis*, 137:106277.

REFERENCES

Deng, X., Koutromanos, I., Murcia-Delso, J., and Panagiotou, M. (2021). Nonlinear truss models for strain-based seismic evaluation of planar RC walls. *Earthquake Engineering & Structural Dynamics*, 50(11):2939–2960.

Dodd, L. and Restrepo-Posada, J. (1995). Model for predicting cyclic behaviour of reinforcing steel. *ASCE Journal of Structural Engineering*, 121:433–445.

Dukes, J. and Sattar, S. (2022a). Challenges in determining nonlinear modeling parameters of FRP-retrofitted shear walls. *NIST Internal Publications*.

Dukes, J. and Sattar, S. (2022b). Framework for developing modeling parameters of FRP-retrofitted reinforced concrete shear walls. *NIST*.

Dukes, J. and Sattar, S. (2023). Retrofit and repair of reinforced concrete walls with FRP: A review of experimental investigations. *NIST Internal Publications*.

Dukes, J. D. and Sattar, S. (2020). Development of a database of experimental tests on FRP retrofitted reinforced concrete shear walls. *NIST*.

El-Kashif, K., Adly, K., and Abdalla, H. (2019). Finite element modeling of RC shear walls strengthened with CFRP subjected to cyclic loading. *Alexandria Engineering Journal*.

El-Sokkary, H. and Galal, K. (2013). Seismic behavior of RC shear walls strengthened with fiber-reinforced polymer. *Journal of Composites for Construction*, 17(5):603–613. Publisher: American Society of Civil Engineers.

El-Sokkary, H., Galal, K., Ghorbanirenani, I., Léger, P., and Tremblay, R. (2013). Shake table tests on FRP-rehabilitated RC shear walls. *Journal of Composites for Construction*, 17(1):79–90. Publisher: American Society of Civil Engineers.

Elnady, M. (2008a). *Seismic Rehabilitation of RC Structural Walls*. Phd. dissertation, McMaster University.

Elnady, M. E. (2008b). Seismic Rehabilitation of RC Structural Walls.

Elnashai, A., Pilakoutas, K., and N.N., A. (1990). Experimental behaviour of reinforced concrete walls under earthquake loading. *Earthquake Engineering and Structural Dynamics*, 19.

Epackachi, S., Sharma, N., Whittaker, A., and Hortacsu, A. (2018). A cyclic backbone curve for squat reinforced concrete shear walls. In *Eleventh U.S. National Conference on Earthquake Engineering: Los Angeles, California*.

FEMA (2004). 389 primer for design professionals. Technical report, Federal Emergency Management Agency.

FEMA (2006). 574 techniques for the seismic rehabilitation of existing buildings. Technical report, Federal Emergency Management Agency.

FEMA (2018a). *P-2006 Example Application Guide for ASCE/SEI 41-13, Seismic Evaluation and Repair of Existing Buildings with Additional Commentary for ASCE/SEI 41-17*. Federal Emergency Management Agency.

FEMA (2018b). *P-2018 Seismic Evaluation of Older Concrete Buildings for Collapse Potential*. Federal Emergency Management Agency.

fib Bulletin 90 (2019). Externally applied FRP reinforcement for concrete structures, bulletin 90. Technical report, Fédération internationale du béton (fib).

Fintel, M. (1995). Performance of buildings with shear walls in earthquakes of the last thirty years. *PCI Journal*, 40:62–80.

Fiorato, A. E., Oesterle, R. G., and Corley, W. (1983). Behavior of earthquake resistant structural walls before and after repair. In *ACI Journal Proceedings*.

REFERENCES

Franssen, R., Courard, L., and Mihaylov, B. (2021). Shear behavior of concrete walls retrofitted with ultra- high-performance fiber-reinforced concrete jackets. *ACI Structural Journal*, 118.

Galan, I., Baldermann, A., and et. al. (2019). Durability of shotcrete for underground support - review and update. *Construction and Building Material*.

Girgin, S., Moharrami, M., and Koutromanos, I. (2018). Nonlinear beam-based modeling of RC columns including the effect of reinforcing bar buckling and rupture. *Earthquake Spectra*, 34:1289–1309.

Harris, J. and Speicher, M. (2018). Assessment of performance-based seismic design methods in ASCE 41 for new steel buildings: Special moment frames. *Earthquake Spectra*, 34.

Hernández-Bassal, Laura, L., and Kunnath, Sashi, K. (2020). Assessing ASCE-41 acceptance criteria for linear and nonlinear procedures using instrumented building data. In *SIMP20*.

Hilti (2025). Interface shear transfer design using the Hilti method for post installed rebar design. https://ask.hilti.com/article/shear-friction-design-using-hilti-method-for-post-installed-rebar-design/63jbgp.

Hiotakis, S. (2004). *Repair and strengthening of reinforced concrete shear walls for earthquake resistance using externally bonded carbon fibre sheets and a novel anchor system*. Phd. dissertation, Carleton University.

Ichikawa, S., Matsuzaki, H., Moustafa, A., ElGawady, M. A., and Kawashima, K. (2016). Seismic-resistant bridge columns with ultrahigh-performance concrete segments. *Journal of Bridge Engineering*, 21(9):04016049.

Iliya, R. and Bertero, V. V. (1980). 'effects of amount and arrangement of wall-panel rein-

forcement on hysteretic behaviour of reinforced concrete walls. Technical report, Earthquake Engineering Research Center.

Işık, E., Avcil, F., Hadzima-Nyarko, M., İzol, R., Büyüksaraç, A., Arkan, E., Radu, D., and Özcan, Z. (2024). Seismic performance and failure mechanisms of reinforced concrete structures subject to the earthquakes in türkiye. *Sustainability*, 16(15).

Jin, L., Zhang, B., Chen, F., and Du, X. (2024a). Cfrp-strengthened shear walls: Combined effects of and reinforcement ratio. *International Journal of Mechanical Sciences*, 282:109634.

Jin, L., Zhang, B., Chen, F., Miao, L., and Du, X. (2024b). Experimental investigation on the size-dependent shear contribution in-strengthened RC shear wall. *Engineering Structures*, 307.

Jin, L., Zhang, B., Chen, Z., and Du, X. (2023). Dynamic contribution of CFRP strips to CFRP-strengthened RC shear walls. *International Journal of Mechanical Sciences*.

Joseph, R., Mwafy, A., and Alam, M. S. (2022). Seismic performance upgrade of substandard RC buildings with different structural systems using advanced retrofit techniques. *Journal of Building Engineering*, 59:105155.

Kabeyasawa, T., Shiohara, H., Otani, S., and Aoyama, H. (1983). Analysis of the full-scale sevenstory reinforced concrete test structure. *Journal of the Faculty of Engineering*, pages 431–478.

Kalfat, R., Al-Mahaidi, R., and Smith, S. T. (2013). Anchorage devices used to improve the performance of reinforced concrete beams retrofitted with frp composites: State-of-the-art review. *Journal of Composites for Construction*, 17(1):14–33.

REFERENCES

Kam, W. Y. and Pampanin, S. (2011). The seismic performance of RC buildings in the 22 february 2011 christchurch earthquake. *Structural Concrete*, 12(4):223–233.

Khalil, A. and Ghobarah, A. (2005). Behaviour of rehabilitated structural walls. *Journal of Earthquake Engineering*, 9(3):371–391. Publisher: Taylor & Francis.

Kim, S. H. and Koutromanos, I. (2016). Constitutive model for reinforcing steel under cyclic loading. *Journal of Structural Engineering*, 142(12):04016133. Publisher: American Society of Civil Engineers.

Kolozvari, K., Orakcal, K., and Wallace, J. (2015). Modeling of cyclic shear-flexure interaction in reinforced concrete structural walls. i: theory. *ASCE J Struct Eng.*

Koutromanos, I. (2024). Femultiphys: A finite element program for the analysis of continua and structures [version 4].

Layssi, H., Cook, W., and Mitchell, D. (2012). Seismic response and CFRP retrofit of poorly detailed shear walls. *Journal of Composites for Construction*, 16:332–339.

Le Nguyen, K., Brun, M., Limam, A., Ferrier, E., and Michel, L. (2014). Pushover experiment and numerical analyses on CFRP-retrofit concrete shear walls with different aspect ratios. *Composite Structures*, 113:403–418.

Lefas, I., Kotsovos, M., and Ambraseys, N. (1990). Behavior of reinforced concrete structural walls: Strength, deformation characteristics, and failure mechanism. *ACI Structural Journal*, 87.

Li, Z., Balendra, T., Tan, K., and Kian Hau, K. (2005). Finite element modeling of cyclic behavior of shear wall structure retrofitted using GFRP.

Linde, P. (1993). Numerical modelling and capacity design of earthquake-resistant reinforced concrete walls. *Diss. Techn. Wiss. ETH.*

REFERENCES

Lombard, J., Lau, D. T., Humar, J. L., Foo, S., and Cheung, M. S. (2000). Seismic strengthening and repari of reinforced cocnrete walls. *12th World Conference on Earthquake Engineering*, page 8.

Lowes, L., Lehman, D., Birely, A., Kuchma, D., Marley, K., and Hart, C. (2012). Earthquake response of slender planar concrete walls with modern detailing. *Engineering Structures*.

Lu, Y. and Panagiotou, M. (2014). Three-dimensional cyclic beam-truss model for nonplanar reinforced concrete walls. *Journal of Structural Engineering*, 140(3):04013071.

Lu, Y., Panagiotou, M., and Koutromanos, I. (2016). Three-dimensional beam-truss model for reinforced concrete walls and slabs – part 1: modeling approach, validation, and parametric study for individual reinforced concrete walls. *Earthquake Engineering & Structural Dynamics*, 45(9):1495–1513.

Maffei, T., Heintz, and Dragovich (2012). Practical recommendations for concrete wall design, based on studies of the 2010 chile earthquake. In *Proceedings 15th World Conference of Earthquake Engineering*.

Mander, J., Priestley, M. N., and Park, R. (1988a). Theoretical stress-strain model for confined concrete. *Journal of Structural Engineering*, 114:1804–1826.

Mander, J. B., Priestley, M. J. N., and Park, R. (1988b). Theoretical stress-strain model for confined concrete. *Journal of Structural Engineering*, 114(8):1804–1826.

Marini, A. and Meda, A. (2009). Retrofitting of r/c shear walls by means of high performance jackets. *Engineering Structures*.

Massone, L. M., Orakcal, K., and Wallace, J. (2009). Modeling of squat structural walls controlled by shear. *ACI Struct J.*, pages 646–655.

REFERENCES

Mostofinejad, D. and Mohammadi Anaei, M. (2012). Effect of confining of boundary elements of slender RC shear wall by FRP composites and stirrups. *Engineering Structures*, 41:1–13.

Murcia-Delso, J., Koutromanos, K., Escobar, K., and Albright, A. (2025). Seismic analysis of RC walls retrofitted with fiber reinforced composites using nonlinear truss models. In *12th International Conference on FRP Composites in Civil Engineering*.

Nagib, M., Sakr, M., El-khoriby, S., and Khalifa, T. (2021). Cyclic behaviour of squat reinforced concrete shear walls strengthened with ultra-high performance fiber reinforced concrete. *Engineering Structures*, 246.

NBC (2015). *Structural Commentaries (User's Guide -NBC 2015: Part 4 of Division B)*. National Research Council of Canada. Code council: National Research Council of Canada and Canadian Commission on Building and Fire Codes.

NBC (2020). *National Building Code of Canada 2020*. National Research Council of Canada.

Neale, K. W. (2000). Frps for structural rehabilitation: a survey of recent progress. *Progress in Structural Engineering and Materials*, 2:133–138.

Oesterele, R. G. (1976). *Earthquake Resistant Structural Walls*. Research and Development Construction Technology Laboratories, Portland Cement Association.

Oesterle, R., Aristizabal-Ochoa, J., Shiu, K., and Corley, W. (1984). Web crushing of reinforced concrete structural walls. *ACI Journal Proceedings*.

Oesterle, R., Fiorato, A., Russell, H., and Corley, W. (1979). *Earthquake Resistant Structural Walls Tests of Isoalted Walls - Phase II*.

Orakcal, K. and Wallace, J. W. (2006). Flexural modeling of reinforced concrete walls - experimental verification. *ACI Structural Journal*, 103(2):196 – 206.

Orakcal, K., Wallace, J. W., and Conte, J. P. (2004). Nonlinear modeling and analysis of slender reinforced concrete walls. *ACI Structural Journal*, 101(5):688 – 698.

Palermo, D. and Vecchio, C. (2002). *Behaviour and analysis of reinforced concrete walls subjected to reversed cyclic loading*. Phd. dissertation, University of Toronto.

Palieraki, V., Vintzileou, E., and Trezos, K. (2014). Shear transfer along interfaces: Constitutive laws. In *Proceedings of the 2nd European Conference on Earthquake Engineering and Seismology, Istanbul, Turkey*.

Pan, Y., Wang, X., Guo, R., and Yuan, S. (2018). Seismic damage assessment of nepalese cultural heritage building and seismic retrofit strategies: 25 april 2015 Gorkha (Nepal) earthquake. *Engineering Failure Analysis*, 87:80–95.

Panagiotou, M., Koutromanos, I., Mavros, M., Deng, X., Alvarez, R., Engineers, M., Restrepo, J. I., Murcia-Delso, J., and Acero, G. (2021). Nonlinear beam-truss model (BTM) for seismic performance evaluation of reinforced concrete wall buildings. In *2021 SEAOC Convention At San Diego,CA*, page 17.

Panagiotou, M. and Restrepo, J. (2011). Displacement-based method of analysis for regular reinforced-concrete wall buildings: application to a full-scale 7-story building slice tested at uc–san diego. *ASCE Journal of Structural Engineering*, 137:677–690.

Panagiotou, M., Restrepo, J., and Conte, J. (2011). Shake-table test of a full-scale 7-story building slice. phase i: Rectangular wall. *ASCE Journal of Structural Engineering*, 137:691–704.

Panneton, M., Léger, P., and Tremblay, R. (2006). Inelastic analysis of a reinforced concrete shear wall building according to the national building code of canada 2005. *Canadian Journal of Civil Engineering*, 33(7):854–871.

REFERENCES

Park, R. (1989). Ductility evaluation from laboratory and analytical testing. In *Bulletin of the New Zealand national society for earthquake engineering*, volume 22, pages 155–166.

Paterson, J. and Mitchell, D. (2003). Seismic retrofit of shear walls with headed bars and carbon fiber wrap. *ASCE Journal of Structural Engineering*.

Paulay, T. and Goodsir, W. j. (1985). The ductility of structural walls. *Bulletin of the New Zealand National Society for Earthquake Engineering*.

Paulay, T. and Priestly, M. (1992). *Seismic Design of Reinforced Concrete and Masonry Buildings*. John Wiley & Sons, LTD.

Prakasam, G. and Murthy, A. (2019). Repair, retrofitting and rehabilitation techniques for strengthening of reinforced concrete beams - a review. *Advances in Concrete Construction*, 8:101–117.

Priestley, M., Calvi, G. nd Kowalsky, M., and Powell, G. (2008). Displacement-based seismic design of structures. *Earthquake Spectra*.

Priestley, M. and Kowalsky, M. (1998). Aspects of drift and ductility capacity of rectangular cantilever structural walls. *Bulletin of the New Zealand Society for Earthquake Engineering*, 31:73–85.

Priestley, M. J. N., Seible, F., and Calvi, G. M. (1996). *Retrofit Design*, chapter 8, pages 585–653. John Wiley & Sons, LTD.

Prudêncio, L. R. (1998). Accelerating admixtures for shotcrete. *Cement and Concrete Composites*, 20:213–219.

Puntel, E., Bolzon, G., and Saouma, V. (2006). Fracture mechanics based model for joints under cyclic loading. *ASCE Journal of Engineering Mechanics*, 132:1151–1159.

REFERENCES

Qazi, S., Michel, L., and Ferrier, E. (2015). Impact of CFRP partial bonding on the behaviour of short reinforced concrete wall under monotonic lateral loading. *Composite Structures*, 128:251–259.

Qazi, S., Michel, L., and Ferrier, E. (2019). Seismic behaviour of RC short shear wall strengthened with externally bonded strips. *Composite Structures*, 211:390–400.

Rajbhandari, P., Yeow, T. Z., Mukai, D., and Kono, S. (2025). Strain-based performance evaluation of planar flexural reinforced concrete walls. *Engineering Structures*, 327:119643.

Raza, S., Khan, K., Menegon, S., Tsang, H., and Wilson, J. (2019). Strengthening and repair of reinforced concrete columns by jacketing: State-of-the-art review. *Sustainability*, page 3208.

Sakr, M. A., El-khoriby, S. R., Khalifa, T. M., and Nagib, M. T. (2019). Modeling of RC shear walls strengthened with ultra-high performance fiber reinforced concrete (UHPFRC) jackets. *Engineering Structures*, 200:109696.

Salonikios, T., Kappos, A., Tegos, I., and Penelis, G. (1999). Cyclic load behavior of low-slenderness r/c walls: Design basis and test results. *ACI Structural Journal*, 96:pp 649–660.

Sattar, S. (2018). Evaluating the consistency between prescriptive and performance-based seismic design approaches for reinforced concrete moment frame buildings. *Engineering Structures*, 174:919–931.

Sattar, S. and Hulsey, A. (2015). Assessment of first generation performance-based seismic design methods: Case study of a 4-story reinforced concrete special moment frame building. In *ASCE Structures Congress*.

Schädlich, B. and Schweiger, H. (2014). A new constitutive model for shotcrete. In *Numerical*

Methods in Geotechnical Engineering - Proceedings of the 8th European Conference on Numerical Methods in Geotechnical Engineering, NUMGE 2014, volume 1, page 103–108.

Schütz, R., Potts, D., and Zdravkovic, L. (2011). Advanced constitutive modelling of shotcrete: Model formulation and calibration. *Computers and Geotechnics*, 38(6):834–845.

Shegay, A. V., Motter, C. J., Elwood, K. J., and Henry, R. S. (2019). Deformation capacity limits for reinforced concrete walls. *Earthquake Spectra*, 35(3):1189–1212.

Shendkar, M., Tantri, A., and Rao, A. U. (2025). Seismic evaluation and retrofit of reinforced concrete structures. *Journal of Infrastructure Preservation and Resilience*, 6.

Strotmann, A. and Jungwirth, J. (2022). Crack control for repair and strengthening of reinforced concrete structures using the multi-cracking behaviour of ultra-high performance fibre reinforced shotcrete (uhpfrsc). In *International Conference on Concrete Repair, Rehabilitation and Retrofitting*.

Tarquini, D., Pacheco Almeida, J., and Beyer, K. (2017). Influence of lap splices on the deformation capacity of RC walls. ii: Shell element simulation and equivalent uniaxial model. *Journal of Structural Engineering*, 23.

Teng, J. G., Chen, J. F., Smith, S. T., and Lam, L. (2002). *FRP-strengthened RC structures*. Wiley, London.

Teng, J. G., fei Chen, J., Smith, S. T., and Lam, L. (2001). *FRP: Strengthened RC Structures*. John Wiley & Sons, LTD.

Thomsen, J. H. and Wallace, J. W. (1995). Displacement-based design of reinforced concrete structural walls: Experimental studies of walls with rectangular and t-shaped cross sec-

tions, report no. cu/cee-95/06. Technical report, Department of Civil and Environmental Engineering, Clarkson University, Potsdam, NY.

Vallenas, J. M., Bertero, V. V., and Popov, E. P. (1979). Hysteric behavior of reinforced concrete structural walls. Technical report, Earthquake Engineering Research Center.

Vecchio, F. and Collins, M. (1986). The modified compression-field theory for reinforced concrete elements subjected to shear. *Journal of the American Concrete Institute*, 83:219–231.

Vecchio, F., Peña, O., Bucci, F., and Palermo, D. (2002). Behavior of repaired cyclically loaded shearwalls. *ACI Structural Journal*, 99:327–334.

Vulcano, A. and Bertero, V. (1986). Nonlinear analysis of r/c structural walls. In *Proceedings of the 8th European Conference on Earthquake Engineering, Lisbon, Portugal*.

Whitman, Z. (2015). Investigation of seismic failure modes in flexural concrete walls using finite element analysis. Master's thesis, University of Washington.

Woods, J. E., Lau, D. T., and Cruz-Noguez, C. A. (2016). In-plane seismic strengthening of nonductile reinforced concrete shear walls using externally bonded CFRP sheets. *Journal of Composites for Construction*, 20(6):04016052. Publisher: American Society of Civil Engineers.

Zealand, S. N. (2017). *Seismic Assessment of Existing Buildings, Part C5: Concrete buildings*. Ministry of Business, Innovation, and Employment. Ministry of Business and Innovation and Employment and the Earthquake Commission and the New Zealand Society for Earthquake Engineering and the Structural Engineering Society and the New Zealand Geotechnical Society.

REFERENCES

Zhang, Z., Li, B., and Qian, K. (2016). Experimental investigations on seismically damaged nonrectangular reinforced-concrete structural walls repaired by FRPs. *Journal of Composites for Construction*, 20(1):04015033. Publisher: American Society of Civil Engineers.

İlker Kazaz, Gülkan, P., and Yakut, A. (2012). Performance limits for structural walls: An analytical perspective. *Engineering Structures*, 43:105–119.

Appendices

Appendix A

Strain Gauge Labels

This appendix contains the full names for each strain gauge on the experimental specimens. This can be used in reference with the raw data for analysis.

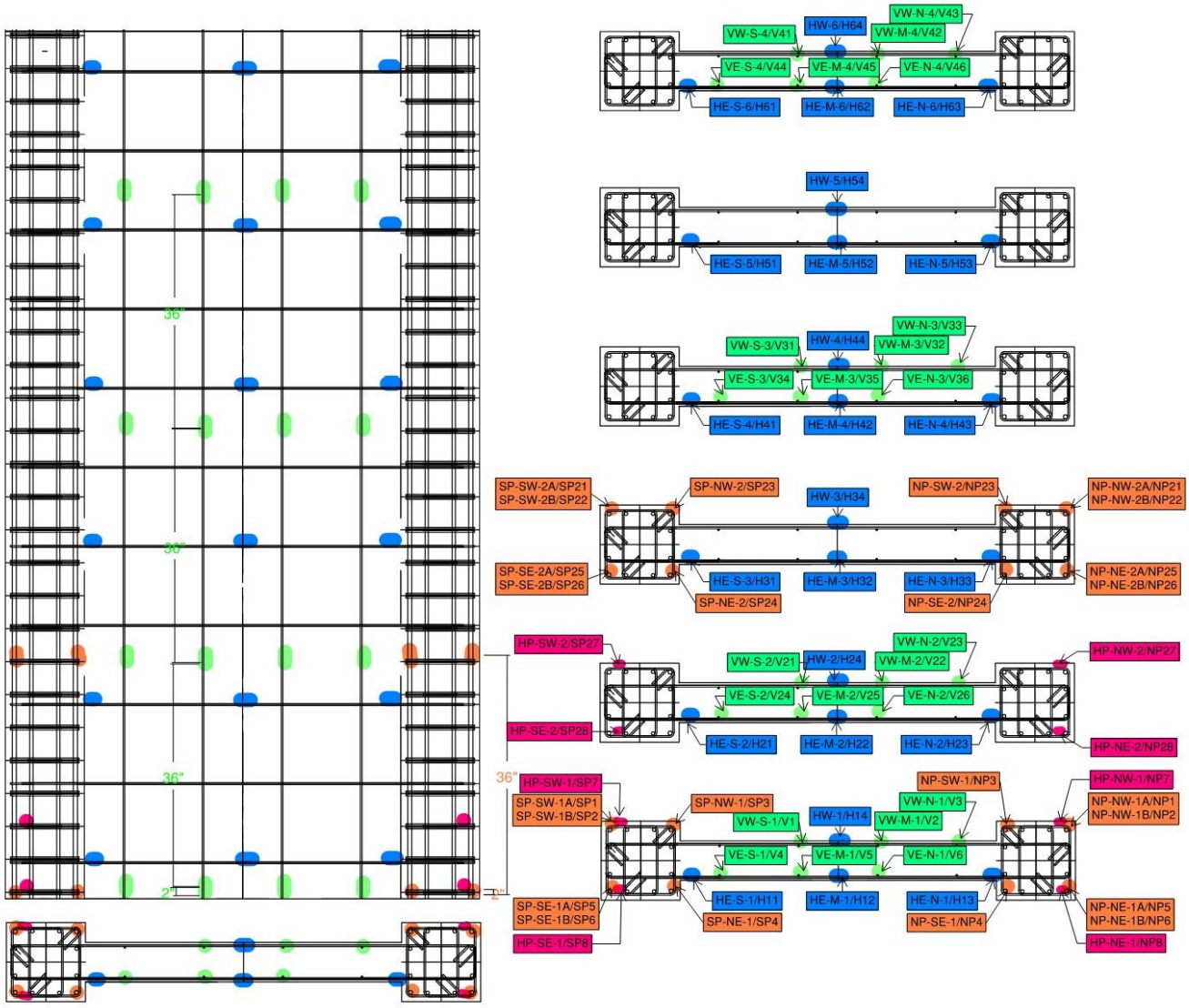

Figure A.1: Strain Gauge Labels

Appendix B

Shear Strain Calculations

This appendix outlines the components of deformation for the specimen.

The shear component of deformation is calculated by determining the shear strain exhibited by the grid of string pots installed on the wall web.

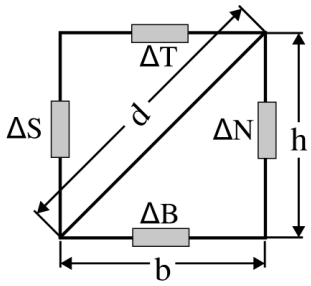

Figure B.1: Undeformed Square Panel

The vertical and horizontal deformations are averaged between the two string pot measurements in the appropriate direction, as shown in Equations 2.1 and 2.2

$$\Delta_v = \frac{\Delta S + \Delta N}{2} \qquad \text{(Eq. 2.1)}$$

$$\Delta_h = \frac{\Delta B + \Delta T}{2} \qquad \text{(Eq. 2.2)}$$

The shear strain can be calculated directly from:

$$\gamma = \frac{\sqrt{(d + \Delta D_s)^2 - (h + \Delta_v)^2} - (b + \Delta_h)}{h + \Delta_v} \qquad \text{(Eq. 2.3)}$$

ΔD_s is the isolated shearing deformation. The extension of vertical and horizontal deforma-

tion, ΔD_{vh}, must be removed in order to effectively determine the shearing deformation

$$\Delta D_s = \Delta D - \Delta D_{vh} \quad \text{(Eq. 2.4)}$$

$$\Delta D_{vh} = \sqrt{(b + \Delta_h)^2 + (h + \Delta_v)^2} - d \quad \text{(Eq. 2.5)}$$